

Dissertation
submitted to the
Combined Faculties of the Natural Sciences and Mathematics
of the Ruperto-Carola-University of Heidelberg. Germany
for the degree of
Doctor of Natural Sciences

Put forward by
Victoria Elisabeth Wagner
born in: Darmstadt
Oral examination: 25.01.2017

Pulse Shape Analysis for the GERDA Experiment
to Set a
New Limit on the Half-life of $0\nu\beta\beta$ Decay of ^{76}Ge

Referees:

Prof. Dr. Manfred Lindner

Juniorprofessorin Dr. Loredana Gastaldo

Pulsformanalyse im GERDA-Experiment zur Bestimmung einer neuen Untergrenze der Halbwertszeit des neutrinolosen Doppelbetazerfalls von ^{76}Ge

Das GERDA-Experiment sucht nach dem neutrinolosen Doppelbetazerfall ($0\nu\beta\beta$) von ^{76}Ge . Dazu werden hochreine Germanium-Halbleiterdetektoren (HPGe) in flüssigem Argon (LAr) betrieben. Ziel des GERDA-Experiments ist es, Halbwertszeiten dieses Zerfalls in der Größenordnung von 10^{26} Jahren zu testen. Dabei wird auf aktive Methoden zur Untergrundunterdrückung gesetzt, wie auf Pulsformanalyse (PSA), welche den zeitliche Verlauf der Germanium Signale analysiert, um signal- von untergrundähnlichen Ereignissen zu unterscheiden. Zum einen werden in GERDA semi-koaxiale Detektoren aus vorherigen Experimenten, aber auch neuartige BEGe (Broad Energy Germanium)-Detektoren mit verbesserter Energieauflösung und Untergrunddiskriminierung verwendet.

Fünf BEGe-Detektoren wurden zum ersten Mal für die Suche nach dem $0\nu\beta\beta$ -Zerfall in GERDA Phase I eingesetzt. Eine PSA basierend auf dem Verhältnis der maximalen Amplitude des Strompulses und der deponierten Energie wurde angewandt. 83% der Untergrundereignisse in einem 232 keV breiten Fenster um die Signalregion wurden verworfen, wobei eine hohe Signaleffizienz von $(92.1 \pm 1.9)\%$ erhalten wurde. Ein Untergrundindex (BI) von $(5.4_{-3.4}^{+4.1}) \cdot 10^{-3} \frac{\text{Ereignisse}}{\text{keV} \cdot \text{kg} \cdot \text{yr}}$ wurde erreicht, welcher eine Größenordnung besser ist, als in vorangegangenen Germanium-basierten $0\nu\beta\beta$ -Experimenten.

Zur weiteren Untergrundunterdrückung in Phase II, wurde der LAr-Kryostat zur Auslese von Argon-Szintillationslicht ausgestattet, das sogenannte LAr-Veto. Des Weiteren wurden 25 neue BEGe-Detektoren eingebaut. Dank PSA und LAr-Veto wird ein BI von $(0.7_{-0.5}^{+1.3}) \cdot 10^{-3} \frac{\text{Ereignisse}}{\text{keV} \cdot \text{kg} \cdot \text{yr}}$ erreicht. Dies ist der bisher niedrigste BI in $0\nu\beta\beta$ -Experimenten. Eine frequentistische statistische Analyse der kombinierten Daten aus GERDA Phase I und Phase II wurde durchgeführt. Es konnte eine neue Untergrenze von $5.3 \cdot 10^{25}$ Jahren bei 90% C.L. auf die Halbwertszeit des $0\nu\beta\beta$ -Zerfalls von ^{76}Ge gesetzt werden, bei einer mittleren Sensitivität von $T_{1/2}^{0\nu} > 4.0 \cdot 10^{25}$ Jahren bei 90% C.L.

Pulse Shape Analysis for the GERDA Experiment to Set a New Limit on the Half-life of $0\nu\beta\beta$ Decay of ^{76}Ge

The GERDA experiment searches for neutrinoless double beta ($0\nu\beta\beta$) decay of ^{76}Ge using high purity germanium (HPGe) detectors operated in liquid argon (LAr). The aim is to explore half-lives of the order of 10^{26} yr. Therefore, GERDA relies on improved active background reduction techniques such as pulse shape discrimination (PSD) in which the time structure of the germanium signals is analyzed to discriminate signal- from background-like events. Two types of HPGe detectors are operated: semi-coaxial detectors previously used in the Heidelberg-Moscow and IGEX experiments and new Broad Energy Germanium (BEGe) detectors which feature an improved energy resolution and enhanced PSD.

In Phase I of the experiment, five enriched BEGe detectors were used for the first time in the search for $0\nu\beta\beta$ decay. A PSD based on a single parameter, the ratio of the maximum current amplitude over the energy A/E is applied. 83% of the background events in a 232 keV region around $Q_{\beta\beta}$ are rejected with a high signal efficiency of $(92.1 \pm 1.9)\%$. The achieved background index (BI) is $(5.4_{-3.4}^{+4.1}) \cdot 10^{-3} \frac{\text{counts}}{\text{keV} \cdot \text{kg} \cdot \text{yr}}$. This is an improvement by a factor of 10 compared to previous germanium based $0\nu\beta\beta$ experiments.

Phase II of the experiment includes a major upgrade: for further background rejection, the LAr cryostat is instrumented to detect argon scintillation light. Additional 25 BEGe detectors are installed. After PSD and LAr veto a BI of $(0.7_{-0.5}^{+1.3}) \cdot 10^{-3} \frac{\text{counts}}{\text{keV} \cdot \text{kg} \cdot \text{yr}}$ is achieved. This is the best BI achieved in $0\nu\beta\beta$ experiments so far.

A frequentist statistical analysis is performed on the combined data collected in GERDA Phase I and the first Phase II release. A new limit on the half-life of $0\nu\beta\beta$ decay of ^{76}Ge is set to $T_{1/2}^{0\nu} > 5.3 \cdot 10^{25}$ yr at 90% C.L., with a median sensitivity of $T_{1/2}^{0\nu} > 4.0 \cdot 10^{25}$ yr at 90% C.L.

Contents

List of Tables	IX
List of Figures	XI
1 Introduction	1
2 Introduction to Neutrino Physics	3
2.1 Neutrinos as a Door to Physics beyond the Standard Model	3
2.2 Neutrinoless Double Beta Decay	14
3 The Germanium Detector Array Experiment	25
3.1 Working Principle of Germanium Detectors	25
3.2 The GERDA Experiment	30
3.3 The GERDA Phase II Upgrade	33
4 Pulse Shape Discrimination Using BEGe Detectors	41
4.1 Signal vs Background Events	42
4.2 Pulse Shape of BEGe Detectors	47
4.3 The A/E Parameter	50
4.4 A/E as Background Reduction Technique in GERDA	55
4.5 Pulse Shape Analysis of BEGe Detectors for GERDA Phase I	58
4.6 Pulse Shape Discrimination for Non-BEGe Type Detectors	64
4.7 Summary	66
5 From Phase I to Phase II: Integration and Commissioning of the GERDA Upgrade	69
5.1 Detector Assembly and Integration	69
5.2 New Phase II Electronics	78
5.3 Background Suppression with LAr Veto and Pulse Shape Analysis	80
5.4 Effect of Noise on Pulse Shape Analysis	83
5.5 Summary	86

6	Pulse Shape Analysis for BEGe Detectors in GERDA Phase II	87
6.1	The BEGe Data Set	88
6.2	Calibration of the A/E Parameter	92
6.3	The A/E Cut	96
6.4	Suppression of ^{228}Th with Pulse Shape Discrimination	98
6.5	$0\nu\beta\beta$ Signal Efficiency of the A/E Cut	100
6.6	Application of the A/E Cut on Physics Data	102
6.7	Background Index of GERDA Phase II BEGe Data Set	108
6.8	Comparison to Phase I Background	109
6.9	Summary	111
7	Limit on the Half-life of $0\nu\beta\beta$ Decay of ^{76}Ge	113
7.1	Data Sets	113
7.2	The Profile Likelihood Method	116
7.3	New Limit on the Half-life of $0\nu\beta\beta$ Decay of ^{76}Ge	118
8	Summary and Discussion	121
	Appendix A Statistical Calculation	127
	Appendix B Decay Schemes of GERDA Background	131
	Appendix C Phase II HPGe Detectors	135
	Appendix D Data Processing: Extraction of A/E Parameter	137
	Appendix E Pulse Shape Analysis of BEGe Detectors in GERDA Phase I	141
	Appendix F Phase II Run Summary	159
	Appendix G A/E Stability in Phase II	161
	Appendix H Comparison of Background Indices of $0\nu\beta\beta$ Experiments	165
	Bibliography	169
	Acknowledgement	177

List of Tables

List of Tables

2.1	Standard Model Particle Content	4
2.2	Neutrino Mixing Parameters	10
2.3	List of $0\nu\beta\beta$ Candidate Isotopes	20
3.1	Properties of Semiconductors	25
3.2	Phase I Background Composition in ROI	34
3.3	Activity of Phase II Detector Holders	36
3.4	Preliminary Phase II Background Model	38
4.1	Summary of Rejection and Survival Fractions in GERDA Phase I BEGe Data Set	59
4.2	$0\nu\beta\beta$ Signal Efficiency of A/E Cut in Phase I	62
5.1	Summary of Phase II Runs	73
5.2	Test Results for Phase-I-like FE and Phase-II VFE	78
5.3	Survival Fractions after PSD and LAr Veto in GERDA Phase II Commissioning	80
6.1	Low and High A/E Cut Positions in Phase II	98
6.2	Rejection and Survival Fractions of ^{228}Th Calibration and Physics Data of Phase II BEGe Data Set	99
6.3	Uncertainties on Signal Efficiency of Phase II A/E Cut	101
7.1	Summary of GERDA Data Sets	114
7.2	Events in ROI	116
7.3	GERDA Sensitivity on $T_{1/2}$ Limit	120
8.1	Comparison of BI for Different $0\nu\beta\beta$ Experiments	123
C.1	Phase II Detector Summary	136
F.1	Summary of GERDA Phase II Runs	160

G.1	<i>A/E</i> Stability for GERDA Phase II BEGe Data Set	164
H.1	Comparison of BI of Different $0\nu\beta\beta$ Experiments	166

List of Figures

List of Figures

2.1	Neutrino Interaction Vertex	5
2.2	Inverse β -decay	7
2.3	Oscillation of Atmospheric Neutrinos Observed by SuperKamiokande	8
2.4	Neutrino Mass Ordering	11
2.5	The Mass Parabola	14
2.6	Feynman Diagram for $2\nu\beta\beta$ and $0\nu\beta\beta$ Decay	15
2.7	$2\nu\beta\beta$ and $0\nu\beta\beta$ Spectrum	16
2.8	Effective Majorana Mass	17
2.9	Effective Majorana Mass vs. Smallest Neutrino Mass	18
2.10	Matrix Elements for $0\nu\beta\beta$ Isotopes	19
3.1	Band Gap of Insulator and Semiconductor	26
3.2	GERDA HPGe Detector Types	29
3.3	Schematic of the GERDA Experiment	31
3.4	GERDA Phase I Array	32
3.5	GERDA Phase I Background Spectrum	33
3.6	Phase II Detector Assembly	35
3.7	Phase II Signal Read-out	37
3.8	Preliminary Phase II Background	37
3.9	Signal vs Background Discrimination	38
3.10	Phase II LAr Instrumentation	39
4.1	Total Photon Cross Section in Germanium	42
4.2	^{228}Th Calibration Spectrum	43
4.3	Simulated ^{228}Th Calibration Spectrum	44
4.4	SSE Fraction of Compton, FEPs and SEP Events	46
4.5	RMS Distribution of DEP and $0\nu\beta\beta$ Events	47
4.6	SSE Fraction of DEP and $0\nu\beta\beta$ Events	48
4.7	Schematic View of BEGe Detector	49

4.8	Weighting Potential of BEGe Detector	49
4.9	Simulated SSE and MSE Pulses	49
4.10	Simulated Pulses Close to the p^+ Contact	50
4.11	^{228}Th Measurement: A/E vs. Energy	51
4.12	A/E Distribution in DEP, FEP, SEP and Compton Region	52
4.13	A/E Distribution of Compton Events and Empirical Fit Function	52
4.14	Simulated A/E Distribution vs Event RMS	54
4.15	A/E Energy Dependence	55
4.16	Experimental Pulse Shapes of MSE, p^+ and n^+ Contact Events	56
4.17	A/E Physics Spectrum of GERDA Phase I BEGe Data Set	60
4.18	A/E Distribution of Physics Events in GERDA Phase I BEGe Data Set	60
4.19	Physics Spectrum of the GERDA Phase I BEGe Data Set	61
4.20	Charge and Current Pulse of the Unblinded Phase I BEGe Event at 2036.6 keV	63
4.21	Weighting Potential and Signal of Semi-coaxial HPGe Detector	64
4.22	Weighting Potential of PPC-type HPGe Detector	65
5.1	Detector Assembly	71
5.2	Assembly of the GERDA Germanium Detector Array	72
5.3	Time-line of the Installation of the GERDA Phase II Upgrade.	74
5.4	Final Installation of the LAr Veto System	75
5.5	Final Detector Configuration of the GERDA Phase II Germanium Detector Array	77
5.6	New Single BEGe Holders	77
5.7	The GERDA Pilot String	79
5.8	^{228}Th Calibration Spectrum with LAr Veto and PSD	81
5.9	^{226}Ra Calibration Spectrum with LAr Veto and PSD	82
5.10	Noise Power Spectrum of GD35B during Phase I, Run 50 and Run 53	84
5.11	A/E Resolution vs Noise Integral	84
5.12	A/E Resolution vs Energy	85
6.1	Example Traces of Pile-up Events	89
6.2	Pre-trigger Pile-up Cut	89
6.3	Calibration Spectrum with Pile-up Cut	90
6.4	A/E Stability for GD61A in Phase II BEGe Data Set	91
6.5	Normalized A/E distribution after Long-term Correction	93
6.6	Stability of A/E During Calibration	93
6.7	A/E Energy Dependence	94
6.8	Energy Dependence of A/E Resolution	94
6.9	A/E of DEP vs Compton at 1593 keV	95
6.10	A/E Distribution of DEP and Physics Events in the Energy Region (1.0- 1.3) MeV	96
6.11	A/E FWHM in DEP of Phase II BEGe Detectors	97
6.12	Survival Fractions in ^{228}Th Calibrations	100
6.13	Rejection Fraction of High A/E Cut	101
6.14	A/E Physics Spectrum of Phase II BEGe Data Set	102
6.15	Example of Physics Events in (2039 ± 200) keV	103
6.16	Survival Efficiency in ^{228}Th Calibration and Physics Data	104
6.17	Physics Spectrum after A/E Cut in $2\nu\beta\beta$ Region	105
6.18	Physics Spectrum Rejected by Low A/E Cut	107

6.19	Physics Spectrum Rejected by High A/E Cut	108
6.20	Unblinded Physics Spectrum of Phase II BEGe Data Set	109
6.21	Comparison of A/E Distributions in GERDA Phase I and Phase II	110
7.1	GERDA Physics Spectra in ROI	115
7.2	Limit on $0\nu\beta\beta$ Decay	119
7.3	GERDA Phase II Sensitivity on $1/T_{1/2}^{0\nu}$ Limit	120
A.1	Background Subtraction in Peak Regions	129
B.1	Decay Schemes of ^{42}Ar and ^{42}K	132
B.2	Decay Scheme of ^{60}Co	132
B.3	Decay Scheme of ^{68}Ge and ^{68}Ga	133
D.1	Data Processing with GELATIO	139

The search for neutrinoless double beta ($0\nu\beta\beta$) decay is a topic of broad and current interest in modern astro-particle physics. Its observation would unambiguously prove lepton number violation, implying new physics beyond the Standard Model of particle physics. Furthermore, if $0\nu\beta\beta$ -decay is allowed, neutrinos must have a Majorana mass component.

The germanium detector array (GERDA) experiment searches for the $0\nu\beta\beta$ decay of ^{76}Ge , one of the few candidate isotopes. Bare high purity germanium (HPGe) detectors are operated in liquid argon (LAr) which serves as coolant and shield of the detectors against background radiation. The GERDA experiment uses two different types of HPGe detector designs: semi-coaxial detectors previously used in the Heidelberg-Moscow [1] and IGEX [2] experiments and new Broad Energy Germanium (BEGe) detectors. To explore half-lives of the $0\nu\beta\beta$ decay of the order of 10^{26} yr, a background index (BI) as low as $10^{-3} \frac{\text{counts}}{\text{keV} \cdot \text{kg} \cdot \text{yr}}$ is needed. Therefore, the GERDA experiment relies on improved active background reduction techniques such as pulse shape analysis (PSA): the time structure of the germanium signals is analyzed to discriminate signal- from background-like events. The new BEGe HPGe detectors feature an enhanced pulse shape discrimination (PSD) compared to the semi-coaxial design.

The GERDA experiment proceeds in two phases: in Phase I of the experiment, eight semi-coaxial and five BEGe detectors were operated. This was the first time BEGe detectors were used in the search for $0\nu\beta\beta$ decay. In Phase II, additional 25 BEGe detectors are deployed. For further background reduction, the GERDA cryostat is instrumented to detect argon scintillation light.

The work presented in this thesis focuses on the PSA of BEGe detectors in GERDA Phase I and Phase II, the integration and commissioning of the GERDA Phase II upgrade, and the final statistical analysis on the half-life of the $0\nu\beta\beta$ decay of ^{76}Ge using the combined Phase I and Phase II data.

This thesis is organized as follows: Chapter 2 gives a brief introduction into neutrino physics with focus on $0\nu\beta\beta$ decay. The GERDA experiment is introduced in Chapter 3.

Chapter 4 discusses the basic concept of the discrimination of signal- from background-like events. The PSA method is based on the ratio of the maximum amplitude of the current pulse over the energy, A/E , and has been developed in [3] for prototype BEGe detectors in vacuum cryostat. In GERDA Phase I, the PSA of BEGe detectors was performed by a group of people. The author of this thesis made a leading contribution to the calibration of the A/E cut and the determination of the signal efficiency after the analysis cut.

The integration of the GERDA Phase II upgrade is presented in Chapter 5. The author of this work is part of the team that assembled the new detector array with special focus on the mounting of the new detector modules. Results from the commissioning of the Phase II array and the LAr instrumentation are presented. As PSD is a key ingredient to achieve the envisioned BI goal, the analysis focuses on the PSD performance which has been performed by the author of this work. The analysis of the LAr veto has been done by A. Wegmann and C. Wiesinger.

The author of this work was responsible for the PSA of the BEGe data in GERDA Phase II. The performed analysis is presented in Chapter 6.

In Chapter 7 a statistical analysis of the combined GERDA Phase I and Phase II data sets is presented using a frequentist approach. The analysis is performed in cooperation with B. Schwingenheuer and is intended as a cross-check of the analysis published in [4].

Part of the work presented in this thesis and the achieved results are published in [4, 5, 6].

Introduction to Neutrino Physics

This chapter will give a short introduction to neutrino physics. So far only upper limits on neutrino masses exist and neutrinos are massless in the Standard Model of particle physics. However, neutrino oscillations unambiguously prove that three neutrinos have different masses. Hence, at least two must have a non-vanishing mass while the lightest could be massless.

Section 2.1 will give a short overview of the experimental prove of neutrino oscillations as well as the theory behind. The actual mechanism to generate neutrino masses remains unknown. As electrical neutral particles, neutrinos may be Majorana particles. If so, lepton number is not a conserved quantum number and neutrinoless double beta ($0\nu\beta\beta$)-decay may occur.

In Section 2.2 the phenomenology of $0\nu\beta\beta$ -decay is discussed. A short summary of the different experimental approaches as well as the current status is given.

The following discussion on neutrino physics is partly taken from [7, 8].

2.1 Neutrinos as a Door to Physics beyond the Standard Model

The Standard Model (SM) of particle physics describes the elementary particles and their interactions. Matter consists of spin- $\frac{1}{2}$ particles, so-called fermions, and force mediators, spin-1 particles, the gauge bosons. The four fundamental forces are the electromagnetic, the weak and the strong force as well as gravitation. The electromagnetic and the weak interaction are unified in the electro-weak interaction. Since there is no complete theory of quantum gravity, it is not included in the SM. Furthermore, the gravitational force is small compared to the other three forces and therefore considered as negligible in elementary particle physics: the Fermi constant characterizing the coupling strength of the weak interaction is $G_F = 1.2 \times 10^{-5}$ whereas Newton's constant, describing the gravitational strength, is only $G_N = 6.7 \times 10^{-39}$ (in natural units $\hbar = c = 1$) [9].

Fermions that underly the strong interaction are called quarks, fermions not interacting strongly are called leptons. Leptons carry a quantum number called *lepton number* $L = +1$, anti-leptons $L = -1$. Up to now there are six known quarks and six leptons which can be divided into three generations of four fermions each: two quarks, one charged lepton and one neutrino. Within a generation the particles are distinct for their electro-weak interaction. Table 2.1 summarizes the SM particle content.

Particle masses and coupling constants giving the strength of the interaction as well as

generation	I	II	III	
quarks				
	up	charm	top	
mass [MeV]	2.3	1275	173.21×10^3	
charge [e]	$\frac{2}{3}$	$\frac{2}{3}$	$\frac{2}{3}$	
	down	strange	bottom	
mass [MeV]	4.8	95	4180	
charge [e]	$-\frac{1}{3}$	$-\frac{1}{3}$	$-\frac{1}{3}$	
leptons				
	e	μ	τ	
mass [MeV]	0.511	105.7	1776.82	
charge	1	1	1	
	ν_e	ν_μ	ν_τ	
mass				
charge	0	0	0	
gauge bosons				
	Z⁰	W[±]	γ	gluons
mass [MeV]	91.19×10^3	80.39×10^3		
charge	0	± 1	0	0
Higg bosons				
	Higgs			
mass [MeV]	125.09×10^3			
charge	0			

Table 2.1: Particle zoo of the Standard Model of particle physics. The masses are taken from [9]. For neutrinos, photon (γ) and gluons only upper limits exists and are not listed since they are massless in the SM.

mixing parameters need to be determined experimentally. Until present the SM proves to be a successful theory. However, it cannot describe massive neutrinos and therefore, cannot be completed. Since neutrino physics experiments are highly challenging, our current knowledge of neutrinos is not yet sufficient to identify the most appropriate extension of the SM describing massive neutrinos.

In the following the discussion will concentrate on neutrinos and the weak interaction. A detailed introduction to the SM and neutrino physics is beyond the scope of this thesis. More details can be found in [10, 11, 12].

Neutrinos and their Interaction

In the Standard Model of particle physics *neutrinos* are massless, neutral leptons. Consequently, neutrinos participate only in weak interactions. There are three neutrino species, each associated with a charged lepton: electron-neutrino, ν_e , muon-neutrino, ν_μ , and tau-neutrino, ν_τ . The weak interaction is mediated by massive gauge bosons: W^\pm and Z^0 .

A typical weak process is the β^- -decay, in which a neutron decays into a proton emitting an electron and electron-antineutrino, $n \rightarrow p + e^- + \bar{\nu}_e$. It is observed that weak interactions

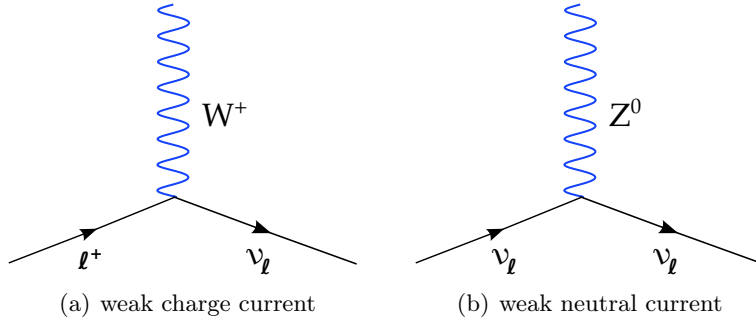


Figure 2.1: Feynman diagrams for the neutrino interaction vertex. The time axis is vertical from left to right.

violate parity, the symmetry which reflects all spatial coordinates at the origin, i.e. $\vec{x} \rightarrow -\vec{x}$. If parity was conserved, any process and its mirrored realization would occur with the same probability. However, Wu et al. [13] could show that in the β -decay of ^{60}Co the electron is predominantly emitted in the direction opposite to the spin of the ^{60}Co mother nucleus, which indicates parity violation.

Weak interactions are maximally parity violating: only left-handed particles and right-handed anti-particles couple to W^\pm . Goldhaber et al. [14] showed that neutrinos are always left-handed, and anti-neutrinos right-handed. A left-handed particle means that the direction of the spin is opposite to the direction of motion. However, this concept of *helicity* is not Lorentz invariant, as for a massive particle one can always find a reference frame faster than the particle. In this reference frame the particle appears to move in the opposite direction. As the spin is untouched, the helicity of the particle is changed. Therefore, each massive left-handed particle has a right-handed component which scales with the ratio of the particle mass over its energy.

Formally, the SM is a quantum field theory. The basic concept is that the particles are described as quantum fields, ψ . The weak interaction is associated with the quantum number *weak isospin*, T . According to their weak interactions, leptons are grouped into left-handed¹ doublets with $T = \frac{1}{2}$ and right-handed singlets with $T = 0$:

$$\begin{aligned} & \begin{pmatrix} \nu_e \\ e^- \end{pmatrix}_L \quad \begin{pmatrix} \nu_\mu \\ \mu^- \end{pmatrix}_L \quad \begin{pmatrix} \nu_\tau \\ \tau^- \end{pmatrix}_L \quad \begin{array}{l} \text{with } T_3 = +\frac{1}{2} \\ \text{with } T_3 = -\frac{1}{2} \end{array} \\ & \begin{pmatrix} e^- \end{pmatrix}_R \quad \begin{pmatrix} \mu^- \end{pmatrix}_R \quad \begin{pmatrix} \tau^- \end{pmatrix}_R \quad \text{with } T_3 = 0 \end{aligned}$$

The weak hypercharge is given by $Y_w = 2(Q - T_3)$ whereas Q is the electric charge.

The quantum field theory is specified by a Lagrange density $\mathcal{L}(\psi, \partial\psi)$. The equation of motion for the fields is the Euler-Lagrange equation

$$-\partial_\mu \left(\frac{\partial \mathcal{L}}{\partial(\partial_\mu \psi)} \right) + \frac{\partial \mathcal{L}}{\partial \psi} = 0. \quad (2.1)$$

The SM Lagrangian for a neutrino can be written as

$$\mathcal{L}_\nu = \sum_{\alpha=e,\mu,\tau} [\bar{\nu}_{\alpha L} i \not{\partial} \nu_{\alpha L} + \frac{g}{\sqrt{2}} (W_\mu^+ \bar{\nu}_{\alpha L} \gamma^\mu \ell_{\alpha L} + \text{h.c.}) + \frac{g}{2 \cos \theta_w} Z_\mu \bar{\nu}_{\alpha L} \gamma^\mu \nu_{\alpha L}]. \quad (2.2)$$

¹Here, the left-handed chirality state is meant. In case of massless particles chirality and helicity are the same.

The lengthy expression can be interpreted as follows: the first is the kinetic term, the second and third are interaction terms. If neutrinos have a non-vanishing mass a corresponding mass term needs to be included. The mass term will be discussed later this section. The Lagrangian is a sum over all three neutrino flavors. The subscript L denotes the left-handed particles. The second term in Equation 2.2 describes the weak charge current. It can be easily interpreted using a Feynman diagram as shown in Figure 2.1(a): ℓ annihilates a charged lepton e, μ, τ or creates an anti-lepton, $\bar{\nu}$ creates a neutrino or annihilates an anti-neutrino. Thus, the term $\bar{\nu}_{\alpha L} \gamma_{\mu} \ell_{\alpha}$ couples left-handed leptons to left-handed neutrinos. W^+ creates or annihilates a gauge boson. The coupling strength to the (charged) lepton and neutrino is given by $\frac{g}{\sqrt{2}}$. The third term in Equation 2.2 is depicted in Figure 2.1(b) in analogy to the charged current: a Z^0 boson couples with the strength $\frac{g}{2 \cos \theta_w}$ to a neutrino and an anti-neutrino.

Neutrino Sources

Neutrinos are produced in nuclear processes, such as β -decays. Various artificial and natural neutrino sources exist. The Sun produces neutrinos in fusion processes, so-called solar neutrinos. Astrophysical sources of neutrinos are e.g. supernovae and gamma ray bursts (GRB). Furthermore, a relic neutrino background from the early Universe is expected to exist similar to the cosmic microwave background (CMB). Radioactive isotopes in the Earth produce neutrinos in β -decays, so-called geo neutrinos. Neutrinos are also produced by the interaction of cosmic rays in the atmosphere, i.e. atmospheric neutrinos. An artificial anti-neutrino source are nuclear reactors. Intense neutrino beams are produced in accelerators.

1968: First Discovery of Solar Neutrinos and the Solar Neutrino Problem

The net reaction to produce energy in the Sun is the fusion of four protons $4p \rightarrow {}^4\text{He} + 2e^+ + 2\nu_e$ producing two electron neutrinos.

The first to detect solar neutrinos were Ray Davis et al. [15, 16]. The experiment was located in the Homestake mine in South Dakota. In a huge chlorine tank the neutrinos were detected by the reaction ${}^{37}\text{Cl} + \nu_e \rightarrow {}^{37}\text{Ar} + e^-$. Subsequently, the ${}^{37}\text{Ar}$ atoms were extracted and detected via β -decay: ${}^{37}\text{Ar} \rightarrow {}^{37}\text{Cl} + e^- + \bar{\nu}_e$.

However, the observed solar neutrino flux was only about a third of the expectation [17]. An obvious conclusion would be that either the experiment, the solar model or the calculated neutrino cross-section was wrong.

Further experiments using a similar approach than the chlorine experiment, confirmed the flux deficit in solar neutrinos: GALLEX/GNO [18, 19] and SAGE [20] detect electron neutrinos via the reaction ${}^{71}\text{Ga} + \nu_e \rightarrow {}^{71}\text{Ge} + e^-$.

The deficit is called the *solar neutrino problem*. Pontecorvo suggested that the ν_e are converted into other neutrino species, namely ν_{μ} or ν_{τ} , for which Davis' experiment was insensitive [21].

1998: Prove of Oscillation of Atmospheric Neutrinos

Super-Kamiokande [22] showed evidence for oscillation of atmospheric neutrinos [23]. Cosmic rays, mainly protons, collide with nuclei in the upper atmosphere and produce hadronic showers. These showers contain charged pions, π^{\pm} and Kaons, K^{\pm} . Atmospheric neutrinos

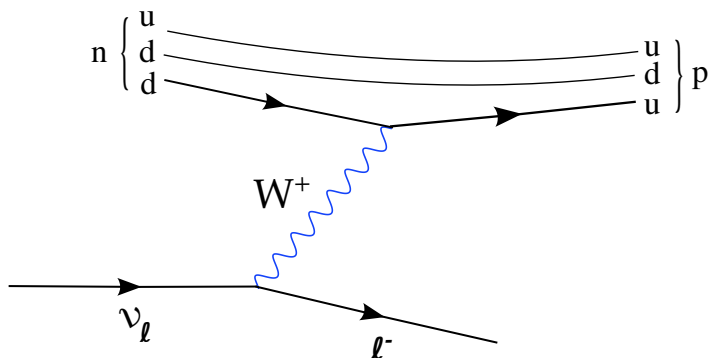


Figure 2.2: Feynman diagram of inverse β -decay $n + \nu_\ell \rightarrow p + \ell^-$: a neutrino of flavor ℓ interacts with a nucleon via the exchange of a W -boson. The charged current reaction changes the neutron into a proton ($d \rightarrow u$ at the quark level) and the neutrino is converted into a lepton of flavor ℓ .

originate from the subsequent decays:

$$\begin{aligned} \pi^+, K^+ &\rightarrow \mu^+ + \nu_\mu & \text{and} & & \pi^-, K^- &\rightarrow \mu^- + \bar{\nu}_\mu \\ \mu^+ &\rightarrow e^+ + \nu_e + \bar{\nu}_\mu & & & \mu^- &\rightarrow e^- + \bar{\nu}_e + \nu_\mu \end{aligned}$$

From this simple equation one expects a ratio of $N_{\nu_\mu} : N_{\nu_e} = 2 : 1$.

Super-Kamiokande is a Japanese underground experiment initially built to search for proton decay. It is a tank filled with 50 kt of ultra pure water. The walls are equipped with photomultiplier tubes (PMTs) to detect Cerenkov light. The latter is emitted by charged particles if they move faster than the speed of light in the surrounding material. The detection principle is based on the inverse β -decay as shown in Figure 2.2:

$$\begin{aligned} \nu_\alpha + n &\rightarrow \ell_\alpha + p \\ \bar{\nu}_\alpha + p &\rightarrow \bar{\ell}_\alpha + n \end{aligned}$$

where $\alpha = e^\pm, \mu^\pm$. The e^\pm/μ^\pm in the final state produce Cerenkov light in the water. Electron and muon events are distinguished by the shape of the resulting light cone: while muons produce a single cone, electrons produce electromagnetic showers which result in a fuzzy light cone. Due to their heavy masses (compare Table 2.1) τ 's are produced below the detection threshold or do not produce a clean ring which can be used for particle identification [24]. Super-Kamiokande measured a muon-to-electron-neutrino ratio of [25]

$$\frac{\frac{N_{\nu_\mu}}{N_{\nu_e}}|_{\text{observed}}}{\frac{N_{\nu_\mu}}{N_{\nu_e}}|_{\text{expected}}} = 0.63 \pm 0.06$$

Thus, more ν_e were observed with respect to the expected ν_μ .

The light cone allows to reconstruct the direction of the charged leptons, which in turn is correlated with the direction of the incoming neutrino. Figure 2.3 shows the observed flux of identified ν_e and ν_μ for different directions. The observed electron-neutrino flux is in good agreement with expectations, the observed muon-neutrino flux is not: Super-Kamiokande observed a deficit in the flux of muon-neutrinos traversing the earth, while those directly coming from the atmosphere are in agreement with predictions [23]. The observation is explained by the fact that neutrinos oscillate, i.e. the ν_μ traversing the Earth have converted into other neutrino species while the ones coming directly from above have not. The favored explanation is the oscillation of ν_μ into ν_τ .

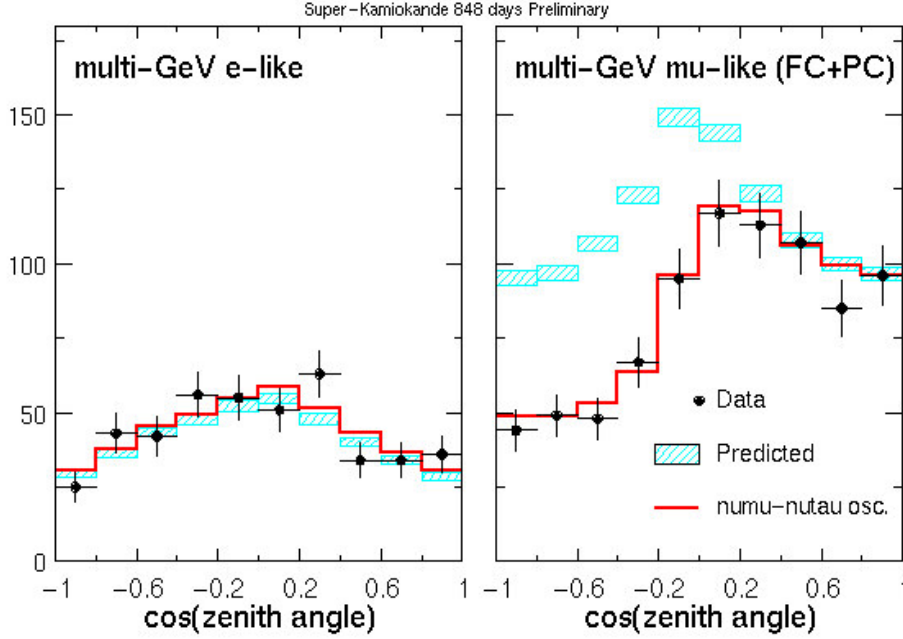


Figure 2.3: Electron and muon-neutrino flux as a function of the direction measured by Super-Kamiokande. $\cos(\text{zenith angle}) = -1$ means that neutrinos are *up-going*, i.e. originating from the other hemisphere and have thus, traveled about 10000 km through the Earth between production and detection. *Down-going* neutrinos have $\cos(\text{zenith}) = +1$. Such neutrinos originate in the atmosphere above the detector location and have traveled only about 10-100 km. One expects to see the same number of up- and down-going neutrinos. The flux should slightly increase towards $\cos(\text{zenith}) = 0$ (i.e. side-ways) since the atmosphere is seen under an increased angle. Figure taken from [26].

2002: Solution to the Solar Neutrino Problem

The Sudbury Neutrino Observatory (SNO) [27] showed that solar neutrinos oscillate and solved the solar neutrino problem. SNO is a Cerenkov detector filled with 1 kt of heavy water, D_2O . Neutrinos are detected via three different channels:

- **charged current:** $\nu_e + \text{d} \rightarrow \text{p} + \text{p} + e^-$ is only possible for ν_e ,
- **elastic scattering:** $\nu + e \rightarrow \nu + e$ is possible for all neutrino species. The dominant contribution, however, is from ν_e as the cross-section of ν_e scattering is highest,
- **neutral current:** $\nu + \text{d} \rightarrow \nu + \text{p} + \text{n}$ dissociation of deuterium is possible for all neutrino species.

The neutral current interaction is flavor independent. Thus, the total solar neutrino flux is measured. The observed flux is in agreement with the solar model [28]. The measured flux of non-electron neutrinos is a strong evidence for neutrino oscillation: since ν_μ and ν_τ cannot be produced in the Sun, the missing ν_e have converted into ν_μ/ν_τ .

Takaaki Kajita from the Super-Kamiokande Observatory and Arthur McDonald from the Sudbury Neutrino Observatory (SNO) were awarded the 2015 Nobel Prize for Physics

for the discovery of neutrino oscillations, which shows that neutrinos have mass [29].

Neutrino Oscillation

Neutrino oscillation can be interpreted as the interference between different wave packages with different group velocities. Thus, in order to observe neutrino oscillation the wave packages need to be coherent, i.e. the separation of the packages needs to be less than their width.

In the following neutrino oscillation is discussed using a quantum mechanical approach with flavor and mass eigenstates. Neutrinos are produced as flavor eigenstates α ($\alpha = e, \mu, \tau$) which are a superposition of the mass eigenstates i ($i = 1, 2, 3$) given by

$$|\nu_\alpha\rangle = \mathcal{U}_{\alpha i}^* |\nu_i\rangle \quad (2.3)$$

where the mixing matrix, the PMNS matrix, is parameterized as

$$\mathcal{U} = \begin{pmatrix} 1 & 0 & 0 \\ 0 & \cos \theta_{23} & \sin \theta_{23} \\ 0 & -\sin \theta_{23} & \cos \theta_{23} \end{pmatrix} \begin{pmatrix} \cos \theta_{13} & 0 & \sin \theta_{13} e^{-i\delta} \\ 0 & 1 & 0 \\ -\sin \theta_{13} e^{i\delta} & 0 & \cos \theta_{13} \end{pmatrix} \begin{pmatrix} \cos \theta_{12} & \sin \theta_{12} & 0 \\ -\sin \theta_{12} & \cos \theta_{12} & 0 \\ 0 & 0 & 1 \end{pmatrix} \quad (2.4)$$

$$\times \text{diag}(1, e^{i\alpha}, e^{i\beta})$$

with the three mixing angles θ_{ij} , $i, j = 1, 2, 3$. The Dirac-phase δ is the possible source of CP violation in neutrino oscillations. If neutrinos are Majorana particles two additional phases, α and β , need to be considered.

The initial neutrino state can be written as: $|\nu(0)\rangle = |\nu_\alpha\rangle = \sum_j \mathcal{U}_{\alpha j}^* |\nu_j\rangle$ with the time evolution $|\nu(t)\rangle = \sum_j \mathcal{U}_{\alpha j}^* e^{-iE_j t} |\nu_j\rangle$.

The probability to find $|\nu_\beta\rangle = \sum_i \mathcal{U}_{\beta i}^* |\nu_i\rangle$ is given by [30]

$$\mathcal{P}(\nu_\alpha \rightarrow \nu_\beta) = |\langle \nu_\beta | \nu(t) \rangle|^2$$

$$= \delta_{\alpha\beta} - 4 \cdot \sum_{j>i} \text{Re}\{J_{\alpha\beta}^{ij}\} \sin^2 \frac{\Delta_{ij}}{2} + 2 \cdot \sum_{j>i} \text{Im}\{J_{\alpha\beta}^{ij}\} \sin \Delta_{ij} \quad (2.5)$$

with $J_{\alpha\beta}^{ij} = \mathcal{U}_{\beta i} \mathcal{U}_{\alpha i}^* \mathcal{U}_{\beta j}^* \mathcal{U}_{\alpha j}$. The phase can be approximated as $\frac{1}{2} \Delta_{ij} \approx 1.27 \left(\frac{\Delta m_{ij}^2}{\text{eV}^2} \right) \left(\frac{L}{\text{km}} \right) \left(\frac{\text{GeV}}{E} \right)$, where E is the neutrino energy, L the distance between neutrino source and detector and Δm_{ij}^2 is the mass-squared difference of mass eigenstate i and j .

Equation 2.5 shows that for neutrino oscillation between three flavors, the three mass eigenstates must be non-degenerate. Therefore, at least two neutrinos must be massive. Since neutrinos are massless in the SM, massive neutrinos comprise physics beyond the SM. Up to nine new parameters need to be introduced and determined in experiments: three mixing angles, three neutrino masses, one Dirac CP violating phase and in case of Majorana neutrinos two Majorana phases. The latter, α and β in Equation 2.4, have no influence on oscillations as they drop out and show up only in lepton number violating processes (see next section for details).

parameter	normal mass ordering	inverted mass ordering
$\sin^2 \theta_{12}$	0.856 + 0.012	
Δm_{21}^2	$(7.53 + 0.18) \times 10^{-5} \text{ eV}^2$	
$\sin^2 2\theta_{23}$	$0.999^{+0.001}_{-0.018}$	$1.000^{+0.000}_{-0.017}$
Δm_{32}^2	$(2.44 \pm 0.06) \times 10^{-3} \text{ eV}^2$	$(2.46 \pm 0.06) \times 10^{-3} \text{ eV}^2$
$\sin^2 2\theta_{13}$	$(8.5 \pm 0.5) \times 10^{-2}$	

Table 2.2: Mixing parameters and mass squared differences obtained by analysis using three-neutrino mixing. Taken from [9].

Neutrino oscillations are sensitive only to the mass-squared differences and further depend on the ratio L/E . If $\alpha = \beta$, Equation 2.5 gives the survival probability between the flavors α and β , for $\alpha \neq \beta$ the transition probability. Neutrino experiments can be divided into appearance and disappearance experiments: appearance experiments search for flavors different from the initial. Disappearance experiments investigate if the neutrino flux of the initial flavor state decreases or if the spectral shape changes with observation distance L .

Since experimentally $\Delta m_{21}^2 \ll |\Delta m_{31}^2| \simeq \Delta m_{32}^2$, most oscillation phenomena can approximately be treated as oscillations between two flavors. The oscillation of atmospheric neutrinos is predominantly the conversion of muon-neutrinos into tau neutrinos and is well described by a two neutrino oscillation: θ_{13} is small and $\frac{\Delta m_{12}^2 L}{E} \ll 1$ (which means in principle that the oscillation driven by Δm_{12}^2 has not yet developed). The observed mixing angle θ_{atm} is associated with θ_{23} and $\Delta m_{atm}^2 = \Delta m_{23}^2$. Similar approximations hold for the survival probability of solar neutrino experiments: in a two-neutrino oscillation framework the mixing angle θ_{\odot} is associated with θ_{12} and $\Delta m_{\odot}^2 = \Delta m_{12}^2$. Table 2.2 summarizes the measured neutrino mixing and mass-squared differences.

The sign of Δm_{\odot}^2 is determined via matter effects. Since neutrinos interact with matter, they can experience coherent forward scattering. All neutrino flavors interact via neutral current interactions with the electrons in matter, while only electron neutrinos interact via charged current interactions. The coherent forward scattering changes the oscillation in matter with respect to vacuum. The effective mixing angle in matter is given by [30]

$$\sin^2 2\theta_{\text{matter}} = \frac{\sin^2 2\theta}{(\cos 2\theta - \frac{A}{\Delta m^2})^2 + \sin^2 2\theta} \quad (2.6)$$

with $A \equiv 2\sqrt{2}G_F N_e E$, where G_F is the Fermi constant, N_e the electron density and E the neutrino energy. For anti-neutrinos A changes sign. For $A \rightarrow 0$ ($N_e \rightarrow 0$) one obtains vacuum oscillations. In the resonant case ($\cos 2\theta = \frac{A}{\Delta m^2}$) the neutrino oscillation probability is maximized, even for small θ . In the Sun a total conversion of ν_e into $\nu_{\mu/\tau}$ is possible [31], which is called the MSW effect. Equation 2.6 shows that the oscillation in matter depends on the sign of Δm^2 . Using the solar neutrino data the sign of Δm_{\odot}^2 is found to be positive, i.e. $m_1^2 < m_2^2$.

Depending on the sign of Δm_{31}^2 , one distinguishes two different neutrino mass orderings as shown in Figure 2.4:

- **normal ordering (NO):** $m_1 \ll m_2 < m_3$
- **inverted ordering (IO):** $m_3 \ll m_1 < m_2$

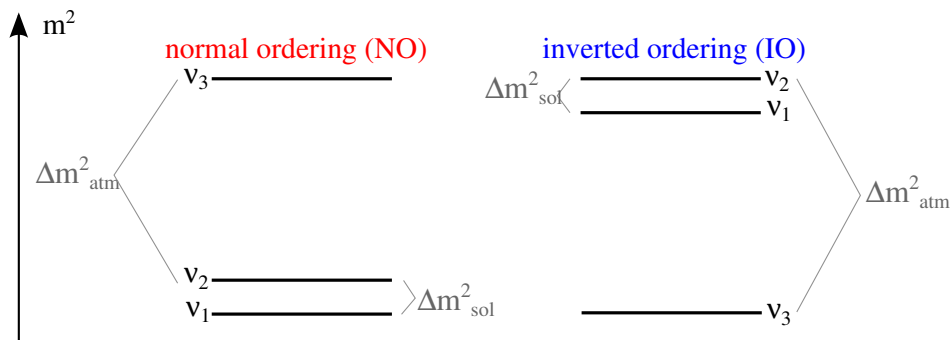


Figure 2.4: Sketch of neutrino mass ordering: in the normal ordering (NO) m_1 is the smallest neutrino mass and $\Delta m_{31}^2 < 0$, the inverted ordering (IO) is characterized by $\Delta m_{31}^2 > 0$ and m_3 is the smallest mass.

However, neutrino oscillation is insensitive to the absolute mass scale of neutrinos. If the mass scale is much larger than the mass splitting, $m_i \gg \Delta m_{ij}$, the neutrino spectrum is called **quasi-degenerate** (QD) with $m_1 \cong m_2 \cong m_3$.

Limits on Neutrino Masses

Laboratory experiments measuring the β -decay endpoint energy as well as Cosmology can put limits on the neutrino mass. The spectral shape of the β -decay close to the end-point energy provides information on the neutrino mass scale. However, this is an enormous experimental challenge as it requires a high precision whereas the statistics of electrons close to the end-point energy is very small. A promising candidate is the ${}^3\text{H}$ β -decay: ${}^3\text{H} \rightarrow {}^3\text{He} + e^- + \bar{\nu}_e$. Since the observed spectrum is the sum over mass eigenstates i , the measured quantity is $m_{\nu_e}^2 = \sum_i |\mathcal{U}_{ei}|^2 m_i^2$. The Mainz experiment sets an upper limit of $m_{\nu_e} < 2.3 \text{ eV}$ at 95 % C.L. [32].

The anisotropies in the cosmic microwave background (CMB) provide information about the structure formation of the universe, such as galaxies and galaxy clusters. Since neutrinos interact only weakly they can escape even high density regions without interacting and thus, transport energy over large distances. This is more efficient the higher the neutrino mass. Consequently, massive neutrinos wash out the structure formation on small scales by mass transport. The higher the neutrino mass, the less structure is formed at (cosmologically) small scales (galaxies and galaxy clusters). In that way Cosmology is sensitive to the total neutrino mass $m_\nu = \sum_i m_{\nu_i}$. The Planck Collaboration sets an upper limit on the neutrino mass of $m_\nu < 0.23 \text{ eV}$ @ 95 % C.L. [33].

These upper limits indicate that neutrino masses are much smaller than the masses of the charged leptons, i.e. $m_e = 511 \text{ keV}$.

Neutrino Mass Terms

In the SM neutrinos are considered massless, and no mass term is needed in the Lagrangian in Equation 2.2. However, neutrino oscillation unambiguously proves the existence of non-zero neutrino masses.

In general a mass term couples the left-handed fermion fields to the right-handed:

$$\mathcal{L}_m = m_D \bar{\psi} \psi = m_D (\bar{\psi}_L \psi_R + \bar{\psi}_R \psi_L). \quad (2.7)$$

In the SM a right-handed neutrino does not exist. There are two possibilities how to introduce right-handed neutrinos and thus, a mass term:

- **Dirac** mass term: extend the SM by a new particle, i.e. a right-handed neutrino, ν_R , which has no gauge interactions. Neutrino masses are then generated in analogy to quarks and charged leptons²:

$$\mathcal{L}_m = m_D \bar{\nu} \nu = m_D (\bar{\nu}_L \nu_R + \bar{\nu}_R \nu_L). \quad (2.8)$$

However, this mechanism does not explain the smallness of neutrino masses and requires undesired fine-tuning.

- **Majorana** mass term: instead of introducing a new particle we require that $\nu_R = (\nu_L)^c$ whereas C denotes the charge conjugate. $(\nu_L)^c$ is a right-handed particle with opposite charge like quantum numbers, i.e. the anti-particle of ν : the SM right-handed anti-neutrino. The neutrino is a so-called Majorana fermion, particle and anti-particle are identical. The Majorana mass term can be written as

$$\mathcal{L}_m = \frac{1}{2} m \bar{\nu}_L^c \nu_L + h.c. \quad (2.9)$$

However, a Majorana mass term can only exist for truly neutral particles. The term $m \bar{\nu}_L^c \nu_L$ is forbidden in the SM: ν_L annihilates a neutrino with $Y_W = -1$ whereas $\bar{\nu}_L^c$ creates a neutrino with $Y_W = +1$. Consequently, hypercharge is not conserved.³

A Majorana mass term does not conserve lepton number. However, lepton number is so-far not associated with a fundamental symmetry, its conservation is motivated only by experiments.

The most general case involves a Dirac and a Majorana mass term. One mechanism to include neutrino masses is the seesaw mechanism in which right-handed neutrinos N_R are added to the SM. In general one has to add one N_R per non-vanishing neutrino mass. The right-handed neutrinos are Majorana particles: truly neutral particles, with $Q = T_3 = 0$ and do not have any gauge interactions.⁴ Considering only one flavor, the mass term can be written as

$$\mathcal{L}_m = -m_D \bar{\nu}_L N_R + \frac{1}{2} m_R \overline{(N_R)^c} N_R + h.c. \quad (2.10)$$

²i.e. via the Higgs mechanism.

³The interaction is not gauge invariant under $U(1)_Y$.

⁴They couple only to the lepton and Higgs field (Yukawa interaction) which after spontaneous symmetry breaking yields the Dirac mass term $-m_D \bar{\nu}_L N_R$.

or in matrix notation with $n = \begin{pmatrix} \nu_L \\ (N_R)^c \end{pmatrix}$

$$\begin{aligned} \mathcal{L}_m &= -\frac{1}{2}\overline{n^c}Mn + h.c. \\ &= -\frac{1}{2}(\overline{\nu_L}, \overline{N_L^c}) \begin{pmatrix} 0 & m_D \\ m_D & m_R \end{pmatrix} \begin{pmatrix} \nu_L \\ (N_R)^c \end{pmatrix} + h.c. \end{aligned} \quad (2.11)$$

Assuming $m_D \ll m_M$ the diagonalization of the mass matrix M gives two mass eigenstates: ν'_L with mass $m_\nu \approx \frac{m_D^2}{m_R} \ll m_D$ and N'_R with $m_N \approx m_R$. Equation 2.11 can be written as

$$\mathcal{L}_m = -\frac{1}{2}\frac{m_D^2}{m_M}\overline{(\nu'_L)^c}\nu'_L - \frac{1}{2}m_R\overline{(N'_R)^c}N'_R \quad (2.12)$$

A light and a heavy neutrino are generated. The light ν'_L is indistinguishable from the SM ν_L , as the component of $(N_R)^c$ in ν'_L is of the order of $\frac{m_D}{m_M} \ll 1$. The mass of ν'_L is suppressed by a factor of $\frac{m_D}{m_M}$ with respect to the SM fermion masses.

The mass term in Equation 2.12 is a pure Majorana mass term, and violates lepton number by two units. The next section will discuss in detail the neutrinoless double beta ($0\nu\beta\beta$) decay which is a lepton number violating process.

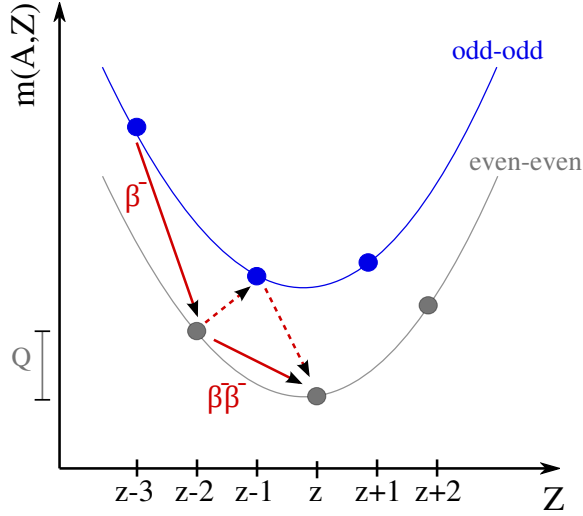


Figure 2.5: Mass as a function of the nuclear charge Z for isobaric nuclei with even A . The pairing energy splits the parabola into two: the parabola of the nuclei with odd Z and odd $N = A - Z$ (odd-odd) are vertically shifted by $2\frac{\delta}{A^{1/2}}$ with respect to the mass parabola of even-even nuclei. For certain even-even nuclei single beta-decay can be energetically forbidden as $m(A, Z) < m(A, Z + 1)$. However, the nucleus may decay via two simultaneous β -decays, the so-called double beta ($\beta\beta$)-decay.

2.2 Neutrinoless Double Beta Decay

The Weizsäcker mass formula for nuclei with same mass number A , so-called isobaric isotopes, is given by [34]

$$m(A, Z) = \alpha \cdot A - \beta \cdot Z + \gamma \cdot Z^2 + \frac{\delta}{A^{1/2}}, \quad (2.13)$$

where α, β, γ are constants and δ represents the pairing energy given by

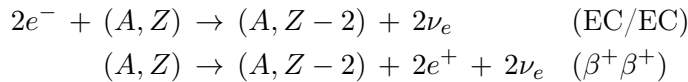
$$\delta = \begin{cases} -11.2 \text{ MeV}/c^2 & \text{if } Z \text{ and } N = A - Z \text{ even} \\ 0 & \text{if } A \text{ odd} \\ +11.2 \text{ MeV}/c^2 & \text{if } Z \text{ and } N = A - Z \text{ odd} \end{cases} \quad (2.14)$$

Figure 2.5 shows the mass as a function of the nuclear charge Z for isobaric nuclei with even A : due to the pairing term the odd-odd nuclei describe a parabola which is vertically shifted by $2\frac{\delta}{A^{1/2}}$ with respect to the mass parabola of even-even nuclei. For certain even-even nuclei single β^- -decay is energetically forbidden, if $m(A, Z) < m(A, Z + 1)$, or suppressed e.g. due to large angular momentum difference of mother and daughter nuclide. This allows for the so-called double β -decay ($2\nu\beta\beta$ -decay) which can be understood as two simultaneous β -decays [35]:



Figure 2.6(a) shows the corresponding Feynman diagram of $2\nu\beta\beta$ -decay. There are 35 candidate $2\nu\beta\beta$ isotopes of which 11 have been measured with half-lives of $10^{19} - 10^{24}$ years [36]: ^{48}Ca , ^{76}Ge , ^{82}Se , ^{96}Zr , ^{100}Mo , ^{116}Cd , ^{128}Te , ^{130}Te , ^{136}Xe , ^{150}Nd and ^{238}U .

Furthermore, double β^+ or electron capture (EC) (or a mixture of both) is possible:



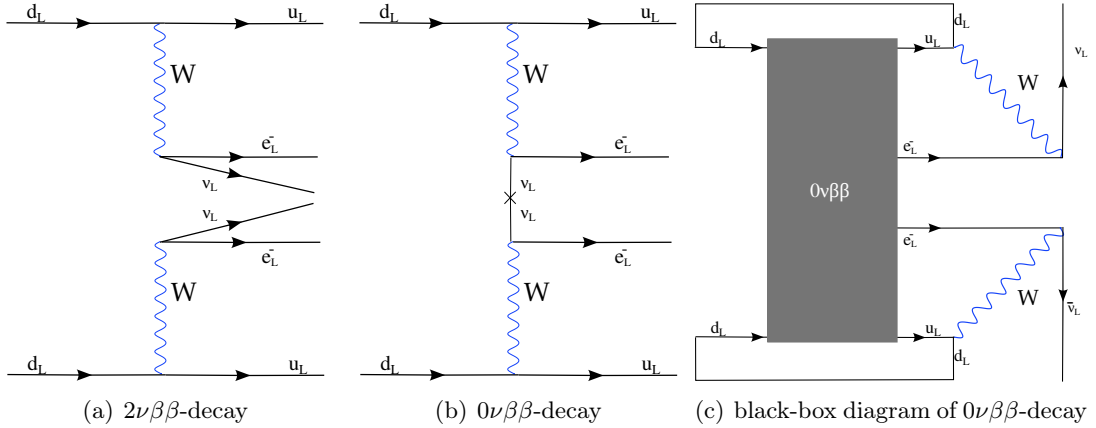


Figure 2.6: (a) The $2\nu\beta\beta$ -decay can be understood as the simultaneous $\beta^{(-)}$ -decay of two nucleons into two electrons and two anti-neutrinos. (b) In $0\nu\beta\beta$ -decay only two electrons are found in the final state. The Feynman diagram shows the standard interpretation in which the process is realized via the exchange of two light Majorana neutrinos. (c) Independent of the realization of $0\nu\beta\beta$ -decay (indicated by the black box) the diagram gives a contribution to the Majorana mass term of neutrinos. See text for details.

The double-EC decay has the lowest half-life and its experimental signature is the emission of x-rays or Auger electrons. Double β^+ decay has a very clean experimental signature of four 511 keV annihilation photons or excited state transitions. However, the predicted half-lives are of the order of 10^{26} years [11]. In the following, the discussion will focus on $2\beta^-\beta^-$ decay as at present it is most relevant for the search of $0\nu\beta\beta$ decay. For further reading on the search of (neutrinoless) double-EC the reader is referred to [37].

As a second order weak process the $2\nu\beta\beta$ -decay is very rare. The decay rate, or the half-life, scales with $\frac{1}{T_{1/2}^{2\nu}} \propto G_F^4 Q^{11}$, where G_F is the Fermi constant and Q is the nuclear transition energy available for electrons and neutrinos in the final state.

$0\nu\beta\beta$ -Decay

A new $\beta\beta$ decay-mode without the emission of neutrinos, the so-called neutrinoless double beta ($0\nu\beta\beta$)-decay has been proposed [38]:

$$(A, Z) \rightarrow (A, Z + 2) + 2e^-. \quad (2.16)$$

$0\nu\beta\beta$ -decay is forbidden in the SM as the process violates lepton number by two units, $\Delta L = 2$. The dependence of the decay rate on the nuclear transition energy is $\frac{1}{T_{1/2}^{0\nu}} \propto Q^5$.

In the standard interpretation the $0\nu\beta\beta$ decay is mediated by light massive Majorana neutrinos. Figure 2.6(b) shows the corresponding Feynman diagram. At the upper vertex a right-handed anti-neutrino is emitted, at the lower vertex a left handed neutrino is absorbed. Besides the Majorana nature, a non-vanishing neutrino mass is required for the helicity match. The right-handed component of the pre-dominantly left-handed neutrino is proportional to $\frac{m_i}{E}$, with $i = 1, 2, 3$. As the flavor states are a superposition of mass eigenstates (compare Equation 2.3) each interaction vertex contains a factor \mathcal{U}_{ei} . The decay rate is proportional to

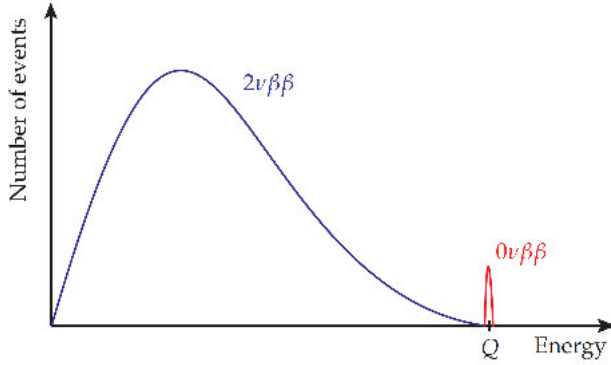


Figure 2.7: Sum spectrum of the two electrons in $2\nu\beta\beta/0\nu\beta\beta$ -decay. In the neutrino accompanied case, the $2\nu\beta\beta$, the electron spectrum is continuous since the decay energy is split among two electrons and two neutrinos. The latter remain undetected and carry away energy. In the neutrinoless case, the $0\nu\beta\beta$, the full decay energy is distributed over the two electrons. Since the sum energy of the electrons is measured, the $0\nu\beta\beta$ signal is a mono-energetic line at the Q -value of the decay. The $0\nu\beta\beta$ peak and the $2\nu\beta\beta$ spectrum are not to scale. Figure taken from [42].

the square of the effective Majorana neutrino mass

$$m_{0\nu} = \left| \sum_{i=1}^3 \mathcal{U}_{ei}^2 m_i \right| \quad (2.17)$$

which is a coherent sum over the three massive neutrinos.

In principle any process that violates lepton number by two units can contribute to $0\nu\beta\beta$ -decay. Besides the light Majorana neutrino exchange, $0\nu\beta\beta$ -decay may be realized by Higgs triplets, or right-handed charged currents. A detailed discussion of alternative $\Delta L = 2$ processes is beyond the scope of this thesis and can be found in [39]. However, it should be mentioned that if the new physics scale is in the TeV range, the LHC is expected to find such processes.

The Schechter-Valle theorem [40] states that independent of the underlying process, the observation of $0\nu\beta\beta$ -decay implies the Majorana nature of neutrinos. If the $0\nu\beta\beta$ -decay is observed, higher order diagrams as shown in Figure 2.6(c) must exist. The diagram represents a $\bar{\nu}_e \rightarrow \nu_e$ transition which is a Majorana mass term as described in the previous section. In other words, even if a Majorana mass term at tree level is not allowed, radiative corrections will contribute. However, this Majorana mass will be extremely small [41].

$0\nu\beta\beta$ Observables and Interpretation

Experimentally, the sum of the total energies of the two electrons is measured: as shown in Figure 2.7 the experimental signature of $0\nu\beta\beta$ decay is a mono-energetic line at the Q -value of the decay. The primary observable in the search for $0\nu\beta\beta$ -decay is the half-life which is related to the number of observed $0\nu\beta\beta$ decays $N^{0\nu}$ via

$$T_{1/2}^{0\nu} = \frac{\ln 2 \cdot N_A \cdot a \cdot M \cdot t}{m_A \cdot N^{0\nu}} \quad (2.18)$$

where a is the isotopic abundance of the $\beta\beta$ isotope, M is the total mass, t the measurement time, m_A the molar mass and N_A Avogadro's constant.

The experiment provides no insight into the underlying process. Consequently, the observation of $0\nu\beta\beta$ would first prove that lepton number is violated and that neutrinos have

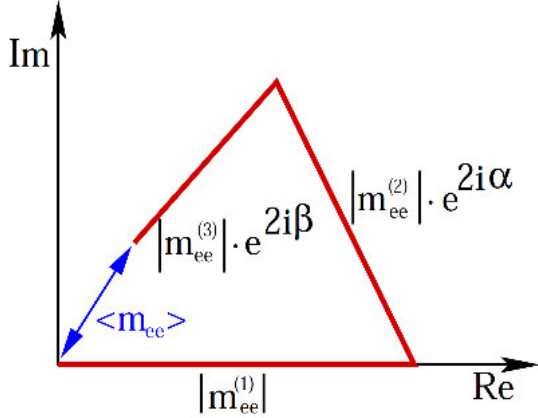


Figure 2.8: Visualization of Equation 2.20: $m_i|\mathcal{U}_{ei}|^2$ is represented by a complex vector, the Majorana phases give the relative orientation of the vectors. The notation of the plot is slightly different: $|m_{ee}|$ gives the effective Majorana mass, denoted in the text as $m_{0\nu}$, $|m_{ee}^i|$ corresponds to $m_i|\mathcal{U}_{ei}|^2$ and the phases are $\alpha = \frac{\alpha_2}{2}$ and $\beta = \frac{\alpha_3}{2}$. Taken from [39].

a non-vanishing Majorana mass which in principle can be arbitrary small. Therefore, the connection to other experiments such as the LHC is crucial.

Assuming the exchange of light Majorana neutrinos, the decay rate is given by

$$\frac{1}{T_{1/2}^{0\nu}} = G^{0\nu}(Q, Z)|M^{0\nu}|^2 \left(\frac{m_{0\nu}}{m_e}\right)^2 \quad (2.19)$$

where $G^{0\nu}(Q, Z)$ is the phase space factor, $|M^{0\nu}|$ the nuclear matrix element, $m_{0\nu}$ the effective Majorana mass (Equation 2.17) and m_e the electron mass. The nuclear matrix element is problematic to calculate and the obtained results spread by a factor of 2 depending on the method. Equation 2.19 allows to calculate the effective Majorana mass $m_{0\nu}$ from the observable $T_{1/2}^{0\nu}$. The mass can be expressed as

$$\begin{aligned} m_{0\nu} &= \left| |\mathcal{U}_{e1}|^2 m_1 + e^{i\alpha_2} |\mathcal{U}_{e2}|^2 m_2 + e^{i\alpha_3} |\mathcal{U}_{e3}|^2 m_3 \right| \\ &= \left| \cos^2 \theta_{12} \cos^2 \theta_{13} m_1 + e^{i\alpha_2} \sin^2 \theta_{12} \cos^2 \theta_{13} m_2 + e^{i\alpha_3} \sin^2 \theta_{13} m_3 \right| \end{aligned} \quad (2.20)$$

using the parametrization from Equation 2.4 and $\alpha_2 = 2\alpha$, $\alpha_3 = 2(\beta - \delta)$. This relates the effective Majorana mass accessible in $0\nu\beta\beta$ -decay with the neutrino oscillation parameters discussed in the previous section. Figure 2.8 depicts Equation 2.20: $m_{0\nu}$ is given as the sum of three complex vectors, $|m_{ee}^{(i)}| = |\mathcal{U}_{ei}|m_i$ and the Majorana phases give the orientation of each vector.

Using neutrino oscillation measurements one can connect the effective Majorana mass to the smallest neutrino mass as shown in Figure 2.9. There are two scenarios:

- in the **normal ordering** ($\Delta m_{31}^2 > 0$) the smallest neutrino mass is m_1 and $m_{2,3}$ can be expressed in terms of m_1 , Δm_{\odot} and Δm_{atm} (compare also Figure 2.4): $m_2 \simeq \sqrt{m_1^2 + \Delta m_{\odot}^2}$ and $m_3 \simeq \sqrt{m_1^2 + \Delta m_{atm}^2}$. Assuming θ_{13} to be small, Equation 2.20 can be approximated as $m_{0\nu} \simeq \left| \cos_{12}^2 m_1 + e^{i\alpha} \sin_{12}^2 \sqrt{m_1^2 + \Delta m_{\odot}^2} \right|$. Both terms can be of compatible size and as $e^{i\alpha} = \pm 1$ for $\alpha = 0, \pi$ $m_{0\nu}$ may vanish. In the quasi-degenerate regime where $m_1 \gg \sqrt{\Delta m_{atm}^2} \gg \sqrt{\Delta m_{\odot}^2}$ the effective Majorana neutrino mass can be approximated by a common neutrino mass m_0 with $m_0 \cos 2\theta_{12} \leq m_{0\nu} \leq m_0$.

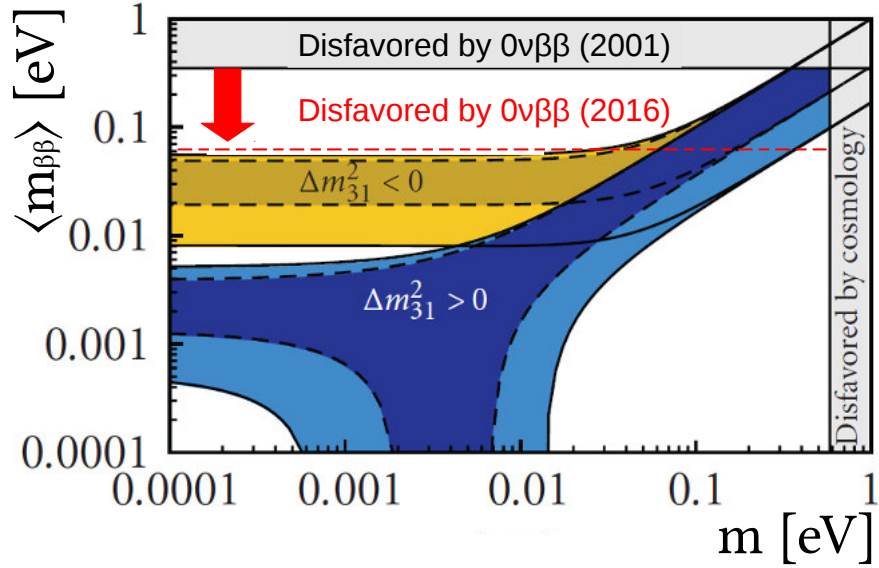


Figure 2.9: The effective Majorana neutrino mass as a function of the smallest neutrino mass. One distinguishes normal ($\Delta m_{31}^2 > 0$) and inverted ($\Delta m_{31}^2 < 0$) ordering. Compare also Figure 2.4. Both scenarios behave similar in the quasi-degenerate mass regime where the neutrino mass is large compared to the mass splitting. At low neutrino masses, the normal and inverted ordering show different behavior. For the NH the effective Majorana mass may even vanish. Modified plot from [43]. Courtesy of W. Maneschg.

- in case of the **inverted ordering** ($\Delta m_{31}^2 < 0$) the smallest neutrino mass is m_3 and $m_{1,2}$ can be approximated by $m_1 \simeq m_2 \simeq \sqrt{m_3^2 + \Delta m_{atm}^2}$. Since both θ_{13} and m_3 are small the term $e^{i\beta} |\mathcal{U}_{e3}|^2 m_3$ can be neglected. In the quasi-degenerate region $m_{0\nu}$ behaves similar as in the NH. For small m_3 the effective Majorana mass is then given by $m_{0\nu} \simeq \sqrt{\Delta m_{atm}^2} \cos \theta_{13}^2 (\cos^2 \theta_{12} + e^{i\alpha} \sin^2 \theta_{12})$. This limits $m_{0\nu}$ between $\sqrt{\Delta m_{atm}^2} \cos^2 \theta_{13} \leq m_{0\nu} \leq \sqrt{\Delta m_{atm}^2} \cos^2 \theta_{13} \cos 2\theta_{12}$.

A detailed calculation can be found in [10, 39].

The search for $0\nu\beta\beta$ -decay constrains Figure 2.9 from the top, the latest result from KamLand-Zen with $m_{0\nu} < (61 - 165) \text{ meV}$ is shown [44]. Direct search for neutrino masses as well as Cosmology provide complementary information on the neutrino mass scale and constrain the plot from the right. However, this direct comparison only holds if $0\nu\beta\beta$ is realized by the same mechanism as neutrino masses. Furthermore, the neutrinos produced in single β -decay are external particles. In $0\nu\beta\beta$ -decay heavy neutrinos may be exchanged as virtual particles which cannot be produced in the single β -decay. If $0\nu\beta\beta$ finds a signal, which is not confirmed by direct neutrino mass experiments, this would be a clear hint that $0\nu\beta\beta$ decay and neutrino masses are realized by a mechanism different from active neutrino exchange [39].

In summary, $0\nu\beta\beta$ -decay tests lepton number conservation. Lepton number is conserved in the SM. Thus, the observation of $0\nu\beta\beta$ -decay implies new physics beyond the SM. Furthermore, in this case neutrinos must have a Majorana mass component. In the standard interpretation of $0\nu\beta\beta$ light Majorana neutrinos are exchanged. An effective Majorana mass

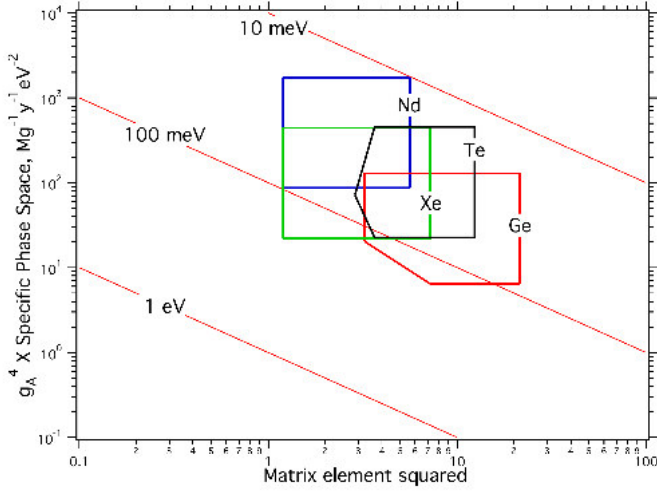


Figure 2.10: Regions of specific phase space factor and squared matrix elements for the $0\nu\beta\beta$ candidate isotopes ^{76}Ge , ^{130}Te , ^{136}Xe and ^{150}Nd . $g_A \simeq 0.6 - 1.269$ is the axial-vector coupling constant. The specific phase space factor is given in activity per unit mass of the isotope in question. The horizontal spread is given by the uncertainty in the matrix element calculation, $|M|^2$, the vertical by the uncertainty on g_A^4 . The lines indicate the effective Majorana mass $m_{0\nu}$ corresponding to 1 signal count per tonne per year. Taken from [46].

is defined which is a coherent sum over neutrino mass eigenstates including oscillation parameters and Majorana phases. Thus, $0\nu\beta\beta$ -decay can access the neutrino mass scale as well as the mass ordering of neutrinos. However, the $0\nu\beta\beta$ -decay alone does not allow to constrain the underlying process. Therefore, the search of $0\nu\beta\beta$ is linked to new physics searches at the LHC or other lepton flavor violating searches, as well as direct neutrino mass experiments and Cosmology. The concept of effective Majorana mass is used to compare the half-lives of $0\nu\beta\beta$ -decay of different isotopes even if the physical neutrino mass is generated via a different mechanism. In case of a discovery, comparing the half-lives of $0\nu\beta\beta$ -decay of different isotopes may discriminate the underlying mechanism [45].

Experimental Aspects

Equation 2.18 and 2.19, show that in order to have a sufficiently large signal, a high phase-space factor and matrix element are desirable. Both are compared in Figure 2.10 for four isotopes, ^{76}Ge , ^{130}Te , ^{136}Xe and ^{150}Nd : all show a comparable sensitivity, no outstanding $0\nu\beta\beta$ isotope exists.

Any radioactive decay with a Q-value above the position of the $0\nu\beta\beta$ signal peak may deposit energy in the signal region and fake a $0\nu\beta\beta$ event. This is called background. Since the expected decay rate is orders of magnitude below the environmental radioactivity, low background techniques need to be applied. Neutrons are a common background source. They are e.g. produced in cosmic ray interactions or fission processes. Radioactive isotopes with high Q-values may be produced by neutron-capture. Especially, the cosmogenic activation of the detector material needs to be avoided. Experiments requiring an ultra low background, are built deep underground. The overburden provides a shielding against cosmic radiation: besides neutrons, protons and muons are shielded which can deposit energy in the detector via electromagnetic interactions. Since the attenuation depends on the overburden, the attenuation is compared to the shielding achieved by a column of water and given in meters of water equivalent (m w.e.). Further details on cosmic activation of the detector material are given in Section 4.4.

Natural radioactivity originates in the decay of ^{40}K with a prominent γ -line at 1461 keV as well as decays from the ^{238}U and ^{232}Th decay chains. The highest γ -line is at 2615 keV from

isotope	Q [keV]	abundance [%]	experiments	FWHM [%]	mass [kg]	enrichment [%]
$^{48}\text{Ca} \rightarrow ^{48}\text{Tl}$	4272	0.187	CANDLES-III [47]	4.7	300	-
$^{76}\text{Ge} \rightarrow ^{76}\text{Se}$	2039	7.8	GERDA [48] MAJORANA [49]	0.1-0.2 0.1	18→36 30	87 86
$^{82}\text{Se} \rightarrow ^{82}\text{Kr}$	2995	9.2	SuperNEMO [50]	4.6	7→100	100
$^{96}\text{Zr} \rightarrow ^{96}\text{Mo}$	3350	2.8				
$^{100}\text{Mo} \rightarrow ^{100}\text{Ru}$	3034	9.6	AMORE [51] NEMO-III [52]	0.2 8	5→200 6.9	96 100
$^{110}\text{Pd} \rightarrow ^{110}\text{Cd}$	2018	11.8				
$^{116}\text{Cd} \rightarrow ^{116}\text{Sn}$	2814	7.5	COBRA [53, 54]	~ 1	~ 0.4(→ 4.0)	(90)
$^{124}\text{Sn} \rightarrow ^{124}\text{Te}$	2287	5.64				
$^{130}\text{Te} \rightarrow ^{130}\text{Xe}$	2527	34.5	SNO+ [55] CUORE [56]	~ 11 0.2	~ 800 → 8000 741	100 -
$^{136}\text{Xe} \rightarrow ^{136}\text{Ba}$	2458	8.9	EXO-200/nEXO [57, 58] KamLAND-ZEN [59, 44] NEXT [60]	1.3→1.0 10 0.5	110→4700 320/383→800 100 - 150	81→>90 91 90
$^{150}\text{Nd} \rightarrow ^{150}\text{Sm}$	3371	5.6				

Table 2.3: $0\nu\beta\beta$ candidate isotopes with Q-values above 2 MeV. Q-values taken from [46]. Isotopic abundance taken from [43]. Running and future experiments searching for $0\nu\beta\beta$ -decay are listed with corresponding energy resolution (FWHM) at $Q_{\beta\beta}$, detector mass and isotopical enrichment. The list is by no means complete. More details on (upcoming) $0\nu\beta\beta$ experiments and R&D projects can be found e.g. in [43, 61].

^{208}Tl . Therefore, a Q-value of the $0\nu\beta\beta$ decay above 2.6 MeV is preferred. Besides γ -rays, β - and α -decays are to be avoided. A material selection based on screening measurements to determine the radioactivity of the built-in materials is made. Active and passive background reduction techniques have been developed. Since the $2\nu\beta\beta$ decay rate is at least 5-6 orders of magnitude larger than for $0\nu\beta\beta$ -decay, the $2\nu\beta\beta$ events are an unavoidable background source. The two decay modes can only be distinguished through good energy resolution. Furthermore, the radio-purity of the detector material itself is of great interest. Since the crystal pulling acts as a purification, the intrinsic radioactive contamination of crystals is quite low, whereas liquids often need to be purified. Crystal detector are, however, limited in size. Therefore, such detectors are typically arranged in arrays to define efficient multiple detector cuts: coincident events in several detectors are regarded as background. The array structure potentially introduces background from the detector support. This is a clear disadvantage compared to liquid scintillator experiments: such experiments are large in size and the event reconstruction allows to define a fiducial volume which is a common technique to reduce background as the liquid acts as a self-shielding against external radiation.

In case of background the sensitivity on the half-life of $0\nu\beta\beta$ -decay scales as

$$T_{1/2}^{0\nu} \propto a \cdot \epsilon \sqrt{\frac{M \cdot t}{\text{BI} \cdot \Delta E}}, \quad (2.21)$$

where a is the isotopic abundance of the $0\nu\beta\beta$ isotope, ϵ accounts for the detection efficiency of $0\nu\beta\beta$ decay and BI is the background index given in $\frac{\text{counts}}{\text{keV} \cdot \text{kg} \cdot \text{yr}}$. M is the detector mass and t the measurement time, the product $M \cdot t$ is called the exposure and given in units of $\text{kg} \cdot \text{yr}$. The energy resolution is given by ΔE .

According to Equation 2.21 the experiments searching for $0\nu\beta\beta$ -decay aim to maximize the detector mass (or exposure), achieve a high isotopical abundance and at the same time minimize the background and the energy resolution. Since the limits on the half-life of $0\nu\beta\beta$ -decay need to be pushed even further, other important aspects of the experimental technique are the scalability and the corresponding costs.

Table 2.3 summarizes the $0\nu\beta\beta$ candidate isotopes. Since the decay rate scales with $\frac{1}{T_{1/2}} \propto Q^5$, only candidates with Q-values above 2 MeV are considered. All except ^{130}Te show a low natural abundance. Thus, experiments need a high mass in the $0\nu\beta\beta$ isotope. In many cases this can only be achieved by isotopic enrichment of the detector material. The detection efficiency is maximized if the detector material itself contains the $\beta\beta$ isotope. The energy resolution greatly depends on the experimental technique. Many different experimental approaches exist. All measure the sum of the energies of the two electrons in the double beta decay. In addition, some techniques can track the particles:

- **Semi-conductors:**

Semi-conductors detectors are distinct for their excellent energy resolution of $\sim 0.1\%$. Experiments such as GERDA or MAJORANA use high purity germanium (HPGe) detectors isotopically enriched in ^{76}Ge , whereas COBRA uses enriched CdZnTe detectors. HPGe typically have a mass of 2-3 kg, newer types with enhanced pulse shape discrimination properties only $\sim 700\text{g}$. The CdZnTe crystals are limited to a mass of $< 10\text{g}$. Both passive and active background reduction techniques such as pulse shape analysis have been developed. More details on HPGe, the GERDA experiment and developed background reduction techniques are given in Chapter 3.

- **Multi-layer:**

NEMO-3 is a multi-layer detector to measure the energy and the particle track. Thin foils contain the double beta isotopes ^{100}Mo and ^{82}Se , as well as ^{116}Cd , ^{150}Nd , ^{48}Ca , ^{96}Zr and ^{130}Te . The source is separated from the tracker and the calorimeter. The tracking allows for a separation of β -particles from α -particles and γ -rays. The resolution is comparably poor with only $\sim 8\%$ at $Q_{\beta\beta}$. However, the experiment may identify the underlying $0\nu\beta\beta$ decay mechanism based on the energy and angular distribution.

- **Scintillators:**

In scintillating materials ionizing radiation such as electrons produce luminescence whereas the actual mechanism of light emission depends on the scintillator. The emitted light is then detected by photo-sensors such as photomultiplier tubes (PMT). Scintillators typically have a poor energy resolution of $\sim 10\%$ at $Q_{\beta\beta}$. In $0\nu\beta\beta$ experiments, the loss in sensitivity due to poor energy resolution is partly compensated by the large mass of the $\beta\beta$ -isotope.

KamLand-Zen uses a liquid scintillator doped with ^{136}Xe . The scintillator with the $\beta\beta$ source is contained in a *mini-balloon* immersed into the center of the KamLAND detector which is filled with an ultra-pure liquid scintillator. The latter does not contain any $\beta\beta$ isotope and is used as active background veto. In SNO+ the heavy water of the SNO detector will be replaced by liquid scintillator doped with ^{130}Tl .

CANDLES uses scintillating crystals made of CaF_2 . ^{48}Ca has by far the highest Q-value, thus the background from γ -rays in the signal region is comparably low. The crystals are

arranged in an array allowing for detector anti-coincidence and immersed into a liquid scintillator which serves as an active veto: since the liquid scintillator has much faster signals, background events are well distinct from signal events. However, the natural abundance of ^{48}Ca is very small.

- **Time projection chambers (TPC):**

EXO-200 is a cylindrical TPC filled with liquid xenon enriched in ^{136}Xe . A drift field is created using two wire grids at different voltages. Both ionization and scintillation light are measured which is used to discriminate background from signal events. Furthermore, the event position can be reconstructed and a fiducial cut can be applied. The energy resolution is $\sim 4\%$ at $Q_{\beta\beta}$.

NEXT will use a high pressure gas xenon TPC. The xenon is isotopically enriched in ^{136}Xe up to 90%. The experiment will use electroluminescence (EL) which allows for an energy resolution as good as 0.5% FWHM at $Q_{\beta\beta}$. Together with the tracking information, the experiment unites excellent energy resolution and information on the event topology.

- **Bolometers:**

The CUORE experiment uses TeO_2 bolometers operated at 10 mK. The detection principle is based on the temperature increase proportional to the energy deposition, $\Delta T \simeq \frac{\Delta E}{C}$ with C being the heat capacity. Bolometers have a good energy resolution, $\sim 0.2\%$. The technique does not allow for particle identification. The detectors are arranged in towers for detector anti-coincidence. Each crystal has a mass of 750 g.

- **Scintillating bolometers:**

Scintillating bolometers measure both heat and scintillation. The AMORE experiment will use $^{40}\text{Ca}^{100}\text{MoO}_4$ crystals. The size of a single detector is about 500 g. The energy resolution is $\sim 0.2\%$. Background reduction techniques are based on the comparison of the scintillation light and phonon yields as well as pulse shape analysis of the phonon signal.

The list is by no means complete, but represents rather a selection for different experimental techniques. More information can be found e.g. in [43, 61].

Current Status

A subgroup of the Heidelberg-Moscow experiment claimed the observation of the $0\nu\beta\beta$ -decay of ${}^{76}\text{Ge}$ with a half-life of $T_{1/2}^{0\nu} = 1.19 \cdot 10^{25}\text{yr}$ [62]. Due to the large uncertainties on the matrix elements, the claim could only be tested by another germanium based experiment. In its first phase, the GERDA experiment could reject the claim with 99% probability.

At the time of writing this thesis the GERDA experiment set a new lower limit on the $0\nu\beta\beta$ decay of ${}^{76}\text{Ge}$ of $5.3 \cdot 10^{25}$ years at 90% C.L.[4]. The half-life limit corresponds to an upper limit on the effective Majorana mass of (150-330) meV. In the course of this thesis the data analysis as well the statistical analysis leading to this result will be discussed further.

KamLAND-Zen set a new limit on the $0\nu\beta\beta$ -decay of ${}^{136}\text{Xe}$ of $1.07 \cdot 10^{26}$ yr corresponding to an upper limit on the effective Majorana neutrino mass of (61-165) meV [44]. With an upgrade KamLAND-Zen will test the inverted mass ordering.

EXO-200 Phase II started in April 2016 [58]. The aim is to achieve a sensitivity of $5.7 \cdot 10^{25}$ yr on the half-life of $0\nu\beta\beta$ -decay of ${}^{136}\text{Xe}$.

CUORE plans to start operation at the end of 2016. After five years, the aim is to reach a sensitivity on the half-life of $0\nu\beta\beta$ -decay of ${}^{130}\text{Te}$ of $9 \cdot 10^{25}$ yr at 90% C.L. and an upper limit on the effective Majorana neutrino mass of (50 – 130) meV [63].

The KATRIN experiment will measure the β -decay endpoint energy of tritium. First data are expected in the beginning of 2017. The experiment aims to reach a sensitivity on $m_{\nu_e}^2$ of 0.2 eV for a limit at 90% C.L. [64].

The Germanium Detector Array Experiment

The GERDA experiment searches for the neutrinoless double beta ($0\nu\beta\beta$) decay of ^{76}Ge . The experimental concept is to operate bare high purity germanium (HPGe) detectors isotopically enriched in ^{76}Ge in liquid argon (LAr), which serves as coolant and shielding against external radiation.

In Section 3.1 the working principle of germanium detectors is sketched. The GERDA experiments uses two different detector technologies which will be introduced in the following. The discussion on HPGe detectors is by no means complete, for further details the reader is referred to [65, 66, 67].

Section 3.2 covers the experimental setup of GERDA. The experiment proceeds in two phases. Phase I of the experiment and the background to be faced will be introduced.

The aim of the GERDA experiment is to explore half-lives of the $0\nu\beta\beta$ -decay of ^{76}Ge of the order of 10^{26} years. This can only be done by reaching an unprecedented background index of $10^{-3} \frac{\text{counts}}{\text{keV} \cdot \text{kg} \cdot \text{yr}}$ in order to stay background free until an exposure of $100 \text{ kg} \cdot \text{yr}$. Therefore, improved active background reduction techniques are required. The hardware upgrade, Phase II, will be motivated in Section 3.3. The focus of the section lies on the discrimination of background from signal events. The expected background components will be discussed shortly.

3.1 Working Principle of Germanium Detectors

Germanium and silicon are direct semiconductors and are widely used for the detection and spectroscopic measurements of ionizing radiation. Table 3.1 compares some of the properties of Si and Ge which will be discussed in the following.

element	atomic number Z	radiation length X_0 [cm]	band gap E_{gap} [eV]	average energy to create e-/h pair [eV]	Fano factor
Si	14	9.36	1.12	3.65	0.115
Ge	32	2.30	0.66	2.96	0.13

Table 3.1: Summary of characteristic properties of the semiconductor materials germanium and silicon which are both widely used as radiation detectors in nuclear and particle physics. Taken from [66].

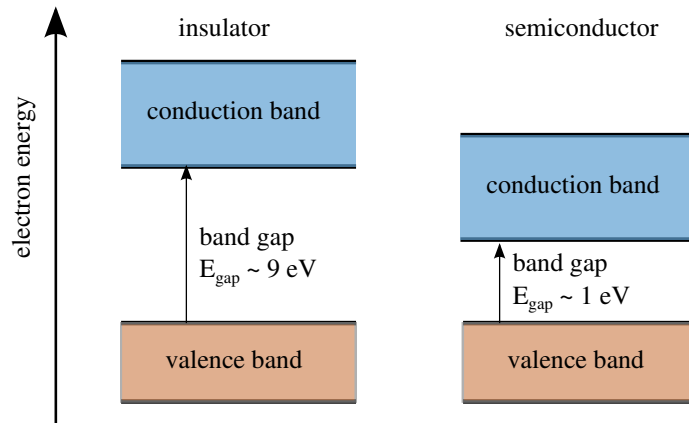


Figure 3.1: Schematic of energy levels of electrons in insulator and semiconductor. Insulators are characterized by a band gap of a few eV, while semiconductors have a small band gap of about 1 eV.

In a crystal the allowed energy levels of electrons are given by two separated bands: the valence- and the conduction band (compare Figure 3.1). Electrons in the conduction band are free to move through the crystal and thus, contribute to the electrical conductivity of the material. Insulators are characterized by a comparably large separation of valence and conduction band, the so-called band gap, E_{gap} . The valence band is fully occupied while the conduction band is empty. In the case of semiconductors the band gap is small, e.g. for germanium $E_{\text{gap}} = 0.66 \text{ eV}$. Consequently, the energy necessary to promote an electron from the valence to the conduction band is small and can be gained e.g. by thermal energy.

For germanium/ silicon the valence band corresponds to the electrons bound in the covalent bonds. If a covalent bond is broken, the electron in the conduction band is free to migrate through the crystal, and a vacancy is left in the valence band, which is referred to as a *hole*. The hole represents a net positive charge migrating through the crystal. Since the conduction electron and the hole occur as a pair, they are referred to as *electron-hole pair*.

The electrical properties of a semiconductor can be changed by proper doping of the material, i.e. introducing impurity atoms. If a semiconductor of group IV, i.e. with four valence electrons, is doped with impurities from group V, the excess valence electrons remain unbound. Thus, more conduction electrons than holes are available in the doped material, the semiconductor is called n-doped.

On the other hand, in p-doped material more holes than valence electrons are available. If a IV-type semiconductor is doped with impurities from group III, which has one covalent electron less than the IV-type material, a covalent bond is left unsaturated. An electron participating in the covalent bond of a germanium and an impurity atom is less bound than an electron in a covalent bond of two germanium atoms. Therefore, the induced impurities create intermediate energy levels in the band gap. In p-type semiconductors the so-called acceptor level is slightly higher than the valence band. The acceptor level is filled through thermal excitation of electrons, leaving some of the germanium covalent bonds unsaturated, i.e. holes in the valence band. The electrons in the acceptor level are fixed, while the holes in the valence band are the free charge carriers which dominate the conductivity of the semiconductor material: in a p-type semiconductor holes are the majority charge carriers, electrons the minority charge carriers.

Semiconductors as Radiation Detectors

Semiconductor detectors are a special type of diode: a n^+p junction as sketched in Figure 3.2. In the following the concept will be explained in detail.

Ionizing radiation loses energy in the semiconductor and electron-hole pairs are created in the interactions. The electron-hole pairs produced in the interaction need to be separated in an electric field. As the charges drift, they induce a mirror current, i.e. a signal. Consequently, all free charge carriers need to be removed from the sensitive detector volume to prevent the production of a current overwhelming the detection signal and/ or recombination of the electron-hole pair. The depletion of free charge carriers is most efficiently achieved by a **p-n junction**, i.e. a diode.

The majority charge carriers in p-type material are holes, for the n-type material electrons. If the two materials are brought into contact, the electrons diffuse from the n-type into the p-type material (drift current) where they occupy the unsaturated covalent bonds, i.e. the holes. Thus, a negative space charge builds up in the p-type material, and a positive in the n-type. Due to the recombination of electrons and holes, no free charges are left in the region of the p-n junction: the so-called *depletion region*. The width of the depleted region can be enlarged by applying a positive bias voltage to the n-type material which enhances the potential difference at the p-n junction. This is called a *reverse bias*. If the doping of the two semiconductors forming the p-n junction is different, the depletion region extends further into the less-doped material.

The depleted region is the sensitive or **active volume** of the detector. For a planar geometry, the thickness, d , of the depletion region depends on the applied reverse bias, V , and impurity concentration, N , of the less-doped material as

$$d \propto \left(\frac{V}{eN} \right)^{1/2}. \quad (3.1)$$

This implies that the depletion depth, d , can be increased by decreasing the impurity concentration of the semiconductor material. To achieve a sensitive region of several cm, the impurity concentration needs to be as low as 10^{10} atoms/cm³. Germanium based semiconductor detectors with such low impurity concentration are called high purity germanium (HPGe) detectors.

Highly doped material (assigned n^+ / p^+) shows a high conductivity and is used to form the ohmic contact. The n^+ electrode is produced by lithium diffusion with a thickness of ~ 1 mm, while the p^+ -electrode is realized by boron implantation (a few hundred nm). The junction of highly and less-doped material of the same type, i.e. n^+n or p^+p , shows similar characteristics as the normal p-n junction: brought into contact the electrons from the n^+ material diffuse into the n-doped material generating a negative space charge, the n^+ region is left with a positive one.

In most part of the highly doped material, i.e. the n^+ / p^+ - electrodes, most of the electrons remain in the conduction band. Thus, the charge collection is incomplete or zero within this volume. Therefore, this region is (partly) insensitive to energy deposition of ionizing radiation: the so-called **dead layer**. A more detailed view on the charge collection efficiency at the border of active to dead volume is given in [68] and briefly discussed in Section 4.4.

Diodes with applied *reversed bias* show so-called **leakage currents**. The drift of minority charge carriers creates a steady-state current, which strongly depends on the temperature.

Furthermore, thermal production of electron-hole pairs in the depleted region causes a significant leakage current proportional to the depletion volume. Since the band gap of germanium is extremely small, germanium detectors can only be operated at low temperatures. Therefore, HPGe are operated at 77 K, typically using liquid nitrogen as coolant. Moreover, surface leakage currents may occur which are strongly influenced by the structure of the surface, i.e. scratches, or surface contamination. Typically, the bulk leakage current dominates. Leakage current introduces noise on the detection signal, which i.e. degrades the energy resolution, and cannot be handled by the read-out electronics. Leakage currents of a few tens of pA are acceptable.

The number of created charge carriers produced in the interaction of ionizing radiation in the semiconductor detector is proportional to the deposited energy. In the case of germanium, the average energy to create an electron-hole pair is $E_{e/h} = 2.96$ eV. γ -rays have typical energies of the order of tens of keV up to a several MeV. Thus, a huge amount of charge carriers is created. For comparison, the average energy to create an electron-hole pair in a gas is typically 15-30 eV [67].

However, the energy resolution is limited by the statistical fluctuation of the produced charge carriers: the higher the number of charge carriers the better the energy resolution. The average energy needed to create an electron-hole pair is about a factor 4-5 higher than the band gap, i.e. part of the energy is lost to excite phonons. Since the number of produced phonons and electron-hole pairs is correlated, the statistical fluctuation in the number of produced charge carriers differs from Poisson statistics. The signal fluctuation is given by $\sigma = \sqrt{N_{e/h} \cdot F}$ where $N_{e/h} = E/E_{e/h}$ is the average number of electron-hole pairs produced in an energy deposition E . The Fano factor F is between 0 and 1, where $F=1$ represents Poissonian statistics. Given the low energy needed to produce electron-hole pairs and the small Fano factor, germanium detectors have small signal fluctuations, thus excellent energy resolution.

The produced signals are typically very small and have to be amplified. Due to the small signal-to-noise ratio, germanium detector signals are read-out using charge sensitive amplifiers (CSA): the charge induced at the read-out electrode is converted into a voltage signal and amplified. The CSA is realized by an inverting operational amplifier with a feed-back capacitor integrating the signal. The capacitor is discharged via a parallel feed-back resistor.

The GERDA HPGe Detectors

The GERDA experiment uses HPGe detectors which are isotopically enriched in ^{76}Ge . The enrichment fraction of the crystals is about 87% in the double beta isotope. Since the crystal pulling acts as a purification, the intrinsic background of the detectors is very low. Only upper limits on the internal activities of ^{226}Ra , ^{228}Th and ^{227}Ac can be set for the GERDA Phase I detectors [71]. Furthermore, to prevent cosmogenic activation of the material, the detectors have been stored underground at any time possible.

All detectors are made of p-type material for which a lithium diffused n^+ -electrode covering nearly the entire detector surface is necessary. The n^+ -contact has a typical dead layer thickness of 0.8-2.0 mm which is much larger than the range of α -particles and of similar range than β -particles (see also Section 4.4). Therefore, the dead layer provides a shielding against surface contamination of α - and (partly) of β -decaying isotopes.

Figure 3.2 shows a schematic view of the two detector types used in GERDA. The signal is

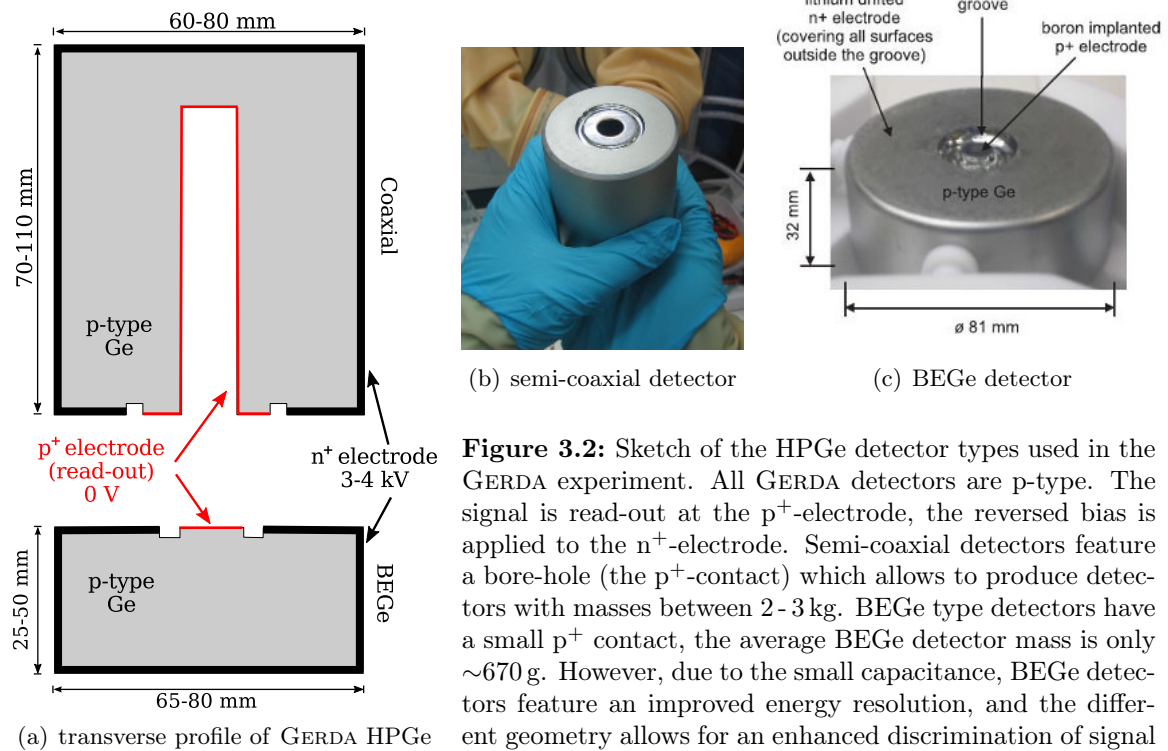


Figure 3.2: Sketch of the HPGe detector types used in the GERDA experiment. All GERDA detectors are p-type. The signal is read-out at the p^+ -electrode, the reversed bias is applied to the n^+ -electrode. Semi-coaxial detectors feature a bore-hole (the p^+ -contact) which allows to produce detectors with masses between 2-3 kg. BEGe type detectors have a small p^+ contact, the average BEGe detector mass is only ~ 670 g. However, due to the small capacitance, BEGe detectors feature an improved energy resolution, and the different geometry allows for an enhanced discrimination of signal against background events compared to semi-coaxial detectors. Figures taken from [69] and [70].

read out at the p^+ electrode, a reverse bias is applied to the n^+ electrode. Both electrodes are separated by a groove. To prevent leakage current due to surface contamination, the groove is covered by an insulating silicon monoxide layer, the so-called **passivation layer**. The two detector types mainly differ in the shape of the p^+ -contact and the accompanying restrictions in the diode size:

- **Semi-coaxial** detectors: the detectors were used in the former Heidelberg-Moscow [1] and IGEX [2] experiments. The boron implanted p^+ electrode is located in the detector bore-hole. The detector mass is 2-3 kg.¹ In the following the semi-coaxial detectors are also referred to as coaxial or coax.
- **BEGe** detectors: Broad energy germanium (BEGe) detectors owe their name to the excellent energy resolution in a broad energy range, from 3 keV to 3 MeV [72]. The GERDA BEGe detectors have an average mass of ~ 670 g. Since the capacitance of the read-out electrode (radius of 1-2 mm) is proportional to its area, the noise which is dominated by this capacitance, is low. Therefore, BEGe detectors have an improved energy resolution compared to the semi-coaxial detectors. Furthermore, the special geometry allows for an enhanced pulse shape discrimination (PSD) with respect to semi-coaxial detectors. The concept of PSD for BEGe detectors will be subject of Chapter 4.

¹ANG1 has a mass of 969 g.

3.2 The GERDA Experiment

The experimental challenge in the search for $0\nu\beta\beta$ -decay is to reduce any background, external and internal, at $Q_{\beta\beta} = 2039$ keV. As discussed in the previous chapter, most dangerous are nuclear decays with a Q-value above $Q_{\beta\beta}$ since they can deposit energy in the ROI and mimic a $0\nu\beta\beta$ signal. Therefore, the experimental setup needs to be optimized to reduce any external and internal background originating from the laboratory or the setup itself as well as cosmic muons.

The GERmanium Detector Array (GERDA) experiment is located in the Italian underground laboratory Laboratori Nazionali del Gran Sasso (LNGS) of INFN. The laboratory site is covered by an overburden of 1.4 km of rock, corresponding to 3500 m w.e. which reduces the cosmic muon flux by six orders of magnitude with respect to the Earth's surface [73].

The basic concept of the GERDA experiment is to operate bare HPGe detectors in liquid argon (LAr). Figure 3.3 shows a schematic view of the GERDA experiment: the HPGe detectors are arranged in strings which are immersed from the top into a cryostat filled with 64 m³ of LAr. The cryogenic liquid serves as coolant of the HPGe detectors (~ 87 K). Furthermore, with its high atomic number, $Z = 18$, the LAr provides a passive shield against α - and β -particles as well as γ -rays from the surrounding material. The inner walls of the cryostat are partly covered with copper plates as shielding against radiation originating from the stainless steel.

The LAr cryostat is embedded in a 590 m³ water tank. The pure water moderates and absorbs neutrons as well as γ -rays. Moreover, the walls of the water tank are equipped with photomultiplier tubes (PMT) to detect muons by the emission of Cherenkov light when they pass through the water. The muon detection system will be referred to as **muon-veto**, since events in coincidence with an event in the water Cherenkov detector are discarded as background. The muon veto system is complemented by plastic scintillators panels on top of the GERDA clean room.

On top of the water tank is a clean room of ISO class 7. The lock to the LAr cryostat is surrounded by a glove box kept under nitrogen atmosphere. The glove box is equipped to prepare and mount the detector strings. Further details are found in Section 5.1.

GERDA Phase I

The GERDA experiment proceeds in two phases. In Phase I of the experiment, physics data were taken from November 2011 until May 2013. The detector array consists of four strings with HPGe detectors (see Figure 3.4): five enriched semi-coaxial detectors from the former Heidelberg-Moscow and three from the IGEX experiment, accounting for a total mass of 17.66 kg. In June 2012, an additional string with five new enriched BEGe detectors totaling a mass of 3.63 kg were installed.

The liquid argon surrounding the detectors contains traces of the radioactive isotope ^{42}Ar with an activity of $A = 101.0_{-3.0}^{+2.5}$ (stat) ± 7.4 (sys) $\frac{\mu\text{Bq}}{\text{kg}}$ [74]. Since the Q-value of ^{42}Ar is only 600 keV, the isotope does not contribute to the background at $Q_{\beta\beta}$. However, the β -decay of its daughter nuclide ^{42}K has a Q-value of 3.5 MeV (see decay scheme in Appendix B). The ^{42}K ions produced in the decay of ^{42}Ar drift in the electric field created by the applied bias voltage. Since the detectors dead layer is not sufficient to fully absorb the β -particles, the detector strings are covered by 60 μm thick copper cylinders to shield the electric field and prevent the accumulation of ^{42}K on the detector surface (see Figure 3.4(c)). All built-in materials were selected based on state-of-the-art screening techniques used for the assessment

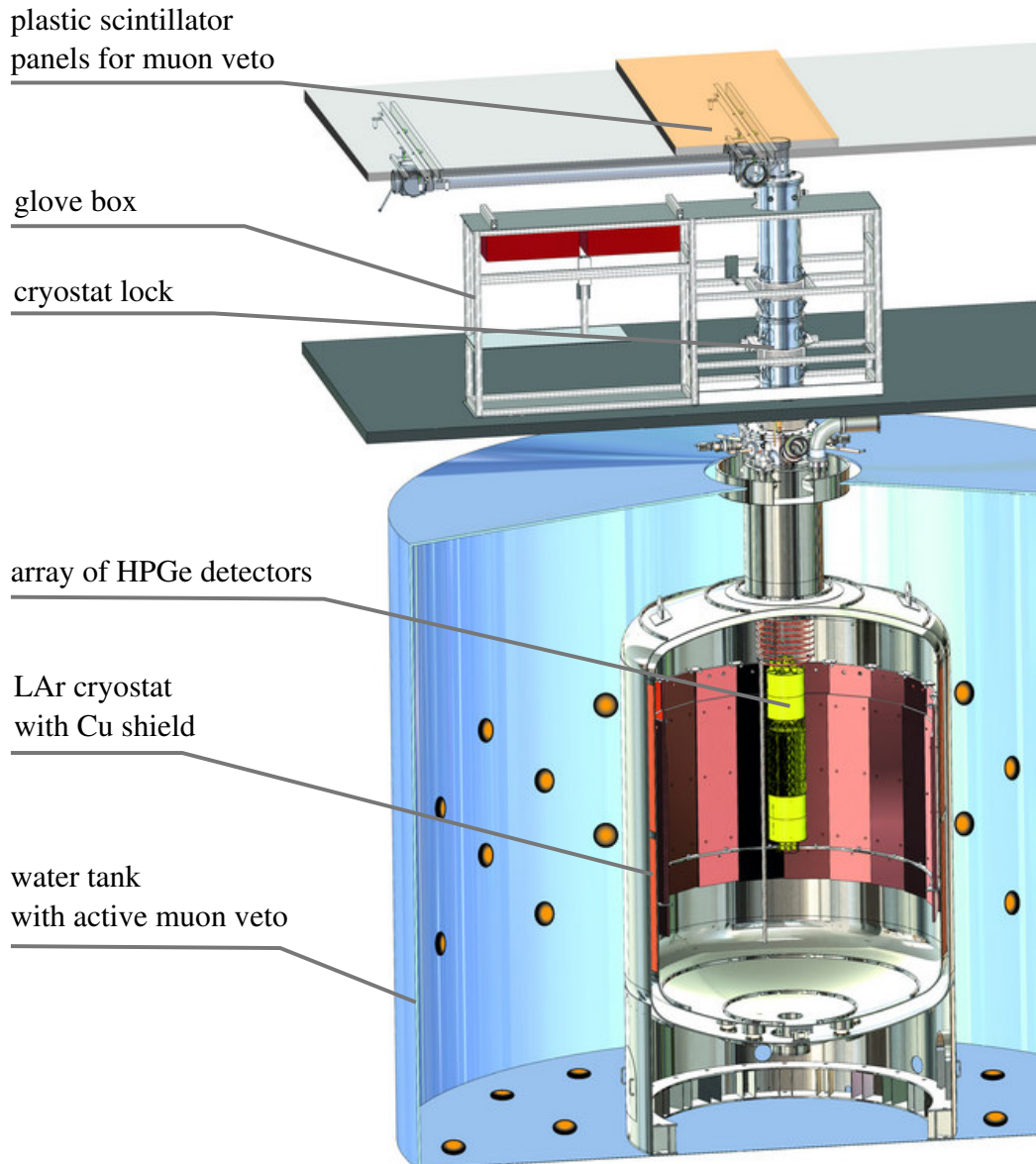


Figure 3.3: Schematic view of experimental setup of the GERMANIUM DETECTOR ARRAY (GERDA): the array of HPGe detectors is placed in a liquid argon (LAr) cryostat. The 64 m^3 LAr serves as coolant and passive shielding of the detectors. The inner walls of the cryostat are partly covered with copper plates to shield against radiation originating from the stainless steel. The cryostat is placed in a tank filled with 590 m^3 pure water. PMTs detect Cherenkov light emitted by muons passing through the detector, the so-called muon veto. On top of the water tank is the clean room with the lock to the cryostat. The lock is surrounded by a glove box which is kept under nitrogen atmosphere for the detector mounting and installation. The muon veto is complemented by plastic scintillator panels installed on top of the clean room. Drawing by GERDA at MPIK, Heidelberg.

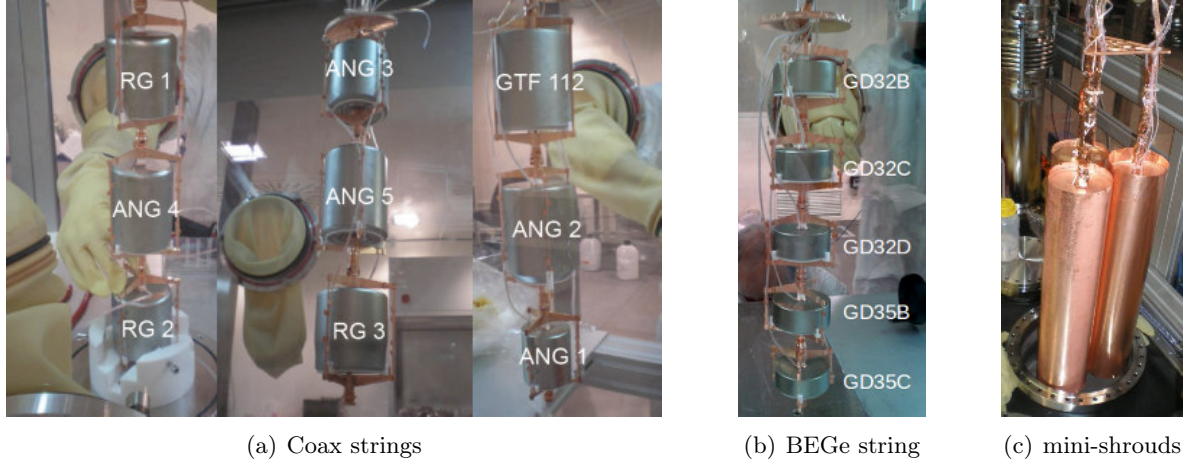


Figure 3.4: In GERDA Phase I three strings (3.4(a)) with 8 enriched semi-coaxial detectors from the HdM (ANG1- ANG5) and IGEX (RG1- RG3) experiment were installed and a HPGe detector (GTF112) with natural germanium were installed. As the detectors have been kept underground for a long period, their intrinsic background is low very compared to detectors kept above ground. In 2012 one string with five enriched BEGe detectors was installed (3.4(b)). To prevent the accumulation of ^{42}K on the detector surface, the strings are packed in $60\ \mu\text{m}$ thick copper cylinders, the so-called mini-shrouds (3.4(c)).

of radiopure materials [48]. Huge screening campaigns including γ -ray spectrometry, e.g. for ^{226}Ra and ^{228}Th identification, as well as ^{222}Rn emanation measurements were performed.

γ -ray screening measurements suggest background contributions from γ -emitting isotopes such as ^{208}Tl , ^{214}Bi and ^{40}K . Corresponding γ -lines are found in the physics spectrum shown in Figure 3.5. While ^{40}K does not contribute to the background at $Q_{\beta\beta}$, the Compton continua of the 2.6 MeV γ -line of ^{208}Tl and several ^{214}Bi γ -lines do. Measurements indicate the presence of ^{222}Rn in LAr. Furthermore, α -decays from a possible ^{210}Po surface contamination of the detectors are observed. The prominent γ -line at 1525 keV shows the relative large amount of the ^{42}Ar daughter nuclide ^{42}K in the LAr. Moreover, intrinsic background from cosmogenic activation of the detector material is expected. A detailed background model for GERDA Phase I is given in [69]. The main background components are summarized in Table 3.2. According to the Phase I background model no full energy peak (FEP) is expected at $Q_{\beta\beta}$: the background is assumed to be flat in a wide energy region, from 1930- 2190 keV excluding a 10 keV window at 2119 keV (the position of a ^{214}Bi FEP) and a 10 keV window around the single escape peak (SEP) of the 2.6 MeV γ -line of ^{206}Tl at 2104 keV.

In Phase I a total exposure of 21.6 kg·yr has been collected. After pulse shape analysis (see Chapter 4.5 and Appendix E) a background index (BI) of $(0.7^{+0.4}_{-0.2}) \cdot 10^{-2} \frac{\text{counts}}{\text{keV} \cdot \text{kg} \cdot \text{yr}}$ is reached for the BEGe data set [5]. The achieved BI is an order of magnitude better than in previous experiments for the search of $0\nu\beta\beta$ decay of ^{76}Ge : the Heidelberg-Moscow experiment reached $\text{BI} = (11.3 \pm 0.7) 10^{-2} \frac{\text{counts}}{\text{keV} \cdot \text{kg} \cdot \text{yr}}$ [62]. In 2004 a subgroup of the Heidelberg-Moscow experiment claimed the observation of the $0\nu\beta\beta$ -decay of ^{76}Ge with a half-life of $1.19 \cdot 10^{25}$ yr [62]. The goal of GERDA Phase I was to test the claim: no signal of $0\nu\beta\beta$ decay was observed. A new limit on the half-life of the $0\nu\beta\beta$ decay of ^{76}Ge was set to $2.1 \cdot 10^{25}$ yr at 90 % C.L., rejecting the claim with 99 % probability [6]. GERDA Phase I reached a sensitivity on the lower limit of the half-life of $2.4 \cdot 10^{25}$ yr.

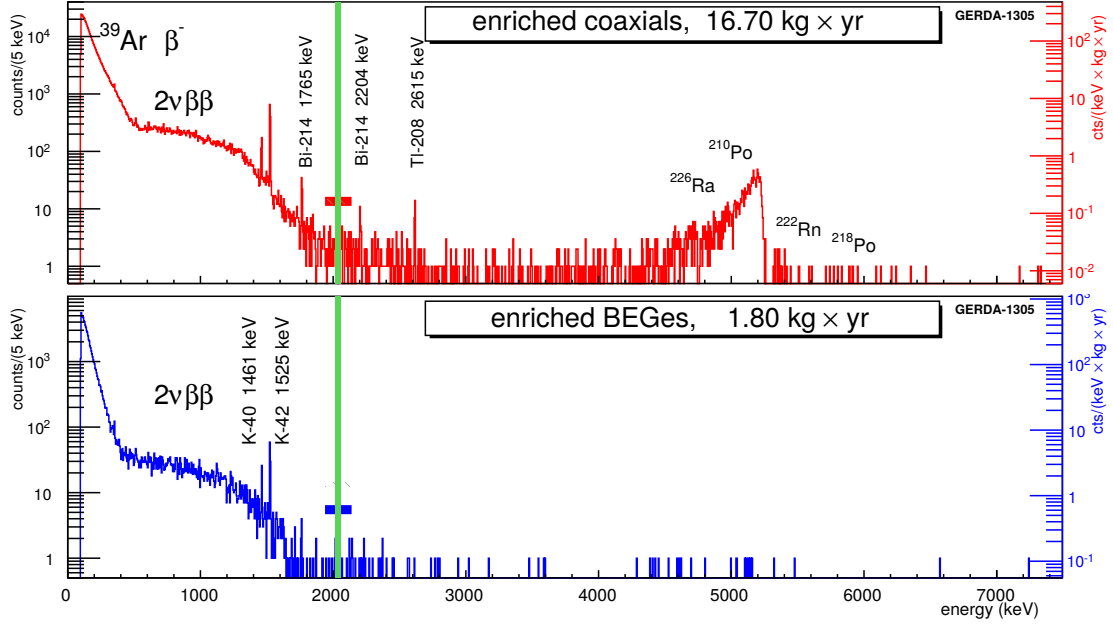


Figure 3.5: Physics spectrum recorded with enriched semi-coaxial (top) and BEGe (bottom) detectors in GERDA Phase I. Identified background sources are indicated. A 40 keV region around $Q_{\beta\beta} = 2039$ keV is blinded for analysis. Figure taken from [69].

3.3 The GERDA Phase II Upgrade

The aim of the GERDA experiment is to test the $0\nu\beta\beta$ -decay of ${}^{76}\text{Ge}$ up to half-lives beyond 10^{26} yr. At the end of GERDA Phase I the sensitivity on the half-life of $0\nu\beta\beta$ -decay became limited by static fluctuations of the background, i.e. at least one background event was expected in the signal region. As given by Equation 2.21, in case of background the sensitivity on the half-life of $0\nu\beta\beta$ -decay scales as

$$T_{1/2}^{0\nu} \propto \sqrt{\frac{M \cdot t}{\text{BI} \cdot \Delta E}}, \quad (3.2)$$

where $M \cdot t$ is the collected exposure, ΔE the energy resolution and BI the background index.

In the zero-background regime the sensitivity scales linearly with the exposure:

$$T_{1/2}^{0\nu} \propto M \cdot t. \quad (3.3)$$

Therefore, in order to reach half-lives as long as 10^{26} years, the background index needs to be lowered significantly in order to stay as long as possible in the background free regime. GERDA Phase II aims to reach a BI of $10^{-3} \frac{\text{counts}}{\text{keV} \cdot \text{kg} \cdot \text{yr}}$ to stay background free, i.e. expect zero background events in the ROI, until an exposure of $100 \text{ kg} \cdot \text{yr}$.

In order to reach the envisioned sensitivity, the detector mass is increased from 21 kg to 36 kg. 20 kg of the Phase II detector mass correspond to BEGe detector type which have a better energy resolution and enhanced pulse shape discrimination of signal from background events compared to coaxial detectors (see Chapter 4). For further identification of background events, the cryostat is instrumented to detect the scintillation light produced in the LAr.

component	location	relative contribution at $Q_{\beta\beta}$ [%]	
		Coax	BEGe
^{42}K	LAr homogeneous	16.2	5.2
^{42}K	n^+ surface	-	54.6
^{60}Co	detector assembly	7.6	-
^{60}Co	germanium	3.2	2.6
^{214}Bi	detector assembly	28.1	13.4
^{214}Bi	p^+ surface	7.6	1.8
^{228}Th	detector assembly	24.3	11.0
α -decays from ^{226}Ra chain	p^+ surface and in LAr close to	13.0	3.9

Table 3.2: Expected background composition at $Q_{\beta\beta} \pm 5$ keV for Coax ($Q_{\beta\beta} \pm 4$ keV for BEGe) according to the Phase I background model [69]. ^{42}K is the daughter nuclide of the β -emitting isotope ^{42}Ar (see decay scheme in Figure B.1). ^{60}Co is present in the detector assembly (i.e. detector holders and their components). Furthermore, an intrinsic contamination of ^{60}Co from cosmic activation of the germanium is expected (see Figure B.2 for the decay scheme and detailed discussion in Section 4.4). ^{226}Ra is expected on the detector surface. From the ^{226}Ra decay chain only ^{214}Bi and ^{214}Pb emit high energy β -particles and γ -rays. The ^{228}Th component contains the daughter nuclides ^{212}Bi and ^{208}Tl which are the only isotopes emitting high energy γ -rays and β -particles in the decay chain. α -emitting isotopes from the ^{226}Ra decay chain include ^{226}Ra , ^{222}Rn as well as ^{210}Po .

The GERDA Phase II Detector Array

Figure 3.6 shows a schematic view of the GERDA Phase II array. In total 40 HPGe detectors are arranged in seven detector strings:

- **enrBEGe** strings: 30 enriched BEGe detectors are mounted with a total mass of 20.0 kg. The detectors are arranged in four strings.
- **enrCoax** strings: 7 enriched coaxial detectors are mounted with a total mass of 15.8 kg. Six coaxial detectors are arranged in two strings, while one (ANG 1) is mounted in a BEGe strings.
- **natCoax** string: the central string consists of three semi-coaxial HPGe detectors with natural abundance of ^{76}Ge totaling a mass of 7.6 kg

Table C.1 summarizes the Phase II detectors, the final Phase II assembly will be discussed in detail in Chapter 5.

The BEGe detectors are mounted back-to-back in pairs as shown in Figure 3.6. Due to their large mass, the semi-coaxial detectors are mounted separately, with the signal contact facing down. Each string contains at maximum four BEGe pairs, or three coaxial detectors. The detector array allows for a dense packing of the detectors, hence for an enhanced multi-detector coincidence cut.

All material in the close vicinity of the detectors are selected according to screening results. Since the average mass of an enriched GERDA BEGe detector is only ~ 670 g (compared to 2471 g of a coaxial detector), the activity of the detector holder needs to be reduced with respect to Phase I. The Phase II detector support consist of one silicon plate per detector and

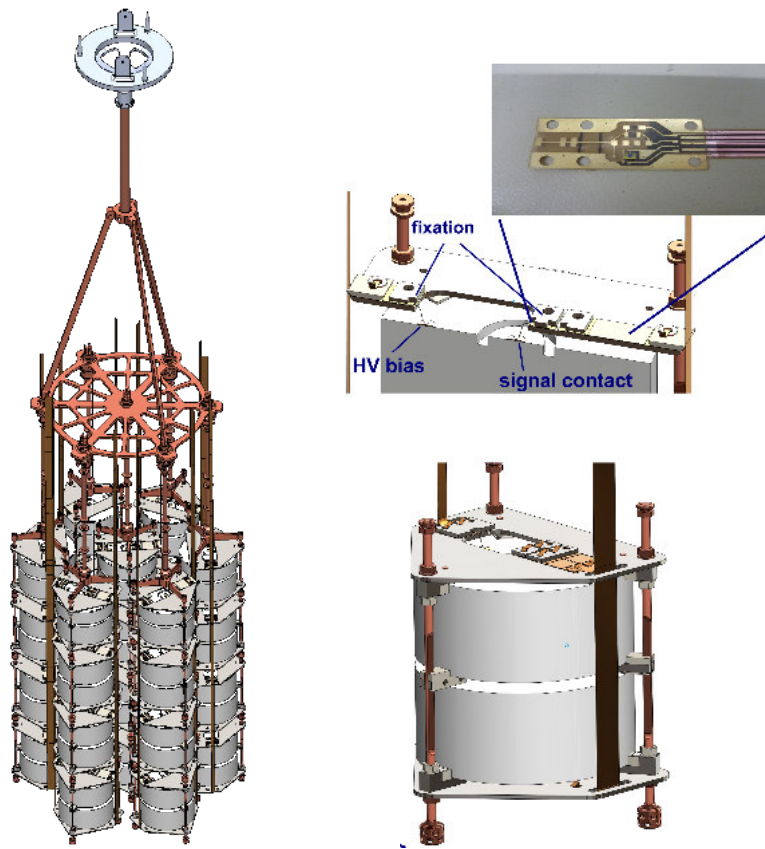


Figure 3.6: The Phase II detector assembly: the HPGe detectors are arranged in strings. The BEGe detectors are mounted as pairs in new low mass holders. Similar holders are used for semi-coaxial detectors. Due to their size only one detector is mounted per holder. HV and signal cables are fixed directly on the silicon plate of the detector module. The contacting is realized by ultrasonic wire bonding. See Section 5.1 for further details on the detector assembly.

high purity copper strings. The detectors lie on silicon steps, covered with PTFE pieces for electrical insulation of the detectors. The custom-made flexible high voltage (HV) and signal cables are mounted directly on the Si plates of the detector support. Table 3.3 compares the components and radioactivity of the Phase I and Phase II holders: the amount of copper and PTFE is greatly reduced. In Phase I, the electrical contacting was realized by a Chinese hat which is pushed by a silicon spring onto the p^+ contact [48]. Consequently, the detector support needed to withstand a certain stress. In Phase II the electrical contacts (bias voltage and signal read-out) are realized by ultrasonic wire bonding. Since no force is necessary to establish stable contacts, much of the copper support is replaced by the fragile, but radiopure silicon. Further details on the Phase II contacting scheme can be found in [75].

Figure 3.7 shows the original design of the Phase II front-end (FE) electronics. The FE is split into two stages [77]: the very front-end (VFE), with JFET and the resistive feed-back circuit, and the four-channel cryogenic charge sensitive preamplifier, CC3. The VFE circuit is printed on the head of the signal flex cable for the placement of a bare in-die JFET (SF291), a custom-made feed-back resistor ($\sim 1 \text{ G}\Omega$) and a printed trace feed-back capacitor ($\sim 0.3 \text{ pF}$) [77]. The JFET is contacted using ultrasonic wire bonding.

material	mass [g]	total activity [μBq]		total activity [μBq]	
		per holder		per kg detector mass	
		^{228}Th	^{226}Ra	^{228}Th	^{226}Ra
Phase I coax					
Cu	84	<1.6	<1.3	<0.6	<0.5
PTFE	7	<0.15	<0.14	<0.1	<0.1
Si	1	-	-	-	-
Phase II coax/BEGe					
Cu	26	<0.5	<0.4	<0.2/ <0.4	<0.2/ <0.3
PTFE	2	0.08	0.09	0.03/ 0.06	0.04/ 0.07
Si	40	-	-	-	-
Bronze	1	<0.3	<0.3	<0.12/ <0.22	<0.12/ <0.22

Table 3.3: Activity of detector holders. Numbers taken from [75] and the total activity is scaled to the average detector mass, in case of BEGe detectors to the average mass of a detector pair. For coaxial detectors an average mass of 2471 g is assumed, for BEGe-type an average detector pair of 1340 g. For Phase I only coaxial detectors are considered.

The serial noise at the input of the preamplifier is proportional to the detector capacitance [66]. Any cable between the detector and the JFET adds to this input capacitance. By placing the VFE as close as possible to the detector, the noise and thus the capacitance is kept low. This is of special interest to take advantage of the low capacitance of BEGe detectors and the corresponding improved energy resolution. Furthermore, the two staged FE electronics, allows to place the second stage, i.e. the CC3, at a larger distance to the detector to reduce the radioactivity budget without worsening the signal-to-noise ratio of the read-out.

GERDA Phase II Background

At the time of writing this thesis only a preliminary background model was available [78]. Figure 3.8 shows the preliminary model: the background composition is similar to GERDA Phase I, at $Q_{\beta\beta}$ no background peak is expected and the background is assumed to be flat. Table 3.4 summarizes the main background components at $Q_{\beta\beta}$ and in the $2\nu\beta\beta$ -region from 1.0- 1.3 MeV for BEGe and coaxial detectors.

Discrimination of Signal from Background Events

The Phase II background goal of $\text{BI} = 10^{-3} \frac{\text{counts}}{\text{keV} \cdot \text{kg} \cdot \text{yr}}$ can only be achieved by improved active background reduction techniques. Such techniques are based on the different interaction of signal (= $0\nu\beta\beta$ -/ $2\nu\beta\beta$ -events) and background events with the detection media: Since the typical range of an electron in germanium is about 1 mm, signal events ($\beta\beta$) deposit their energy very locally within a single crystal. On the other hand, γ -rays may deposit energy via multiple Compton scattering in several locations of the crystal, resulting in a so-called multi-site event (MSE), while α - or β -particles deposit energy on the detector surface. Both MSE and surface background events can be discriminated using pulse shape analysis (PSA), i.e. by analyzing the time structure of the signals. Further details on the concept of PSA as

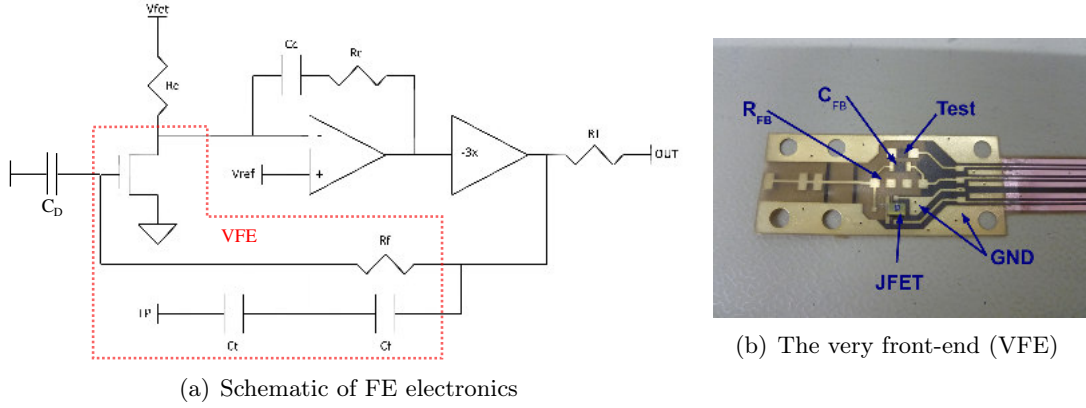


Figure 3.7: The Phase II signal read-out is split into two stages: the very front-end (VFE) with JFET, feed-back resistor R_f and capacitor C_f , and the first amplifying stage, CC3. Schematic from [76]. The VFE components are arranged at the head of the flexible signal cable.

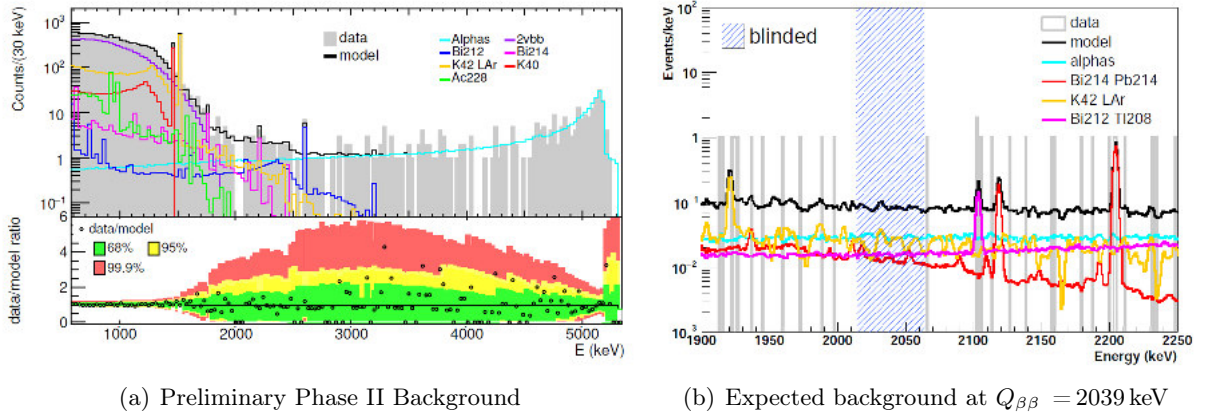


Figure 3.8: Preliminary Phase II background model for the BEGe data set at the time of this thesis. Neither PSD nor LAr veto is applied. As in Phase I no background peak is expected at $Q_{\beta\beta}$ and the background is assumed to be flat. Figures taken from [78].

well as the performed analysis in GERDA Phase I and Phase II will be subject of Chapter 4 and 6. Contrary to $\beta\beta$ -events, background events likely interact in more than one detector e.g. by multiple Compton scattered γ -rays. Thus, coincident events in multiple detectors are regarded as background. The so-called detector-detector anti-coincidence cut (AC) is optimized by a dense packing of the detector array.

Similar to the coincident detector events, background events may deposit energy in the surrounding LAr, e.g. by multiple Compton scattering or in the case of ^{42}K by a γ -ray accompanied β -decay. Therefore, the LAr cryostat is instrumented to read out the argon scintillation light. The scintillation light is emitted at a wavelength of 128 nm. As the maximum sensitivity of photon detectors such as photomultiplier tubes (PMT) and silicon photomultipliers (SiPM) is typically around 400-500 nm, the wavelength of the scintillation light needs to be shifted. Events in coincidence with scintillation light are regarded as background events. In the analysis the LAr instrumentation will be referred to as **LAr veto**. The concept of a LAr

component	location	relative contribution [%]			
		at $Q_{\beta\beta}$		in 1.0-1.3 MeV	
		Coax	BEGe	Coax	BEGe
^{40}K	mini-shroud	-	-	8.5	10.6
^{42}K	LAr homogeneous	39.3	24.3	23.5	24.4
^{226}Ra	bias + signal cables	14.3	17.1	0.9	1.1
^{228}Th	detector assembly	12.1	19.3	0.1	0.2
α -model	p^+ surface and in LAr close to	35.0	36.4	0.2	0.2
$2\nu\beta\beta$	enr^{HPGe}	-	-	66.1	62.3

Table 3.4: Preliminary background composition in the ROI, (2039 ± 25) keV, and the energy region (1.0-1.3) keV (dominated by $2\nu\beta\beta$ -decays) before pulse shape discrimination and LAr veto. ^{228}Th contains the isotopes ^{212}Bi and ^{208}Tl from the decay chain, ^{226}Ra includes ^{214}Bi and ^{214}Pb . The α -model includes decays from ^{210}Po , ^{226}Ra on the p^+ contact, as well as ^{222}Rn dissolved in LAr. Numbers taken from [78].

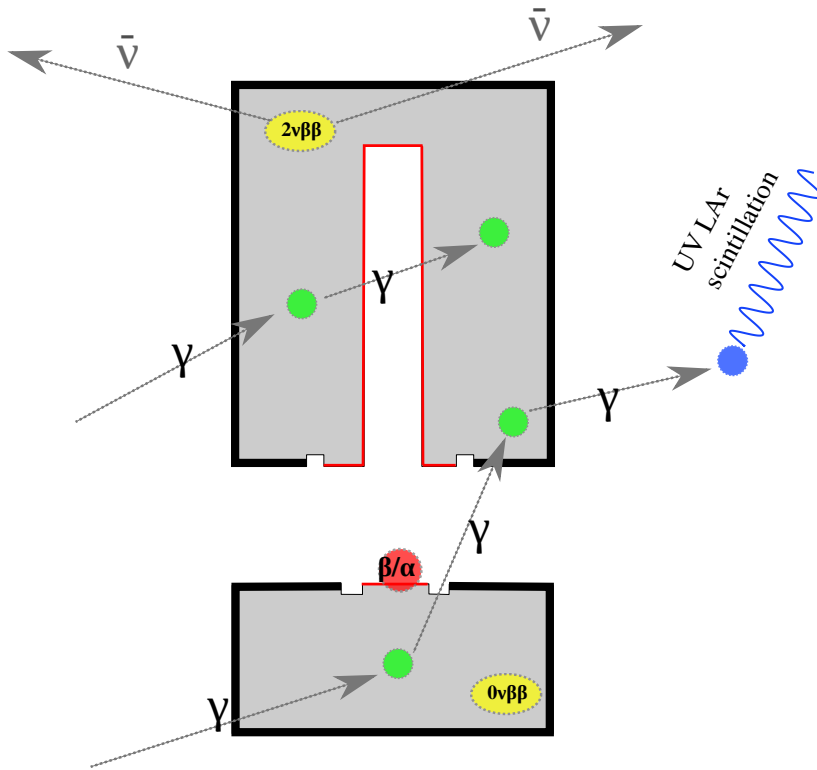


Figure 3.9: The principle idea behind the discrimination of signal ($0\nu\beta\beta/2\nu\beta\beta$ -events) from background events: signal events deposit the energy very locally, in a single detector (~ 1 mm). Background events, e.g. γ -rays, may deposit energy via multiple Compton scattering in several locations inside a single detector, several detectors or additionally in the LAr. α or β -decays deposit locally energy on the detector surface. See text for details. Modified figure from [69].

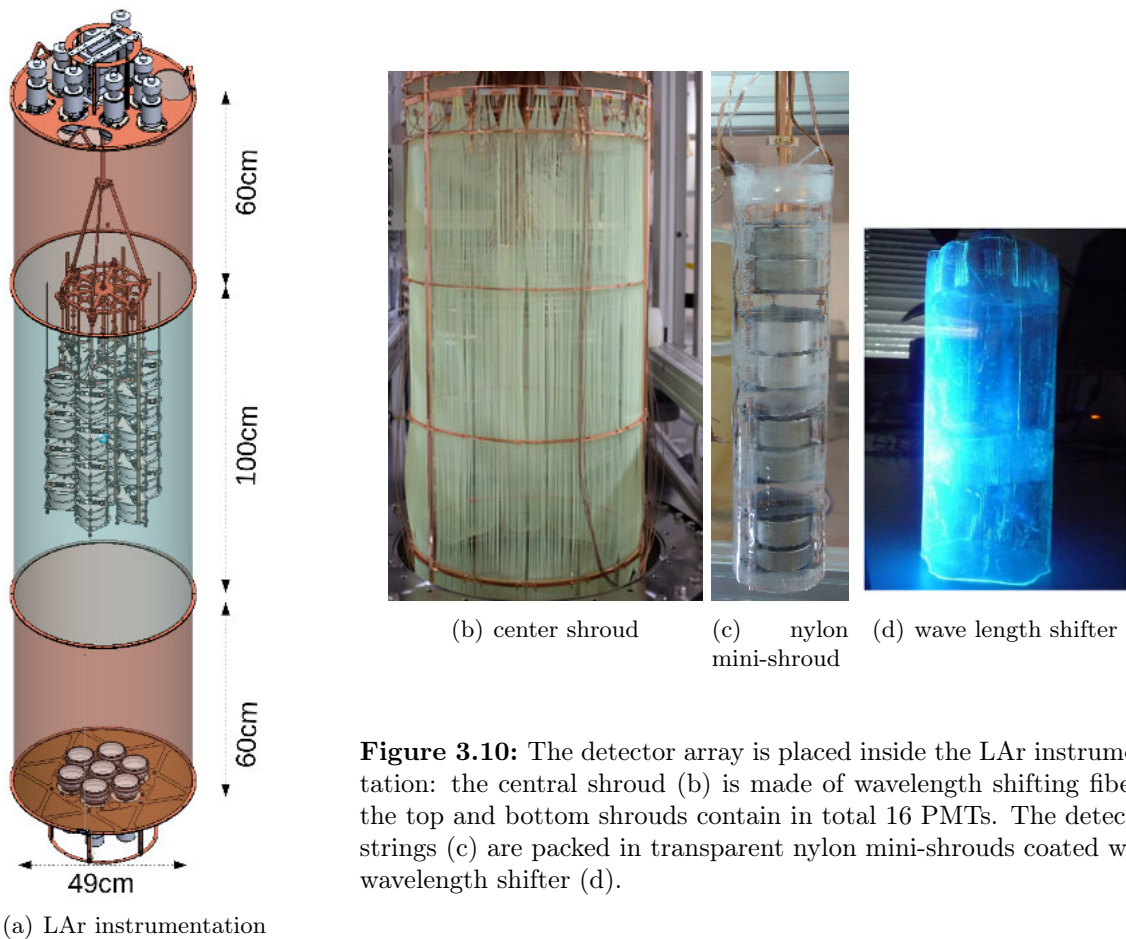


Figure 3.10: The detector array is placed inside the LAr instrumentation: the central shroud (b) is made of wavelength shifting fibers, the top and bottom shrouds contain in total 16 PMTs. The detector strings (c) are packed in transparent nylon mini-shrouds coated with wavelength shifter (d).

veto as active background reduction technique has been successfully tested in the GERDA test cryostat LArGe [79]. Since the LAr volume is large compared to the detector volume, this is a very efficient active background reduction technique.

Figure 3.10(a) shows a schematic view of the GERDA Phase II LAr instrumentation: the array is surrounded by a 2.2m long shroud. The central part of the shroud is made of wavelength shifting fibers which are read-out with SiPMTs. The bottom and top shroud contain in total 16 photomultiplier tubes (PMTs) mounted in copper cylinders which are covered with wavelength shifting reflective foil. In Phase I, the detector strings were surrounded by copper cylinders, in order to shield the electrical field of the germanium detectors and prevent the accumulation of ^{42}K ions. To detect the scintillation light produced in the close vicinity of the detectors, the Phase II detector strings are packed in transparent nylon cylinders, so-called nylon mini-shrouds (see Figure 3.10(c)). The nylon is coated with wavelength shifter, in order to collect energy deposition in the nylon itself. Further details on the LAr instrumentation can be found in [80, 81, 82]. The final integration of the GERDA Phase II array as well as first results on the background suppression obtained during commissioning will be discussed in Chapter 5.

Pulse Shape Discrimination Using BEGe Detectors

This chapter describes the pulse shape discrimination for BEGe detectors.

Section 4.1 explains the basic principle of the discrimination of signal-like from background-like events: $0\nu\beta\beta$ events deposit their energy very localized whereas incident γ -rays likely interact multiple times in the detector material. The fraction of single interacting γ -rays from an external ^{228}Th source is estimated using Monte Carlo (MC) simulations. Furthermore, the use of double escape peak (DEP) events as a proxy for $0\nu\beta\beta$ events is motivated.

Section 4.2 explains the underlying principle of the superior pulse shape discrimination of BEGe detectors. The different pulse shapes of events with single and multiple interactions inside the detector are discussed.

The pulse shape analysis applied to the GERDA Phase I/ II BEGe data is based on a single parameter, namely the ratio of the maximum of the current pulse over the energy, A/E [3]. The basic principle of the method using ^{228}Th calibration data is described in Section 4.3.

One of the main background sources in the GERDA experiment are β -decays from ^{42}K , a daughter nuclide of ^{42}Ar . A further background contribution at $Q_{\beta\beta}$ originates in γ -ray emitting isotopes from the detector assembly as well as α -decays on the detector surface or close-by. Moreover, intrinsic background from cosmogenic produced germanium isotopes may provide a crucial background at $Q_{\beta\beta}$. Section 4.4 discusses the discrimination of external γ -, β -, α - and intrinsic background from signal events using the A/E parameter.

The A/E based pulse shape analysis has been applied to the GERDA Phase I BEGe data. Analysis details on the calibration of the A/E cut are found in Appendix E which has been published in the GERDA publication 'Pulse Shape Discrimination for GERDA Phase I Data' to which the author of this work made a leading contribution. Section 4.5 discusses the main results: the achieved background index before and after PSD as well as the signal efficiency of the A/E cut in GERDA Phase I are presented. The determined signal efficiency is cross-checked with the acceptance of $2\nu\beta\beta$ events. All results are revised and may differ from the results in Appendix E.

Finally, Section 4.6 discusses PSD for non-BEGe-type HPGe detectors, such as semi-coaxial detector as used in GERDA and p-type point-contact (PPC) detectors used by the MAJORANA collaboration.

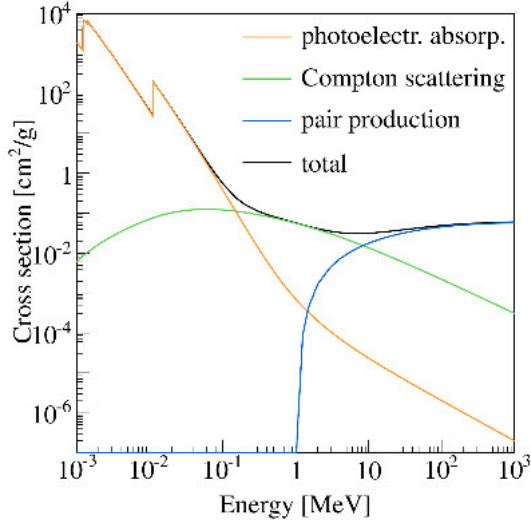


Figure 4.1: Total photon cross section in germanium. There are three main contributions: photoelectric effect (dominant at energies below 100 keV), Compton scattering (dominant around ~ 1 MeV) and pair production (dominant at energies above 10 MeV). Figure taken from [83].

4.1 Signal vs Background Events

Ionizing radiation loses energy via ionization and excitation of the atoms of the detector material. Electrons are created which produce large showers of electron-hole pairs. The produced charges drift in the electric field and induce charges on the electrode, which build up the read-out signal, as will be discussed in Section 4.2 in more details. For germanium at a temperature of 77 K the average energy needed to create an electron-hole pair is 2.96 eV [65] and is independent of the type and energy of the incident radiation [67].

HPGe detectors are excellent devices for γ -ray spectroscopy. However, no particle identification is possible. The discrimination of signal, i.e. $0\nu\beta\beta$ events, from γ -induced background is based on the different interaction of electrons and γ -rays with the detector material and the resulting spatial distribution of the energy deposition. In the case of germanium a 1-2 MeV electron describes a random walk inside the detector with a total length of the order of 1-2 mm [84] until it is totally stopped. The range is given by the so-called stopping power of the material. For photons the definition of a range is significantly different. The parameter of interest is the mean free path, i.e. the average distance a photon travels until it interacts with the detector material. For germanium this is of the order of centimeter.

Figure 4.1 shows the three main interaction mechanisms of γ -rays with matter:

- **Photoelectric absorption:** the photon transfers its full energy to an electron of the detector material which is ejected from the atom. This is the dominant effect at low energies up to a few hundred keV.
- **Compton scattering:** the incident γ -ray is elastically scattered off an electron of the detector material and loses part of its energy.
- **Pair production:** at energies ≥ 1022 keV the incident γ -ray can be converted into an electron-positron pair in the Coulomb field of a nucleus of the detector material.

Figure 4.2 shows a ^{228}Th spectrum from a typical GERDA Phase II calibration run. The ^{228}Th daughter nuclide ^{208}Tl dominates the spectrum with its 2.6 MeV γ -line. The full energy peak (FEP) at 2.6 MeV consists of fully absorbed γ -rays. Typically, the full absorption

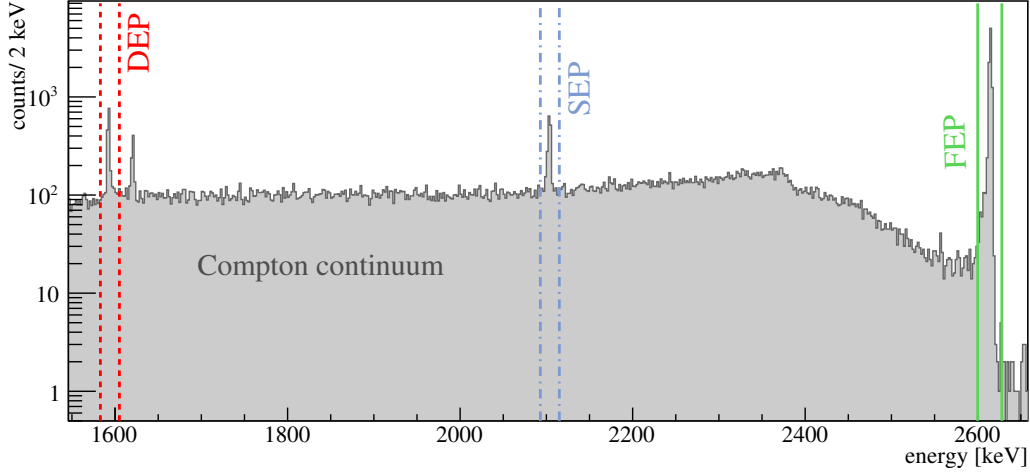


Figure 4.2: ^{228}Th spectrum recorded in GERDA Phase II calibration runs with one representative BEGe detector. The spectrum is dominated by γ -rays from the ^{208}Tl decay: its full energy peak (FEP) at 2615 keV with a prominent double escape (DEP) and single escape peak (SEP) as well as a broad Compton continuum. In a pair-production process the 2615 keV γ -ray is converted into an electron-positron pair. The positron annihilates into two 511 keV photons. If both photons escape the detection, this is called a DEP event. Thus, the DEP is found 2×511 keV below the FEP. In a SEP event one of the two annihilation photons is fully absorbed in the detector, the SEP is found 511 keV below the FEP.

is realized in multiple interactions with the detector material. Furthermore, the spectrum features a strong Compton continuum. Such events translate only part of their energy to the detector in single or multiple interactions. The ratio of Compton to FEP events depends on the detector size and geometry as well as the source position. The Compton edge around 2380 keV represents the maximum energy deposited in a single Compton event by a full-back scattering of the incident γ -ray. The Compton edge, i.e. the maximum energy is given by [66]

$$T_{\max} = E_{\gamma} \frac{2\epsilon}{1 + 2\epsilon} \quad (4.1)$$

whereas $\epsilon = \frac{E_{\gamma}}{m_e c^2}$.

All in all, γ -rays likely interact multiple times with the detector material until they are fully absorbed or escape the detection. Events with multiple energy deposition inside the active volume of the detector are called multi-site events (MSE). This is a distinct feature to $0\nu\beta\beta$ events which are characterized by single local energy deposition. Such events are called single-site events (SSE). The pulse shape discrimination method used in this work is based on the discrimination of SSE from MSE, i.e. on the spatial extension of the energy deposition of an event inside the detector material.

In the following the SSE fraction in different energy regions of the ^{228}Th spectrum as well as $0\nu\beta\beta$ events is investigated using Monte Carlo (MC) simulations. It will be demonstrated that $0\nu\beta\beta$ events are typically fully absorbed within $< 1 \text{ mm}^3$. However, the analysis can only give an estimate on the SSE fraction as noise or electronic response may influence the discrimination of SSE from MSE and are not considered in the following.

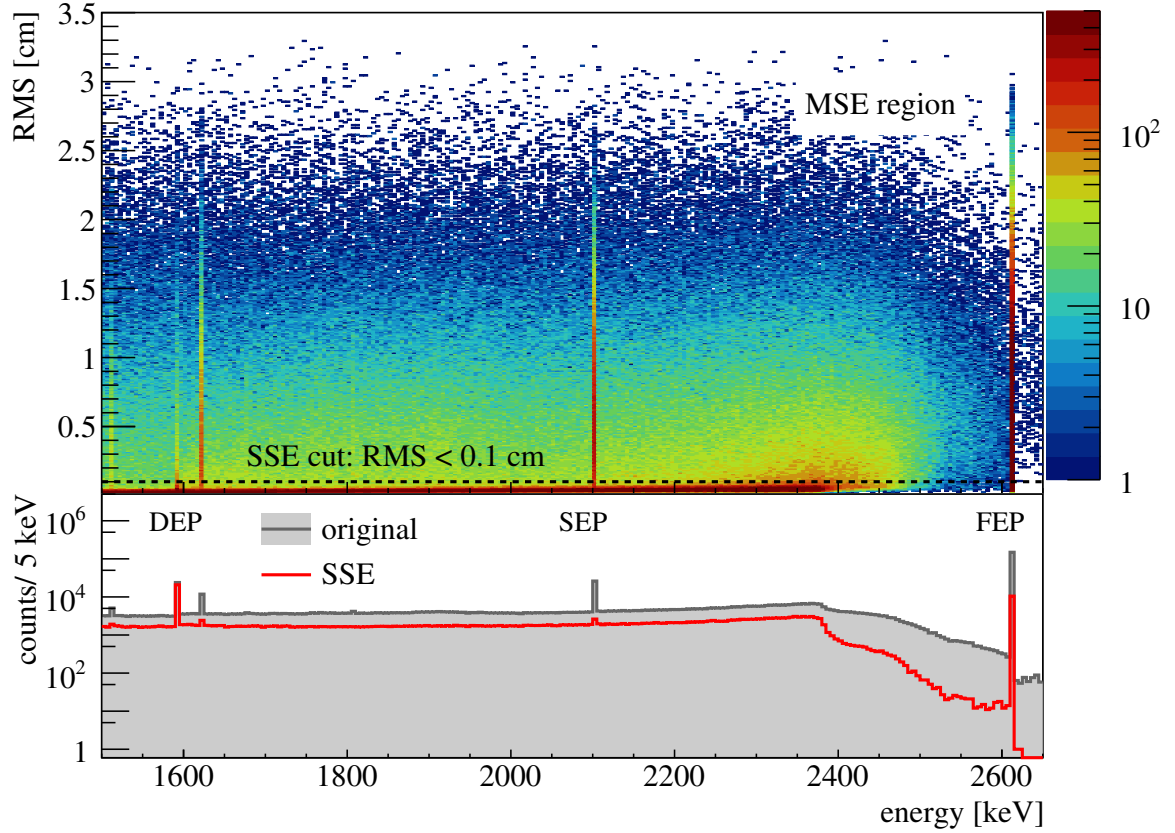


Figure 4.3: ^{228}Th simulated MC spectrum for GD91A. **Top:** RMS as a function of energy. The RMS is defined as the root-mean-square of all hits within the detector. Each hit position is weighted with its energy fraction. FEP of ^{208}Tl at 2615 keV and SEP at 2103 keV feature strong high RMS tails. The DEP at 1593 keV is seen as a high density spot. Single Compton scattered events describe a horizontal band of high density. The RMS maximum is chosen according to the detector radius. **Bottom:** Full energy spectrum (gray) and SSE spectrum (red). SSE are defined as events with RMS < 0.1 cm. FEPs, SEP and events above the Compton edge show a small SSE contribution whereas the DEP shows a high SSE fraction.

SSE Fractions of FEP and Compton Continuum of the ^{228}Th Spectrum

A selection of GERDA Phase II calibration runs are simulated with the MaGe framework based on Geant4 [85]. In the simulation 28 out of 30 BEGe detectors are considered. An event typically consists of multiple interactions, called hits in the following. For each event the center of gravity of all hit positions, i.e. energy depositions, and the corresponding root-mean-square, denoted RMS, is calculated. Each hit is weighted with the deposited energy fraction. The RMS is used as a measure for the spatial extension of an event inside the detector and to distinguish SSE from MSE.

Figure 4.3 shows the scatter plot of RMS vs. energy of a simulated ^{228}Th calibration run for one detector. The RMS reaches up to the full radius of the detector. Several prominent features are found in the spectrum:

- **Compton Continuum:** single scattered Compton events describe a narrow horizontal band seen as a high density region in the RMS scatter plot. The position and width of the

band slightly increases with increasing energy. A possible explanation is the increased electron energy which results in an increase of the event size, i.e. RMS. Furthermore, a high RMS tail from multiple Compton scattered events is observed. The single Compton band reaches until the Compton edge, above the number of events with high RMS increases promptly.

- **FEP:** FEP events show a strong tail towards high RMS values. Since the full absorption of a γ -ray is likely realized in multiple interactions, such events are large sized, i.e. have a high RMS.
- **DEP:** the DEP is seen as a high density region in the single Compton scattering band. If the incident γ -ray interacts via pair production in the detector material, the created electron is stopped, the positron annihilates into two 511 keV photons within a short range. In a DEP event the two annihilation photons escape the detection. Thus, the energy deposition is very localized inside the detector.
- **SEP:** in a SEP event one of the two annihilation photons is fully absorbed whereas the other escapes the detection. As the photon is typically absorbed with some distance to the electron, SEP events are non-localized and feature a high RMS tail.

The band of single Compton scattered events and the DEP distribution in Figure 4.3 peak well below 0.1 cm. Therefore, in the following analysis an SSE is defined as an event with an $\text{RMS} < 0.1$ cm. The bottom panel of Figure 4.3 shows the simulated ^{228}Th spectrum before and after the SSE cut. FEPs, SEP and events above the Compton edge show a small SSE contribution whereas the DEP shows an exceptionally high SSE fraction.

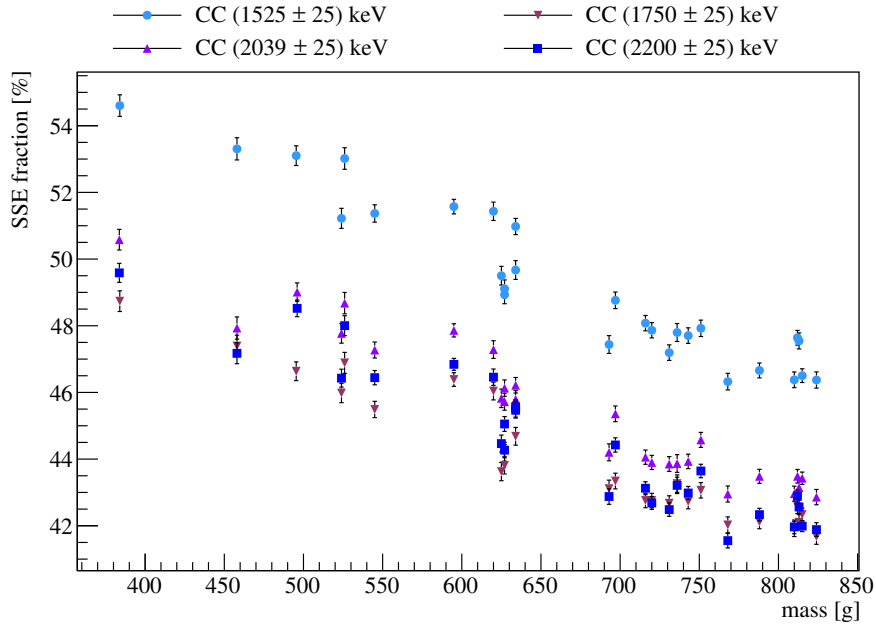
The SSE fraction in different energy and peak regions of the simulated ^{228}Th spectrum are calculated for 28 GERDA BEGe detectors. Figure 4.4(a) and Figure 4.4(b) show the SSE fraction in several Compton and peak regions of the ^{228}Th spectrum. On average (45.4 ± 2.1) % of Compton events around $Q_{\beta\beta}$ are single-site¹. The SSE fraction is clearly mass dependent: the larger the detector the higher the detection probability of large MSE whereas SSE are not effected.

The average SSE fraction in the FEP at 2.6 MeV is (6.2 ± 0.7) %, at 1.6 MeV (8.2 ± 1.0) %. The SEP features an exceptional low SSE fraction: on average only (2.9 ± 0.4) % of the events are single site.

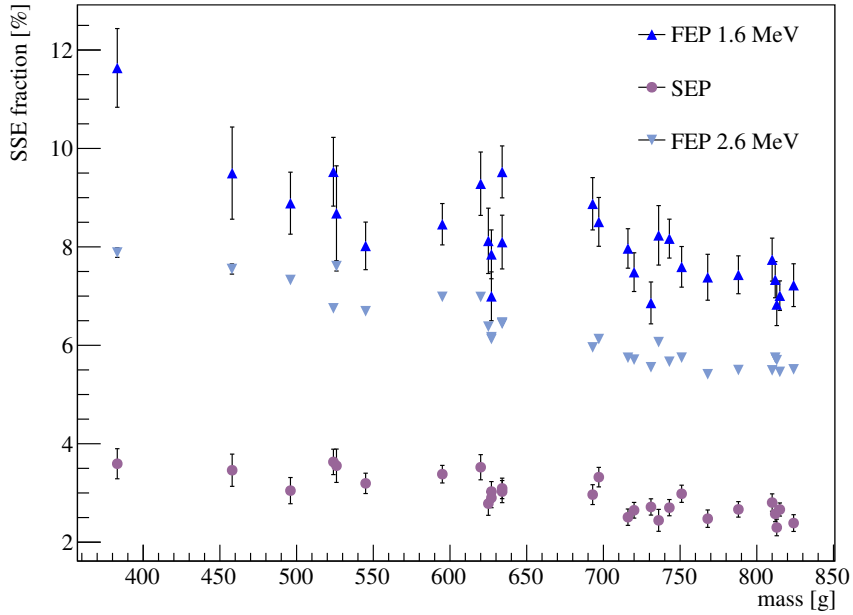
The DEP: A Proxy for $0\nu\beta\beta$ Events

As discussed before DEP events have single-site energy deposition. The event topology is very similar to $0\nu\beta\beta$ events, i.e. two electrons. Both DEP and $0\nu\beta\beta$ show a very localized energy deposition within the detector material. The SSE fraction is the parameter of interest to understand the similarity of both event types. There are two crucial differences between DEP and $\beta\beta$ events which influence the SSE fraction: DEP events may interact with the detector material, e.g. via Compton scattering, before pair-production. Thus, a certain fraction of DEP events will end-up as MSE. Furthermore, the SSE fraction is influenced by the emission of bremsstrahlung which may produce MSE. The energy loss via bremsstrahlung is energy dependent. As the DEP is about 450 keV below $Q_{\beta\beta}$, $0\nu\beta\beta$ events of ^{76}Ge are expected to emit more bremsstrahlung photons.

¹the SSE fraction of Compton events might change with detector-source geometry



(a) Compton regions



(b) peak regions

Figure 4.4: SSE fraction of Compton (top panel), FEPs and SEP events (bottom panel) in the simulated ^{228}Th spectrum for 28 BEGe detectors. SSE are defined as events for which the full energy is deposited within less than 1 mm inside the detector. Shown are different Compton regions at $Q_{\beta\beta}$ ($= 2039$ keV), above and below. All peaks are Compton background subtracted, efficiencies including statistical uncertainties are calculated according to Appendix A.

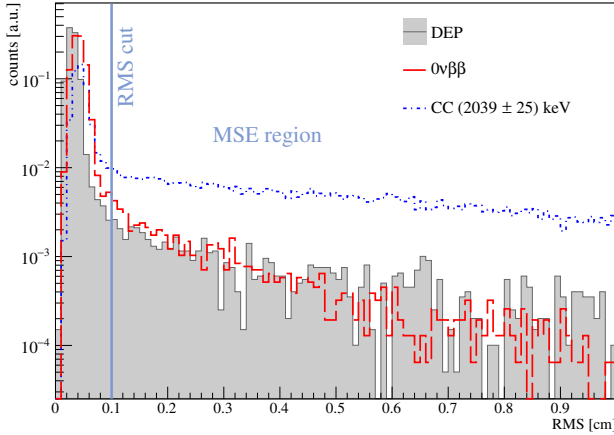


Figure 4.5: RMS distribution in the DEP of the 2.6 MeV γ -line of ^{208}Tl and the corresponding Compton continuum around $0\nu\beta\beta$, i.e. (2039 ± 25) keV based on Monte Carlo simulated ^{228}Th GERDA Phase II calibration runs as well as simulated $0\nu\beta\beta$ decays. Simulations for GD91A are shown. The RMS is defined as the spatial root-mean-square of all interaction points within the detector. Each hit position is weighted with the hit energy fraction. Events with an $\text{RMS} \geq 1$ mm are defined as MSE in the analysis. Distributions are normalized to unity integral.

Figure 4.5 shows the RMS distribution of simulated DEP and $0\nu\beta\beta$ events. The $0\nu\beta\beta$ distribution is shifted to higher RMS and broadened with respect to the DEP. Both the peak shift and the broadening might be explained by the increased number of high energy electrons produced in the particle interaction with the detector material. This is supported by the fact that the RMS distribution of Compton events in the energy range $Q_{\beta\beta} \pm 25$ keV shows a similar shift and broadening as the $0\nu\beta\beta$ events. DEP events feature a stronger high RMS tail which might be explained by the presence of events that interact via Compton scattering before the pair production.

Figure 4.6 shows the SSE fraction of DEP and $0\nu\beta\beta$ events. A small mass dependence is observed. On average $(94 \pm 0.7)\%$ of the $0\nu\beta\beta$ are SSE according to the RMS definition. This is on average $(1.8 \pm 0.6)\%$ higher than the SSE fraction in the DEP, no mass-dependence is observed. The difference of DEP and $0\nu\beta\beta$ events in the SSE fraction is similar for larger RMS: shifting the RMS cut to 0.2 cm or 0.3 cm yields a difference of about 2%. Therefore, the DEP is considered a good proxy for $0\nu\beta\beta$ events, however, a small difference due to the different event topologies at the few percentage level remains and needs to be taken into account in the signal efficiency of the pulse shape analysis applied in $0\nu\beta\beta$ search.

In the future, the analysis based on simulated $0\nu\beta\beta$ decays and ^{228}Th calibration runs should be combined with pulse shape simulations (PSS) and measurements. To minimize the different SSE fraction in DEP and $0\nu\beta\beta$ events introduced by the energy difference, a DEP closer to $Q_{\beta\beta}$ is desired. For further investigation of the energy dependence of the SSE fraction a broader spectrum of DEP is needed. The spectrum of ^{56}Co features many γ -lines up to 3.2 MeV and prominent DEPs at 1576 keV, 2180 keV, 2231 keV and 2251 keV correspondingly. A low energy DEP source is ^{88}Y with a prominent DEP at 814 keV.

4.2 Pulse Shape of BEGe Detectors

In the interaction of ionizing radiation with the detector material electron-hole pairs are created. The produced charge carriers drift along the electric field lines to the electrodes. Figure 4.7 shows a schematic of a BEGe detector and illustrated drift paths of charges through the detector. The signal is read-out at the small-sized p^+ contact. The read-out electrode is connected to the amplifier whereas a high positive bias voltage is applied to the outer detector surface, i.e. the n^+ contact. Electrons drift to the detector surface, holes to the read-out

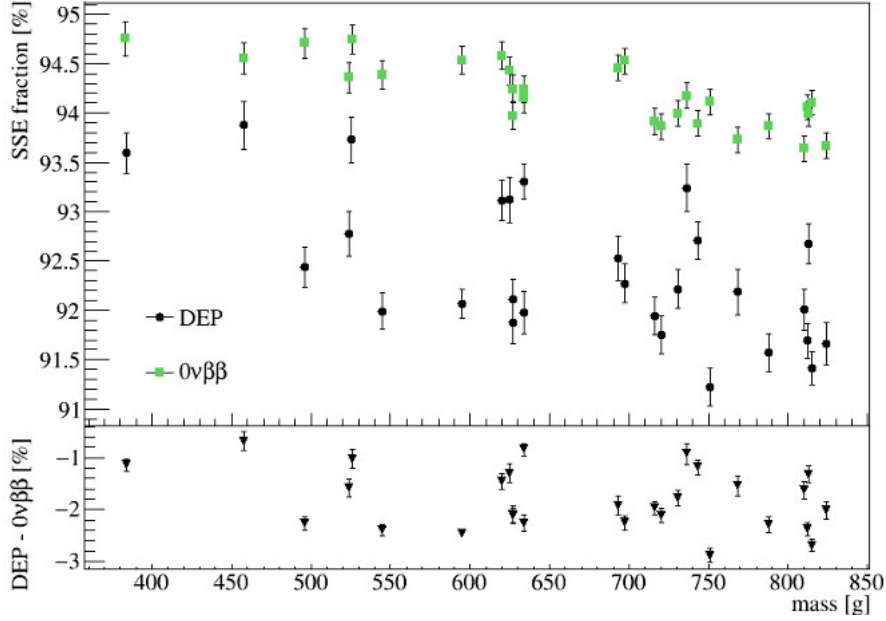


Figure 4.6: Top: SSE fraction of simulated DEP and $0\nu\beta\beta$ events for 28 GERDA Phase II BEGe detectors. SSE are defined as events with an RMS of less than 1 mm. The RMS is defined as the spatial root-mean-square of all interaction points within the detector, whereas each hit is weighted according to the deposited energy fraction. The DEP is Compton background subtracted. All efficiencies including statistical uncertainties are calculated according to Appendix A. **Bottom:** Difference in SSE fraction of DEP and $0\nu\beta\beta$ events.

electrode. The electric field created by the applied bias voltage is weak but close to the p^+ contact. If it were only for the electric field of the electrodes charges would not drift from the bulk to the electrodes. BEGe detectors feature an impurity gradient along the detector axis. In a depleted BEGe the space charges build up an electrical field which drifts the holes to the middle slice of the detector. Finally, the holes are drifted by the electrode potential towards the read out electrode. Therefore, the end of the drift paths of holes are very similar and independent from the interaction point.

As the charge clusters drift they induce mirror charges on the surface of the electrodes which build up the detection signal. The induced charge, Q , is described by the Shockley-Ramo theorem [87]:

$$Q = -q \cdot W(x) \quad (4.2)$$

where $W(x)$ is the so-called dimensionless weighting potential for the charge q at the position x .

Figure 4.8 shows the cross-section of a BEGe detector and the calculated weighting potential. The weighting potential is weak everywhere but in the vicinity of the read-out electrode. Consequently, only charges drifting close to the read out electrode contribute to the charge signal. As shown in Figure 4.7 the final drift paths of holes are similar independent of where the interaction occurred. Thus, their pulse shapes must be very similar except for a shift in time according to the different arrival time of the charges in the high weighting potential region. As electrons drift to the outer detector surface, they drift in the region of low weighting

Figure 4.7: Schematic view of a BEGe detector. The small circular p^+ read-out electrode is shown in red. A positive bias voltage is applied to the detector surface, the n^+ electrode. Drift paths for electrons and holes are simulated for three different interactions in the bulk volume of the detector. Figure taken from [86].

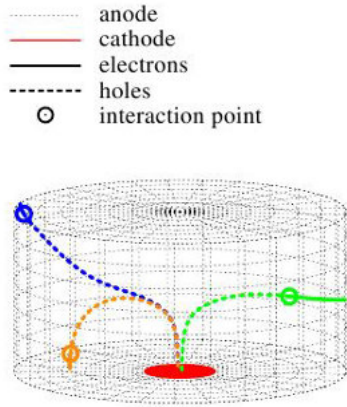


Figure 4.8: Cross-section of a BEGe detector. The color code indicates the strength of the dimensionless weighting potential. The signal is read out at the p^+ electrode which is marked in gray. Figure taken from [5].

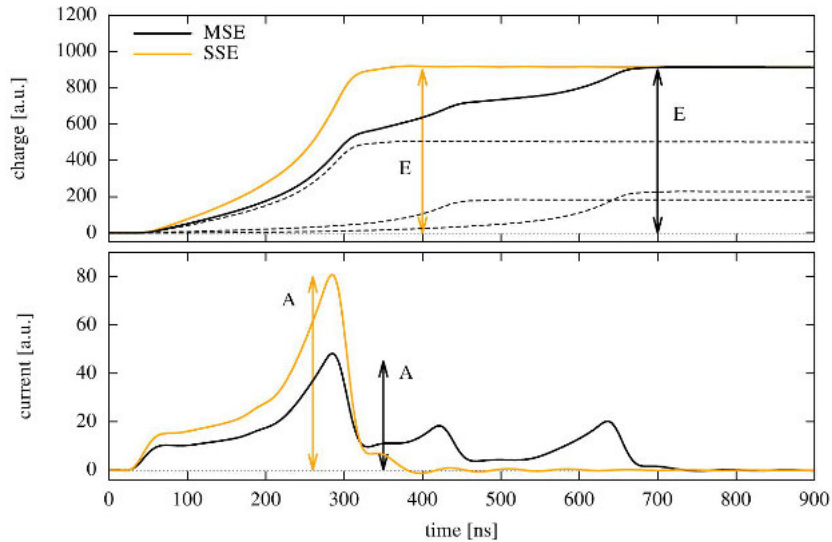
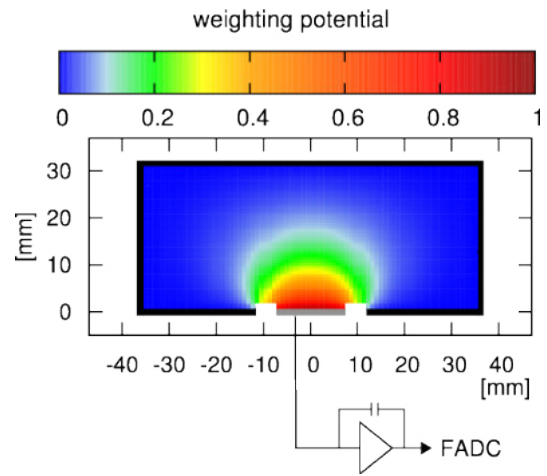


Figure 4.9: Simulated charge (top) and current (bottom) pulse of single-site (SSE) and multi-site events (MSE) with the same total energy. The MSE consists of three simulated interactions. The dashed lines represent the charge pulses for each single interaction in the MSE. Figure taken from [86].

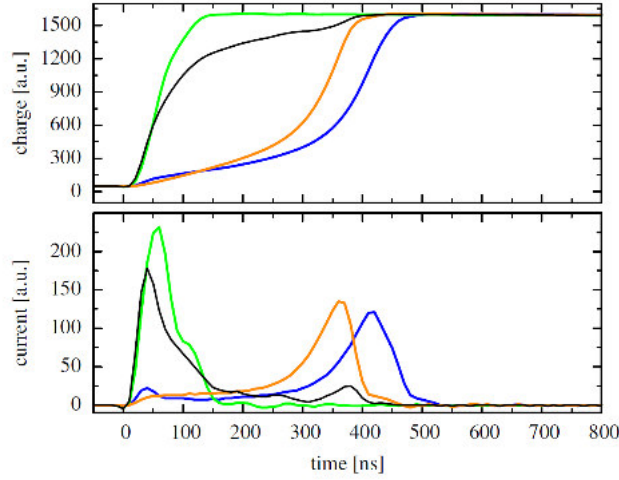


Figure 4.10: Simulated charge (top panel) and current (bottom panel) pulses for events occurring close to the p^+ contact (green and black). In orange a simulated event in the bulk of the detector volume is shown. The blue pulse is a simulated event further away from the p^+ contact. The current pulse shows a characteristic peak at the beginning of the trace which corresponds to the fast collection of the electron. Figure taken from [86].

potential and do not contribute much to the signal.

Figure 4.9 shows the time profile for a simulated pulse from local energy deposition, a so-called single-site event (SSE) [86]. The current pulse features a single peak like structure with an amplitude proportional to the energy deposition [3]. The current signal is largest when the holes drift through the region of highest weighting potential gradient. For comparison the pulse shape for multiple energy deposition is shown. An MSE can be interpreted as a superposition of several SSE since the total event energy is distributed over several charge clusters. As the charge clusters arrive in general with small time differences in the region of high weighting potential the current signal features a multiple peak structure.

The above described pulse shape holds only for interactions occurring in low weighting potential. Interactions in the volume close to the p^+ contact and the groove, i.e. the region of high weighting potential, produce very sharp rising pulses as holes are collected quickly. Moreover, the electrons contribute significantly to the signal. Figure 4.10 shows simulated pulses of energy deposition close to the p^+ contact. Further details on charge trajectories and the resulting signals in a BEGe detector can be found in [86].

4.3 The A/E Parameter

As discussed in Section 4.1 background from γ -rays likely interact multiple times inside the detector, i.e. are likely MSE, whereas $0\nu\beta\beta$ events are mainly SSE. Figure 4.9 demonstrates the basic principle of the A/E analysis: the maximum of the current pulse is roughly proportional to the energy deposited in a single interaction. The maximum amplitude, A , of the current pulse of an MSE is smaller than the amplitude of an SSE of the same total energy. Therefore, A/E is a promising parameter to discriminate signal-like from background-like events. The pulse shape discrimination method based on A/E was first developed in [3]. Figure 4.11 shows the A/E spectrum of a ^{228}Th measurement with several prominent features:

- **SSE-band:** single Compton scattered events, i.e. SSE, describe a prominent horizontal band up to the Compton edge. SSE above the Compton edge are highly suppressed.
- **MSE region:** multiple Compton scattered events are found at A/E values below the SSE band.

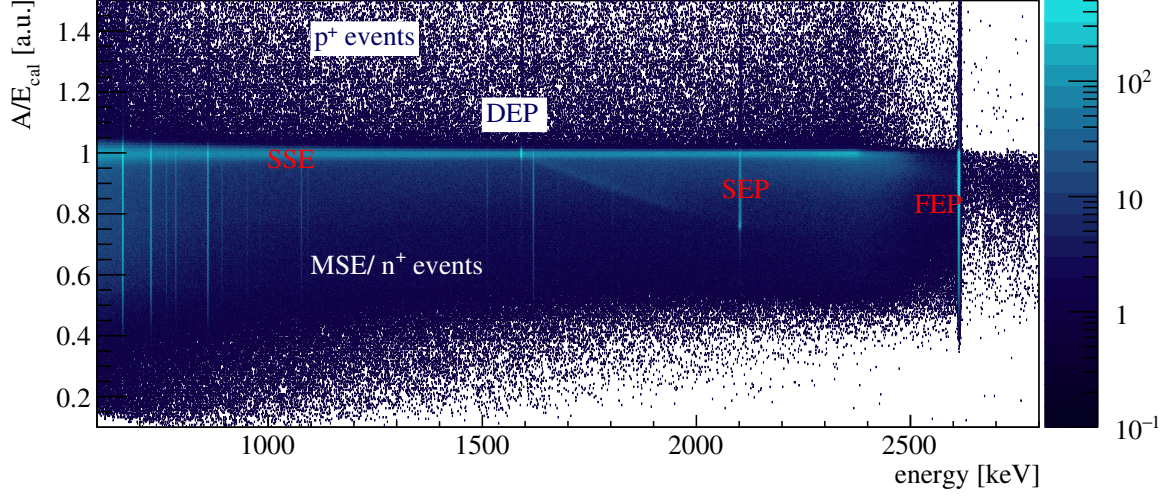


Figure 4.11: A/E as a function of energy for a ^{228}Th measurement. The prominent band at $A/E = 1$ is called single site band as it consists of single site events (SSE). Multi-site events (MSE) are populated below. Events on the p^+ contact and in the groove typically have high A/E values. Full energy peaks (FEP) and the single escape peak (SEP) at 2103 keV feature strong tails towards low A/E values. The DEP at 1593 keV is seen as a high density spot in the SSE band. A/E values are corrected for energy dependence such that the SSE band is centered at $A/E = 1$. A/E values extracted according to Appendix D.

- **p^+ events:** events close to the p^+ contact, i.e. in high weighting potential feature compatibly high A/E values.
- **DEP:** the DEP at 1593 keV is a high density region in the SSE band due to its large fraction of SSE.
- **SEP/ FEP:** the FEPs and SEP feature strong tails to low A/E values due their high MSE fraction.

Figure 4.12 shows the A/E distributions in the DEP, SEP and FEP of the 2.6 MeV γ -line of ^{208}Tl . For all peaks the underlying Compton background is subtracted according to Appendix A. The A/E distribution of DEP events has a Gaussian shape whereas the FEP shows a strong tail to lower A/E values. The SEP distribution peaks at $A/E \sim 0.76$ which corresponds to the ratio of the energy deposited by the pair-production, i.e. 1593 keV over the total energy, i.e. 2103 keV. Compton events feature a Gaussian distribution and a low side A/E tail.

Figure 4.13 shows a typical A/E distribution of Compton events in the ^{228}Th spectrum. Single-site events (SSE) are modeled by a Gaussian distribution, whereas multi-site events (MSE) are describe by a low side tail. The distribution is described by the function [5]:

$$f(x = A/E) = \frac{n}{\sigma_{A/E} \cdot \sqrt{2\pi}} \cdot e^{-\frac{(x-\mu_{A/E})^2}{2\sigma_{A/E}^2}} + m \cdot \frac{e^{f \cdot (x-l)} + d}{e^{(x-l)/t} + l} \quad (4.3)$$

$\mu_{A/E}$ and $\sigma_{A/E}$ are the mean and standard deviation of the Gaussian, n the integral. The second part is an empirically found function to describe the MSE tail. The parameters of interest in Equation 4.3 are the mean, $\mu_{A/E}$, and the sigma, $\sigma_{A/E}$, of the A/E distribution as

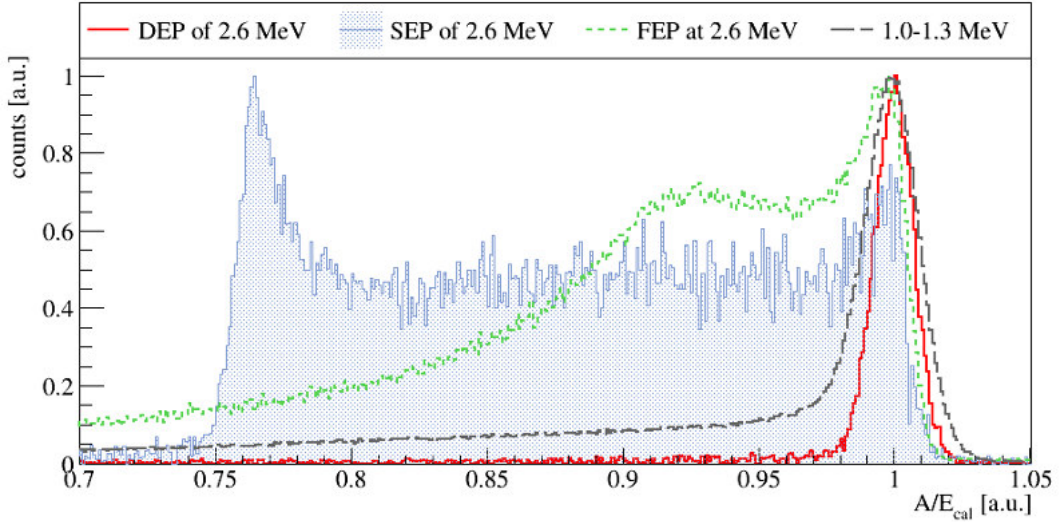


Figure 4.12: A/E distribution in different peaks of ^{228}Th spectrum. The FEP at 2.6 MeV shows a strong low A/E tail. A/E values in the DEP are mainly Gaussian distributed, whereas the single escape peak (SEP) features a characteristic peak at ~ 0.76 . A/E distributions in DEP, SEP and FEP are Compton background subtracted according to Appendix A. For comparison the A/E distribution in the energy region 1.0-1.3 MeV is shown in green. A/E values are corrected for energy dependence such that the SSE band is centered at $A/E = 1$. Distributions are normalized to equal maximum height. A/E values extracted according to Appendix D.

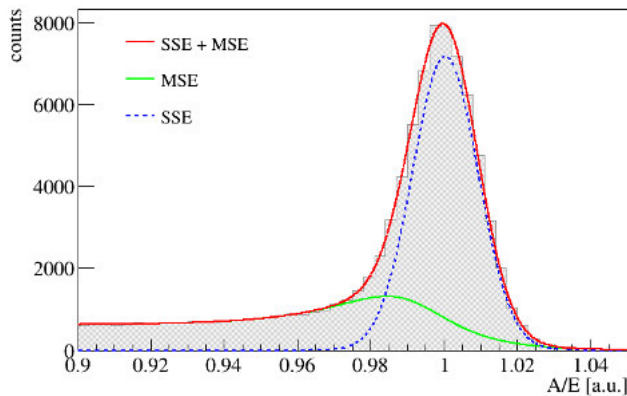


Figure 4.13: A/E distribution of Compton events from ^{228}Th fitted with the empirical function described in Equation 4.3. The distribution of SSE is modeled by a Gaussian (blue), the MSE distribution by a low side tail (green). A/E values are corrected for energy dependence such that the SSE band is centered around $A/E = 1$. A/E values extracted according to Appendix D.

they represent the position and width of the SSE band.

A/E vs Event RMS

In Section 4.1, the definition of an SSE is based on the event RMS, i.e. the root-mean-square, of all event hits within the detectors, each hit weighted with the energy fraction. According to this definition SSE have an $\text{RMS} < 0.1$ cm. However, RMS and A/E cannot be compared directly: while RMS considers the full spacial distribution of the interactions, the A/E parameter is only sensitive to the difference in the arrival time of the charge clusters in the region of high weighting potential.

Therefore, a simple pulse shape simulation based on the simulation toolkit ADL3 (AGATA Detector Library) [88] and adopted geometry for the GERDA detectors [89] has been performed. Neither detector response nor noise has been added to the pulses. Figure 4.14 shows the simulated A/E distribution of GD35C for events with $\text{RMS} < 0.1$ cm (SSE) and $\text{RMS} \geq 0.1$ cm (MSE) in different energy regions of the ^{208}Tl spectrum. SSE events peak around $A/E = 1$. The low A/E tails are nearly entirely MSE. SSE and MSE have a small overlap at $A/E = 1$.

Energy Dependence of A/E

The A/E parameter shows a small energy dependence. For simplicity in Figures 4.11 - 4.13 the A/E values are energy corrected such that the SSE band is centered around 1.

The A/E energy dependence is given by the slope of the SSE band and can be approximated above 1 MeV by a linear function. To determine the energy dependence the uncorrected A/E distributions of Compton events at different energies are fitted with the function described by Equation 4.3. The Gaussian mean of the distributions represent the position of the SSE band at a given energy. Figure 4.15 shows the uncorrected mean A/E values in the energy range 1.0 - 2.3 MeV. The slope of the SSE band is of the order of $-10^{-7}/\text{keV}$. For the fit 43 Compton regions with a width of 20 keV between 1 MeV and the Compton edge of the 2.6 MeV γ -rays of ^{208}Tl are selected. Regions close to the FEP of ^{208}Tl and ^{212}Bi as well as the SEP and DEP are omitted. The energy region between the DEP and SEP include events from the photon annihilation and a partial energy deposition by one of the two 511 keV photons. Similar to the second peak at $A/E \sim 0.76$ in the SEP, such events produce an additional peak at low A/E . The peak leads to a mis-fit of the MSE tail and a wrong estimation of the Gaussian mean and sigma. Therefore, a 200 keV region above the DEP is omitted. At higher energies the second peak is below $A/E = 0.9$ which is outside the fit range.

The A/E energy dependence includes several effects. Noise on the current pulse might slightly increases the A value, whereas the effect is stronger at lower energies, and decreases with better signal-to-noise ratios. Physical effects may be introduced by the increased number of high energy delta electrons and the increasing Bremsstrahlung emission of electron at higher energies. This would results in an increased size of the starting charge distribution [90, 91]. Such an effect might have already been seen as a shift and broadening of the event RMS in simulated ^{228}Th calibration data as described in Section 4.1.

Further investigation and a detailed study using pulse shape simulation is required to understand the energy dependence of A/E but is beyond the scope of this work. In the following the A/E energy dependence derived using ^{228}Th calibration data as shown in Figure 4.15.

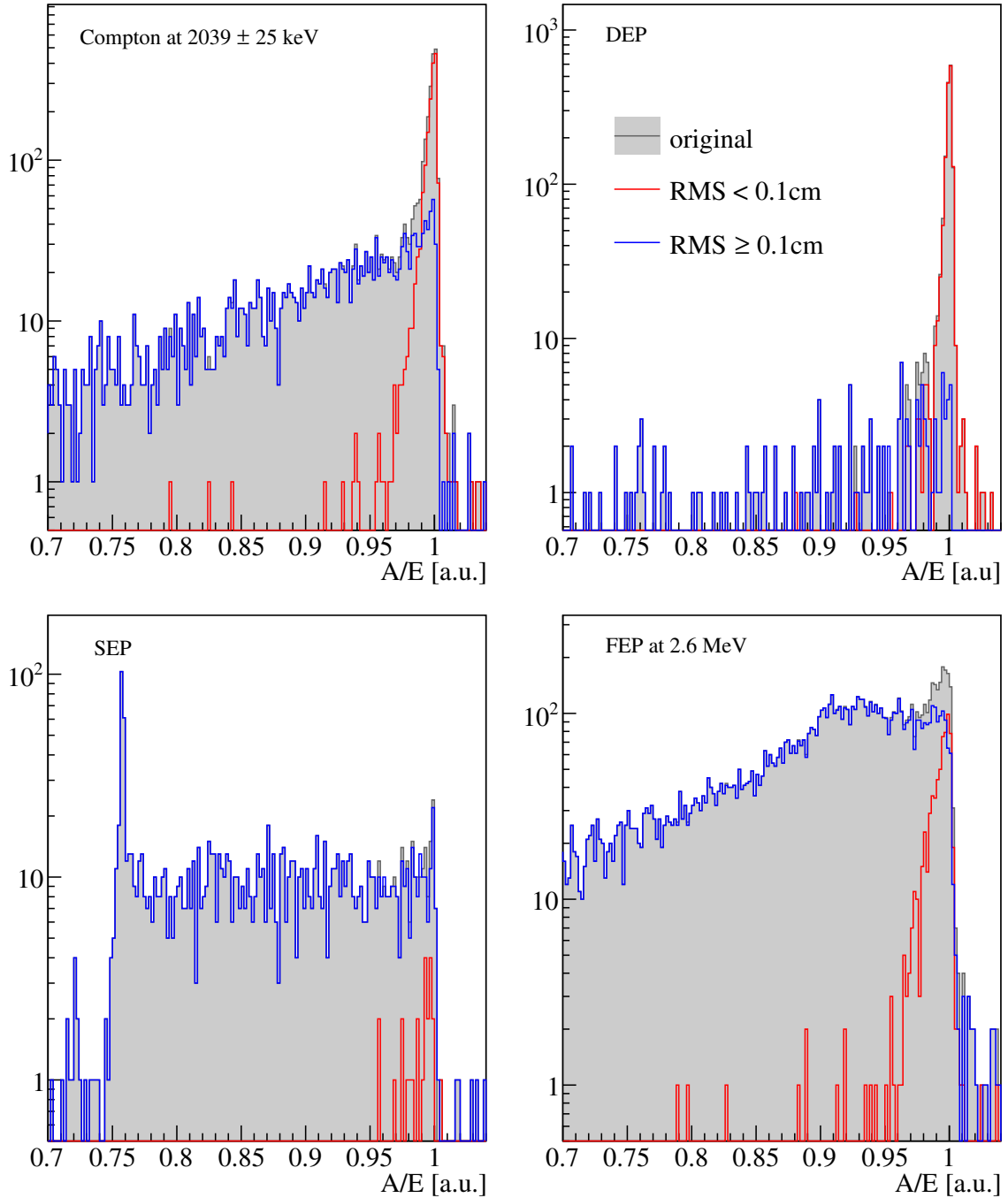


Figure 4.14: Simulated A/E distribution for GD35C in the DEP and SEP of the 2.6 MeV γ -line of ^{208}Tl , the FEP and the Compton region around $Q_{\beta\beta} = 2039$ keV. The red distribution are the SSE according to an RMS cut at 0.1 cm, in blue the MSE with $RMS \geq 0.1$ cm. See also Section 4.1 for more details on the event RMS.

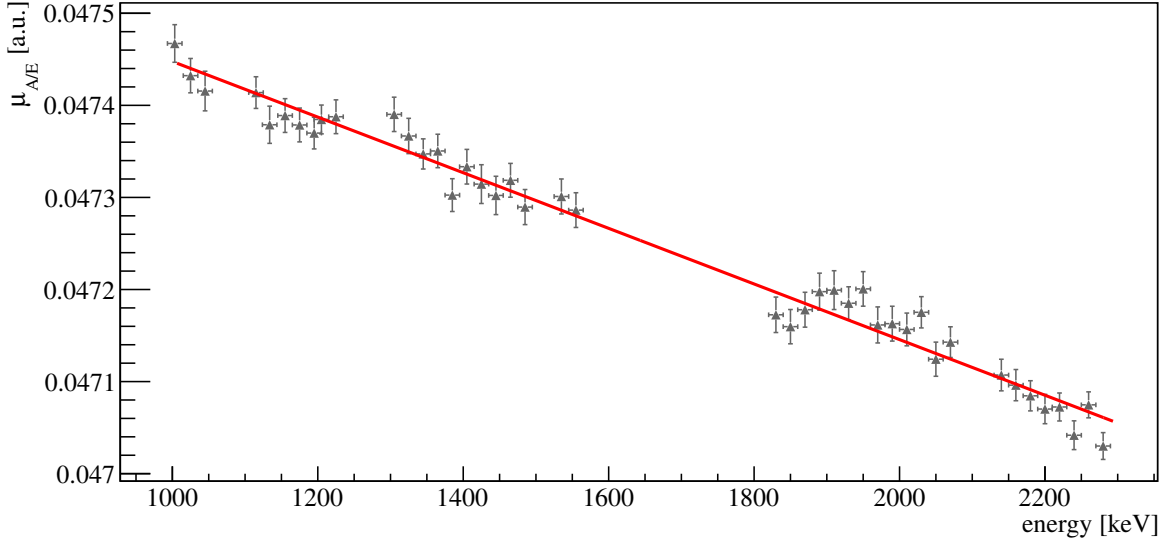


Figure 4.15: Gaussian mean, $\mu_{A/E}$, of the uncorrected A/E distribution of Compton events in the ^{228}Th spectrum between 1 MeV and the Compton edge of the 2.6 MeV γ -line. A/E distributions are fitted with Equation 4.3. $\mu_{A/E}$ represent the position of the SSE band at a given energy. Uncertainties are given by the fit errors. The energy dependence of the SSE band is described by a linear function.

4.4 A/E as Background Reduction Technique in GERDA

The main background components at $Q_{\beta\beta}$ are summarized in Table 3.2 for Phase I and in Table 3.4 for Phase II:

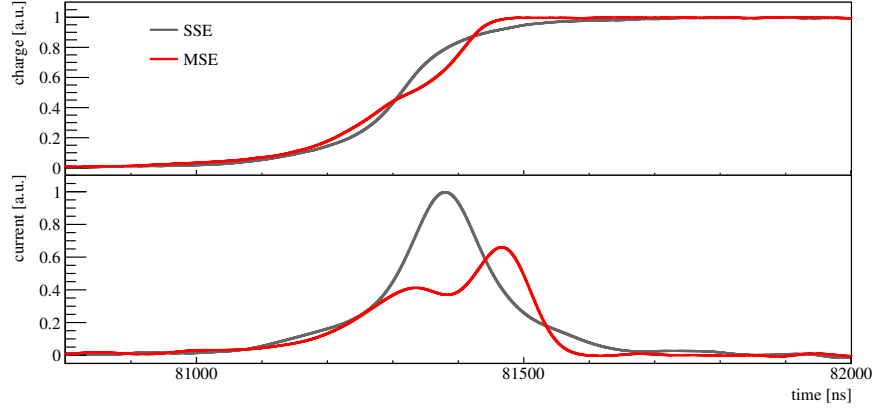
- β -decays of ^{42}K on the detector surface,
- external γ -rays from the decays of ^{214}Bi , ^{208}Tl and ^{60}Co ,
- ^{60}Co as an intrinsic contamination of the germanium detectors and
- α -emitting isotopes such as ^{226}Ra , ^{222}Rn and ^{210}Po on the detector surface.

As described in the previous sections, the Compton background shows a high MSE fraction which allows to separate Compton events from SSE, i.e. $\beta\beta$ events. MSE feature a smaller A/E value compared to SSE of the same energy, see Figure 4.16 and Section 4.3 for details. In the following the principle of discriminating non- γ background components using A/E will be discussed.

Suppression of ^{42}K β -decays

The by far biggest mass close to the GERDA detector array is the liquid argon (LAr). Argon has two long-lived radioactive isotopes, ^{39}Ar and ^{42}Ar with half-lives of 269 y and 33 y respectively [93]. ^{39}Ar and ^{42}Ar are produced via neutron capture [94]





(a) multi-site (MSE) vs single-site event (SSE)

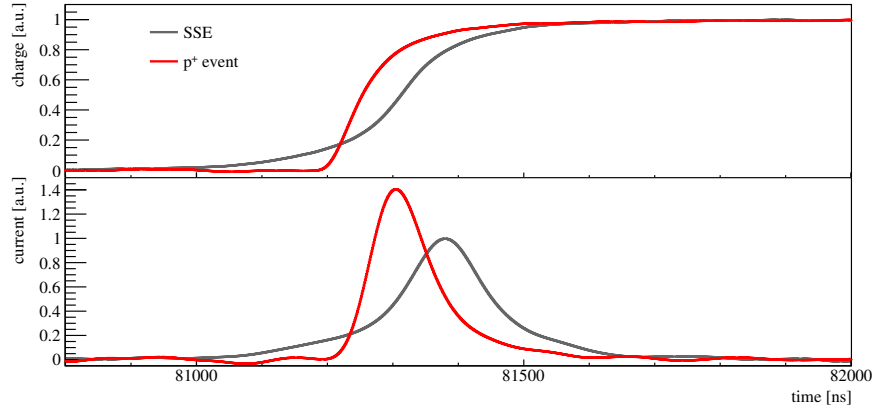
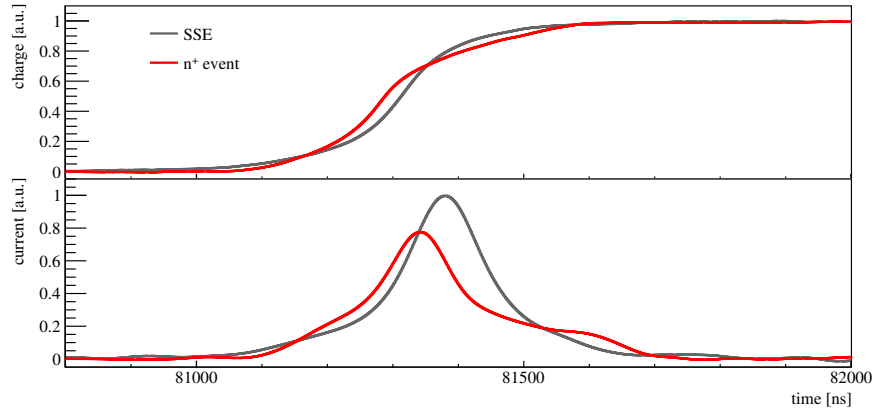
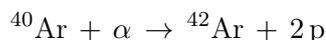

 (b) p^+ vs single-site event (SSE)

 (c) n^+ vs single-site event (SSE)

Figure 4.16: Experimental charge and current pulse of a typical SSE in the bulk volume of the detector compared to an MSE (a), an event with energy deposition on the p^+ contact or groove (b) and an event on the n^+ surface of the detector (c). Pulses are recorded in GERDA Phase II and processed with the GERDA software framework GELATIO [92]. Charge pulses are smoothed with a 3×50 ns moving window average. Current pulses are obtained by a 10 ns differentiation. Both pulses are interpolated to 1 ns. Charge pulses and SSE current pulses are normalized to 1. Current pulses of MSE, p^+ and n^+ event are normalized to the A/E values: 0.66 (MSE), 1.40 (p^+) and 0.78 (n^+).

and cosmic ray interactions in the upper atmosphere [95]



The latter being the dominant production process for ${}^{42}\text{Ar}$. Both decays have a comparably low Q-value of 565 keV and 600 keV and do not contribute to the background at $Q_{\beta\beta}$ of ${}^{76}\text{Ge}$. However, ${}^{42}\text{K}$, the daughter nuclide of ${}^{42}\text{Ar}$ has a Q-value of 3525 keV, see Figure B.1. As a β -emitting isotope ${}^{42}\text{K}$ is a serious background source at $Q_{\beta\beta}$. In about 18% of the decays the β -particles is accompanied by a 1525 keV γ -ray. With 12 h the half-life of ${}^{42}\text{K}$ is much shorter than the half life of its mother nuclide, ${}^{42}\text{Ar}$. Therefore, ${}^{42}\text{K}$ remains in secular equilibrium with ${}^{42}\text{Ar}$, i.e. the concentration of ${}^{42}\text{K}$ in the LAr of the GERDA cryostat remains roughly constant. Furthermore, in the ${}^{42}\text{Ar}$ decay a ${}^{42}\text{K}$ ion is produced which is attracted by the applied bias voltage applied to the detectors and is collected in the vicinity of the detector array or on the detector surface.

The n^+ contact covering nearly the full detector surface is insensitive ('dead') to ionizing radiation. For the GERDA Phase II BEGe detectors a typical dead layer of 0.7-1.0 mm has been chosen. This provides a partial shielding against background from β -decays on the detector surface. However, the range of β -particles with an energy up to 3.5 MeV is of the order of 1 mm. Therefore, a good fraction of ${}^{42}\text{K}$ decays on the n^+ surface may still penetrate into the active volume of the detector.

Furthermore, the transition between dead and active detector volume is not sharp. The insensitive dead-layer is followed by a so-called transition layer with incomplete charge collection. This layer features a zero electric field. Charges from energy deposition in this layer diffuse slowly until they reach the volume of non-zero electric field and drift towards the read-out electrode. The incomplete charge collection leads to an energy loss. Due to the diffusion such pulses feature a slow rise, they are so-called 'slow pulses'. Thus, β -decays from ${}^{42}\text{K}$ decays on the n^+ surface typically produce slow-pulses as shown in Figure 4.16. More details on the transition layer and slow pulses can be found in [68].

Suppression of α -decays

The range of α -particles in germanium is of the order of tens of μm . Therefore, the 0.7-1.0 mm thick dead-layer on the n^+ surface provides an efficient shielding against α -decays. However, the p^+ contact and the groove feature a very thin dead layer of a few hundred nm and α -decays may penetrate. However, the region close to the p^+ contact is the region of high weighting potential, interactions produce very fast rising pulses. Consequently, α -decays, e.g. from ${}^{210}\text{Po}$, feature high A/E values compared to SSE in the bulk volume, see Figure 4.16.

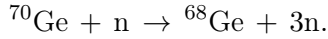
Suppression of Detector Intrinsic Contamination

Cosmogenic activation of the detector material is one of the most dangerous backgrounds. To keep the exposure to cosmic radiation as short as possible the detectors are stored underground. The most dangerous cosmogenically produced isotopes are ${}^{60}\text{Co}$ and ${}^{68}\text{Ge}$ (or rather ${}^{68}\text{Ga}$) as they have Q-values above $Q_{\beta\beta} = 2039$ keV and long half-lives. Both are produced by spallation of ${}^{70}\text{Ge}$ by high energy neutrons. ${}^{60}\text{Co}$ is produced via [96]



Neutrons with energies higher than 80 MeV are needed for this reaction channel. About 4 atoms/(kg·d) are produced at sea-level [96]. The half-life of ^{60}Co is five years. As crystal pulling and zone refinement act as purification processes the intrinsic contamination by ^{60}Co becomes important only afterwards. Figure B.2 shows the decay scheme of ^{60}Co : a β^- -particle is emitted followed by two γ -rays. The Q-value of the decay is $Q_\beta = 2824$ keV. To deposit energy at $Q_{\beta\beta}$, the β -particle as well as a partial energy deposition by the two γ -rays is needed. The corresponding signature is very likely to be MSE with a low A/E value.

^{68}Ge is produced via [96]



Neutrons with energies higher than 20 MeV are needed. About 1 atom/(kg·d) is produced [96]. As an intrinsic contamination by a radioactive germanium isotope the contribution is already important after the germanium enrichment. The decay energy of ^{68}Ge is only 106 keV, therefore does not contribute to the background at $Q_{\beta\beta}$. However, its daughter nuclide ^{68}Ga has a decay energy of 2921 keV and is a potential background source. ^{68}Ga is in secular equilibrium with ^{68}Ge , as its half-life is 68 min and small compared to the half-life of ^{68}Ge , 271 d. Figure B.3 shows the decay scheme of ^{68}Ga : the dominant decay mode is β^+ -decay. The positron deposits 1899 keV [97] in the detector before annihilating into two 511 keV photons. Therefore, to deposit energy at $Q_{\beta\beta}$ at least one of the annihilation photons must deposit part of its energy in the detector material. Thus, the event is likely an MSE with low A/E value.

4.5 Pulse Shape Analysis of BEGe Detectors for GERDA Phase I

The A/E based pulse shape analysis is applied to the data collected with the BEGe detectors in GERDA Phase I. Due to instabilities in the energy scale, one BEGe detector, GD35C, is excluded from the physics analysis and will not be considered in the following. (Bi-)weekly calibrations with a ^{228}Th source are used to extract the A/E cut since the DEP of the 2.6 MeV γ -line of ^{208}Tl is used as a proxy for $0\nu\beta\beta$ events. A total expose of 2.4 kg·yr has been collected. The physics data in the energy window $Q_{\beta\beta} \pm 25$ keV are blinded and not available for the analysis. Only after finalizing the full analysis the events in the region from 2035-2044 keV are made available. Recorded events are processed with the GERDA software framework GELATIO [92], the extraction of the A/E parameter is explained in Appendix D in detail. The A/E values are normalized to correct for instabilities. Furthermore, an energy correction as discussed in Section 4.3 is applied such that SSE are centered around $A/E = 1$. An energy, time and detector independent A/E cut is applied. The full analysis is summarized in Appendix E. In the following only the obtained results will be discussed.

The A/E Cut in GERDA Phase I

In GERDA Phase I an energy, time and detector independent A/E cut is applied. The A/E cut is applied above 1 MeV. Events with $0.965 < A/E < 1.07$ are accepted as signal-like. Table 4.1 summarizes the fraction of events rejected by the low and high A/E cut as well as the survival fractions in different energy regions of the ^{228}Th calibration spectra. A high acceptance of signal-like DEP events of $(93.3 \pm 0.5)\%$ is achieved whereas only $(54.3 \pm 0.2)\%$ of the Compton events survive around $Q_{\beta\beta}$. The FEP of ^{208}Tl at 2.6 MeV (^{212}Bi at 1.6 MeV)

Table 4.1: Summary of rejection and survival fractions in different energy regions of the ^{228}Th calibration and physics spectrum of the GERDA Phase I BEGe data set. The $0\nu\beta\beta$ simulation is taken from [86]. The signal efficiency is composed of the acceptance of DEP by the low A/E cut and the acceptance of simulated $0\nu\beta\beta$ events by the high cut. The BI window is defined as the energy window from (1930-2190) keV omitting a 8 keV signal region as well as two 10 keV regions around known γ -lines. The acceptance of $2\nu\beta\beta$ events is calculated using the acceptance of physics events in the range 1.00-1.45 MeV and corrected for background contribution. The $2\nu\beta\beta$ acceptance is reduced by 1.5% with respect to the $0\nu\beta\beta$ events due to events in the transition layer [68]. Fractions are calculated according to Appendix A and may differ from [5]. Only for the $0\nu\beta\beta$ efficiency systematic uncertainties according to Table 4.2 are considered. The uncertainties of the $2\nu\beta\beta$ acceptance follow from the Gaussian error propagation.

region	low cut [%] $A/E < 0.965$	high cut [%] $A/E > 1.07$	surviving fraction [%] $0.965 < A/E < 1.07$
^{228}Th calibration runs			
DEP at 1592.5 keV	5.30 ± 0.47	1.43 ± 0.12	93.27 ± 0.48
FEP at 1620.5 keV	74.42 ± 0.76	0.89 ± 0.16	21.68 ± 0.75
SEP at 2103.5 keV	81.56 ± 0.38	1.11 ± 0.08	17.34 ± 0.38
FEP at 2614.5 keV (2039 ± 35) keV	74.41 ± 0.08 44.12 ± 0.15	1.05 ± 0.02 1.58 ± 0.04	24.53 ± 0.08 54.30 ± 0.15
physics runs			
FEP at 1524.7 keV	70.80 ± 4.84	2.65 ± 1.52	26.55 ± 4.76
(1000 - 1450) keV (2039 ± 200) keV	23.00 ± 1.06 30 / 40	2.16 ± 0.37 3 / 40	74.84 ± 1.09 7 / 40
BI window > 3.5 MeV	17 / 23 2 / 38	3 / 23 35 / 38	3 / 23 1 / 38
$0\nu\beta\beta$ simulation			
$Q_{\beta\beta} = 2039$ keV	7.07 ± 0.03	2.45 ± 0.02	90.29 ± 0.03
signal efficiency			
$0\nu\beta\beta$: low DEP + high $0\nu\beta\beta$ cut			92.25 ± 1.87
$2\nu\beta\beta$ from 1.0 - 1.45 MeV			89.91 ± 5.20
$2\nu\beta\beta$ corrected for n^+ events			91.28 ± 5.27

is accepted with $(24.5 \pm 0.1)\%$ ($(21.7 \pm 0.8)\%$). SEP events show a low survival efficiency of $(17.3 \pm 0.4)\%$.

A/E Physics Spectrum

Figure 4.17 shows the A/E physics spectrum recorded with the GERDA Phase I BEGe detectors. The spectrum shows characteristic features for the different background contributions as discussed in the previous section:

- **α region:** all but two events above the endpoint energy of ^{42}K , i.e. 3.5 MeV, feature a high A/E value. Since α -particles cannot penetrate the thick n^+ dead layer of the detector, only decays on the p^+ contact, in the detector groove or in their close vicinity are recorded. Such events feature a high A/E .

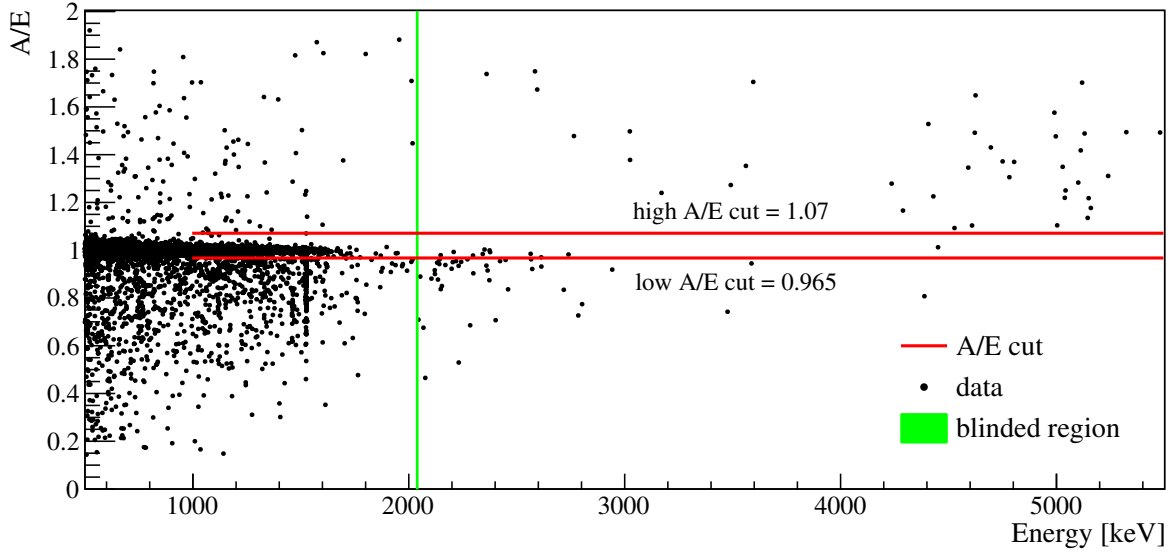


Figure 4.17: A/E physics spectrum for GERDA Phase I BEGe detectors. A/E values are calibrated according to Appendix E. The red bands indicate the acceptance region. Events in the energy region $Q_{\beta\beta} \pm 4$ keV are blinded, i.e. not available for the analysis.

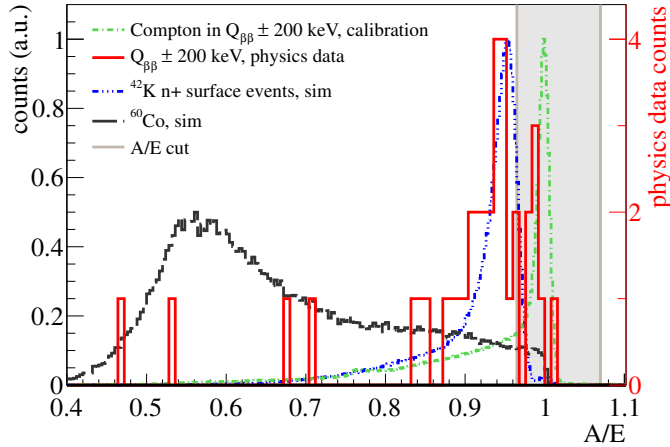


Figure 4.18: A/E distribution of physics events in the 200 keV region around $Q_{\beta\beta}$ and expected background sources at $Q_{\beta\beta}$. A/E distributions for Compton events in the energy region 1.8-2.2 keV from ^{228}Th calibration runs, simulated ^{42}K decay on the detector n^+ surface [68] and simulated intrinsic ^{60}Co decays [86]. The gray band indicates the acceptance region of the A/E cut.

- **^{42}K FEP at 1525 keV:** the FEP features a prominent low A/E tail in the physics spectrum due to its high MSE fraction. The survival efficiency of the ^{42}K FEP in the physics spectrum is compatible within uncertainties with the survival efficiency of the ^{212}Bi FEP in calibration data, see Table 4.1.
- **$2\nu\beta\beta$ region:** The energy region above 600 keV (the endpoint of ^{39}Ar) and below ~ 1800 keV is dominated by $2\nu\beta\beta$ decays, i.e. signal-like events. As expected such events are centered around $A/E = 1$. Events with high A/E values are predominantly decays in the small detector value around the p^+ contact. The low A/E tails are multiple Compton scattered events e.g. from ^{42}K and β -decays on the n^+ detector surface
- **The Region of Interest (ROI):** about 55 % of the events at $Q_{\beta\beta} \pm 4$ keV are expected from ^{42}K , 13 % from ^{214}Bi and 11 % from ^{208}Tl in the detector assembly [69]. Figure 4.18 shows the A/E distribution of physics events in the 400 keV region around $Q_{\beta\beta}$

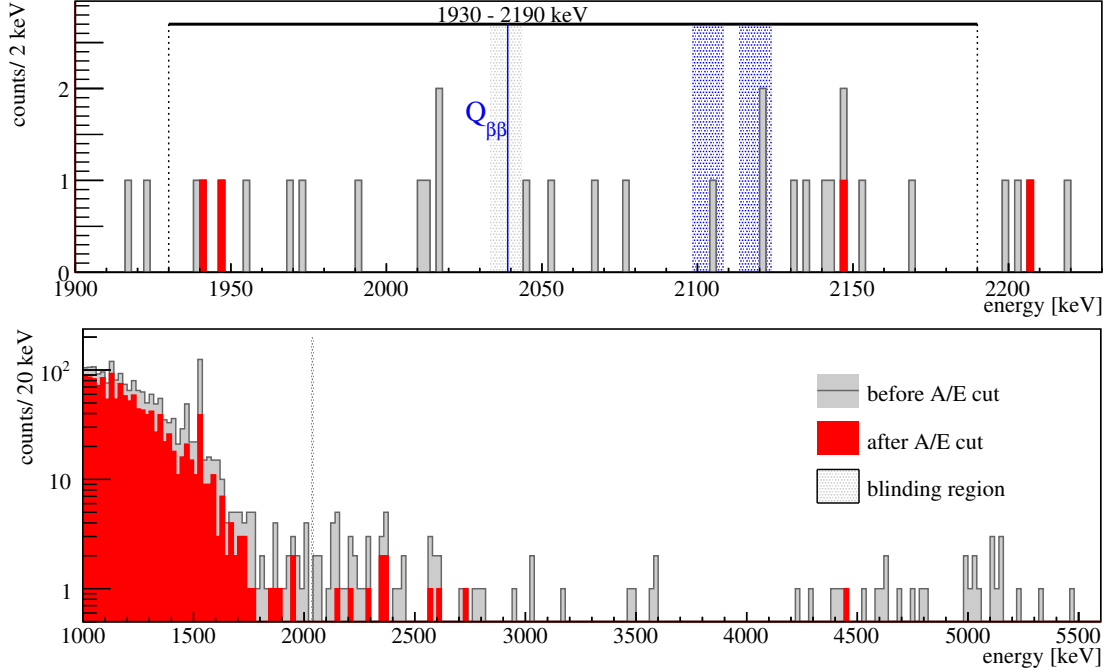


Figure 4.19: Physics spectrum of the GERDA Phase I BEGe data set before and after A/E cut. The top panel shows a close-up of the region of interest. The background index is calculated in the energy range (1930-2190) keV whereas the 8 keV blinding region as well as two 10 keV regions around the SEP of the 2.6 MeV γ -line of ^{208}Tl and the FEP of ^{214}Bi are omitted (blue regions).

and expected background sources: the peak with maximum at 0.94 can be attributed to β -decays of ^{42}K on the n^+ detector surface. The low A/E tail may originate in an intrinsic ^{60}Co background or Compton events. The A/E cut rejects 83% of the events in the 400 keV region around $Q_{\beta\beta}$.

Table 4.1 summarizes the fraction of events rejected by the low and high A/E cut as well as the survival efficiency in different energy regions of the physics spectrum.

Background Index of the GERDA Phase I BEGe Data Set

The background index (BI) is calculated in the energy range (1930-2190) keV. The 8 keV signal region as well as two 10 keV regions around the SEP of the 2.6 MeV γ -line of ^{208}Tl and the FEP of ^{214}Bi are omitted. Figure 4.19 shows a close-up of the BI window: the A/E cut rejects 20 out 23 events. Thus, the BI is reduced from

$$\text{BI} = (41.2 \pm 8.6) \cdot 10^{-3} \frac{\text{counts}}{\text{keV} \cdot \text{kg} \cdot \text{yr}} \quad (4.4)$$

before PSD to

$$\text{BI}^{\text{PSD}} = (5.4^{+4.1}_{-3.4}) \cdot 10^{-3} \frac{\text{counts}}{\text{keV} \cdot \text{kg} \cdot \text{yr}} \quad (4.5)$$

after PSD.

uncertainty from	[%]
statistics in DEP	0.48
difference in phy and cal data	0.36
A/E energy dependence	$7.4 \cdot 10^{-3}$
topology of $0\nu\beta\beta$ events	1.77
total	1.87

Table 4.2: Summary of uncertainties considered for the $0\nu\beta\beta$ signal efficiency of the A/E cut applied to the GERDA Phase I BEGe data set. The statistical uncertainty in the DEP is calculated according to Appendix A. For the estimate on the uncertainty introduced by the different topologies of $0\nu\beta\beta$ and DEP events a $0\nu\beta\beta$ decay simulation from [86] is used. All statistical and systematic uncertainties are summed in quadrature.

Signal Efficiency of Phase I A/E Cut

The efficiency of the A/E cut to accept $0\nu\beta\beta$ events is estimated using simulated $0\nu\beta\beta$ and DEP events from ^{228}Th calibration data. For the survival efficiency of the low A/E cut DEP events are used as a proxy (see Section 4.1). DEP events occur predominantly close to the detector surface, as the probability for the two annihilation photons to escape is highest. Therefore, the fraction of high A/E values in the DEP is not representative for events homogeneously distributed in the bulk, such as $0\nu\beta\beta$ decays. To estimate the signal acceptance by the high A/E cut, a simulated $0\nu\beta\beta$ A/E distribution [86] is used. The rejection fractions are summarized in Table 4.1: the low A/E cut rejects $(5.3 \pm 0.5)\%$ DEP events, the high A/E scrutinizes $(2.45 \pm 0.02)\%$ of the simulated $0\nu\beta\beta$ events.

In the analysis, A/E values are corrected for energy dependence. The uncertainty on the A/E energy scale introduces a systematic uncertainty on the signal efficiency. Extrapolating the largest fit uncertainty on the slope of the A/E energy dependence of the four Phase I BEGes from the DEP at 1593 keV to 2039 keV changes the A/E cut by $3.85 \cdot 10^{-5}$. The change in the cut position results in a change of the DEP acceptance of $7.4 \cdot 10^{-5}$ and is the estimate for the systematic uncertainty on the signal efficiency.

GD32B shows the largest difference of the A/E distributions between physics and calibration data: 0.0037. Moving the A/E cut by this difference changes the DEP acceptance by 0.36%.

The largest uncertainty on the signal efficiency comes from the different event topologies of DEP and $0\nu\beta\beta$ events. The latter have a higher energy and therefore different fraction of MSE due to the emission of Bremsstrahlung. Furthermore, DEP may interact with the detector material before the γ -ray is converted into an electron-positron pair. Thus, the MSE fraction of the DEP is similar to the fraction of $0\nu\beta\beta$ but can differ on the percent level, see also Section 4.1. The low A/E cut rejects $(7.07 \pm 0.03)\%$ of the simulated $0\nu\beta\beta$ events. This is about 1.77% more than in the DEP. The later is used as an estimate for the systematic uncertainty introduced by the different topologies of DEP and $0\nu\beta\beta$ events.

Table 4.2 summarizes the uncertainties on the signal efficiency. Statistical and systematic uncertainties are summed in quadrature. The final signal efficiency for the A/E cut applied to the GERDA Phase I BEGe data set is

$$\epsilon_{0\nu\beta\beta} = (92.3 \pm 0.5(\text{stat}) \pm 1.8(\text{sys}))\% \quad (4.6)$$

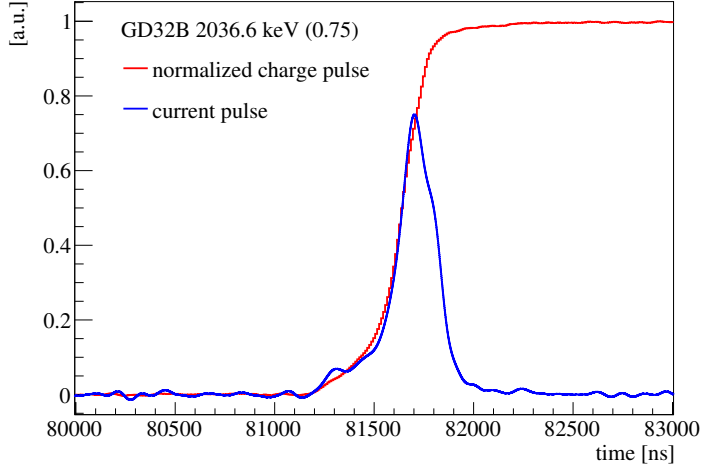


Figure 4.20: Charge and Current pulse of the unblinded BEGe event at 2036.6 keV. A moving window average of 3×50 ns. The current pulse is obtained by a 10 ns deconvolution of the charge pulse. Both pulses are interpolation to 1 ns. The maximum of the charge pulse is normalized to 1, the maximum of the current pulse to $A/E = 0.75$. The event is potentially due to a β -decay on the detector n^+ surface.

$2\nu\beta\beta$ Efficiency

$2\nu\beta\beta$ events are signal events with lower energies. Therefore, the $2\nu\beta\beta$ survival efficiency provides an important cross-check of the determined signal efficiency.

$(74.8 \pm 1.1)\%$ of the physics events in the energy range 1.00-1.45 MeV are accepted by the A/E cut. To extract the $2\nu\beta\beta$ survival efficiency the background contribution as well as the survival efficiency of the individual background components needs to be taken into account. The survival efficiency of the $2\nu\beta\beta$ events is given by [5]

$$\epsilon_{2\nu\beta\beta} = \frac{\epsilon_{data} - \sum_i \epsilon_i \cdot f_i}{f_{2\nu\beta\beta}} \quad (4.7)$$

where ϵ_{data} is the fraction of events in the energy region 1.00-1.45 MeV after A/E cut, f_i the fraction of background component i and ϵ_i the corresponding survival efficiency. $f_{2\nu\beta\beta}$ is the fraction of $2\nu\beta\beta$ events in the physics spectrum at 1.00-1.45 MeV and determined to $(66.3 \pm 2.7)\%$ [69]. The background decomposition and corresponding efficiencies can be found in Table 3 in Appendix E.

The calculated acceptance of $2\nu\beta\beta$ events is

$$\epsilon_{2\nu\beta\beta} = (89.9 \pm 5.2)\% \quad (4.8)$$

Only the statistical uncertainty is given. The $2\nu\beta\beta$ efficiency is reduced by 98.5% with respect to the $0\nu\beta\beta$ efficiency [68] since the continuous spectrum of $2\nu\beta\beta$ contains events in the transition layer. Such events loose energy, i.e. are not present in a mono energetic $0\nu\beta\beta$ peak, and feature a low A/E . The corrected $2\nu\beta\beta$ efficiency is

$$\epsilon_{2\nu\beta\beta}^{\text{corr}} = (91.3 \pm 5.3)\% \quad (4.9)$$

The determined $2\nu\beta\beta$ efficiency is in good agreement with the determined signal efficiency of $(92.3 \pm 1.9)\%$.

Opening the Box – the Unblinded ROI

In June 2013 the energy window at $Q_{\beta\beta} \pm 4\text{ keV}$ was unblinded. In the BEGe data set a single event at 2036.6 keV is found. With an $A/E = 0.75$ the event is clearly characterized as background. Figure 4.20 shows the unblinded event recorded with GD32B. The pulse shape might suggest that the event is a β -decay from ^{42}K on the detector surface. After PSD no event remains in the signal region, i.e. $Q_{\beta\beta} \pm \sigma_E$, whereas $\sigma_E = 2.7\text{ keV}$ is the FWHM at $Q_{\beta\beta}$ of the BEGe data set.

4.6 Pulse Shape Discrimination for Non-BEGe Type Detectors

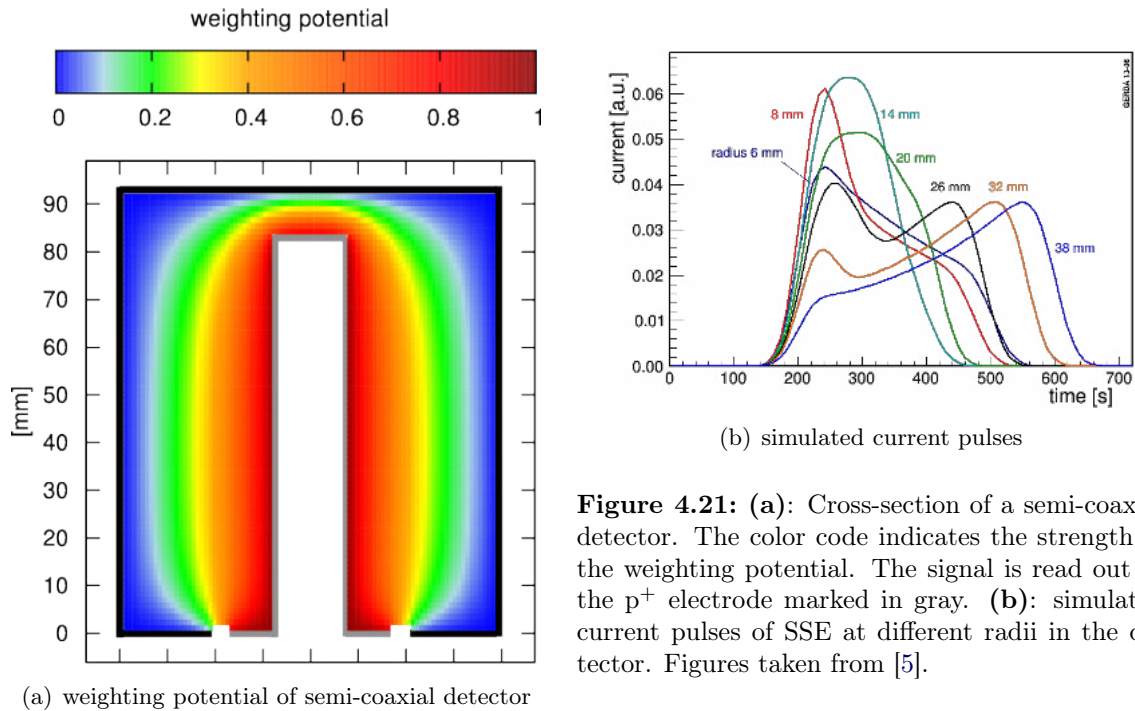


Figure 4.21: (a): Cross-section of a semi-coaxial detector. The color code indicates the strength of the weighting potential. The signal is read out at the p^+ electrode marked in gray. (b): simulated current pulses of SSE at different radii in the detector. Figures taken from [5].

BEGe detectors are distinct for their excellent energy resolution and enhanced pulse shape discrimination (see Section 4.2 for details). In the following the PSD of other HPGe detector types such as semi-coaxial, segmented and point-contact detectors will be discussed.

Semi-Coaxial Detectors in GERDA Phase I

The experimental exposure of GERDA Phase I was dominated by the semi-coaxial detectors formerly used in the Heidelberg-Moscow (HDM) experiment [1] and the International Germanium Experiment (IGEX) [2, 98]. Such detectors feature a high mass of 2-3 kg. For comparison the average mass of the Phase II BEGe detectors is only 667 g. Thus, the ratio of surrounding material (which may introduce background) to detector mass is much smaller for semi-coaxial than for BEGe detector.

Figure 4.21(a) shows the weighting potential of a semi-coaxial detector. The potential is non-zero in most of the detector volume. Therefore, both charge carrier types, electron

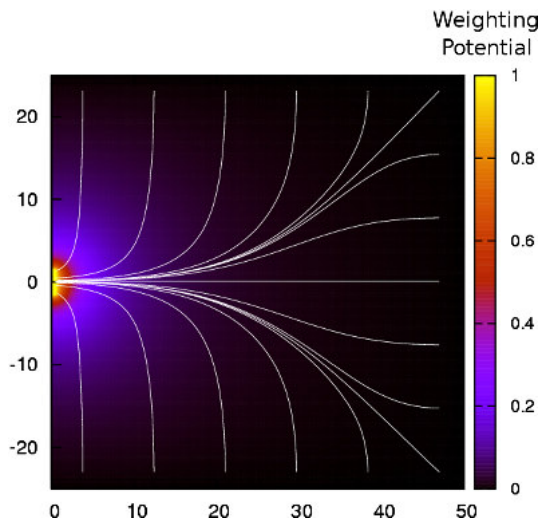


Figure 4.22: Cross-section of a 50 mm \times 50 mm PPC-type HPGe detector with a 5 mm point contact. The color code indicates the weighting potential inside the detector: similar to BEGe detectors (compare Figure 4.8) the potential shows a large position dependence. As the weighting potential is small but close to the p^+ contact electrons do not contribute much to the signal. Holes created in an SSE describe very similar drift paths (gray lines) through the volume with a large gradient of the weighting potential. The latter is the region where the current pulse is largest. Hence, PPC detectors like BEGe detectors SSE have similar pulse shapes independent from the interaction point. Figure taken from [101].

and holes, contribute to the signal. Simulated current pulses for single energy deposition at different radii are shown in Figure 4.21(b). The contribution of electrons and holes highly depends on the location of the energy deposition and the current signal of an SSE may feature two peaks. Therefore, the A/E parameter is not suitable for the pulse shape analysis of semi-coaxial detectors. Due to the complexity of the pulse shape, the PSD is based on a multi-parameter analysis. In GERDA Phase I, a method based on an artificial neural network is used to identify signal-like from background events, see [83] for details. The PSD method rejects 31 out of 76 background events in a 230 keV window around $Q_{\beta\beta}$, this corresponds to a background suppression of 41 % only. The semi-coaxial detectors in GERDA Phase I reach a $BI = (11 \pm 2) \cdot 10^{-3} \frac{\text{counts}}{\text{keV} \cdot \text{kg} \cdot \text{yr}}$ after PSD [5]. However, the signal efficiency is reduced to $(83 \pm 3) \%$ only [83].

Segmented HPGe Detectors

The identification of MSE may be enhanced by the segmentation of the surface electrode and individual read-out of each segment. A detector characterization of an 18-fold segmented true coaxial n-type detector is presented in [99]. While an SSE ideally creates a signal in one segment only, an MSE is identified via several coincident signals in more than one segment. Compton scattered γ -events from ^{208}Tl decays at $Q_{\beta\beta}$ have a survival efficiency of $\sim 60 \%$ with $\sim 92 \%$ acceptance of DEP events [100]. This is similar to the PSD achieved with the non-segmented semi-coaxial detectors in GERDA. However, the segmentation requires an enhanced number of read-out contacts, cables and electronics which increase the amount of material in the close vicinity of the detectors and thus, the background.

PPC Detectors in the MAJORANA DEMONSTRATOR

The MAJORANA DEMONSTRATOR uses p-type point-contact HPGe detectors (PPC) enriched in ^{76}Ge [49]. Such detectors are of cylindrical shape, with a small read-out contact (typical diameter of 2 to 6.5 mm) and a mass up to 1 kg. Just like BEGe diodes, PPC detectors feature a low capacitance which allows for an improved energy resolution and a low energy threshold. The PPC detectors used in the MAJORANA DEMONSTRATOR are produced

by AMETEK/ ORTEC.

Figure 4.22 shows a cross-section of a PPC detector and the calculated weighting potential: similar to BEGe detectors the weighting potential is highly position dependent, non-zero only in the close vicinity of the read-out electrode. The electrical field drifts holes such that the path through the large weighting potential gradient is very similar for interactions in different locations of the bulk volume. Thus, the pulse shape of single local energy deposition is independent from the interaction point. To discriminate signal- from background-like events, the MAJORANA collaboration uses the A/E based pulse shape analysis developed by GERDA. The MAJORANA PPC detectors are operated in a vacuum cryostat. At 90% acceptance in the DEP, the SEP is reduced to $\sim 6\%$ whereas the acceptance of Compton events around $Q_{\beta\beta}$ is reduced to about 40% [102]. This is compatible with the best survival efficiencies achieved with the enriched GERDA BEGe detectors in vacuum cryostat [103, 104].

PPC detectors proved to be an alternative to BEGe detectors. However, the PPC detectors as integrated in the MAJORANA vacuum cryostat yield a decisive disadvantage: the detector surface at the p^+ contact is passivated only, featuring a small dead-layer. As discussed previously the lithium diffused n^+ contact provides a dead-layer of 0.5-1 mm which acts as a shielding against α - and β -decays. As a consequence, a large fraction of the PPC detector surface is exposed to surface contamination, e.g. by α -decaying isotopes such as ^{210}Po or ^{222}Rn [102]. For a PPC detector operated in LAr β -decays from ^{42}K would mean an unavoidable background source. Since the passivated surface covers volume with low weighting potential the A/E method does not scrutinize such events. To reject α -decays on the passivated surface, the MAJORANA collaboration has developed a pulse shape discrimination method based on the charge collection time [102]. Typically part of the energy is collected promptly, followed by a slow collection of the remaining energy. This delayed charge collection results in a distinct pulse shape to SSE. At 90% acceptance of bulk events, about 95% of the surface α -events are rejected [102].

4.7 Summary

In the interaction of ionization radiation with the detector material electron-hole pairs are produced which induce a signal on the read-out electrode. $0\nu\beta\beta$ events feature a very localized energy deposition. Background events, e.g. from external γ -rays, likely interact multiple times with the detector material. The PSD is based on the discrimination of local energy deposition, so-called single-site events (SSE) against multiple interacting events, multi-site events (MSE). Due to the special geometry of the BEGe detector design the pulse shape of an SSE is independent from the interaction point in a large part of the bulk volume. DEP events, e.g. from the 2.6 MeV γ -line of ^{208}Tl , show a very localized energy deposition and are used as a proxy for $0\nu\beta\beta$ events. MSE are described as a superposition of SSE at different locations of the crystal.

A pulse shape analysis (PSA) based on a single parameter, the ratio of the maximum of the current pulse, A , over the total energy, E , A/E , has been developed in [3]. The maximum of the current pulse is roughly proportional to the energy deposited in a single interaction. As the total energy of an MSE is deposited in several interactions, MSE feature a low A/E value compared to SSE of the same total energy. The A/E distribution of a full energy peak (FEP) which consists mainly of MSE, is well distinct from an SSE dominated peak such as $0\nu\beta\beta$. Thus, in case of a discovery, PSA will show if a peak in the region of interest is an unknown

γ -line or the $0\nu\beta\beta$ signal.

The A/E based pulse shape analysis is successfully applied to the data collected with four BEGe detectors in GERDA Phase I. The A/E cut is calibrated using ^{228}Th calibration data. DEP events from the 2.6 MeV γ -line of ^{208}Tl are used as a proxy for $0\nu\beta\beta$ events. A total exposure of 2.4 kg·yr is collected with the GERDA Phase I BEGe detectors and included into the analysis for the search of $0\nu\beta\beta$ of ^{76}Ge [6]. To avoid any bias a blind analysis is performed, i.e. physics events in a 40 keV window around $Q_{\beta\beta}$ are not available until the analysis and all cuts are finalized.

83 % of the physics events in a 232 keV window around $Q_{\beta\beta}$ are rejected by the A/E cut while keeping a high $0\nu\beta\beta$ signal efficiency of (92.1 ± 1.9) %. The signal efficiency is calculated using ^{228}Th calibration data and simulation. The later dominates the uncertainty. (91.3 ± 5.3) % of the $2\nu\beta\beta$ events are accepted which is in very good agreement with the derived signal efficiency. The background index is reduced from $(4.1 \pm 0.9) \cdot 10^{-2} \frac{\text{counts}}{\text{keV} \cdot \text{kg} \cdot \text{yr}}$ to $0.5_{-0.3}^{+0.4} \cdot 10^{-2} \frac{\text{counts}}{\text{keV} \cdot \text{kg} \cdot \text{yr}}$ after the A/E cut.

The A/E analysis clearly identifies different background components. For BEGe detectors the main background originates in ^{42}K β -decays on the detector surface which is clearly seen in the A/E distribution of the physics data. Most of the high energy events have high A/E values as expected for α -decays on the p^+ contact. As expected the γ -line of ^{42}K at 1525 keV features a prominent low A/E tail and is suppressed by a factor of 3 to 4.

After fixing all analysis parameters and cuts the signal region from 2035 - 2043 keV is made available. One event with an energy of 2036.6 keV is found in the BEGe data set. The event is clearly characterized as background and no event in the BEGe data set remains in the signal region $Q_{\beta\beta} \pm \sigma_E$.

The BEGe detectors in GERDA Phase I proved to be a reliable and efficient detector technology for the search of $0\nu\beta\beta$ decay in ^{76}Ge . The total exposure in Phase I is small, however, the BEGe data set has an extremely low background at a high signal efficiency. In GERDA Phase II, additional 25 BEGe detectors will be deployed.

From Phase I to Phase II: Integration and Commissioning of the Gerda Upgrade

The original design of the GERDA Phase II upgrade has been discussed in Section 3.3. Section 5.1 presents the germanium detector and final array assembly. Minor changes to the original design are discussed.

Based on pulse shape discrimination results, the Phase II front-end design has been changed. Results are presented in detail in Section 5.2. Section 5.3 covers the commissioning of the liquid argon (LAr) veto system. Achieved background suppression using LAr veto and PSD are presented. Section 5.4 discusses the noise in the GERDA Phase II setup and its influence on pulse shape discrimination.

5.1 Detector Assembly and Integration

A major effort has been undertaken to keep the germanium detectors in an ultra clean environment to avoid radioactive contamination of the surface. This includes the detectors as well as all material and tools they get in contact with. Therefore, to remove dust particles all materials are cleaned using isopropanol. If possible the cleaning is performed in an ultra-sonic bath. The cleaning is repeated after each assembly step. Furthermore, all copper pieces which are deployed in the GERDA cryostat are electropolished and etched with H_2SO_4 and H_2O_2 to remove radioactive surface contamination during exposure to air[105]. PTFE parts are etched using a solution of HNO_3 . Furthermore, the detectors are kept in nitrogen atmosphere or vacuum containers for transport. That way, oxidation of the non-passivated detector groove is prevented which causes leakage current when operating the detectors.

The detectors are mounted into the holders in the Germanium Detector Laboratory (GDL). The laboratory is located at LNGS in close vicinity of the GERDA site. GDL is equipped with a clean bench and a large glove box flushed with nitrogen for mounting and contacting of the germanium detectors in an ultra clean environment. The detector mounting procedure is sketched in Figure 5.1:

1. The HV and signal cables are mounted on the silicon plates in the GDL clean bench.
2. The detectors are removed from their transport container inside the GDL glove box under nitrogen atmosphere and mounted in the low mass holders within the jigs (Figure

- 5.1(b)). The latter is a support structure from stainless steel used for handling during bonding and transport.
3. The contacting is realized via wire bonding. The procedure is done inside the GDL glove box (Figure 5.1(c)-(d)). The jig fixes the detectors during bonding.
 4. In a last step the detectors are packed into their transport containers to be brought to the GERDA clean room (Figure 5.1(e)-(f)).

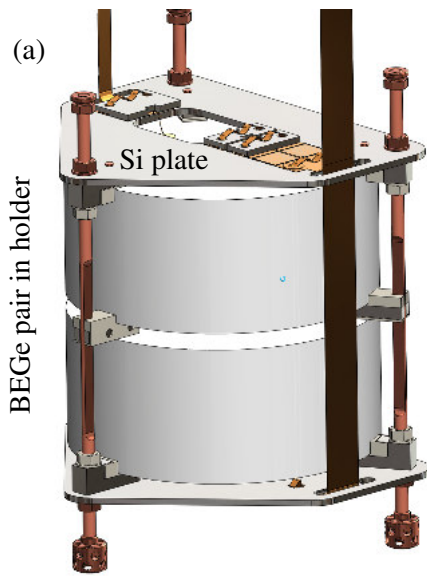
Typically, one to two detectors are mounted per day. Since the GERDA detectors are p-type they have a relatively robust n^+ surface and the handling of the detectors is compatibly easy. Only the thin p^+ -contact and the groove need to be treated with special care. Even invisible scratches damage the contact/ groove surface and high leakage currents develop even at small bias voltage. This can only be repaired by a new implantation of the p^+ -contact or etching the groove.

The strings are assembled in the GERDA clean room (class ISO 7) located on top of the cryostat. The clean room is equipped with a glove box surrounding the lock to the LAr cryostat (Figure 5.2(e)). The glove box is under nitrogen atmosphere and provides enough space for mounting the strings and the array. The procedure for the string assembly in the GERDA glove box is sketched in Figure 5.2:

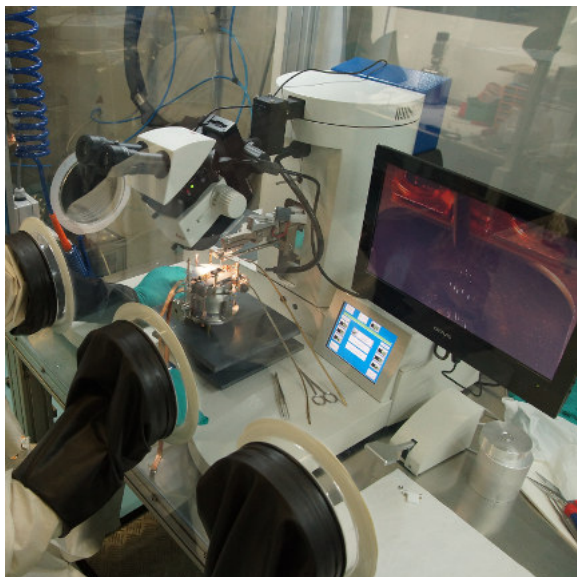
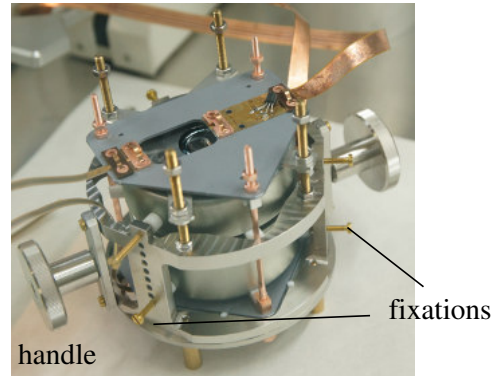
1. The lid of the nylon mini-shroud is fixed to the top detector beneath the copper star (Figure 5.2(b)). The latter is connected to a copper string which will be fixed at the hexagonal plate.
2. The detectors are mounted into strings using the string assembly unit (SAU) (Figure 5.2(a)): the detector inside its transport jig is placed on the movable table, the copper stick is fixed at the top of the SAU. The detector is moved towards the copper stick or already mounted detector. Detector holders are connected via two copper half-spheres.
3. Finally, the detector fixation of the jig are loosened and the jig is removed by lowering the table of the SAU. When the full string is assembled, the string is brought to the lock to be mounted to the hexagonal copper plate (Figure 5.2(h)) and the nylon mini-shroud is fixed to the string (Figure 5.2(g)).
4. In a final step the cables are arranged and connected to the front end electronics (FE) and high voltage (HV).

Typically, one to two strings are mounted per day whereas the cabling takes about half of the time.

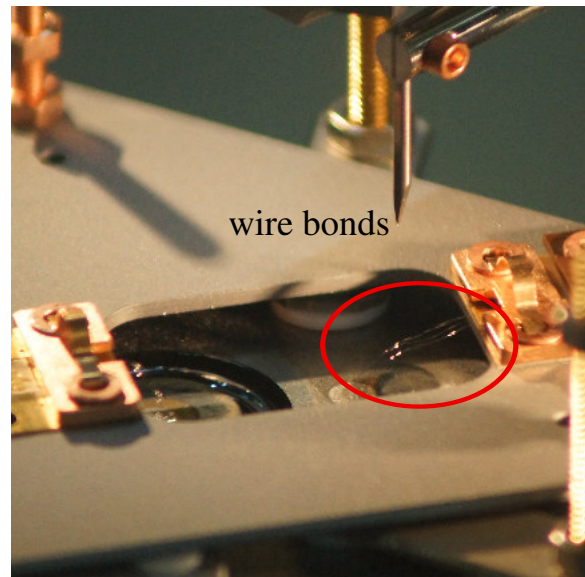
When exposed to air, the lock especially the cables with their large surface, adsorb radioactive contaminants such as ^{222}Rn . To ensure that the LAr does not get contaminated, the cables need to outgas prior to opening the shutter and lowering the detector array. Therefore, the lock is evacuated and kept at low pressure for several hours. Subsequently, the lock is flushed with argon gas and evacuated in several cycles such that remaining radiative contaminants are removed. Only after this procedure the shutter of the LAr cryostat is opened and the detector array with the LAr veto is lowered. The detectors cool down to LAr temperature (89 K) within minutes once immersed into the liquid. For disassembly, the detector array is lifted to warm-up in argon gas over several hours. For comparison, evacuating and cooling of



(b) detector in jig with handles for bonding



(c) GDL glove box with bonding machine



(d) detector contacting



(e) semi-coaxial detector in jig prepared for transport



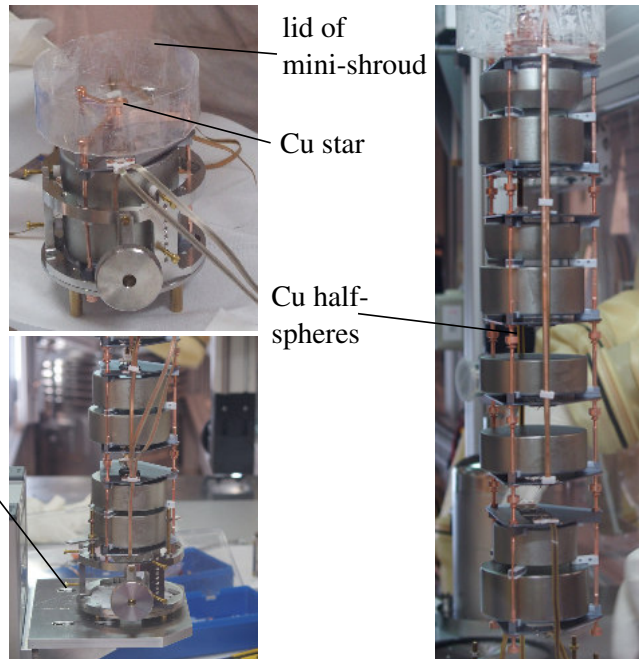
(f) transport container

Figure 5.1: Detector assembly including wire bonding for contacting. See text for details.

(a) string assembly unit (SAU)



(b) top detector pair

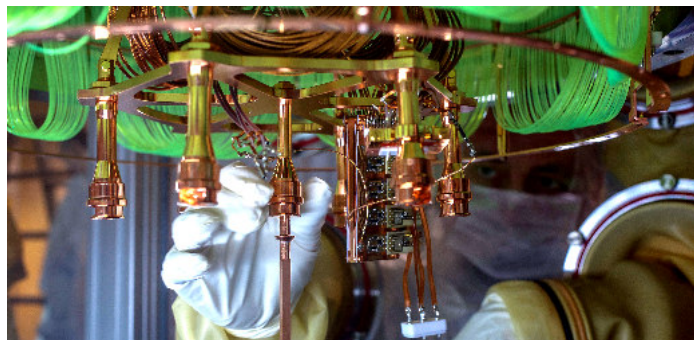


(c) lifting detector pair out of jig

(d) full mounted string



(e) Phase II lock in glove box



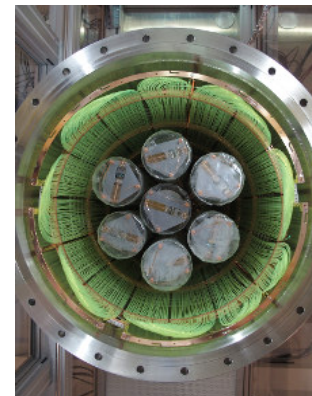
(h) hexagonal Cu plate with read-out electronics



(f) view through lock into cryostat on top PMT plate



(g) full assembled Phase II array with nylon mini-shrouds



(i) bottom view array positioned in fiber shroud

Figure 5.2: Assembly of the GERDA germanium detector array. See text for details.

run	strings		no. detector		comment
		BEGe		Coax	
Integration Test					
Jan '15	1	8 (3)	-		Phase I- and Phase II-like VFE
LAr Veto Commissioning					
April '15	1	8	-		^{228}Th calibration
May '15	1	8	-		^{226}Ra calibration
Germanium Detector Commissioning July - Dec' 2016					
50	5	22	5		
51	3	8	4		
52	7	22	6		new single BEGe holders
GERDA Phase II					
53	7	30	10		no blinding applied
54-64	7	30	10		events in (2039 ± 25) keV blinded

Table 5.1: Summary of the Phase II commissioning runs. The run IDs follow the GERDA Phase I numbering.

the MAJORANA cryostat takes about two weeks, for CUORE cooling to operational temperature of a few mK takes months. Thus, the GERDA infrastructure provides an easy and fast accessible setup. Repair and maintenance work are done on a comparably short timescale.

The GERDA Phase II upgrade has been assembled in several steps. Figure 5.3 sketches the time-line of the installation, commissioning and testing: GERDA Phase I physics data taking was stopped at the end of September 2013. In December 2013 a calibration source which was lost during Phase I commissioning was removed from the bottom of the cryostat. In the following months the GERDA Phase II lock was fully installed and operational by May 2014. The first germanium detectors were immersed into the GERDA cryostat using the Phase II lock in July 2014.

The LAr veto system (Figure 5.4(d)) has been fully installed in the GERDA setup by November 2014. Details are found in [80, 81]. Figure 5.4 shows the installed setup: nine PMTs are mounted on the top plate (5.4(a)). The top PMT plate lays on a small copper plate mounted on the cable chain (5.4(b)) such that the plate can be fixed at the top part of the lock and the hexagonal plate with the string suspension (5.4(c)) can be lowered separately for mounting the germanium strings. The germanium array is surrounded by the center shroud which consists of a curtain of wavelength shifting fibers (5.4(e)). Seven PMTs are mounted to the bottom plate. Both top and bottom plate are immersed in a copper shroud connected to the fiber shroud (5.4(f)). The inner part of the copper shrouds are covered with Tetratex soaked in wavelength shifter tetra-phenyl butadiene (TPB) solution [106] (5.4(g)).

Integration of the GERDA Phase II setup started in January 2015. Many unforeseen problems had to be faced and solved [107]. New cables had to be ordered since the bond wire

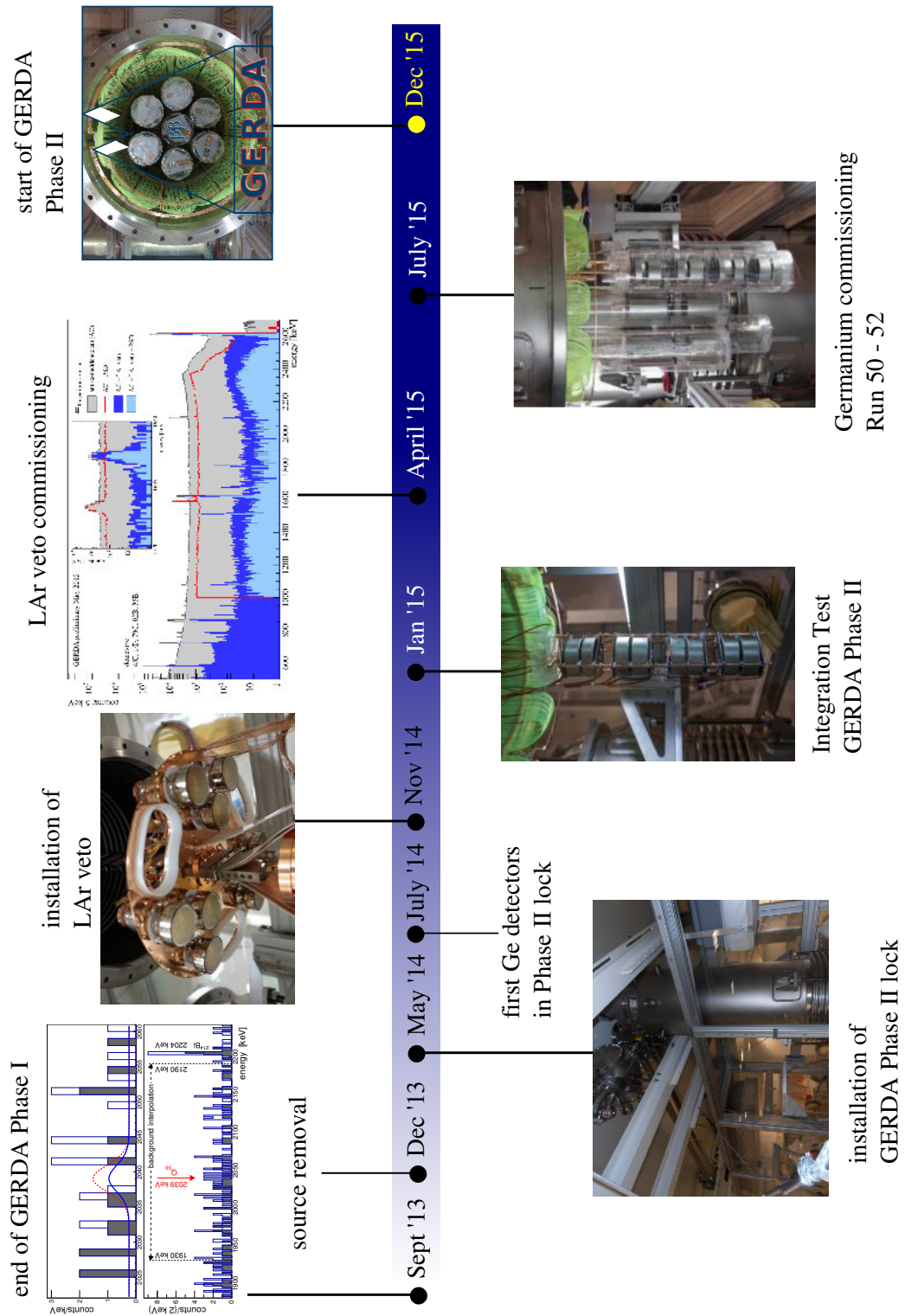


Figure 5.3: Time-line of the Installation of the GERDA Phase II Upgrade.

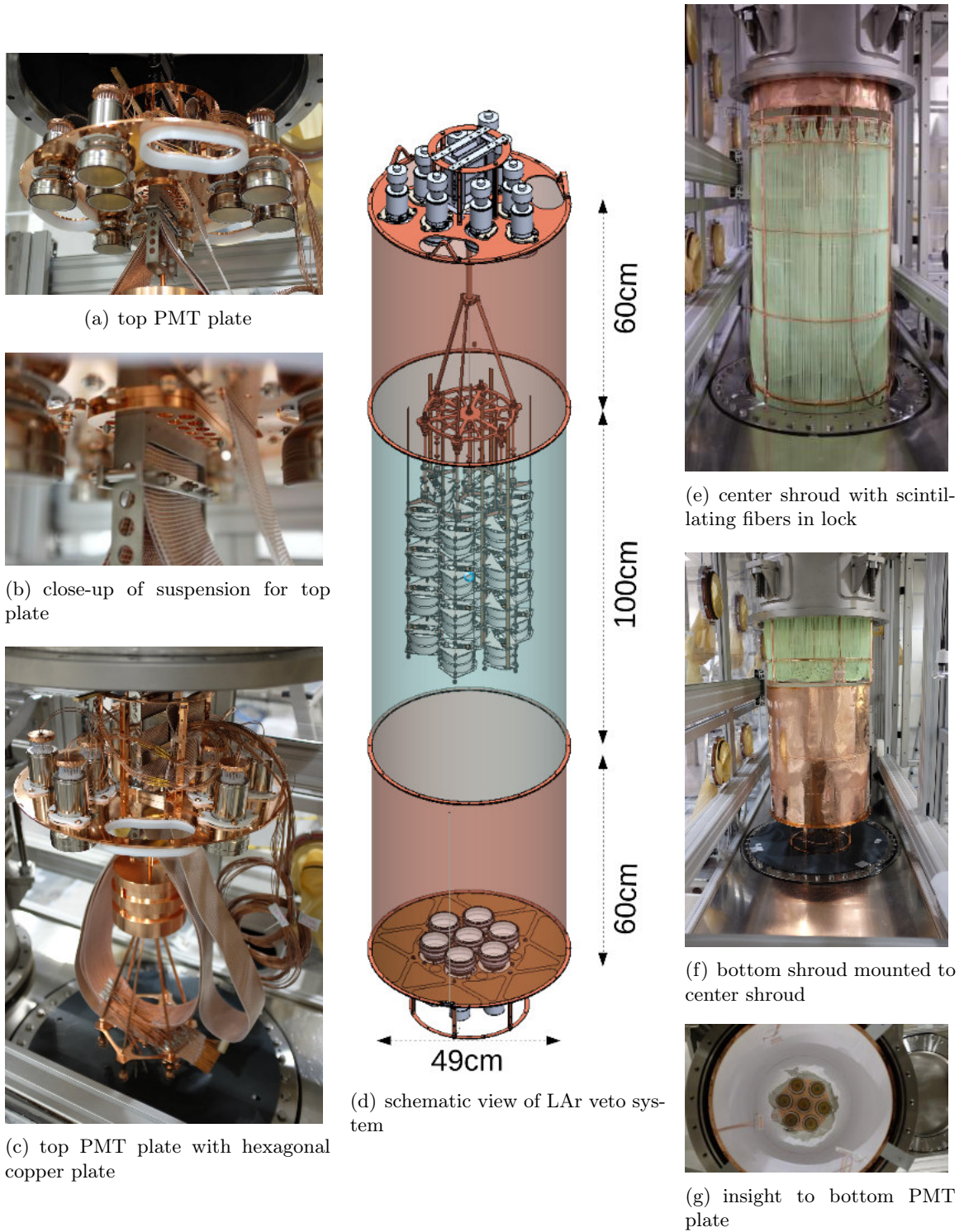


Figure 5.4: Final installation of the LAr veto system.

did not stick to many of the cables. After cooling-warming-cycles bond wires detached or broke. A high mortality of the JFETs in the VFE electronics was observed and caused serious delay during mounting. Therefore, the design of the VFE has been changed (see text below). Moreover, many diodes showed high leakage current: the handling procedure has been slightly changed and a new detector support has been developed (see text below). In 2015, 15 out of 30 BEGe detectors were sent to the manufacturer for etching and passivation of the groove (covering the groove with an insulating silicon monoxide layer). The assembly procedure has been optimized over many months. Table 5.1 gives an overview of the following iterations:

- **Integration Test:** in January 2015 a string with four prototype and four enriched Phase II BEGe detectors was installed to test the new electronics. Details are presented in Section 5.2. Only three out of eight detectors were operational: two detectors had a detached bond wire from the cable to the detector, one to the JFET. One detector had no signal-HV connection, another one lost the connection after cooling.
- **LAr Veto Commissioning:** a string with two prototype and six enriched Phase II BEGe detectors was installed to test the background suppression of the LAr veto and pulse shape analysis. Details are presented in Section 5.3.
- **Run 50:** five strings with 22 BEGe and five semi-coaxial detectors were installed. Three coaxial and seven BEGe detectors drew leakage current of more than 100 pA well below the operational bias voltage.
- **Run 51:** three strings with eight BEGe and four semi-coaxial detectors were installed. It became evident that top detectors have a higher probability to draw leakage current. It is believed that the chance to collect dust particles in the groove during mounting procedure is higher for top detectors. The latter causes leakage current. In some cases it was possible to cure the detector by rinsing the groove with methanol.
- **Run 52:** seven strings with 22 BEGe and six semi-coaxial detectors were installed. Six BEGe detectors were mounted in new single detector holders (see Figure 5.6). The groove faces downwards to prevent accumulating dust particles in the groove, the silicon plate is the same as in the pair holder.
- **Run 53:** seven strings with 30 BEGe and ten semi-coaxial detectors were deployed. The full array is sketched in Figure 5.5. In total 18 BEGe detectors are installed in the new single detector holders. The new holders seem to reduce the number detectors drawing leakage current.

During Run 50-52 calibration as well as background data have been taken for commissioning of the germanium detectors to investigate the performance of the new setup. On Dec 25th, 2016, (start of Run 53) GERDA Phase II started physics data taking. Starting from Run 54 events in the energy region (2039 ± 25) keV are blinded, i.e. not available for analysis.

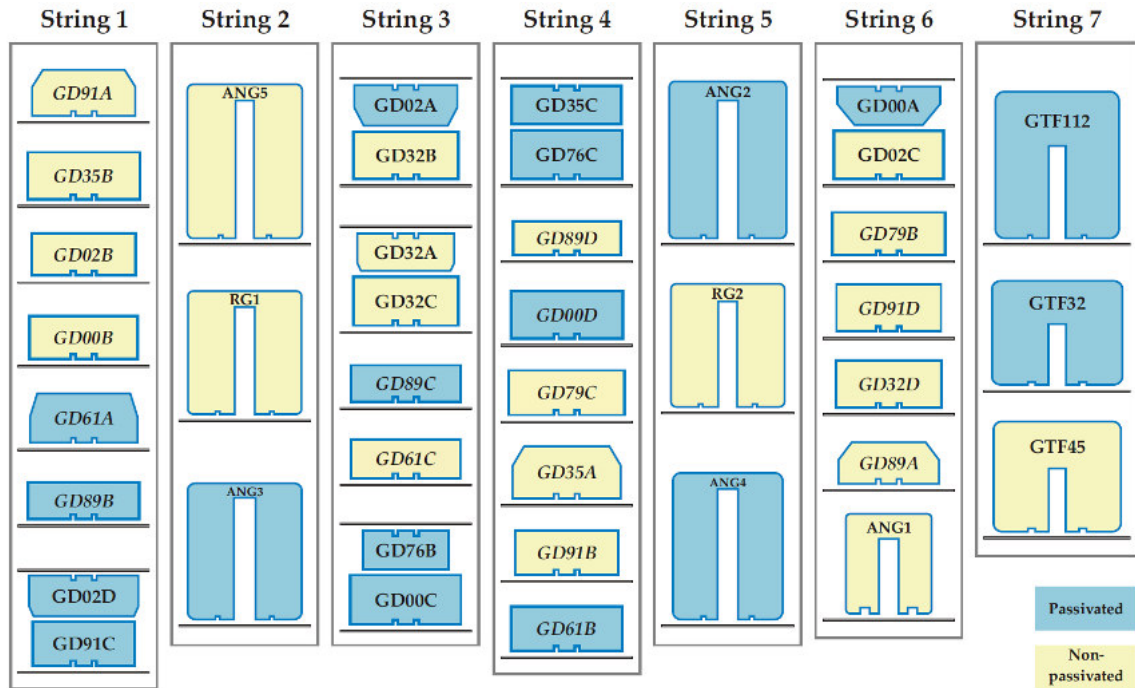
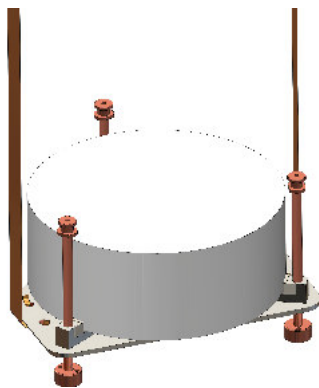
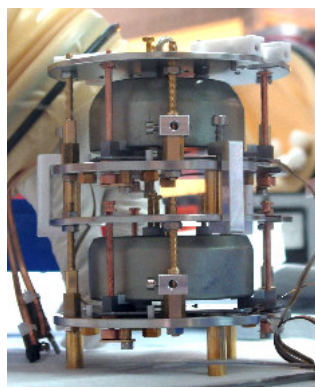


Figure 5.5: Final detector configuration of the GERDA Phase II germanium array. 18 BEGe detectors are mounted in single holders, 12 in pair holders. Seven semi-coaxial HPGe detectors enriched in Ge^{76} are deployed, the GTF detectors are made of germanium with natural isotopic abundance. Detectors marked in blue have a passivation layer in the detector groove. String 7 is installed in the middle of the string, surrounded by strings 1 - 6 as shown in Figure 5.2(i). All strings are surrounded by a nylon mini-shroud. Drawing by K. Gusev.



(a) schematic view of single mounted BEGe



(b) single mounted BEGe detectors in jig



(c) BEGe string

Figure 5.6: New single BEGe holders. In the original design two BEGe detectors are mounted back-to-back in a holder. Thus, the groove of the top detector faces upwards (compare Figure 5.1(a)). 5.6(a): in the new single BEGe holder, each BEGe is mounted on a silicon plate with the groove/ p^+ contact facing downwards. Drawing by GERDA at MPIK, Heidelberg. New jigs for the single holders have been designed and produced, see 5.6(b). 5.6(c) shows a partially assembled string with three BEGe's in single holders. All grooves/ p^+ contacts face downwards to prevent collection of dust particles and the development of leakage current.

	HADES	GD35B		2/B: PII VFE	
		PI VFE	Phase I	HADES	PII VFE
FWHM [keV]					
1592.5 keV	2.07 ± 0.03	2.37 ± 0.05	3.09 ± 0.15	1.91 ± 0.03	2.71 ± 0.06
2614.5 keV	2.57 ± 0.01	2.87 ± 0.01	3.21 ± 0.03	2.48 ± 0.02	3.38 ± 0.06
FWHM A/E					
DEP [%]	0.75	1.4	1.7	0.63	1.45
survival fraction at 90% DEP acc					
SEP	6.02 ± 0.47	7.35 ± 1.01	10.01 ± 2.39	4.92 ± 0.54	11.68 ± 0.96
FEP at 2614.5 keV	7.72 ± 0.09	13.58 ± 0.15	15.04 ± 0.39	7.63 ± 0.10	13.37 ± 0.15
2039 ± 35 keV	33.47 ± 0.25	44.75 ± 0.35	46.45 ± 0.91	31.13 ± 0.27	45.09 ± 0.35

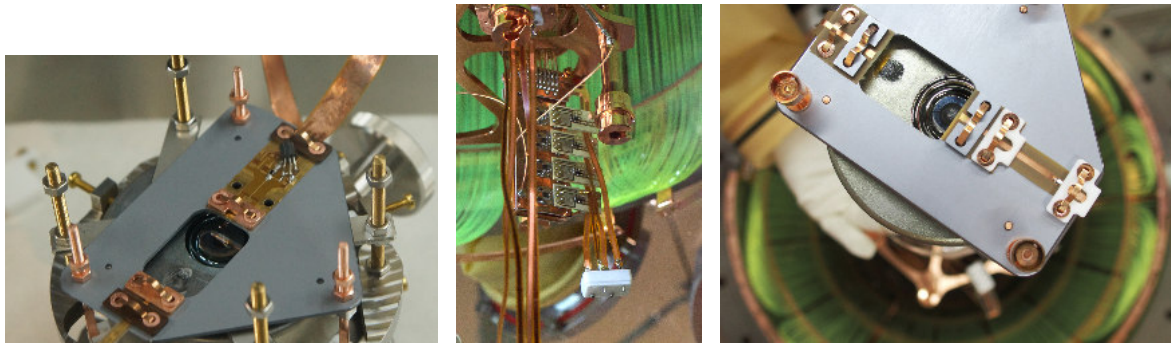
Table 5.2: Comparison of energy resolution, A/E resolution in DEP and survival fractions measured in vacuum cryostat (HADES), Phase I and Integration Test January 2015 with Phase I-like very front-end (PI VFE) and Phase I-like VFE (PII VFE). Phase I values are for a single calibration.

5.2 New Phase II Electronics

The Phase II read-out electronics is presented and discussed in Section 3.3. In the original design, the front end (FE) electronics is split into two stages: the very front-end (VFE), with JFET and the resistive feed-back circuit, and the four-channel cryogenic charge sensitive preamplifier, CC3 (compare Figure 3.7). In earlier tests a high mortality of the JFET due to electrostatic discharges during the detector/ string assembly has been observed. No protective diode exists for the used JFET. Therefore, during detector mounting the gate of the JFET is connected to ground via a bond wire. This connection increases the survival of the VFE JFETs and can easily be removed during string assembly. However, once the grounding of the gate is removed the JFET may again be destroyed by discharges. The destroyed JFET of the original Phase II VFE design (see Figure 5.7(a)) cannot be repaired easily. The detector(s) have to be disassembled in the GDL glove box to exchange the VFE on the silicon plate.

A fast and easy solution is to change the design of the Phase II VFE: the VFE is installed on a small PCB directly connected to the CC3 (see Figure 5.7(b)). The original signal cable with the VFE is replaced by a flex cable without printed circuit (see Figure 5.7(c)). The so-called *Phase I-like* front-end electronics has several advantages over the original design: the PCB with the VFE is much easier to exchange than the mounted cables on the silicon plates which can only be done in GDL. Moreover, by moving the electronics parts further away from the detector the overall radioactivity in the close vicinity of the detectors is reduced.

In January 2015 the performance of the Phase I-like VFE was tested. A full string with four prototype BEGe detectors with Phase II VFE and four Phase II BEGe detectors using the new Phase I-like VFE were deployed, see Figure 5.7(d). Only three out of eight detectors were operational. Table 5.2 summarizes the results obtained in a ^{228}Th calibration measurement with the prototype BEGe 2/B and the Phase II BEGe GD35B. Both BEGe detectors were tested in vacuum cryostat during the acceptance tests of the Phase II detectors in the HADES underground laboratory [103]. During Phase I the BEGe detectors showed an acceptable performance (see Section 4.5). The A/E resolution is of special interest since it determines the separation of signal-like events against β -events on the n^+ surface (compare Figure 4.18).



(a) Phase II VFE

(b) PCB with Phase I-like VFE at CC3

(c) contacting for Phase I-like VFE



(d) pilot string in Integration Test January 2015

detector	connected
Phase II VFE	
4/C	✗
1/D	✗
3/D	✓
2/B	✓
Phase I VFE	
GD61C	✗
GD91C	✗
GD02B	✗
GD35B	✓

Figure 5.7: The pilot string integrated in the GERDA LAr cryostat in January 2015. The four prototype BEGe detectors are read out with Phase II very front-end (VFE) electronics as described in Section 3.3. The four Phase II BEGe detectors are tested with the Phase I-like VFE electronics: the VFE is installed on a PCB directly connected to the CC3, the signal flex cable on the silicon plate is replaced by a flex cable without printed circuit. Detectors are listed from top to bottom of the string. Three out of eight detectors are connected (marked with ✓). Five detectors lost connection or bond wires. Pictures courtesy of Yura Suvorov.

energy [keV]	survival fraction [%] after		
	PSD	LAr veto	PSD + LAr veto
²²⁸Th calibration			
DEP	90.93 ± 1.44	0.04 ± 0.32	0.13 ± 0.13
FEP 1.6 MeV	14.82 ± 1.49	94.80 ± 2.20	14.12 ± 0.71
SEP	10.10 ± 0.84	1.03 ± 0.18	0.14 ± 0.08
FEP 2.6 MeV	15.22 ± 0.13	19.22 ± 0.16	3.02 ± 0.07
2004-2074	47.27 ± 0.32	1.03 ± 0.07	0.29 ± 0.04
²²⁶Ra calibration			
FEP 2204 keV	12.82 ± 0.30	96.36 ± 0.35	12.16 ± 0.28
2023-2047	28.08 ± 0.87	23.07 ± 0.86	4.00 ± 0.40

Table 5.3: Survival fractions after PSD, LAr veto and combined PSD and LAr veto. Survival efficiencies for LAr veto are corrected for a pulser acceptance of 87.3% in the ²²⁸Th and 91.3% in the ²²⁶Ra measurement [80].

The following is observed in the January 2015 Integration Test (see Table 5.2):

- **Energy resolution:** the energy resolution of the Phase I-like read-out is better than the original Phase II read-out, but worse than the energy resolution in vacuum cryostat.
- **A/E resolution:** the observed A/E resolution is similar for Phase I and Phase II-like read-out, but significantly worse than in vacuum cryostat. In Phase I the A/E resolution was between 1.5- 1.9% only.
- **PSD survival fraction:** the survival efficiencies in SEP, FEP and Compton regions are similar for Phase I- and Phase II-like read-out but significantly worse than the results in vacuum cryostat. The obtained survival fraction in the SEP and FEP at 2.6 MeV is slightly better than in Phase I: on average the survival fraction in the SEP is $\sim 11\%$, in the FEP $\sim 15\%$ and at $Q_{\beta\beta} \pm 35$ keV $\sim 45\%$ ¹.

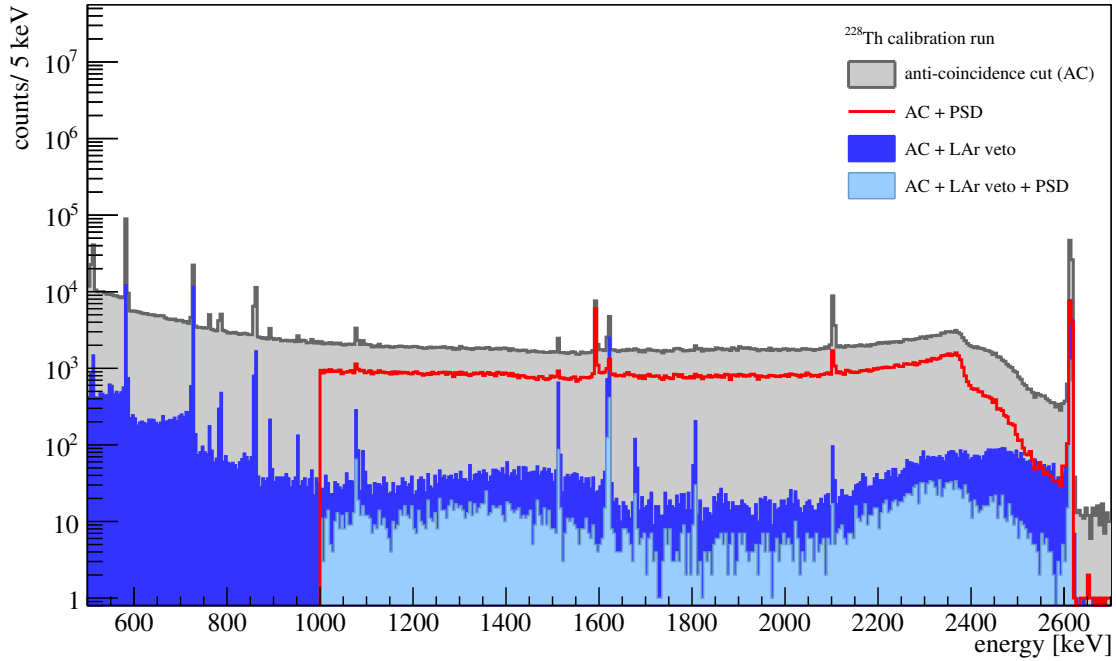
To conclude, the performance of the Phase I- and Phase II-like VFE is found to be very similar. Given the advantages in handling and the lower radioactivity as discussed above, it was decided to install the Phase I-like VFE for the first installation of the full GERDA Phase II array. In the future the GERDA experiment may resume the original Phase II read-out scheme.

5.3 Background Suppression with LAr Veto and Pulse Shape Analysis

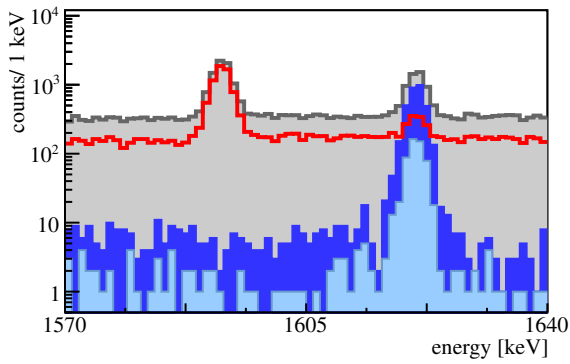
In April/ May 2015 the LAr veto system was commissioned. A similar string configuration as in January 2015 was deployed: two prototype BEGe detectors, 4/C and 1/D, and six Phase II BEGe detectors. The string was covered with a nylon mini-shroud. All germanium channels were equipped with Phase I-like read-out as described in the previous section.

Two main background components in the region of interest are ²⁰⁸Tl and ²¹⁴Bi. Therefore, the suppression of the LAr veto in combination with pulse shape discrimination was studied using the mother nuclide sources ²²⁸Th and ²²⁶Ra.

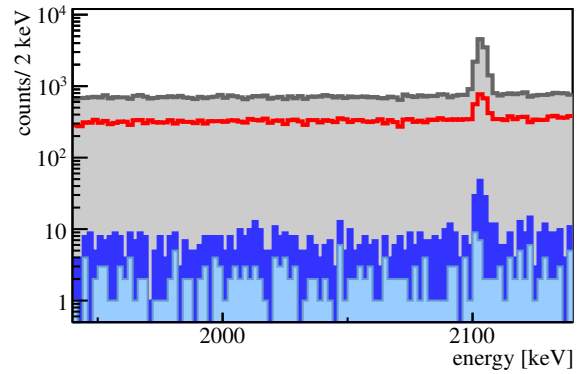
¹SSE fraction of Compton events may depend on the geometry of source and detector



(a) ^{228}Th energy spectrum



(b) close-up around DEP



(c) close-up around $Q_{\beta\beta}$

Figure 5.8: Energy spectrum of the ^{228}Th calibration measurement performed during LAr veto commissioning. The spectrum is shown after detector-detector anti-coincidence (AC), PSD, LAr veto and the combination of PSD and LAr veto. PSD is applied above 1 MeV only.

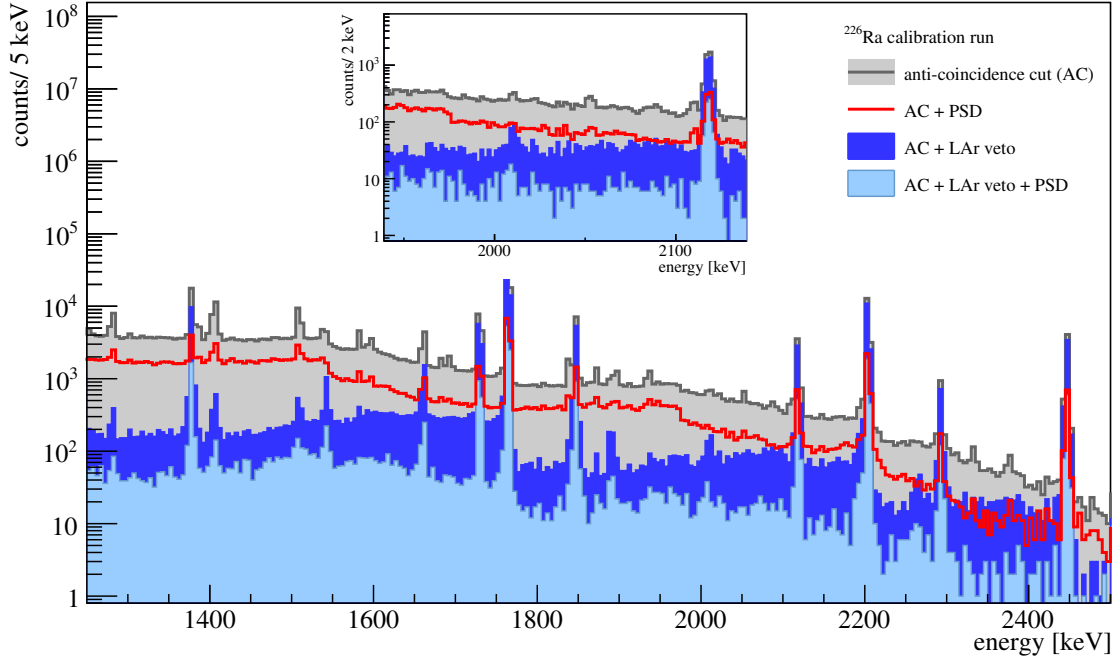


Figure 5.9: Energy spectrum of the ^{226}Ra calibration measurement performed during LAr veto commissioning. The spectrum is shown after detector-detector anti-coincidence (AC), PSD, LAr veto and the combination of PSD and LAr veto. PSD is applied above 1 MeV only.

Figure 5.8 and 5.9 show the energy spectra after detector-detector anti-coincidence, PSD, LAr veto, and PSD and LAr veto combined. The corresponding survival fractions are summarized in Table 5.3. Both measurements show:

- **DEP:** Figure 5.8(b) shows a close-up of the spectrum around the DEP of the 2.6 MeV γ -line of ^{208}Tl . The survival fraction of DEP events is about $(91 \pm 1)\%$ while the peak is fully suppressed by the LAr veto due to the two escaping annihilation photons.
- **FEP:** the ^{212}Bi FEP at 1.6 MeV in Figure 5.8(b) is highly accepted by the LAr veto since the full energy is deposited in the germanium detector. PSD accepts only $(15 \pm 1)\%$ of the FEP events. The survival fraction after LAr veto of the 2.6 MeV γ -line of ^{208}Tl is only 17% since the 2615 keV γ -ray is in coincidence with a 583 keV γ -ray.
- $Q_{\beta\beta}$: Figure 5.8(c) shows a close-up of the ^{228}Th energy spectrum around $Q_{\beta\beta}$. The Compton continuum of the ^{208}Tl 2.6 MeV γ -line is suppressed by a factor of 345 ± 48 [80]. The high suppression is reached due to the coincidence of the 2614 keV and 583 keV γ -rays: the total energy available is 3467 keV, i.e. for a germanium detector event at $Q_{\beta\beta}$ up to 1428 keV may still be deposited in the LAr to trigger the veto. The in-lay of Figure 5.9 shows the energy region around $Q_{\beta\beta}$ in the ^{226}Ra spectrum. The survival fraction after PSD is lower than in the same energy region of the ^{228}Th spectrum since $Q_{\beta\beta} = 2039$ keV is above the Compton edge of the prominent γ -line at 2204 keV. As discussed in Section 4.1 events above the Compton edge feature a higher MSE fraction. The LAr veto is less efficient since the γ -lines are not in coincidence and the total energy available to deposit energy in the LAr is much less than in the Compton

continuum of ^{208}Tl at the same energy. The suppression factor at $Q_{\beta\beta}$ of PSD and LAr veto combined is 25.0 ± 2.5 [80].

The survival fractions of PSD and LAr veto are correlated, i.e. the product of the survival fractions is smaller than the suppression obtained by the combination of PSD and LAr veto. Furthermore, the suppression of the LAr veto depends on the position of the source and the calibration measurements may not be representative for actual background components. Further details are found in [80].

The measurements prove that the LAr veto and PSD are efficient active background reduction techniques. High suppression factors of potential background events from ^{208}Tl and ^{214}Bi sources close to the detectors are achieved.

5.4 Effect of Noise on Pulse Shape Analysis

Noise is caused by statistical fluctuations of voltage or currents in the read-out electronics whereas the most important source is at the beginning of the read-out chain. The superposition of noise on a detector signal degrades the carried information: low frequency noise effects the energy resolution, whereas high frequency noise influences the pulse shape discrimination. Therefore, noise is discussed using a frequency spectrum. The latter is obtained by the Fourier transform of the signal baseline.

Important noise sources are e.g. detector leakage current or the serial noise produced by voltage fluctuations at the gate of the JFET. Furthermore, the frequency spectrum may feature characteristic lines, called pick-up noise. More details on noise can be found in [66, 65]. A detailed analysis on the noise spectrum and the noise origin is beyond the scope of this work. In the following the influence of noise on pulse shape analysis (PSA), i.e. the A/E parameter is discussed.

The noise in the GERDA Phase II setup is investigated using a fast Fourier transform (FFT) of the first 40 μsec of the baseline of events recorded during calibration measurements. Figure 5.10 shows the calculated noise spectrum of GD35B in Phase I, Run 50 and Run 53. Between Run 50 and 53 the grounding of the HV filters has been improved. This is clearly visible in the significant reduction of pick-up noise. So far the individual noise peaks cannot be attributed to individual sources and a more detailed analysis is needed.

To evaluate the A/E resolution the A/E distribution in the energy range 1.0-1.3 MeV from ^{228}Th calibration data are fitted with Equation 4.3. For PSA the relevant frequency range is roughly between 2.0-6.5 MHz, corresponding to 150-500 ns. Figure 5.11 shows the A/E FWHM as a function of the noise integral in the relevant frequency range. A clear correlation is observed, even in very different setups: Phase I shows a similar behavior as the Commissioning Runs 50 and 51 and the final Phase II setup (Run 53). The higher the noise in the frequency range 2.0-6.5 MHz, the broader the A/E resolution. Furthermore, Figure 5.11 shows that the majority of the BEGe detectors has a much higher noise contribution and broader A/E distribution than in Phase I. In the standard pulse processing as described in Appendix D a 3×50 ns moving window average (MWA) is applied to smooth the pulse. Increasing the size of the MWA improves the A/E resolution but has no effect on the pulse shape discrimination efficiency.

To further investigate the broadening of the A/E distribution template pulses are produced for each BEGe channel. These templates are averaged DEP pulses recorded during Phase II calibration runs. A strong energy and A/E cut is applied for selection. The template pulses

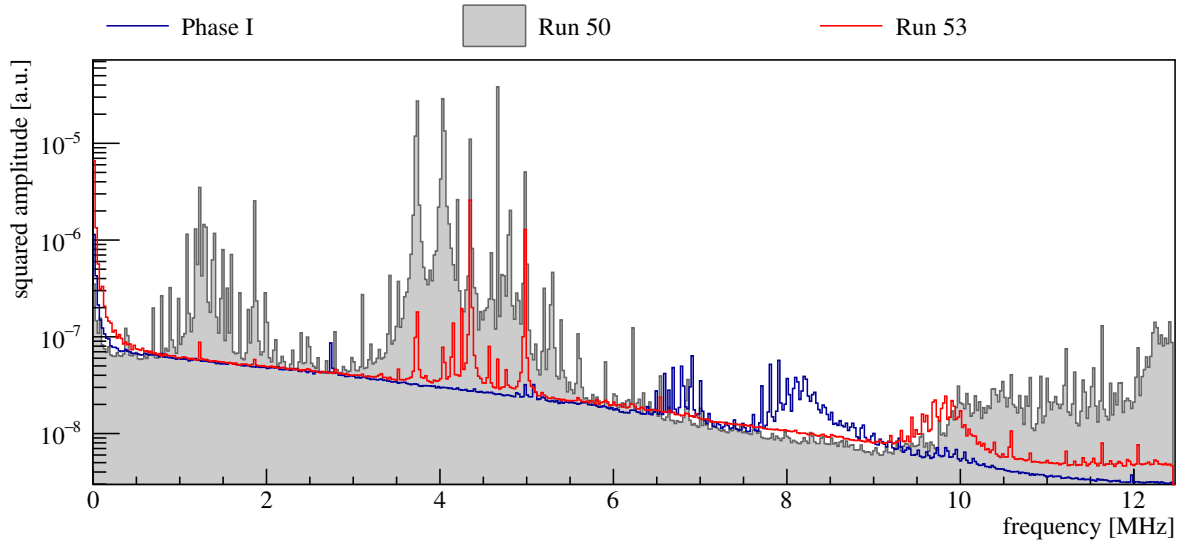


Figure 5.10: Noise power spectrum of GD35B during Phase I, Commissioning Run 50 and Phase II Run 53. Between Run 50 and 53 work on the grounding has been performed. Squared amplitudes are normalized according to the amplification in the individual measurements.

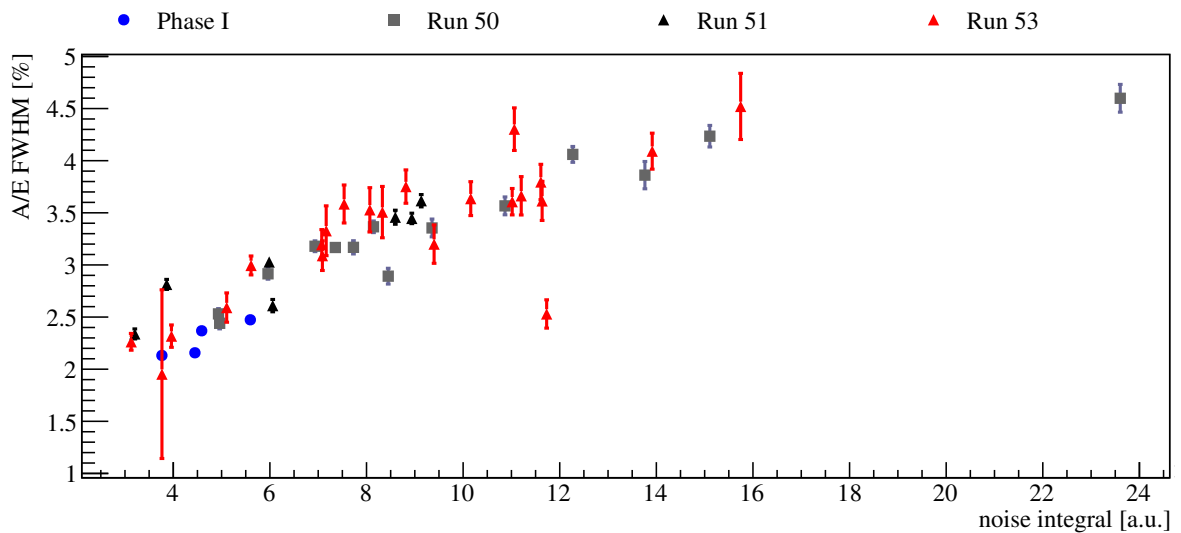


Figure 5.11: A/E resolution in energy region 1.0-1.3 MeV as a function of the noise integral in the region 2.0-6.5 MHz. The frequency range roughly corresponds to signal rise-times of about 150-500 ns.

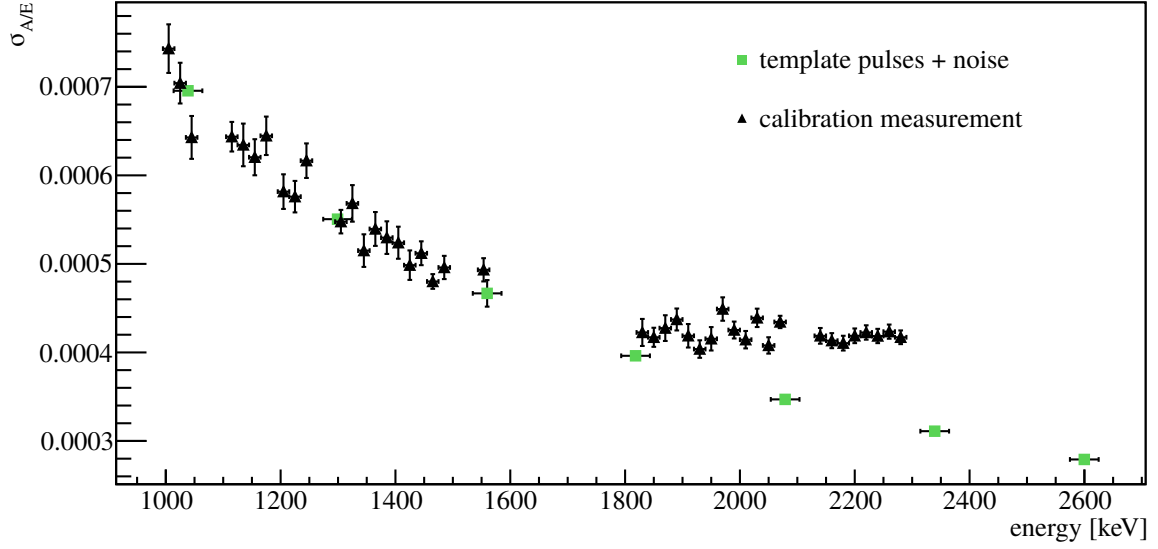


Figure 5.12: A/E resolution in different energy regions for A/E distributions of the template pulses (green) and ^{228}Th calibration measurements. The A/E resolution is obtained in a similar procedure the extraction of the energy calibration described in Section 4.3. A/E values are not normalized.

are scaled to artificially represent different event energies. Furthermore, the pulses are overlaid with baselines recorded during Phase II physics data taking in the corresponding channel. The latter represent the Phase II noise.

Figure 5.12 shows the resolution of the A/E distribution of the template pulses at different energies for GD61C. For comparison the A/E resolution for a ^{228}Th calibration measurement is shown. Below the DEP the resolution of the template pulses follows the calibration data, above, the resolution may be influenced by further effects.

The different BEGe channels show that the higher the noise, the better the agreement between A/E resolution of template pulses and calibration measurements. For six channels with comparably low noise and good A/E resolution, the resolution of the template pulses is found below the calibration measurements. This may hint to further broadening effects not considered using template pulses. A detailed analysis including pulse shape simulation for further investigation of the broadening is beyond the scope of this work. Nevertheless, the analysis using template pulses suggests that A/E is broadened due to noise. Furthermore, it shows that calibration data can be used to derive the energy dependence of the A/E resolution.

5.5 Summary

The strength of the GERDA design, i.e. the operation of bare germanium detectors in LAr, provides a fast and easy access with respect to other $0\nu\beta\beta$ experiments. Repair and maintenance work can be done on a short time scale.

The Phase II upgrade includes an array of 37 isotopically enriched and three natural germanium detectors surrounded by a new LAr veto system to detect scintillation light. Its integration was finalized in several iterations and finished in December 2015. Unforeseen problems with the bondability of the cables, the new VFE electronics and the development of leakage current due to handling were encountered and had to be solved. The original Phase II design foresees a two-staged front-end electronics (FE): the very-front end electronics consists of a JFET and feed-back circuit printed on a flex cable. The latter is mounted directly on the silicon plate of the detector holder to be as close as possible to the detector. The second stage is the CC3 preamplifier. A high mortality of the JFETs during detector assembly is observed. Since no protective diode exists, the FE design is changed in a first solution. Presently GERDA Phase II uses an FE similar to Phase I: the JFET and feedback circuit components are installed on a PCB which is connected directly to the CC3. The energy and A/E resolution as well as the pulse shape discrimination is found to be similar for the Phase I- and Phase II-like FE.

Commissioning results prove that pulse shape discrimination and the LAr veto are efficient active background reduction techniques: main background components at $Q_{\beta\beta}$ such as close ^{208}Tl and ^{214}Bi sources are suppressed up to two orders of magnitude.

The noise in the GERDA Phase II setup is investigated. A clear correlation between noise and the resolution of the A/E parameter is found. The majority of the detector channels shows a higher noise level and broader A/E than in Phase I. Furthermore, it is shown that the energy dependence of the A/E resolution can be derived using ^{228}Th calibration data.

Pulse Shape Analysis for BEGe Detectors in Gerda Phase II

As discussed in Section 4.5 the A/E analysis proved to be an efficient active background reduction technique for BEGe-type detectors in GERDA Phase I. This chapter summarizes the A/E analysis for BEGe detectors in the first data release of GERDA Phase II. From December 2015 to July 2016 a total exposure of $6.2 \text{ kg} \cdot \text{yr}$ has been collected with the BEGe detectors. Like in Phase I, a blind analysis is performed, i.e. events in the energy region $2014 \text{ keV} - 2064 \text{ keV}$ are not available for the analysis until all analysis cuts are fixed. Weekly ^{228}Th calibrations are used to calibrate the A/E parameter and determine the signal efficiency.

Section 6.1 discusses the BEGe data set including data selection and quality cuts. A new cut to reject pre-trigger pile-up events is introduced.

The calibration of the A/E parameter is based on the experience obtained in GERDA Phase I. Section 6.2 presents the A/E calibration including corrections of instabilities and energy dependence.

A detector based A/E cut is applied. Moreover, the cut is energy dependent to account for the broadening of A/E towards lower energies. The definition of the Phase II A/E cut is described in detail in Section 6.3. The suppression of γ -ray background using ^{228}Th calibration data is discussed in Section 6.4. The signal efficiency is derived in Section 6.5 using DEP events recorded in ^{228}Th calibration data.

In Section 6.6 the A/E cut is applied to the physics data. The A/E spectrum is compared to expectations from the different background contributions such as $2\nu\beta\beta$, α - and β -decays as well as γ -rays. The behavior of the A/E cut in calibration and physics data is investigated and compared. Furthermore, the derived signal efficiency using DEP events is cross-checked with the survival efficiency of $2\nu\beta\beta$ events. In a last step a method to obtain information on the background contribution using A/E is sketched.

Section 6.7 presents the background index (BI) of the GERDA Phase II BEGe data set. In Section 6.8 the results of the A/E analysis are compared to the ones obtained in GERDA Phase I.

6.1 The BEGe Data Set

GERDA Phase II started physics data taking on December 25th, 2015. The data set for the first GERDA Phase II release extends until June 1st, 2016, summarized in Table F.1. A blind analysis is performed, i.e. events in a 50 keV window around $Q_{\beta\beta}$ are not available for the analysis. Prior to releasing the events in the energy region from 2014 - 2064 keV, data selection as well as quality and analysis cuts were fixed.

For the following A/E analysis only BEGe detectors are taken into account. Since the active volume of GD02D is unknown [108], the detector is not considered in the physics analysis and used for a multi-detector coincidence cut only. GD91B shows a high leakage current worsening the energy resolution to about 10 keV in the DEP at 1593 keV. The small separation of the DEP and the FEP at 1621 keV do not allow for a proper background subtraction of the Compton events in the DEP. Furthermore, the bias voltage has been decreased below the depletion voltage. A partially depleted detector has incomplete and delayed charge collection. Therefore, the active volume and the signal efficiency cannot be estimated reliably. GD91B is used for multi-detector coincidence cut only.

Quality Cuts

A major effort has been done to find non-physical events while keeping physical ones with a high efficiency. In Phase II about 20% of the recorded events in the physics data feature a reverse polarity and are classified as discharges [109]. So far it is unclear where the discharges originate. Through cross talk between different channels in the read-out electronics such discharge events might fake a physical event. In GERDA Phase I, the rate of discharge events was negligible.

As described briefly in Appendix D, the event selection is based on the slope of the baseline, the position of the leading edge, the rise time and the polarity of the pulse. Events passing the quality selection are considered as physical. The efficiency of the quality cuts is more than 99.9% [109]. A multi-detector coincidence (or detector multiplicity) is defined by the number of channels containing physical pulses in a recorded event. The detector-detector anti-coincidence cut (AC), rejects all events with a detector multiplicity larger than 1. Furthermore, events within 10 μs in coincidence with the muon trigger are discarded.

For calibration data an additional cut for pile-up rejection is applied. The pile-up rate is proportional to the event rate and negligible in physics data. Most of the PSD methods use part of the calibration data as a proxy for $0\nu\beta\beta$ events. Since pile-up events represent a sample which is not present in physics data it is crucial to remove these events from the analysis.

Figure 6.1 shows traces of typical pile-up and random coincidence events in a calibration. In-trace pile-up events feature multiple leading edges in the trace and may be misidentified as MSE. In-trace pile-up events are scrutinized by requiring only one leading edge in the trace. Random coincidences feature a leading edge of the pulse much later than the middle of the trace. They are easily rejected by requiring the trigger position within a small window around the center of the trace. Pre-trigger pile-up events are events where the baseline is not yet restored due to a previous event and the baseline shows a prominent slope. To reject pre-trigger pile-up events a cut on the baseline slope is applied, see also Appendix D. For further rejection a new cut parameter is introduced in Phase II: the ratio of the baseline RMS in the first 70 μs over the first 10 μs of the trace (compare Figure D.1(a)). Figure 6.2 shows the distribution of the pre-trigger pile-up parameters. In a pre-selection a cut on the absolute

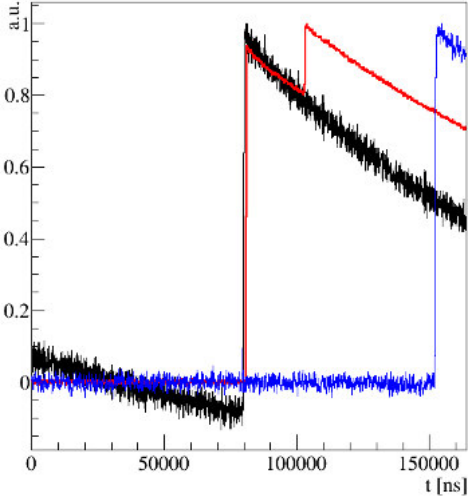


Figure 6.1: Example traces of different pile-up event types. The baseline of pre-trigger pile-up (black) shows a prominent slope. In-trace pile-up (red) are events with multiple coincident physical events and feature multiple leading edges. The blue trace shows a random coincidence event with the leading edge far beyond the center of the trace. The maximum of the traces is normalized to 1. See also Appendix D for details.

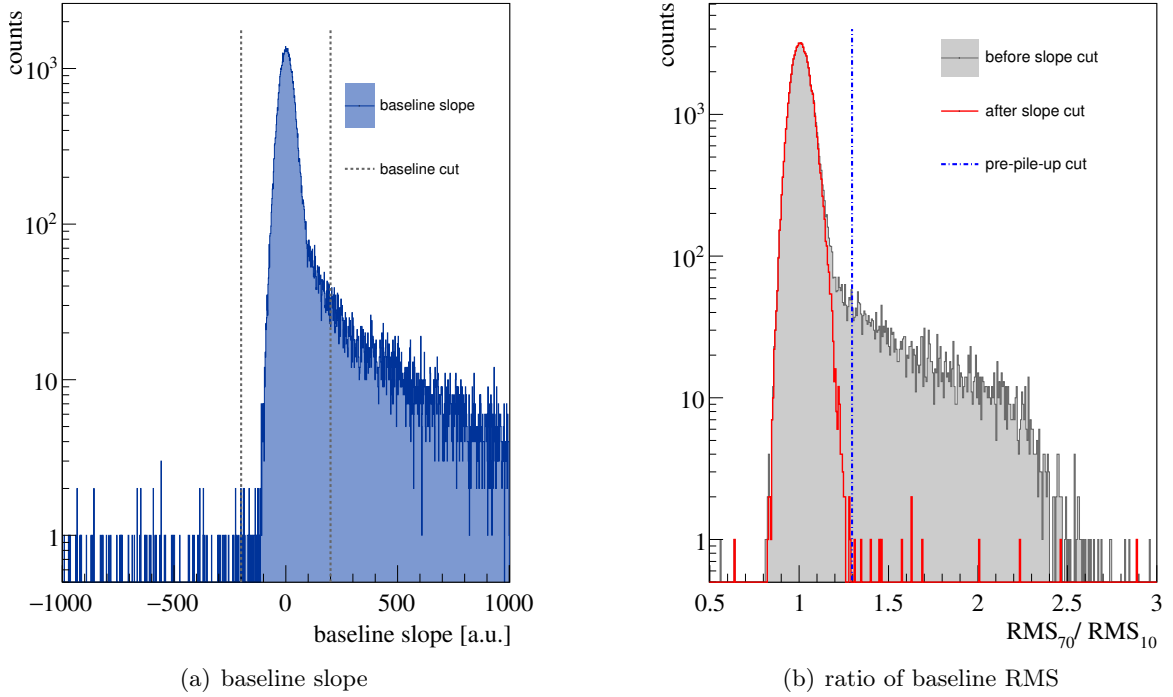


Figure 6.2: Distribution of the pre-trigger pile-up parameters: **(a)** shows the distribution of the baseline slope. The dashed line indicate the acceptance region. **(b)** shows the ratio of the baseline RMS in the first $70 \mu\text{s}$ (RMS_{70}) over the first $10 \mu\text{s}$ (RMS_{10}) of the trace. A pre-selection based on the baseline slope is applied (red histogram). The blue dashed line indicates the position of the RMS ratio cut: events with an RMS ratio larger than 1.3 are rejected.

value of the baseline slope is applied. An additional pile-up cut on the RMS ratio is set to 1.3. The cut is equally applied to semi-coaxial and BEGe detectors.

Typically, for pile-up events the measure of the amplitude, hence the energy estimation, is incorrect. Therefore, calibration spectra with a high pile-up rate feature a low energy tail of

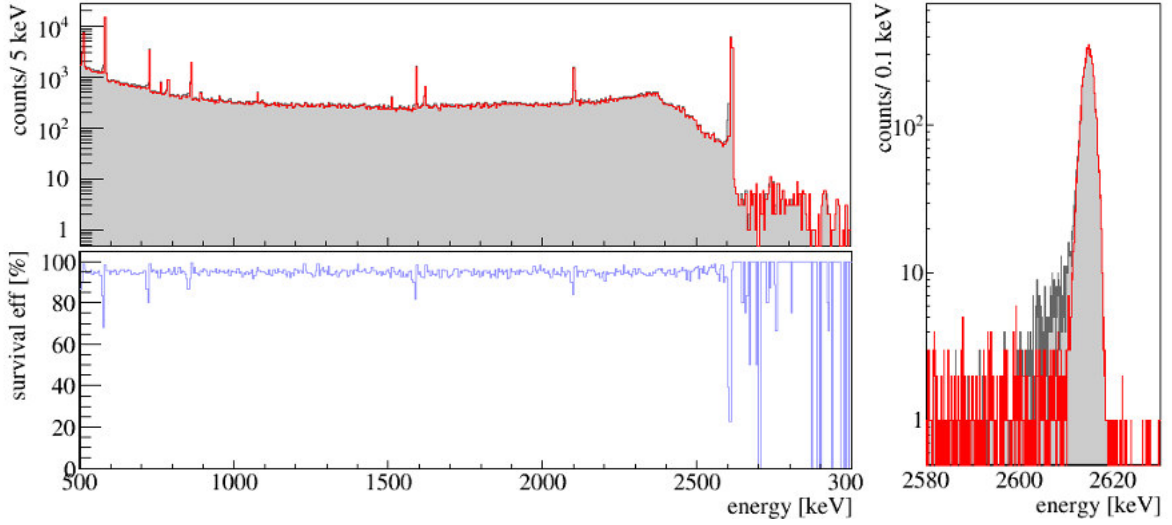


Figure 6.3: **Top:** calibration spectrum before (gray) and after (red) pile-up cut. **Bottom:** survival efficiency of the events in different energy regions. In the Compton region the efficiency is about 95%. The efficiency is given by the ratio of the two spectra. **Right:** close up of the 2.6 MeV FEP of ^{208}Tl .

the FEP. Figure 6.3 shows a calibration spectrum before and after the pre-trigger pile-up cut: the low energy tails are reduced and the Gaussian shape of the FEP is restored. This shows that the cut efficiently removes pile-up events. No hint is found that physical events in the background data are removed. As the cut is applied to calibration data only, no cut efficiency is determined.

Data Selection

A first data selection is based on the stability of the energy scale using the stability of the test pulse (TP), i.e. pulses artificially injected into the electronics chain every 20 sec. Detectors considered as unstable, or detectors for which the bias voltage has been changed within a run, are used for detector-detector anti-coincidence only. Table F.1 summarizes the GERDA Phase II BEGe data set and lists all detectors in anti-coincidence mode for the individual runs.

As described in Appendix E, A/E instabilities of the order of 1-5% have been observed in GERDA Phase I: A/E decreased exponentially with a time constant of about one month. Furthermore, a change up to 1% common to all four channels could be attributed to a power failure. However, it was shown that the behavior of the A/E of the test pulse does not coincide with the A/E of the physical pulses. As the event rate in the physics data is low, only calibration runs can be used to monitor the time stability of the A/E parameter.

In Phase II, further data selection for the BEGe detectors is defined by the applicability of the A/E analysis in a given time period. Even small changes in the read-out electronics, e.g. in the electronic bandwidth, might change the A/E parameter. This provides several challenges for the pulse shape analysis as it must be guaranteed that the A/E level in the physics data is well represented by the A/E recorded in calibration runs. Similarly, the A/E resolution must stay constant over the data set, as the resolution is directly connected to the acceptance of the A/E cut.

Figure 6.4 shows the time stability of the A/E parameter in 26 calibrations during Run 53 -

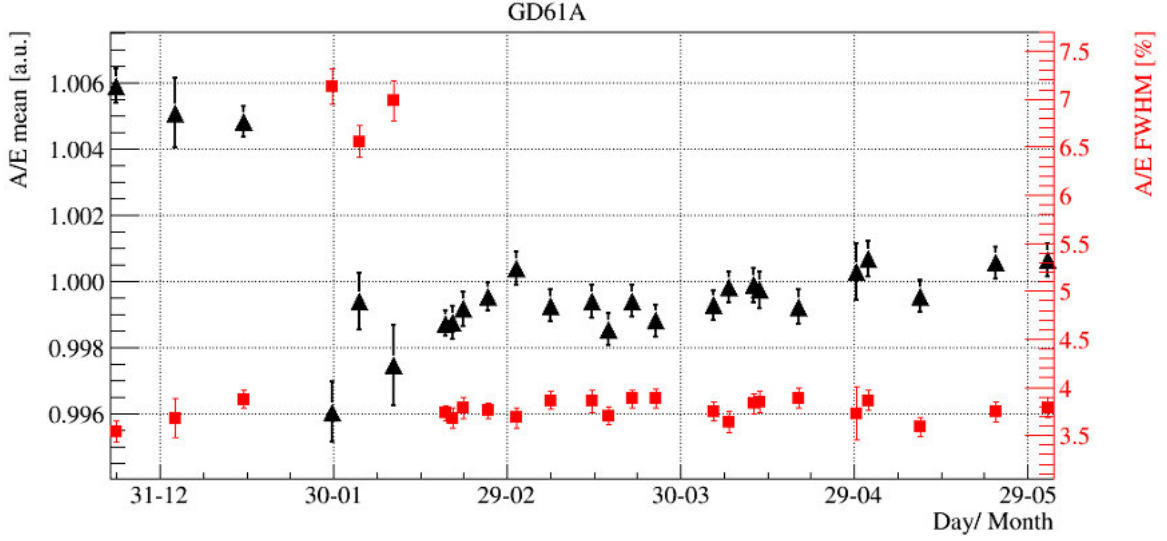


Figure 6.4: Mean of the A/E distribution in the energy region 1.0-1.3 MeV for calibration runs recorded with GD61A. A/E mean values are normalized to the average A/E mean. The corresponding FWHM of the distributions is shown. FWHM are given with respect to the A/E mean.

64 for GD61A. For each calibration run the A/E distribution in the energy region 1.0 - 1.3 MeV is fitted with a Gaussian and a low-side tail, see Equation 4.3. To monitor the stability of the A/E parameter, the mean and sigma of the Gaussian are extracted. The A/E level of SSE is represented by the mean of the Gaussian, changes in the noise are reflected in a change of the width of the Gaussian distribution. The step in A/E in Figure 6.4 corresponds to a lowering of the bias voltage from 4500 kV to 4400 kV. The increase of the FWHM between 29.01.16 and 11.02.16 shows the increase of noise introduced by a broken test pulse input cable. Appendix G summarizes the A/E monitoring plots for all 28 BEGe detectors considered in the pulse shape analysis.

The selection of the BEGe data set is based on the stability of the mean and width of the A/E distributions. It is required that the mean A/E is stable within 0.5 %, which corresponds roughly to the resolution (in sigma) of the A/E distribution in the DEP. Periods with increased FWHM, i.e. increased noise, are excluded. According to these requirements the BEGe data set is divided into periods of stable A/E . Table G.1 summarizes the periods in which A/E is considered stable for all 28 BEGe detectors in the A/E analysis. Only nine detectors are stable within the requirements over the full data period. Detectors are grouped into one to six periods of stable A/E . Individual detectors are partly excluded from the analysis in the following periods:

- 20.12.15 - 09.02.16: The bias voltage of GD32B was changed during this period.
- 25.01.16 - 11.02.16: GD61A (Figure 6.4), GD89B and GD91C are excluded as the noise level is increased due to problems with the input test pulse to the CC3.
- 25.01.16 - 29.01.16: GD32C, GD61C, GD35C and GD79C are excluded due to instabilities in Run 54, the A/E level in physics data is unclear.
- 11.02.16 - 19.02.16: GD00B is excluded due to an unexplained drop of A/E , the A/E

level in physics data is unclear.

- 06.04.16 - 12.04.16: GD32B is excluded due to an unexplained drop of A/E , the A/E level in physics data is unclear.
- 19.04.16 - 29.04.16: GD35B is excluded due to an unexplained drop of A/E , the A/E level in physics data is unclear.

The exposure of the BEGe data set based on the A/E selection is 5.8 kg·yr. The data set for which no A/E analysis can be applied has an exposure of 0.4 kg·yr only. Since the background index (BI) cannot be reduced using PSA and the exposure is comparably small, these data are discarded in the physics analysis.

6.2 Calibration of the A/E Parameter

In GERDA Phase II the A/E calibration followed a similar approach as in Phase I, see Appendix E. A/E is normalized to correct for instabilities during and in-between the physics runs. According to the Phase I analysis this correction is referred to as long-term correction. No A/E instabilities during calibration runs have been observed in Phase II. A/E is corrected for an energy dependence, such that the SSE band is centered at $A/E = 1$. Finally, A/E is normalized to the mean A/E in the DEP. As described in Section 5.4 the noise level in Phase II is much higher than in Phase I. Therefore, the energy dependence of the A/E resolution needs to be taken into account.

The A/E calibration is evaluated and applied on a detector-by-detector basis. In the following the individual calibration steps will be discussed referring to exemplary BEGe detectors.

Long Term Correction

As described in the previous section data are grouped into periods of stable A/E , see Table G.1. The aim of the long-term correction is to merge all calibration data in order to increase statistics and avoid splitting the pulse shape analysis into several data sets. This is achieved by a normalization of the A/E values in the individual periods.

Figure 6.4 shows the mean A/E for 26 calibration runs recorded with GD61A for the first data release of GERDA Phase II. From the calibration run taken on 25.01.16 (Run 54) until the beginning of calibration run 11.02.16 (Run 56) GD61D is excluded from the analysis due to higher noise level. The A/E level before and after the excluded period changes by about 6%. A simple merging of the calibration runs would result in a double structure or broadening of the A/E distribution. Therefore, the A/E values are normalized to the average A/E mean of the Compton region from 1.0 - 1.3 MeV within each period according to Table G.1.

Figure 6.5 shows the normalized A/E distribution in the energy region 1.0 - 1.3 MeV for the calibration runs taken on 23.12.15 (Run 53) and 23.05.16 (Run 63) compared to the merged calibration runs in the full BEGe data set for GD61A: peak position, shape and width of the three distributions are similar. None of the BEGe channels shows a shift or broadening of the A/E distribution due to the normalization and merging of the calibration runs.

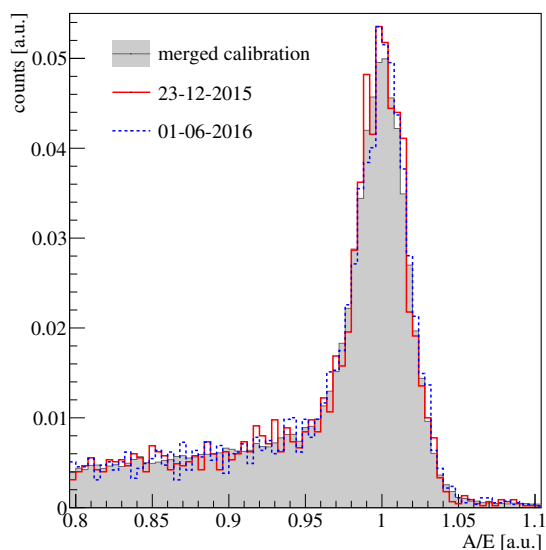


Figure 6.5: A/E distribution in the energy region 1.0 - 1.3 MeV for GD61A. The normalized A/E distribution for GD61A for the merged calibrations (gray), compared to the first calibration in Run 53 (green) and the last calibration run in Run 64 (blue). Distributions are normalized to the integral.

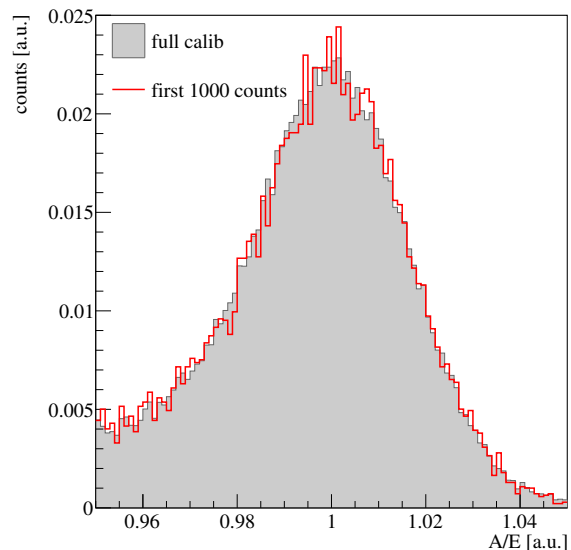


Figure 6.6: Normalized A/E distribution in the energy range 1.0 - 1.3 MeV for the fully merged calibration runs (gray) and the first 1000 events recorded in each calibration run (red).

Stability during Calibration Runs

In Phase I an increase of A/E up to 1% during calibration runs is observed and a correction is applied. Figure 6.6 shows the normalized A/E distribution for the merged calibration runs in Run 53 - 64 for GD61A. The A/E distribution in the energy range 1.0 - 1.3 MeV for the full calibration is shown in comparison to the distribution of the first 1000 events recorded in each calibration. A Phase I like increase of A/E during the calibration would shift the distribution of the full calibration to higher A/E values with respect to the distribution of the first 1000 events. No such effect is observed, the maximum and shape of the two A/E distributions in Figure 6.6 are in good agreement. Furthermore, no increase of A/E as a function of the integral count rate is observed. Neither passivated nor non-passivated BEGe detectors show an increase of A/E during the calibration. So far, the reason for the Phase I drift during calibration remains unclear. However, the non-observation indicates that the drift is not a bulk but rather a surface effect.

Energy Dependence

After the long-term correction all calibration runs are merged channel-wise. As described in Section 4.3 and Section 5.4, the A/E of SSE as well as the A/E resolution show an energy dependence. The energy dependence is derived from ^{228}Th calibration data following the procedure described in Section 4.3 in which single Compton scattered (SCS) events represent SSE. A/E distributions at different energies are fitted with a Gaussian and low-side tail. The mean of the Gaussian, $\mu_{A/E}$, and the width $\sigma_{A/E}$ are extracted to determine the A/E energy

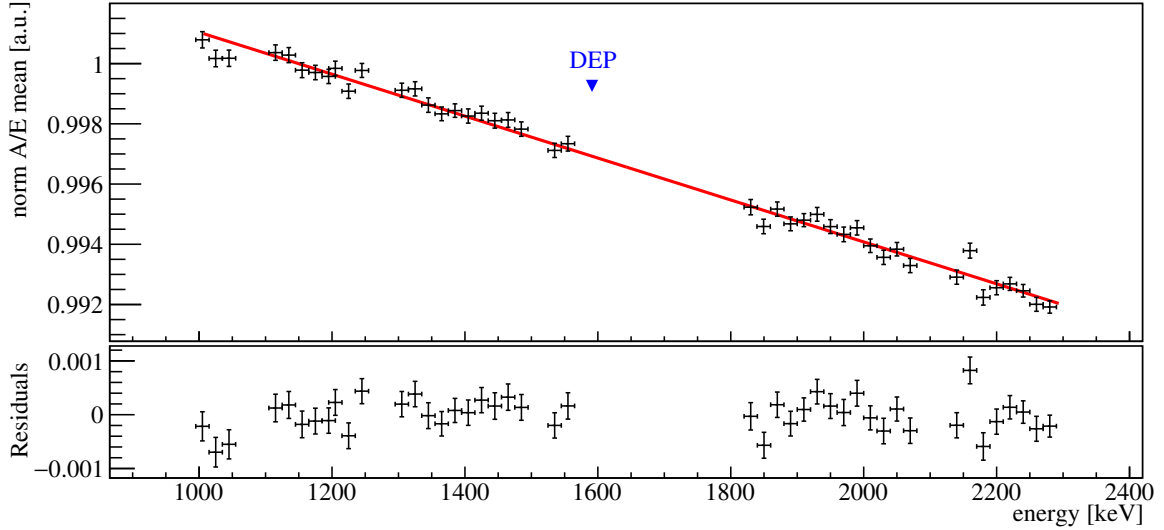


Figure 6.7: Gaussian mean of the A/E distribution for different energy regions. The energy dependence is approximated with a linear function. The corresponding residuals are shown in the panel below. The error bars represent the fit uncertainty of the A/E distribution. For comparison the Gaussian mean of the A/E distribution in the DEP is shown in blue.

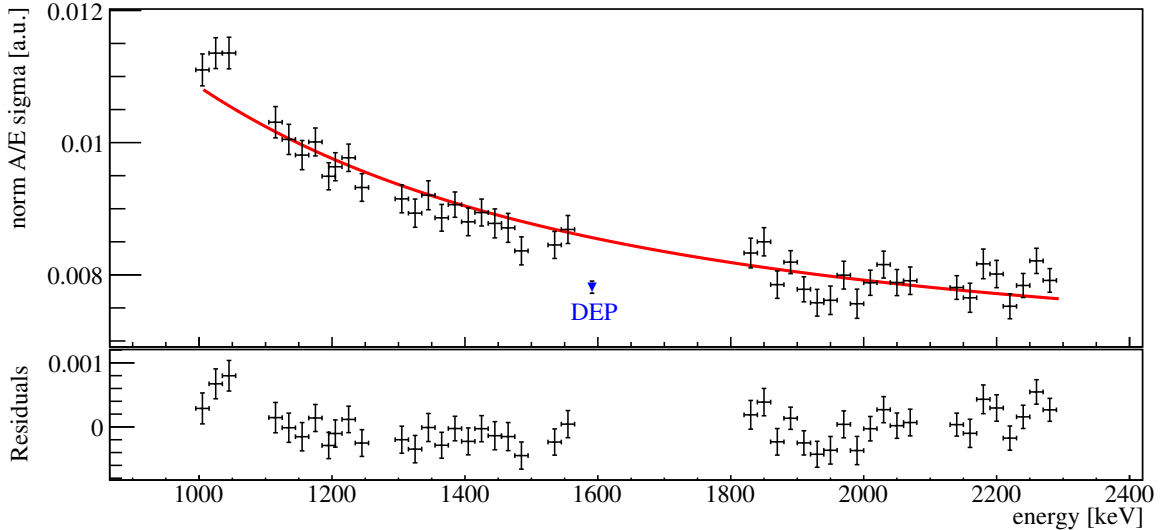


Figure 6.8: Sigma of the A/E distributions in different energy regions. The energy dependence of the mean A/E is approximated with function 6.2. The corresponding residuals are shown in the panel below. The error bars represent the fit uncertainty of the A/E distribution. For comparison the Gaussian sigma of the A/E distribution in the DEP is shown in blue.

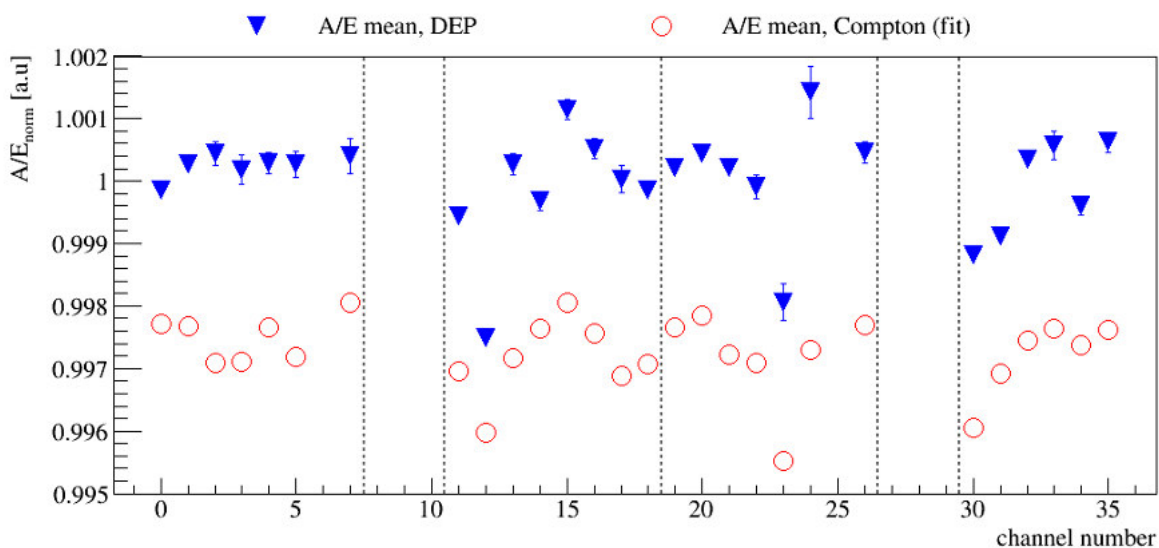


Figure 6.9: Gaussian mean of the Compton subtracted A/E distributions in the DEP (blue) according to the A/E fit described in Section 4.4. The mean A/E of single Compton scattered events is calculated using the linear energy dependence of A/E , Equation 6.1, evaluated at the DEP energy (red). A/E values are corrected for long term instability only. Detector names and corresponding channel number are summarized in Table C.1.

dependence.

Figure 6.7 shows the Gaussian mean A/E in the 44 Compton regions between 1.0-2.3 MeV for GD02A. The energy dependence of the mean A/E is approximated with the linear function

$$A/E(E) = a + m \cdot E, \quad (6.1)$$

where a is the offset and m the slope. To center the SSE band at $A/E = 1$, A/E values are normalized to $A/E(E)$ given by Equation 6.1.

The corresponding width of the A/E distributions is shown in Figure 6.8. The energy dependence of the Gaussian sigma is approximated with the empirical function [5]

$$\sigma_{A/E}(E) = \sqrt{b + \frac{c}{E^2}}. \quad (6.2)$$

Normalization to DEP A/E

A/E values are calibrated such that the SSE band is centered at $A/E = 1$. As the A/E cut position will be defined according to the SSE band, its exact position is crucial.

Figure 6.9 compares the Gaussian mean of the A/E distribution of DEP and single Compton events of the same energy. The A/E distributions in the DEP are Compton background subtracted and fitted with a Gaussian and a low-side tail to extract the mean value. The mean A/E of Compton events is determined according to Equation 6.1 evaluated at the DEP energy. A systematic shift of 0.25% between the mean A/E in the DEP and the Compton events is observed. It is believed that the difference originates in an underestimation of the Gaussian

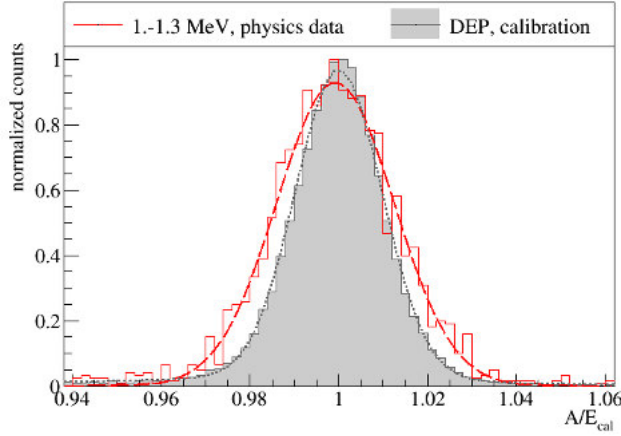


Figure 6.10: A/E distribution of DEP and physics events in the energy region (1.0-1.3) MeV of the full Phase II BEGe data set. A/E values are calibrated according to Section 6.2. The Compton background of the DEP distribution is subtracted according to Appendix A. Physics events are in anti-coincidence with the LAr veto. The DEP A/E distribution is fitted with Equation 4.3, the physics A/E distribution with a Gaussian only.

mean in Equation 4.3 due to the presence of the MSE tail of the Compton distribution.

Since the DEP features only a small MSE tail the mean of the Gaussian is believed to be more trust worthy. Therefore, to correct the offset and align the SSE band to $A/E = 1$, all A/E values are normalized to the mean A/E in the DEP. This justifies the definition of the A/E cut with respect to the SSE band as it will be discussed in more detail in Section 6.3.

Calibrated A/E in Physics and Calibration Data

Figure 6.10 compares the A/E distribution in the DEP and the distribution of the physics events in the energy region 1.0-1.3 MeV for the full BEGe data set, i.e. all channels and runs merged. A/E values are corrected for long-term instabilities and energy dependence, and are normalized to the DEP A/E . The A/E distribution in the DEP is Compton background subtracted according to Appendix A and described by a Gaussian centered at $\mu_{A/E}^{cal} = 1.00011$. The selected physics events are in anti-coincidence with the LAr veto and contain about 97% of $2\nu\beta\beta$ events [110]. The A/E distribution of the physics events is described by a Gaussian centered at $\mu_{A/E}^{phy} = 0.99923$. 51% of the DEP as well as the physics events in Figure 6.10 have an A/E value below the Gaussian mean of the corresponding distribution.

The good agreement of the center of the A/E distributions proves that the calibration procedure determined using calibration data is equally valid in physics runs.

6.3 The A/E Cut

Figure 6.11 shows the resolution of the Compton background subtracted A/E distributions in the DEP. The distributions are fitted with a Gaussian and a low-side tail (see Equation 4.3) to extract the FWHM of the Gaussian. In all four strings the A/E resolution worsens from top to bottom detector by nearly a factor of 2. As a consequence, a common A/E cut for all 28 BEGe detectors would result in very different signal acceptances. Therefore, the A/E cut is determined for each BEGe channel separately. Furthermore, the A/E cut must be energy dependent to account for the broadening of the A/E distribution to lower energies.

A two-sided A/E cut around the SSE band is applied. MSE and n^+ surface events are removed by a cut on the low A/E side. The cut position is chosen according to 90% acceptance of DEP events. The distance of the cut position to the SSE band ($A/E = 1$) can be expressed

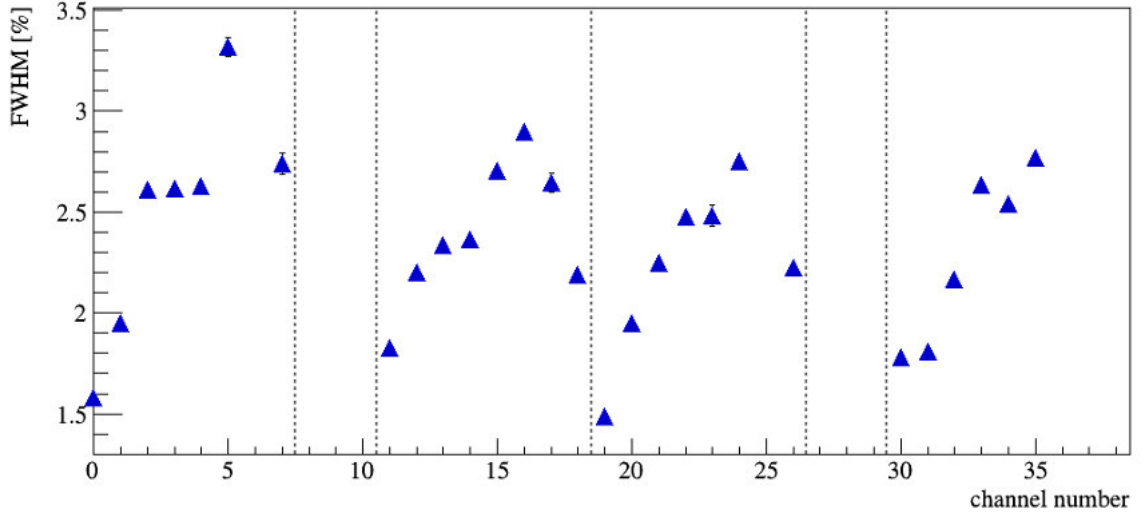


Figure 6.11: Full-width at half-maximum (FWHM) of the A/E distribution in the DEP for all 28 BEGe detector in the A/E analysis. A/E values are corrected for long-term instabilities and energy dependence. The distributions are Compton background subtracted according to Appendix A and fitted with a Gaussian and low-side tail, as described in Section 4.4. The FWHM of the Gaussian is normalized to the corresponding Gaussian mean. The dashed lines separate the detector strings. Channel numbers increase from top to bottom detector within each string, see Table C.1

in sigma of the A/E distribution at the DEP energy, whereas the energy dependence of the A/E width is given by Equation 6.2. Hence, the energy dependent low A/E cut is defined as

$$C_{A/E}^l(E) = 1 - n \cdot \sigma_{A/E}(E) \quad (6.3)$$

To reject events on the p^+ contact and in the detector groove a cut on the high A/E side is applied. Such events are much better separated from the SSE band than n^+ events and MSE. Therefore, the high A/E cut is chosen twice as loose as the low cut. The cut position is defined as

$$C_{A/E}^h(E) = 1 + 2 \cdot n \cdot \sigma_{A/E}(E) \quad (6.4)$$

with $A/E = 1$ being the position of the SSE band and $n \cdot \sigma_{A/E}(E)$ the cut position expressed in A/E resolution according to 90% acceptance of DEP events by the low A/E cut. Table 6.1 summarizes the A/E cut positions for all 28 BEGe detectors in the first GERDA Phase II data release. Events with $C_{A/E}^l(E) \leq A/E \leq C_{A/E}^h(E)$ are accepted as signal like events.

Since the energy dependence of the A/E parameter as well the its resolution is determined only above 1 MeV the A/E cut will not be applied to events with energies below. Thus, the relevant energy range for this work is 1.0-5.4 MeV.

Detector	$C_{A/E}^l$	$C_{A/E}^h$	Detector	$C_{A/E}^l$	$C_{A/E}^h$
GD91A	-1.8	3.5	GD02A	-1.7	3.4
GD35B	-1.6	3.2	GD32B	-1.4	2.9
GD02B	-1.7	3.4	GD32A	-1.4	2.8
GD00B	-1.4	2.9	GD32C	-1.5	3.0
GD61A	-1.5	3.1	GD89C	-1.4	2.9
GD89B	-1.7	3.3	GD61C	-1.5	3.0
GD02B			GD76B	-1.4	2.8
GD91C	-1.6	3.3	GD00C	-1.6	3.2
GD35C	-1.7	3.4	GD00A	-2.1	4.1
GD76C	-1.6	3.1	GD02C	-1.9	3.8
GD89D	-1.5	3.0	GD79B	-1.8	3.6
GD00D	-1.7	3.4	GD91D	-1.7	3.3
GD79C	-1.7	3.3	GD32D	-1.7	3.3
GD35A	-1.7	3.5	GD89A	-1.5	3.0
GD91B					
GD61B	-1.7	3.3			

Table 6.1: Summary of low ($C_{A/E}^l$) and high ($C_{A/E}^h$) A/E cut positions. The cut position is given in number of sigma of the A/E resolution. See also Equations 6.3 and 6.4 for the definition. The positions of the low A/E cut is chosen according to to 90% acceptance in the DEP. Detectors are grouped string-wise, from top to bottom. GD02B and GD91B are excluded from the analysis.

6.4 Suppression of ^{228}Th with Pulse Shape Discrimination

As described in the previous section, a two-sided A/E cut is applied in the final physics analysis. The low A/E cut is chosen such that 90% of the DEP events are accepted, whereas the high A/E cut is twice as loose. To understand the overall performance of the A/E cut, the survival fraction is investigated for different energy regions in the ^{228}Th calibration. Table 6.2 summarizes the rejection of the low and high A/E cut as well as the acceptance of the two sided cut for the full BEGe data set, i.e. all calibration runs and BEGe channels combined. The survival fraction of Compton events from ^{208}Tl around $Q_{\beta\beta}$ is 45.3%. FEP events are rejected with a survival fraction of 14.9-14.6%. SEP events are stronger suppressed as the MSE fraction is higher. In total, 87.3% of the DEP events are accepted by the two-sided A/E cut.

Figure 6.12 shows the survival fraction of the A/E cut for different energy and peak regions in the ^{228}Th spectrum in the individual BEGe channels. The average survival fraction does not take into account the different detector masses. Therefore, the average value might differ from the survival fraction in the full BEGe data set. On average $(10.0 \pm 0.1)\%$ and $(2.7 \pm 0.2)\%$ of the DEP events are rejected by the low and high A/E cut, respectively. This gives an average acceptance of $(87.3 \pm 0.2)\%$ in the DEP, which is in very good agreement with the calculated acceptance of the DEP events in the full BEGe data set.

Compton events in a ± 35 keV energy window around $Q_{\beta\beta}$ are accepted with an average value of $(43.4 \pm 0.5)\%$. The average survival fraction for the FEP at 1.6 MeV is $(15.0 \pm 0.5)\%$ and $(12.7 \pm 0.4)\%$ at 2.6 MeV. The different FEP acceptances might be explained by the different MSE to SSE fractions. As expected, the SEP has the highest suppression with an average survival fraction of $(9.7 \pm 0.4)\%$.

The survival fraction in the peak and Compton region in Figure 6.12 increases from top to bottom in the detector string. This is the same pattern as observed in Figure 6.11 where the increase of the A/E resolution originates in the increase of noise from the top to the bottom

region	low cut [%]	high cut [%]	survival fraction [%]
^{228}Th calibration runs			
DEP at 1592.5 keV	10.00 ± 0.21	2.68 ± 0.06	87.32 ± 0.21
FEP at 1620.5 keV	83.48 ± 0.29	1.62 ± 0.08	14.90 ± 0.29
SEP at 2103.5 keV	87.83 ± 0.16	1.55 ± 0.04	10.62 ± 0.16
FEP at 2614.5 keV	83.58 ± 0.03	1.82 ± 0.01	14.60 ± 0.02
(2039 \pm 35) keV	52.46 ± 0.07	2.29 ± 0.02	45.25 ± 0.07
physics runs			
FEP at 1460. keV	81.65 ± 2.70	2.16 ± 0.87	16.19 ± 2.64
FEP at 1524.7 keV	84.13 ± 1.87	1.79 ± 0.59	14.09 ± 1.81
(1000 - 1300) keV [†]	11.36 ± 0.69	4.50 ± 0.45	84.15 ± 0.79
BI window	13 / 21	3 / 21	5 / 21
BI window [†]	3 / 6	2 / 6	1 / 6
> 3.5 MeV	1 / 234	233 / 234	0 / 234
signal efficiency			
$0\nu\beta\beta$	$87.32 \pm 0.21(\text{stat}) \pm 2.43(\text{sys})$		
$2\nu\beta\beta$ from 1.0 - 1.3 MeV	$84.15 \pm 0.79(\text{stat}) + 1.67(\text{sys})$		
$2\nu\beta\beta$ corrected for n^+ events	$85.43 \pm 0.79(\text{stat}) + 1.67(\text{sys})$		

Table 6.2: Summary of rejection and survival fractions in different energy regions of the ^{228}Th calibration and physics spectrum of the full BEGe data set. The signal efficiency is given by the acceptance of DEP events. The acceptance of $2\nu\beta\beta$ events is calculated using the acceptance of physics events in anti-coincidence with the LAr veto in the range 1.0 - 1.3 MeV. The $2\nu\beta\beta$ acceptance is reduced by 98.5 % with respect to the $0\nu\beta\beta$ events due to events in the transition layer [68]. Survival fractions marked with [†] require the LAr veto prior to the A/E cut. Fractions are calculated according to Appendix A. Only for the $0\nu\beta\beta$ efficiency, systematic uncertainties according to Table 4.2 are considered. The $2\nu\beta\beta$ acceptance systematic uncertainty accounts for residual background in the physics spectrum after LAr veto for which only an estimation is available at present. See text for details.

of the string. The survival fraction of the low A/E cut shows a clear dependence on the A/E FWHM for all peak and Compton regions whereas the high A/E cut does not. This is partly because the high cut is much looser than the low A/E cut. Furthermore, the high A/E cut rejects events created in the region of high weighting potential, i.e. close to the p^+ contact. Since the A/E is much larger than 1 for such events, the survival fraction does not depend on the A/E resolution and is similar for all detectors [90].

The fluctuations in the DEP acceptance in Figure 6.12 have a different origin: while the low A/E cut is fixed to 90 % acceptance, the high A/E cut shows a mass dependence. Figure 6.13 shows the fraction of Compton and DEP events rejected by the high A/E cut as a function of the detector mass. It is observed that the smaller the detector in mass the higher the fraction of rejected events. This is consistent with expectations: since the size of the p^+ -contact and the groove are similar, the size of the volume with high A/E is similar for all BEGe detectors. Consequently, the volume fraction with high A/E increases with decreasing detector mass. The DEP acceptance of GD76B (channel 17) is exceptionally low. While the low A/E cut accepts 90 % of the DEP events, the high A/E cut rejects (6.6 ± 0.6) % of the events which is about three times as much as the average rejection. With 384 g and a diameter of 58.27 mm this

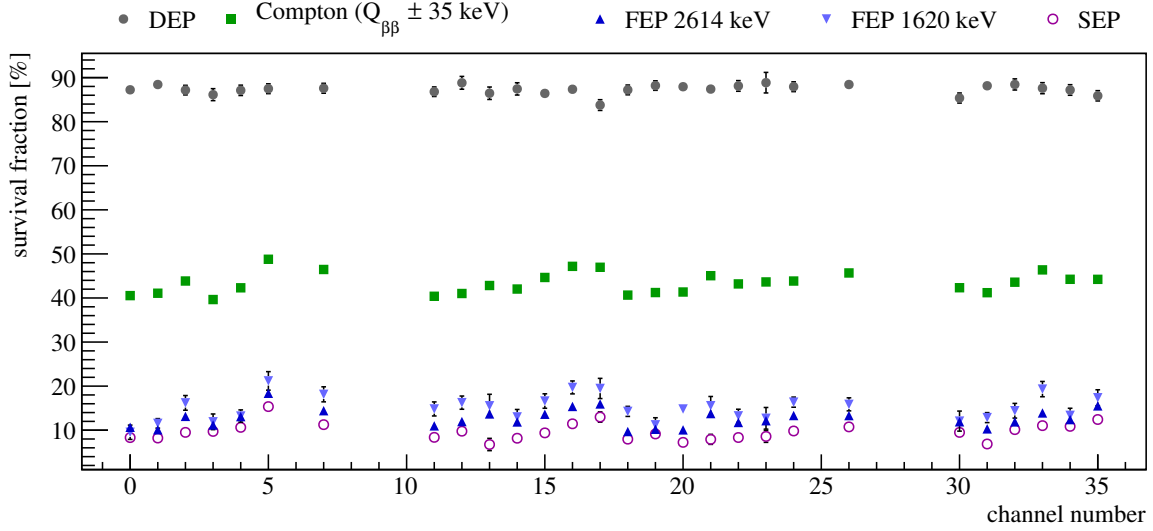


Figure 6.12: Survival efficiency in DEP (blue) and SEP (violet) of the 2615 keV γ line of ^{208}Tl , the FEP of ^{208}Tl at 2615 keV and the FEP of ^{212}Bi at 1620 keV after A/E cut. The survival fraction of Compton events in a 70 keV window centered around $Q_{\beta\beta} = 2039$ keV is shown. Only statistical uncertainties are shown. Detector names and channel number are summarized in Table C.1.

detector is by far the smallest BEGe in GERDA Phase II. No dependence on the bias voltage is found. Conical shaped detectors, denoted $\text{GD}xx\text{A}$, show similar behavior as cylindrical diodes. The difference in the rejection fraction in the DEP and Compton may originate in the different geometrical distributions of the events. Furthermore, the Compton distribution contains a high fraction of MSE. Such events created in the region of high weighting potential might be shifted to lower A/E values if enough energy is deposited in the bulk volume with low weighting potential. Five detectors show a significant difference in the DEP and Compton rejection: GD76B, GD32A, GD00A, GD89A, GD89C and GD00B. The effect seems to be higher for smaller detectors, but needs further investigation.

Table 6.2 lists the fraction of events rejected by the high A/E cut for the full BEGe data set. 2.7% of the DEP events are rejected by the high A/E cut, 2.3% in the Compton region around $Q_{\beta\beta}$. The rejection by the high A/E cut in the FEP at 1.6 MeV and 2.6 MeV are compatible within 3σ of the statistical uncertainties.

6.5 $0\nu\beta\beta$ Signal Efficiency of the A/E Cut

The signal efficiency is given by the acceptance of DEP events, the proxy for $0\nu\beta\beta$ events. The total survival fraction in the DEP is $(87.32 \pm 0.22)\%$, whereas the low A/E cut rejects $(10.00 \pm 0.21)\%$, the high cut $(2.69 \pm 0.06)\%$ respectively.

Figure 6.10 shows the difference in the A/E distributions of DEP and physics events in anti-coincidence with the LAr veto. The latter selects a sample containing $\sim 97\%$ $2\nu\beta\beta$ events [110]. Moving the A/E cut by the difference of the A/E centroids changes the DEP survival fraction by 0.80%. This gives an estimate on the uncertainty introduced by the difference between calibration and physics data.

The energy dependence of the A/E cut introduces an additional uncertainty on the signal

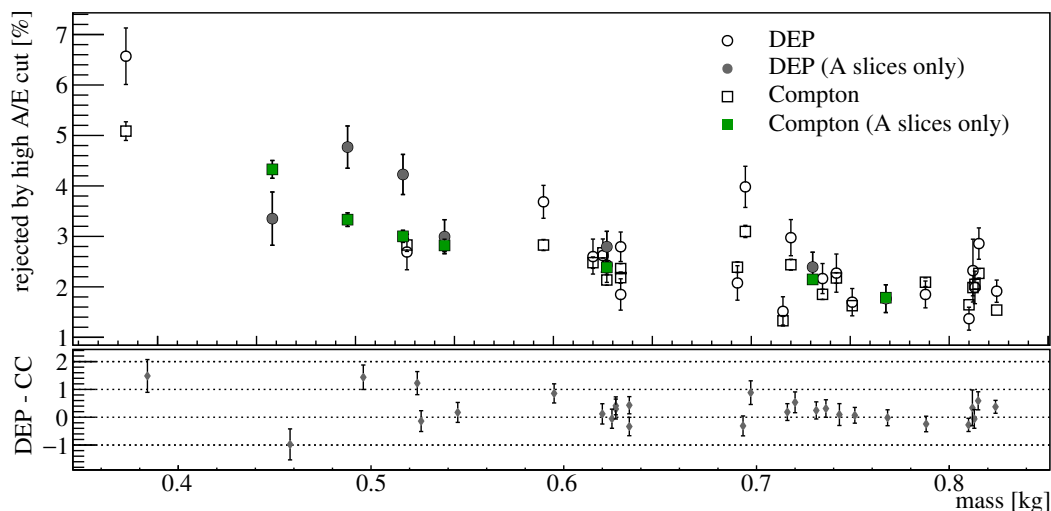


Figure 6.13: Fraction of events rejected by the high A/E cut in DEP and 2039 ± 25 keV Compton region of the 2.6 MeV γ line of ^{208}Tl as a function of detector mass. Conical shaped detectors are labeled A -slice. The panel below shows the difference between rejection fraction in DEP and Compton events. Only statistical uncertainties are shown.

efficiency. For an estimate, the A/E cut is changed within the parameter uncertainties of the $\sigma_{A/E}$ fit in Equation 6.2. This changes the DEP acceptance by 0.24% , which is the estimate for the uncertainty introduced by the energy dependence of the cut.

Furthermore, the uncertainty on the energy scale given by Equation 6.1 has to be considered. As the DEP is about 600 keV below $Q_{\beta\beta} = 2039$ keV the uncertainty is estimated by moving the A/E cut by the product of the uncertainty on the slope parameter $\times 600$ keV. This changes the DEP acceptance by 0.06% .

As discussed in Section 4.1, $0\nu\beta\beta$ and DEP events differ in their MSE fraction due to the different event topologies. Moreover, the two event types have a different geometrical distribution inside the detector. Pulse shape simulation as shortly presented in Section 4.3 are performed to compare the A/E distributions of DEP and $0\nu\beta\beta$ events. An A/E cut according to Section 6.3, i.e. the low A/E cut accepts 90% of the DEP events, is applied to the $0\nu\beta\beta$ simulation to estimate the systematic uncertainty originating in the different event topologies of DEP and $0\nu\beta\beta$ events.

The high A/E cut rejects events in the volume close to the p^+ -contact. DEP events occur predominantly close to the surface of the detector whereas $0\nu\beta\beta$ events are homogeneously distributed. This introduces a systematic difference in the rejection fraction of DEP and $0\nu\beta\beta$ events. According to the performed simulation, the high A/E cut rejects 1.03% more $0\nu\beta\beta$ than DEP events.

Uncertainty from	[%]
statistics in DEP	0.21
difference phy and cal data	0.80
energy dependence of cut	0.24
energy scale of A/E	0.06
geometrical distribution	1.03
topology of $0\nu\beta\beta$ events	2.03
total	2.43

Table 6.3: Summary of uncertainties on signal efficiency. The total uncertainty is given by the sum in quadrature of the individual contributions.

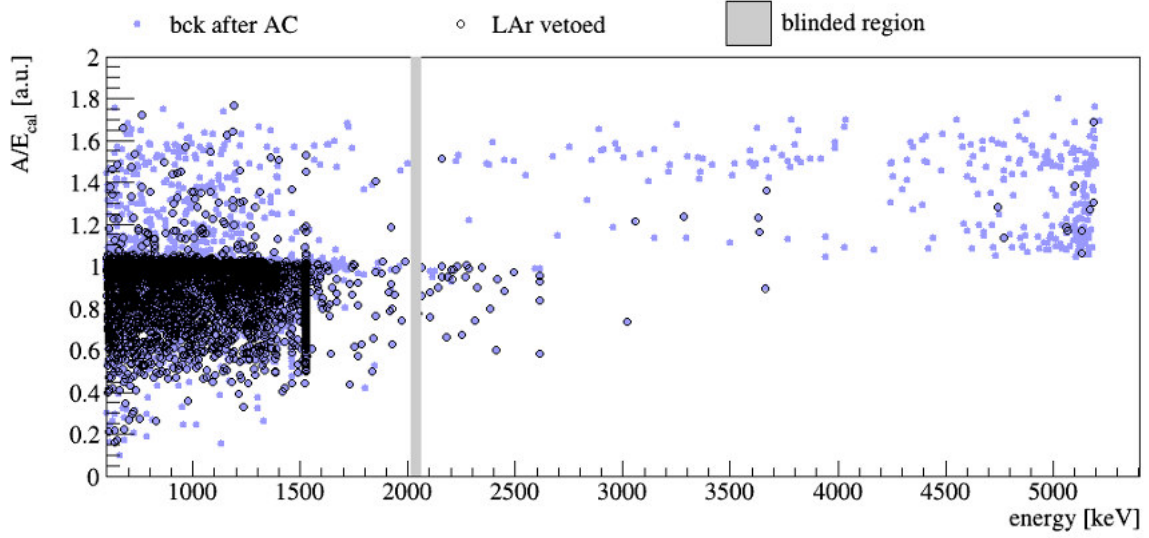


Figure 6.14: A/E spectrum of the first released Phase II BEGe data after detector-detector anti-coincidence (AC). Events in coincidence with the LAr veto are marked with a black circle. A 50 keV window centered around $Q_{\beta\beta} = 2039$ keV is blinded for analysis.

The low A/E cut rejects about a factor of 2 more $0\nu\beta\beta$ than observed $2\nu\beta\beta$ events (see Section 6.6 for details). This is a clear hint, that the performed simulations need to be revised. For lack of reliable alternatives, the simulated distribution of the event RMS (i.e. the root-mean-square of all event hits within the detector) as introduced in Chapter 4 is used to estimate the systematic uncertainty. $0\nu\beta\beta$ events typically deposit their energy within 1 mm. Figure 4.14 shows the correlation between the A/E parameter and the event RMS. As discussed in Section 4.1 the fraction of events with $\text{RMS} > 0.1$ cm is about 2% higher for the simulated $0\nu\beta\beta$ decay than for DEP events. Since this difference is similar for high RMS values and believed to originate in the event topology, it is used for the estimate of the systematic uncertainty on the signal efficiency.

Table 6.3 summarizes the statistical and considered systematic uncertainties. The final $0\nu\beta\beta$ signal efficiency is

$$\epsilon_{0\nu\beta\beta} = (87.32 \pm 0.21 (\text{stat}) \pm 2.4 (\text{sys}))\%. \quad (6.5)$$

6.6 Application of the A/E Cut on Physics Data

Figure 6.14 shows the A/E spectrum for the Phase II BEGe physics data set. A 50 keV region around $Q_{\beta\beta}$ is blinded, i.e. events in this energy window are not available for analysis until all analysis cuts are fixed. Events in coincidence with the LAr veto are marked with a black circle. The spectrum shows clear features for the different background event populations (see Section 4.4 for more details):

- **α -region:** all but one event above the endpoint of the ^{42}K spectrum, i.e. 3.5 MeV feature a high A/E . As α -particles have a range of a few μm in germanium, only α -decays on the p^+ contact, in the groove or in close vicinity are detected. Such events feature a

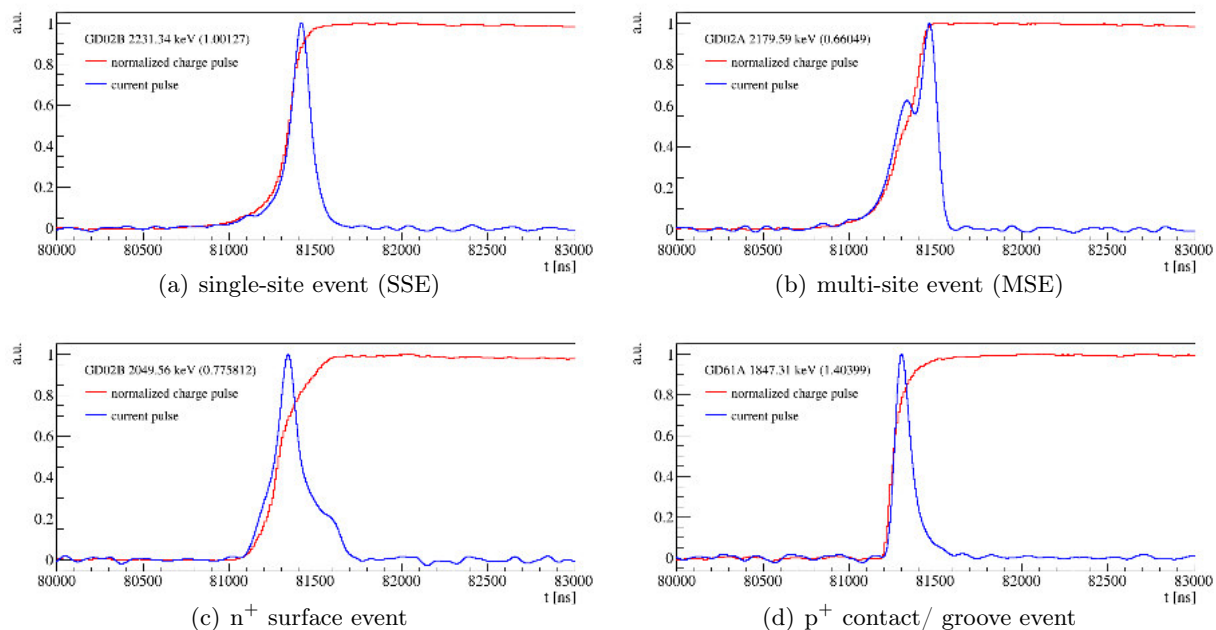


Figure 6.15: Example of events in the (2039 ± 200) keV energy window. Detector name and energy (A/E) are given. Charge pulses are smeared with a 3×50 ns moving window average. The current pulses are derived by a 10 ns differentiation. Maximum amplitude of pulses are normalized to 1 and interpolated to 1 ns.

high A/E . A/E values describe two bands around ~ 1.2 probably from events on the p^+ contact and a second band around ~ 1.6 from decays in the groove [68].

- **FEP region:** the FEPs of ^{208}Tl at 2615 keV, ^{40}K at 1461 MeV and ^{42}K at 1525 keV are clearly visible by their low A/E tail from MSE. The ^{42}K FEP is highly suppressed by the LAr veto. The corresponding Compton continuum below the FEP features many events in coincidence with the LAr veto and low A/E .
- **$Q_{\beta\beta}$ region:** The region around $Q_{\beta\beta} = 2039$ keV features a tail into the MSE and slow pulse region as well as a few high A/E events. Figure 6.15 shows a selection of events found in the energy region (2039 ± 200) keV. All event types are represented; SSE, MSE, p^+ - and n^+ -surface events.

To understand if the low A/E cut behaves similar in calibration and physics data, the survival fraction as a function of the A/E cut position is investigated. Figure 6.16 shows the survival fraction in several energy regions in the ^{228}Th calibration and the physics spectrum of the full BEGe data set for different A/E cut position. The cut position is given in $\sigma_{A/E}$ to account for the energy dependence of the cut.

Physics events in the energy region 1.0-1.3 MeV contain a high fraction of $2\nu\beta\beta$ events: before LAr veto $\sim 62\%$ [78], after 97% [110]. Besides the energy difference, $2\nu\beta\beta$ events have the same event topology as $0\nu\beta\beta$ events. Thus, the physics spectrum in coincidence with the LAr veto in the energy window 1.0-1.3 MeV provides a very clean sample of signal-like events. The selected $2\nu\beta\beta$ events show a very high acceptance. Only at cut positions close to $A/E = 1$ the survival fraction sharply decreases. This suggests a peak like distribution

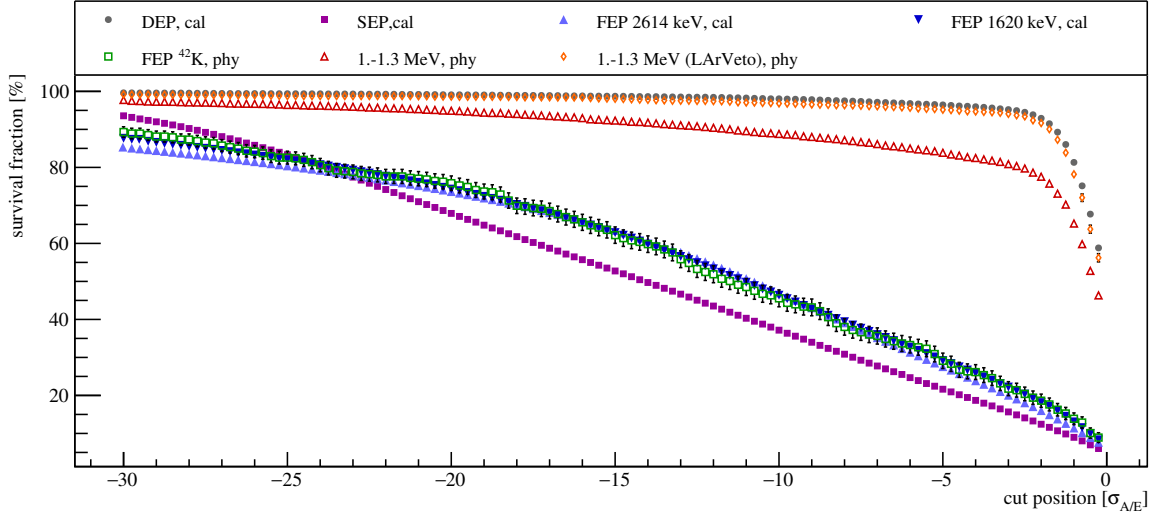


Figure 6.16: Survival fraction in the different energy regions in calibration and physics runs as a function of the low A/E cut position for the full BEGe data set. The cut position is given in $\sigma_{A/E}$ with respect to the SSE band, i.e. $A/E = 1$. $\sigma_{A/E} = 0$ corresponds to the SSE band position. The FEPs partly overlap and may be hardly visible.

centered at $A/E = 1$ or close to. The survival fraction of DEP events from calibration runs is at all cut positions in good agreement with the $2\nu\beta\beta$ acceptance. Physics events in the energy region 1.0-1.3 MeV without LAr veto applied show a reduced survival fraction. Furthermore, the survival fraction slowly decreases with a stronger cut. The observation is consistent with $2\nu\beta\beta$ and Compton events where the latter feature an MSE tail. The FEP of ^{42}K contains a high fraction of MSE. The survival fraction of the ^{42}K FEP is in good agreement with the survival fraction of the FEP and SEP recorded in calibration data.

To conclude, the A/E cut behaves similar in calibration and physics data. The $2\nu\beta\beta$ survival fraction is a meaningful cross-check of the $0\nu\beta\beta$ signal efficiency derived from DEP events of ^{228}Th calibration runs. Furthermore, the A/E analysis provides information on the background composition.

The $2\nu\beta\beta$ Spectrum

Figure 6.17 shows the physics spectrum in anti-coincidence with the LAr veto before and after PSD cut. The survival fraction of the ^{42}K FEP at 1461 keV is $(16.2 \pm 2.6)\%$ which is consistent with the FEP suppression in calibration runs. As the ^{42}K γ -ray is in coincidence with the β -decay, the FEP is highly suppressed by the LAr veto. The survival fraction of the ^{42}K FEP is $(2.9 \pm 1.2)\%$ after PSD and LAr veto.

The survival fraction of the physics events in the 1.0-1.3 MeV region in anti-coincidence with the LAr veto is $(84.2 \pm 0.8)\%$. The low A/E cut removes $(11.4 \pm 0.7)\%$ of the events, the high A/E cut $(4.5 \pm 0.5)\%$. To extract the $2\nu\beta\beta$ survival fraction the different background components in the energy region as well as the corresponding survival fraction need to be

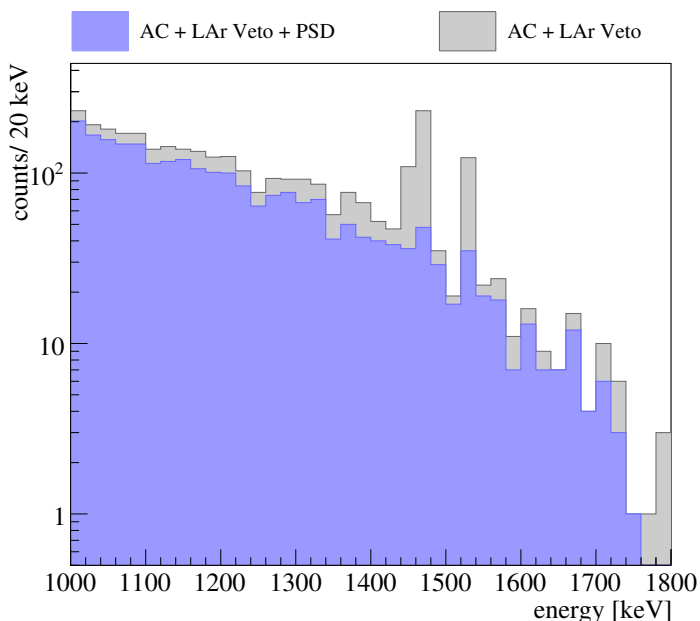


Figure 6.17: Physics spectrum in anti-coincidence with the LAr veto before and after PSD for the full BEGe data set in the $2\nu\beta\beta$ region. The LAr selects an event sample with high fraction of $2\nu\beta\beta$ events ($\sim 97\%$). FEP of ^{40}K and ^{42}K are highly suppressed by LAr and PSD. Furthermore, the spectral shape resembles the expected shape of $2\nu\beta\beta$ spectrum.

$2\nu\beta\beta$ have the same event topology than $0\nu\beta\beta$ signal events, except for the energy difference. Therefore, the survival fraction of $2\nu\beta\beta$ events is used as a cross-check of the $0\nu\beta\beta$ signal efficiency derived from DEP events from ^{228}Th calibration data.

considered. The $2\nu\beta\beta$ efficiency is given by [5]

$$\epsilon_{2\nu\beta\beta} = \frac{\epsilon_{data} - \sum_i \epsilon_i \cdot f_i}{f_{2\nu\beta\beta}} \quad (6.6)$$

where ϵ_{data} is the fraction of events in the energy region 1.0-1.3 MeV after A/E cut, f_i the fraction of background component i , ϵ_i the corresponding survival fraction and $f_{2\nu\beta\beta}$ is the fraction of $2\nu\beta\beta$ events in the energy window. At the time of writing this thesis, only an estimate of the background composition before and after LAr veto is available. In the energy range 1.0-1.3 MeV the two main background contributions are:

- ^{42}K contributing with 10% to the background [78]. After LAr veto the contribution is reduced to 1% [110].
- 24% of the events should be ^{40}K decays [78]. After LAr veto the contribution is reduced to 2% [110].

As the ^{40}K background in the energy region 1.0-1.3 MeV consists predominantly of Compton scattered events, the survival fraction is estimated to be 50%, according to ^{228}Th calibration runs discussed in Section 6.4. The fraction of γ -rays to β -decays in the ^{42}K background in the same energy region is unknown. For ^{42}K a suppression factor of 5 is assumed.

A $2\nu\beta\beta$ survival fraction of 85.8% is calculated. The low A/E cut has an acceptance of 90.5% which is in good agreement with the DEP acceptance.

Since the background contribution to the $2\nu\beta\beta$ spectrum is small and the $2\nu\beta\beta$ survival fraction is based on assumptions on the background contribution, the $2\nu\beta\beta$ efficiency is given by the survival fraction of physics events in the energy region 1.0-1.3 MeV. The presence of background reduces the $2\nu\beta\beta$ efficiency, which is expressed in a systematic uncertainty given by the difference in the efficiencies of the calculated $2\nu\beta\beta$ events and the physics events in the

region 1.0-1.3 MeV. The final $2\nu\beta\beta$ survival fraction is

$$\epsilon_{2\nu\beta\beta} = (84.2 \pm 0.8(\text{stat}) + 1.7(\text{sys}))\% \quad (6.7)$$

Events with energy deposition in the transition layer between the active and dead detector volume have a reduced energy since the charge collection is incomplete. Thus, $0\nu\beta\beta$ events in the transition layer are not reconstructed in the full energy peak. On the contrary, $2\nu\beta\beta$ events in the transition layer are shifted in energy but still counted in the continuous $2\nu\beta\beta$ spectrum. As discussed in Section 4.4 such events feature a low A/E reducing the survival fraction of the $2\nu\beta\beta$ events by 1.5% with respect to the $0\nu\beta\beta$ efficiency [68].

Correcting the survival fraction of the $2\nu\beta\beta$ events given in Equation 6.7 gives an efficiency of

$$\epsilon_{2\nu\beta\beta}^{\text{corr}} = (85.4 \pm 0.8(\text{stat}) + 1.7(\text{sys}))\% \quad (6.8)$$

This is in good agreement with the $0\nu\beta\beta$ signal efficiency given by Equation 6.5 and strengthens the validity of the signal efficiency derived using DEP events from ^{228}Th calibration data.

Suppression by Low A/E Cut

The low A/E cut highly suppresses FEP and Compton events. Figure 6.18 shows the spectrum of events rejected by the low A/E cut in the energy range 1000-1600 keV. This part of the spectrum is dominated by ^{40}K and ^{42}K . Compton edges and the FEP of ^{40}K and ^{42}K are indicated in the figure. The panel below shows the suppression by the low A/E cut in the physics spectrum. The suppression in the physics spectrum increases slightly at energies higher than the Compton edge. The FEPs are highly suppressed by the low A/E cut:

- ^{40}K FEP at 1461 keV is suppressed by $(81.7 \pm 2.7)\%$,
- ^{42}K FEP at 1525 keV is suppressed by $(84.1 \pm 1.9)\%$

The peaks are corrected for Compton background, the suppression is calculated according to Appendix A. The FEP suppression in the physics spectrum is in agreement with the rejection fraction of the 1621 keV FEP of ^{212}Bi (2615 keV FEP of ^{208}Tl) of $(83.3 \pm 0.6)\%$ ($(85.3 \pm 0.5)\%$)

The FEP's and events from γ -rays with energies higher than the corresponding Compton edge feature an increased suppression by the low A/E cut. Hence, the rejection spectrum may be used to identify γ -ray background components. However, the current statistics is too low for a background analysis based on the low A/E spectrum. This method may be used in the future to verify the background model. As the low A/E cut rejects both MSE and n^+ surface events, this technique can be further enhanced if the two event types are discriminated.

Rejection of α -particles by High A/E Cut

Figure 6.19 shows the physics spectrum above 2 MeV rejected by the high A/E cut. In the region above the ^{42}K endpoint energy, 3.5 MeV all but one event feature a high A/E and are rejected. This is consistent with α -decays as the dominant background source.

The non-scrutinized event at 3662 keV has an $A/E = 0.90$ and is in coincidence with the LAr veto. The event shape was checked by eye and is characteristic for MSE. Therefore, the event might be neutron-induced. Neutron capture in ^{40}Ar produces γ -rays of 4.1 MeV [93].

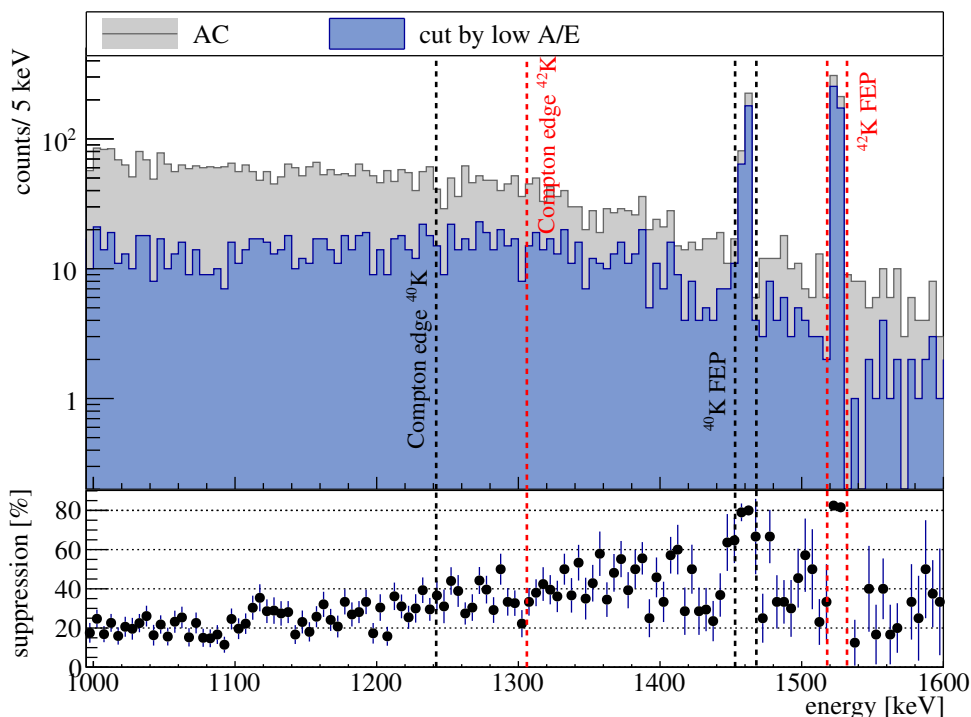


Figure 6.18: Physics spectrum after anti-coincidence cut (gray) compared to the spectrum rejected by the low A/E cut (blue). The position of the FEP and corresponding Compton edges of the ^{42}K FEP and the ^{40}K FEP are indicated. The panel below shows the suppression by the low A/E cut for the energy region. The suppression is given by the ratio of the two spectra. Uncertainties are calculated according to Appendix A.

6% of the high A/E events with energies larger than 3.5 MeV are in coincidence with the LAr veto. As this fraction is higher than the 2.3% of random coincidences [80, 111], a small fraction of α events is rejected by the LAr veto.

Figure 6.19 shows a dominant peak at 5150 keV attributed to ^{210}Po α -decays on the detector groove/ p^+ contact. The emitted α -particles have an energy of 5304 keV [93] and lose further energy in the dead layer shifting the peak to lower energies. Preliminary Monte Carlo (MC) simulations show that in addition to the ^{210}Po a flat component from ^{226}Ra and ^{222}Rn dissolved in LAr is needed to describe the physics spectrum at high energies [78]. However, this comparison can only be done above the end point of ^{42}K , i.e. 3.5 MeV. The preliminary background model [78] predicts an α contribution of $5.1 \cdot 10^{-3} \frac{\text{counts}}{\text{keV} \cdot \text{kg} \cdot \text{yr}}$ at (2039 ± 25) keV. The main contribution coming from ^{222}Rn in LAr gives a flat contribution. Three physics events around $Q_{\beta\beta}$ are rejected by the high A/E cut. This gives a background index $\text{BI} = (2.7^{+2.1}_{-1.7}) \cdot 10^{-3} \frac{\text{counts}}{\text{keV} \cdot \text{kg} \cdot \text{yr}}$ (see Section 6.7 and Figure 6.20 for the definition of the energy window). As the high A/E cut selects α - as well as β -decays from ^{42}K on the p^+ contact, a BI higher than the α only contribution is expected. Moreover, one of the three high A/E events is in coincidence with the LAr veto. Thus, the coincident event may be non- α background but ^{42}K β decay possibly with a coincident γ -ray. The high A/E spectrum suggests that the α contribution may be overestimated by the preliminary background model.

Since the high A/E cut selects a sample with very high α contribution even below 3.5 MeV, the high A/E spectrum may help to better identify α background components. The energy

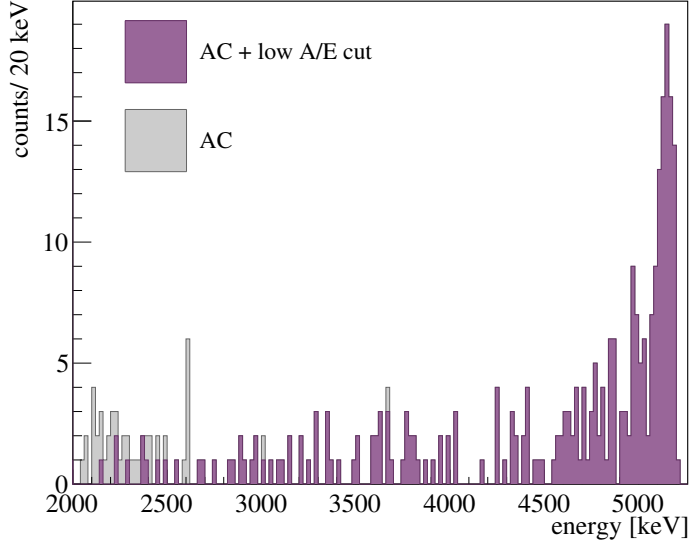


Figure 6.19: Physics spectrum after detector anti-coincidence (AC) compared to the spectrum rejected by the high A/E cut (magenta). All but one event above the endpoint energy of ^{42}K , i.e. 3.5 MeV, show a high A/E value. The high A/E spectrum selects α -decays in the detector groove or the on the p^+ contact. Thus, the spectrum can be used to constrain the α -model.

region for the α fit could be increased below 3.5 MeV which may give a better separation of a flat contribution from α -decays in the LAr and on the p^+ contact. However, at energies below 3.5 MeV ^{42}K β -decays on the p^+ contact and in the groove need to be considered. To extend the analysis to 2039 keV γ ray background from ^{214}Bi and ^{208}Tl need to be taken into account. The high A/E cut rejects about 2% in the FEP of ^{40}K and ^{42}K . This is in good agreement with the rejection fraction obtained in ^{228}Th calibration runs. Unfortunately, the exposure of the first data release is not enough for a statistically powerful analysis of the α contribution using the high A/E spectrum as shown in Figure 6.19.

6.7 Background Index of GERDA Phase II BEGe Data Set

On June 17th, the analysis cuts were frozen and the physics data in Run 54 - 64 have been unblinded. In the BEGe data set four events are found in the blinding window around $Q_{\beta\beta} \pm 25$ keV. The background index is calculated in the energy window from 1930 - 2190 keV, whereas 10 keV windows around the SEP and the ^{214}Bi FEP at 2119 keV are omitted. In addition, events in the signal region 2039 ± 5 keV are discarded. This gives a net energy interval of 230 keV for the BI calculation, referred in the following to as the BI window. Figure 6.20 shows the unblinded BEGe data set in the BI window. About half of the events are both in coincidence with the LAr veto and rejected by PSD.

After detector-detector anti-coincidence (AC), 21 events are left in the BI window:

$$\text{BI}^{\text{AC}} = (1.6 \pm 0.3) \cdot 10^{-2} \frac{\text{counts}}{\text{keV} \cdot \text{kg} \cdot \text{yr}} \quad (6.9)$$

16 out of 21 events are rejected by PSD:

$$\text{BI}^{\text{AC} \times \text{PSD}} = 3.7_{-1.7}^{+2.1} \cdot 10^{-3} \frac{\text{counts}}{\text{keV} \cdot \text{kg} \cdot \text{yr}} \quad (6.10)$$

Out of the five non-scrutinized events, four are in coincidence with the LAr veto. The BI after

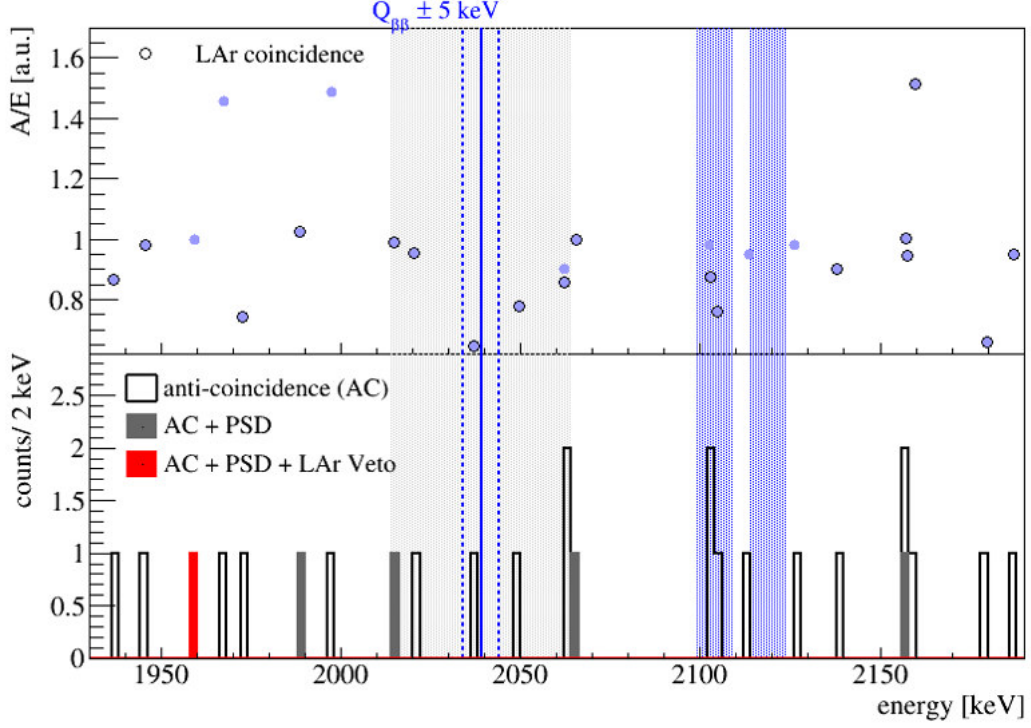


Figure 6.20: Top: A/E spectrum of the unblinded BEGe data set. The background index is calculated in the energy window 1930-2190 keV. 10 keV windows around the SEP of ^{208}Tl at 2103 keV, the FEP of ^{214}Bi at 2119 keV and $Q_{\beta\beta} = 2039$ keV are discarded. Events in coincidence with the LAr veto are marked with a black circle. **Bottom:** Energy spectrum in the 1930-2190 keV region after detector anti-coincidence (AC), after AC and PSD (gray) and after AC, PSD and LAr veto (red).

AC, PSD and LAr is

$$\text{BI}^{\text{AC}\times\text{PSD}\times\text{LAr}} = 7.5_{-4.7}^{+13.1} \cdot 10^{-4} \frac{\text{counts}}{\text{keV} \cdot \text{kg} \cdot \text{yr}} \quad (6.11)$$

The GERDA Phase II BEGe data set achieves the Phase II design goal of a BI of $10^{-3} \frac{\text{counts}}{\text{keV} \cdot \text{kg} \cdot \text{yr}}$. After LAr veto and PSD no event is left in the signal region, i.e. $Q_{\beta\beta} \pm 5$ keV.

6.8 Comparison to Phase I Background

In Phase I, the BEGe string was separated from the three semi-coaxial strings giving a less efficient AC. Therefore, the BEGe Phase I BI need to be compared to the Phase II BI before detector-detector anti-coincidence (AC). In Phase I, the BI after AC of the BEGe data set is $\text{BI} = (0.041 \pm 009) \frac{\text{counts}}{\text{keV} \cdot \text{kg} \cdot \text{yr}}$ which is a factor of 2 higher than the Phase II BEGe background before AC; $\text{BI} = (0.021 \pm 0.004) \frac{\text{counts}}{\text{keV} \cdot \text{kg} \cdot \text{yr}}$.

In Phase I, the A/E -based PSD rejects 20 out of 23 events in the BI window. This corresponds to $(87 \pm 7)\%$ of the background events with a signal efficiency of $(92 \pm 2)\%$. The rejection fraction in Phase II is compatible within the uncertainties: 16 out 21 events are scrutinized, corresponding to $(76 \pm 9)\%$. However, the Phase II signal efficiency is reduced by

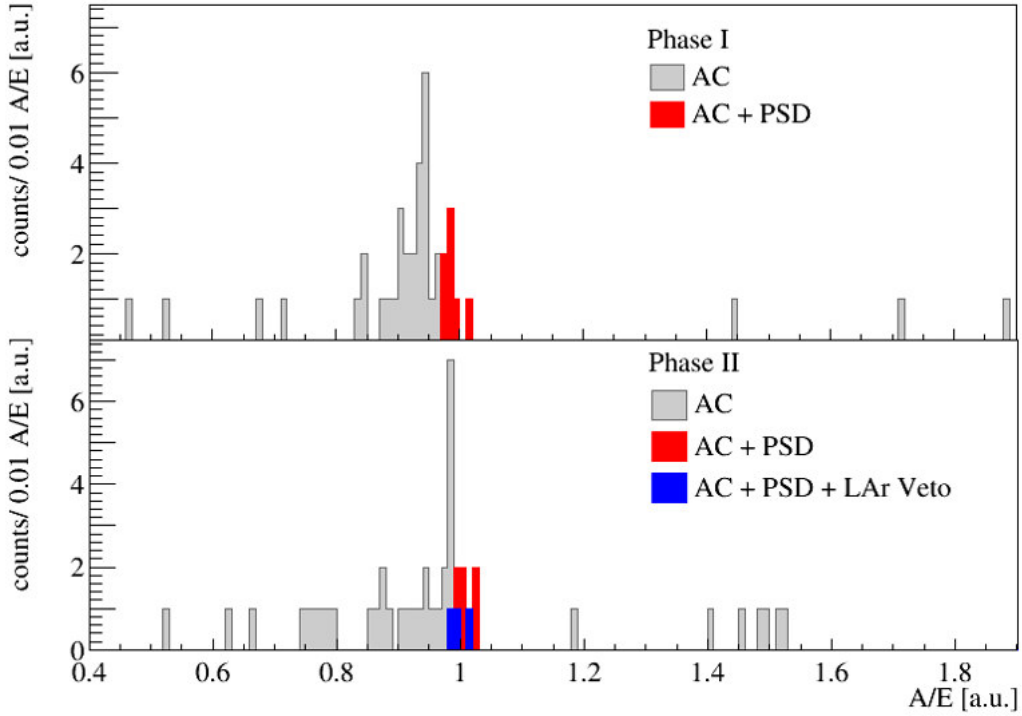


Figure 6.21: Top: Phase I A/E distribution in the energy region (2039 ± 200) keV after detector anti-coincidence (gray) and PSD (red). **Bottom:** A/E distribution in same energy window in Phase II. The blue events are in anti-coincidence with the LAr veto.

5% compared to Phase I.

In Phase I, about 55% of the events in the ROI are ^{42}K decays on the n^+ surface [69]. Other background contribution in the $Q_{\beta\beta}$ region is considerably small: the contribution from α -decays is estimated to 4%, from ^{214}Bi 13% and from ^{228}Tl 11%. The top panel of Figure 6.21 shows the A/E distribution in a 400 keV window centered at $Q_{\beta\beta}$. The distribution features a peak-like structure which is compatible with ^{42}K decays on the detectors surface. The Phase I A/E cut position falls into the minimum of the A/E distribution shown in Figure 6.21. A loose cut is applied, i.e. a high signal efficiency is kept, since the exposure of the BEGe Phase I data set is small, and thus the expected background.

The bottom panel in Figure 6.21 shows the A/E distribution in the 400 keV energy region around $Q_{\beta\beta}$ for the Phase II BEGe data set: the distribution peaks around $A/E = 1$, the peak like structure around $A/E \approx 0.95$ is absent. This suggests that the main background contribution in Phase II is γ induced. A preliminary background model suggests a contribution of 24% from ^{42}K decays only, 19% from ^{208}Tl and 17% from ^{214}Bi (compare Table 3.4). The reduction of the β -component may originate in the increased detector dead layer (DL) in Phase II: the average DL of the Phase I BEGe detectors is ~ 0.9 mm, in Phase II ~ 1 mm [112]. Furthermore, after the diode production in 2012 and until the deployment in the GERDA cryostat in 2015, the BEGe detectors were kept most of the time at room temperature and the DL is expected to have grown. In order to achieve the required BI of $10^{-3} \frac{\text{counts}}{\text{keV} \cdot \text{kg} \cdot \text{yr}}$ a stronger low A/E cut with 90% acceptance of DEP events is applied.

6.9 Summary

The first GERDA Phase II data release consists of Run 53 - 64. The Phase II BEGe data set is selected according to the applicability of the A/E analysis. This data set has an exposure of 5.83 kg·yr corresponding to 94% of the total BEGe data. A blind analysis is performed, i.e. events in the energy region $Q_{\beta\beta} \pm 25$ keV are not available for analysis.

Weekly ^{228}Th calibration runs are used to calibrate the A/E cut. Events in the DEP of the ^{208}Tl γ -line are used as a proxy for $0\nu\beta\beta$ events. Due to the high rate in calibration runs, the data feature a high fraction of pile-up events which are not present in physics data. Therefore, an additional cut to reject pile-up events is applied to calibration data. This ensures that the calibration data set is as close as possible to the physics data.

A/E values are corrected for instabilities during data acquisition. Most of the observed instabilities are attributed to changes in the hardware or DAQ system. However, neither a Phase I-like exponential decrease of A/E nor an increase of A/E during the calibration is observed. A/E values are corrected for an energy dependence, such that the SSE band is centered at $A/E = 1$. As the A/E cut is defined according to the SSE band, the A/E values are normalized to the mean of the A/E distribution in the DEP. After the A/E corrections, calibration and physics data are in very good agreement. The LAr veto selects a high sample of signal-like events in the energy region 1.0-1.3 MeV of the physics spectrum: 97% of the events are $2\nu\beta\beta$ decays [110]. The centroid of the A/E distribution of $2\nu\beta\beta$ and DEP events agree better than 0.1% which validates the applied corrections.

The A/E resolution of the individual BEGe detectors differ by up to a factor of 2. Therefore, the A/E cut is channel-based. A two-sided PSD cut is applied: the low A/E cut is given by 90% acceptance of DEP events, the high A/E cut is chosen twice as loose. Due to the high noise the A/E distribution broadens significantly at lower energies. The A/E cut is energy dependent following the broadening derived from calibration data. This ensures that the survival efficiency of $2\nu\beta\beta$ events derived from physics events at 1.0-1.3 MeV can be used as a cross-check of the $0\nu\beta\beta$ signal efficiency obtained from the acceptance of DEP events.

The background rejection of the A/E cut is tested on the acceptance of ^{208}Tl and ^{212}Bi in calibration runs. The A/E cut rejects about 55% of Compton background from ^{208}Tl around $Q_{\beta\beta}$. The FEP of ^{208}Tl and ^{212}Bi are accepted with 15% only. It is observed that the acceptance of the high A/E depends on the detector mass. No difference between conical shaped and classical cylindrical shaped BEGe detectors is found.

To understand if the A/E cut behaves similar in calibration and physics data, the survival efficiency as a function of the A/E cut is investigated. The acceptance of the ^{42}K FEP is in very good agreement with the acceptance of calibration FEP's. Both DEP from calibration data and the $2\nu\beta\beta$ sample from physics data show the same behavior. This further validates the applied cut and shows that DEP events are a good proxy for $0\nu\beta\beta$ events.

The A/E physics spectrum shows the expected features for the different event populations: α -decays on the p^+ contact and in the groove are characterized by a high A/E . The FEP of ^{40}K and ^{42}K show strong low A/E tails. In the ROI, typical MSE and n^+ surface events with a low A/E are observed.

The A/E analysis can give important input to the background model or may be used as a cross-check. The high A/E spectrum selects a sample of events with high α -event fraction and might suggest that the α contribution in the preliminary background model may be overestimated.

The signal efficiency is derived from the DEP acceptance only. The $0\nu\beta\beta$ signal efficiency is

$$\epsilon_{0\nu\beta\beta} = (87.3 \pm 0.2(\text{stat}) \pm 2.4(\text{sys}))\%.$$

Which is in very good agreement with the acceptance of $2\nu\beta\beta$ events, $\epsilon_{2\nu\beta\beta}^{\text{corr}} = (85.4 \pm 0.8(\text{stat}) + 1.7(\text{sys}))\%$. The uncertainty on the signal efficiency is dominated by the difference in the topologies of $0\nu\beta\beta$ and DEP events.

Before detector anti-coincidence (AC), LAr veto and PSD the background index of the BEGe data set is $\text{BI} = (2.1 \pm 0.4) \cdot 10^{-2} \frac{\text{counts}}{\text{keV} \cdot \text{kg} \cdot \text{yr}}$. This is about a factor of 2 smaller than the BI in Phase I.

After AC, PSD and LAr a

$$\text{BI}^{\text{AC} \times \text{PSD} \times \text{LAr}} = 7.5_{-4.7}^{+13.1} \cdot 10^{-4} \frac{\text{counts}}{\text{keV} \cdot \text{kg} \cdot \text{yr}}$$

for the Phase II BEGe data set is achieved.

After LAr veto and PSD no event is left in the $0\nu\beta\beta$ signal region, i.e. $Q_{\beta\beta} \pm 5 \text{ keV}$.

Limit on the Half-life of $0\nu\beta\beta$ Decay of ^{76}Ge

In this chapter the lower limit on the half-life of the $0\nu\beta\beta$ decay of ^{76}Ge based on the full data collected in GERDA Phase I and the first Phase II release is determined.

Section 7.1 covers the data sets used in the statistical analysis. The profile likelihood method and the performed frequentist analysis used to extract the half-life limit is presented in Section 7.2.

The central experimental result, i.e. the new limit on the half-life of the $0\nu\beta\beta$ decay of ^{76}Ge is presented in Section 7.3. Furthermore, the claim of the observed $0\nu\beta\beta$ decay of ^{76}Ge with a half-life of $T_{1/2} = 1.19 \cdot 10^{25}$ years [62] is tested. The achieved experimental sensitivity of the first GERDA Phase II data release is highlighted.

7.1 Data Sets

As of June 2016 the GERDA data sets include in total six subsets from Phase I and Phase II. The subdivision is based on the different background indices (BI) and energy resolutions:

- **Phase I golden/silver/BEGe:** the Phase I physics data which were recorded with enriched coaxial and BEGe detectors from November 2011 until May 2013. In a short period after the insertion of the BEGe string in July 2012, the background for the semi-coaxial detectors increased. Therefore, the coax physics data sets are split into the *golden* and *silver* (increased BI) data set. For coaxial detectors a pulse shape analysis based on a neural network is applied with a signal efficiency of $\epsilon_{PSD} = 0.83 \pm 0.03$ [83]. Due to the improved energy resolution and enhanced PSD (i.e. lower BI) compared to the coaxial detectors, the BEGe data is treated separately. The PSD of the BEGe data set has been presented in Section 4.5: the signal efficiency is $\epsilon_{PSD} = 0.92 \pm 0.02$. The three data sets have already been published in [6]. A new energy reconstruction is applied to the data sets [113] which improves the energy resolution and shifts the physics events independently in energy with respect to [6].
- **Phase I extra:** after the unblinding of Phase I, additional physics data were taken with the coaxial detectors until September 2013. The collected exposure is $1.9 \text{ kg} \cdot \text{yr}$. The same pulse shape analysis as in Phase I is applied with a signal efficiency of $\epsilon_{PSD} = 0.83 \pm 0.03$. The data were unblinded together with the first Phase II data in June 2016.

data set	exposure [kg · yr]	$\langle\epsilon\rangle \times \epsilon_{LAr} \times \epsilon_{PSD}$	FWHM [keV]	BI [$10^{-3} \frac{\text{counts}}{\text{keV} \cdot \text{kg} \cdot \text{yr}}$]
Phase I golden	17.9	0.57 ± 0.03	4.3 ± 0.2	11 ± 2
Phase I silver	1.3	0.57 ± 0.03	4.3 ± 0.2	30 ± 10
Phase I BEGe	2.4	0.66 ± 0.02	2.7 ± 0.2	5_{-3}^{+4}
Phase I extra	1.9	0.58 ± 0.04	4.2 ± 0.2	4_{-2}^{+5}
Phase II coax	5.0	0.53 ± 0.05	4.0 ± 0.2	3_{-1}^{+3}
Phase II BEGe	5.8	0.60 ± 0.01	3.0 ± 0.2	$0.7_{-0.5}^{+1.3}$

Table 7.1: Summary of the GERDA data sets. See Equation 7.2 for definition of the exposure averaged efficiency. The signal efficiency of the PSD method as well as the achieved BI of the Phase I BEGe data set is presented in Section 4.5 and of the Phase II BEGe data set in Sections 6.5 and 6.7. Numbers taken from [114].

- **Phase II Coax/ BEGe:** physics data recorded with coaxial and BEGe-type detectors in GERDA Phase II from December 2015 until May 2016. The LAr veto introduces a dead time of 98% [80, 81, 82], denoted ϵ_{LAr} . For BEGe detectors the applied PSD method is presented in Chapter 6, the PSD signal efficiency is $\epsilon_{PSD} = 0.87 \pm 2.4$. For semi-coaxial detectors a PSA method similar to Phase I is applied, the signal efficiency is $\epsilon_{PSD} = 0.79 \pm 0.05$.

The number of $0\nu\beta\beta$ decays in each data set is given by [114]

$$N^{0\nu} = \frac{\ln 2 \cdot N_A}{m_{76}} \frac{\mathcal{E}}{T_{1/2}^{0\nu}} \cdot \langle\epsilon\rangle \cdot \epsilon_{PSD} \cdot \epsilon_{LAr}, \quad (7.1)$$

where $\mathcal{E} = \sum_i M_i \cdot t_i$ is the total exposure, the index i runs over all detectors, M_i is the detector mass, t_i the specific observation time, N_A is Avogadro's constant, m_{76} is the molar mass of ^{76}Ge and $T_{1/2}^{0\nu}$ the half-life of the $0\nu\beta\beta$ decay of ^{76}Ge . The exposure averaged efficiency is given by

$$\langle\epsilon\rangle = \frac{\sum_i f_{AV,i} \cdot f_{76,i} \cdot M_i \cdot t_i \cdot \epsilon_{FEP,i} \cdot \frac{m_{76}}{m_{enr,i}}}{\mathcal{E}}, \quad (7.2)$$

where the sum over all detectors in the data set is formed; $f_{AV,i}$ is the active volume fraction ($\sim 86\%$ for coaxial and $\sim 89\%$ for BEGe [82]), $f_{76,i}$ is the enrichment fraction ($\sim 86\%$), $\epsilon_{FEP,i}$ is the efficiency to detect a $0\nu\beta\beta$ event in the full energy peak ($\sim 92\%$ [68]) and $m_{enr,i}$ is the average molar mass. Table 7.1 summarizes the exposure, efficiencies, energy resolution and background indices for the six GERDA data sets.

Figure 7.1 shows the physics spectra around $Q_{\beta\beta} = 2039\text{keV}$ for the combined Phase I (golden/silver/BEGe/extra), the Phase II enriched coaxial and Phase II enriched BEGe data sets. The number of expected and observed events in the signal region, i.e. $Q_{\beta\beta} \pm 5\text{keV}$, are compatible (see Table 7.2).

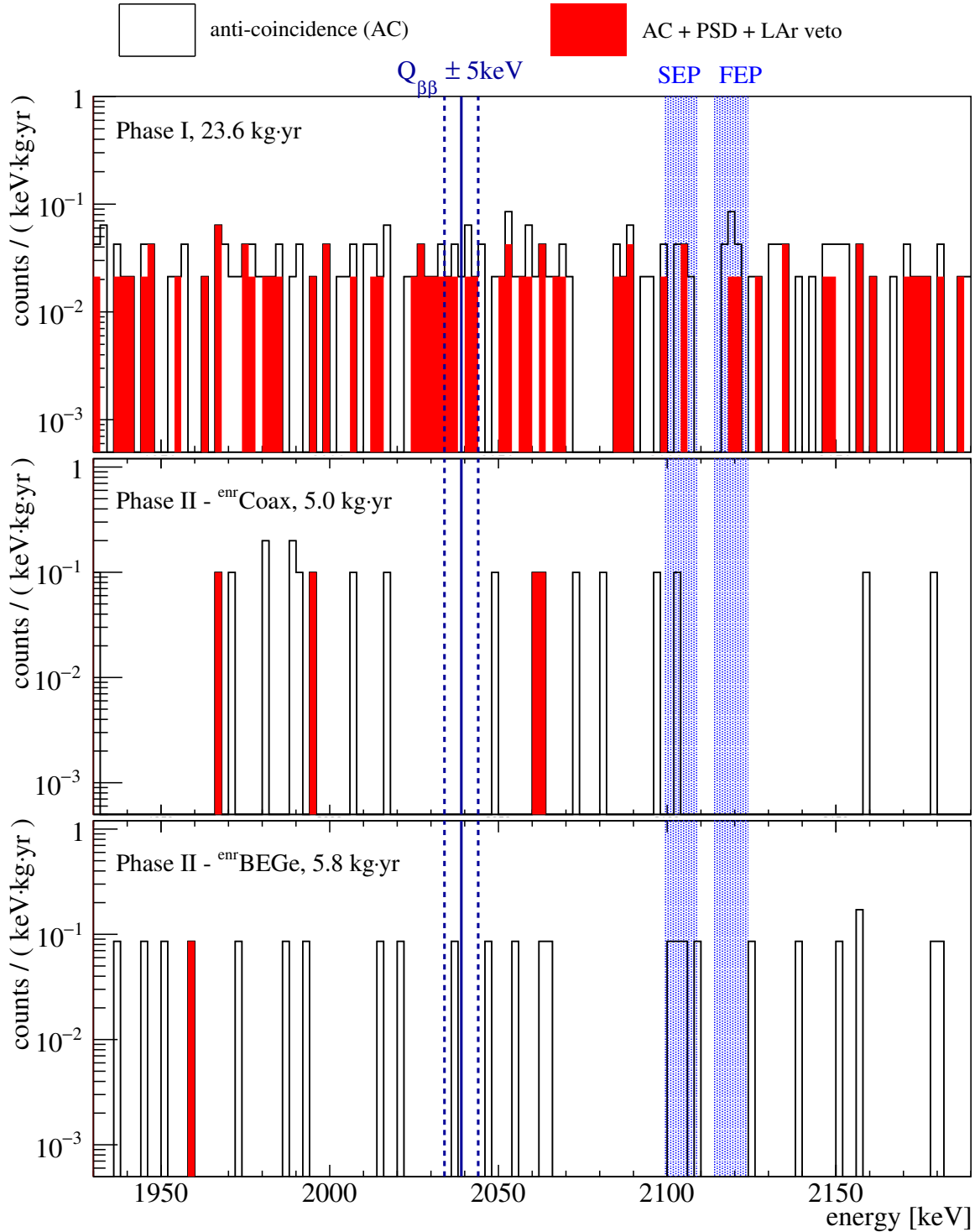


Figure 7.1: Unblinded physics spectra for the combined Phase I (golden/silver/BEGe/extra), Phase II coax and Phase II BEGe data sets around the region of interest. Events after detector-detector anti-coincidence (AC), PSD and LAr veto are shown in red. 10 keV regions around the SEP of the 2.6 MeV γ -line of ^{208}Tl at 2104 keV and the FEP of ^{214}Bi at 2119 keV are omitted.

events in $Q_{\beta\beta} \pm 5 \text{ keV}$	Phase I				Phase II	
	golden	silver	BEGe	extra	Coax	BEGe
expected	2.0	0.4	0.1	0.1	0.2	<0.1
observed	3	1	0	0	0	0

Table 7.2: Number of expected and observed events in the signal region, i.e. $Q_{\beta\beta} = 2039 \pm 5 \text{ keV}$ after PSD and LAr. Expected events are given according to the background indices and exposures in Table 7.1.

7.2 The Profile Likelihood Method

As discussed in Chapter 3 the background is assumed to have a flat shape in a wide region around $Q_{\beta\beta}$. Therefore, the energy spectra in the range 1930-2190 keV (Figure 7.1) are modeled with a flat background, b , and a Gaussian signal centered at $Q_{\beta\beta} = 2039 \text{ keV}$, with a width according to the energy resolution, $\sigma_E = \text{FWHM}/2.355$. The probability distribution function (pdf) is defined as [115]

$$f(E | b, 1/T_{1/2}^{0\nu}) = \frac{1}{240 \text{ keV} \cdot b + N^{0\nu}} \left(b + \frac{N^{0\nu}}{\sqrt{2\pi} \cdot \sigma} e^{-\frac{(E - Q_{\beta\beta})^2}{2\sigma^2}} \right), \quad (7.3)$$

where $N^{0\nu} (\propto \frac{1}{T_{1/2}^{0\nu}})$ is the number of signal events given by Equation 7.1. The pdf is normalized to the expected number of events $\mu = b \cdot 240 \text{ keV} + N^{0\nu}$.

An extended unbinned likelihood fit is performed. The likelihood function is defined as

$$L(b, 1/T_{1/2}^{0\nu}) = \frac{\mu^N \cdot e^{-\mu}}{N!} \prod_{i=0}^N f(E_i | b, 1/T_{1/2}^{0\nu}), \quad (7.4)$$

where i runs over all observed events in the energy window 1930-2190 keV, excluding the regions of the ^{214}Bi peak and the SEP (*unbinned*). The (*extended*) Poisson term considers the fact that the number of observed events is Poisson distributed and may differ from the expected number of events.

All six GERDA data sets from Table 7.1 are included in the fit. The full likelihood function is given by

$$L(b, 1/T_{1/2}^{0\nu}) = \prod_k L_k(b_k, 1/T_{1/2}^{0\nu}) = \prod_k \frac{\mu_k^{N_k} \cdot e^{-\mu_k}}{N_k!} \prod_{\text{events}} f(E | b_k, 1/T_{1/2}^{0\nu}), \quad (7.5)$$

where k runs over the different data sets. The fit has seven free parameters: the background indices, b_k , and a common $\frac{1}{T_{1/2}^{0\nu}}$ with the physical constraints $b_k, \frac{1}{T_{1/2}^{0\nu}} \geq 0$. For each data set the systematic uncertainties on the peak position ($\pm 0.2 \text{ keV}$), the energy resolution and efficiency (see Table 7.1) are included as pull terms in the likelihood function.

Since the parameter of interest is $1/T_{1/2}^{0\nu}$ and the background indices b_k are treated as (unknown) nuisance parameters, the profile likelihood ratio λ is defined as [115]

$$\lambda(1/T_{1/2}^{0\nu}) = \frac{L(\widehat{b}_k, 1/T_{1/2}^{0\nu})}{L(\widehat{b}_k, 1/\widehat{T}_{1/2}^{0\nu})}. \quad (7.6)$$

\widehat{b}_k is the conditional maximum likelihood estimator for b_k , i.e. the value for which L is maximized given a fixed $1/T_{1/2}^{0\nu}$. \widehat{b}_k and $1/\widehat{T}_{1/2}^{0\nu}$ are the maximum likelihood estimators, i.e. L is maximized for b_k and $1/T_{1/2}^{0\nu}$ being free parameters.

In the frequentist approach, probability is interpreted as the frequency to find a certain results in a large number of trials. The performed analysis follows the method described by Cowen et al. [116] in which a frequentist test statistics is constructed using a profile likelihood ratio. The test statistic is defined as

$$t_{1/T_{1/2}^{0\nu}}(1/T_{1/2}^{0\nu}) = -2 \log \lambda(1/T_{1/2}^{0\nu}). \quad (7.7)$$

The agreement (or disagreement) of the observed data and a given hypothesis (i.e. a given b_k and signal strength according to $1/T_{1/2}^{0\nu}$) is quantified by the p-value:

$$p = \int_{t_{1/T_{1/2}^{0\nu}}^{obs}}^{\infty} f(t_{1/T_{1/2}^{0\nu}} | 1/T_{1/2}^{0\nu}) dt_{1/T_{1/2}^{0\nu}}, \quad (7.8)$$

where $t_{1/T_{1/2}^{0\nu}}^{obs} = -2 \log \lambda(1/T_{1/2}^{0\nu})$ for the observed data. $f(t_{1/T_{1/2}^{0\nu}} | 1/T_{1/2}^{0\nu})$ is the pdf of the test statistics for a given $1/T_{1/2}^{0\nu}$ and is determined by Monte Carlo simulations. For a given $1/T_{1/2}^{0\nu}$, the p-value gives the probability to find a test statistic t higher than the observed $t_{1/T_{1/2}^{0\nu}}^{obs}$. Thus, low p-values correspond to low agreement of data and hypothesis.

7.3 New Limit on the Half-life of $0\nu\beta\beta$ Decay of ^{76}Ge

Figure 7.2 shows the distribution of $-2\log\lambda(1/T_{1/2}^{0\nu})$ for the observed data (red points). The best fit is obtained for zero signal counts. The two-sided 90% coverage limit is given by the probability distribution of the test statistic t . For a fixed $1/T_{1/2}^{0\nu}$ 10^6 MC simulations are generated according to the parameters given in Table 7.1 and the test statistic $t_{1/T_{1/2}^{0\nu}}$ is calculated as defined in Equation 7.7. The limit corresponds to the value of the test statistic, for which 90% of the generated MC simulations have a t smaller (i.e. better) than the threshold (black distribution in Figure 7.2). Per definition this corresponds to a p-value of $p=0.1$; for larger $1/T_{1/2}^{0\nu}$ the probability to obtain the observed data is less than 10%. The 90% C.L. threshold corresponds to $t = 2.79$.

For the combined Phase I and Phase II data set the 90% C.L. upper limit on $1/T_{1/2}^{0\nu}$ is 0.19, corresponding to 1.9 signal events. The derived lower limit on the half-life of $0\nu\beta\beta$ decay of ^{76}Ge is

$$T_{1/2}^{0\nu} > 5.3 \times 10^{25} \text{ yr at 90\% C.L.} \quad (7.9)$$

Assuming the exchange of light Majorana neutrinos, the limit on the half-life of ^{76}Ge converts into an upper limit on the effective Majorana neutrino mass (see Equation 2.19) of

$$m_{0\nu} < (0.15 - 0.32) \text{ eV.} \quad (7.10)$$

For the calculation a nuclear matrix element for ^{76}Ge between 2.8-6.0 (see [117] and reference therein) and a phase space factor of $2.34 \cdot 10^{-15} \text{ yr}^{-1} \cdot g_A$ ($g_A = 1.27$) [118] is assumed.

The full GERDA data is tested against the hypothesis of a $0\nu\beta\beta$ decay half-life of $T_{1/2}^{0\nu} = 1.19 \cdot 10^{25} \text{ yr}$ as claimed in [62]. According to the claim we expect 9 signal events. The hypothesis test yields a p-value of $< 10^{-3}$ at $1/T_{1/2}^{0\nu} = 0.84$. Thus, the claim is rejected at $> 99.9\%$ C.L., i.e. with three standard deviations C.L.

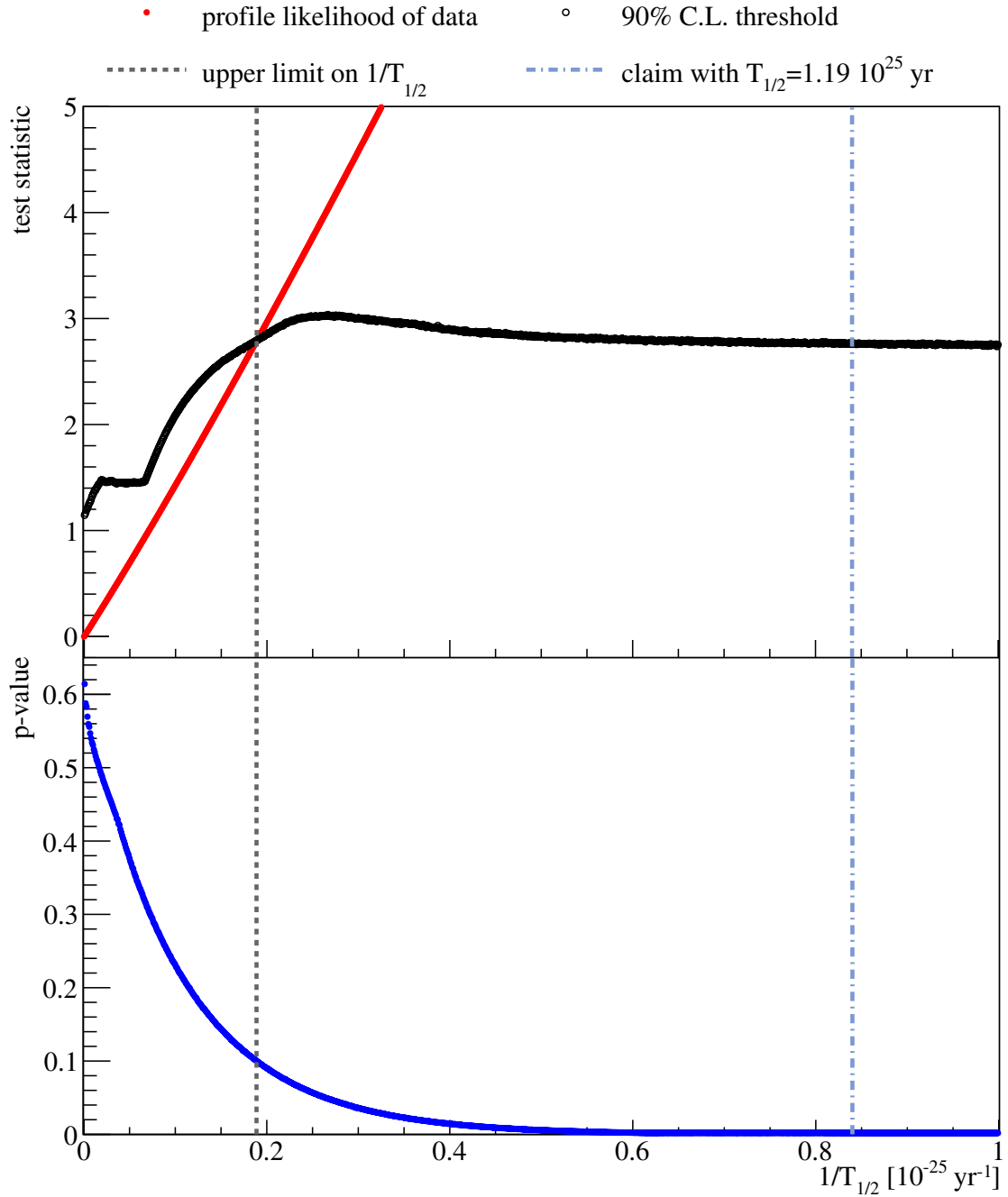


Figure 7.2: $-2 \log \lambda(1/T_{1/2}^{0\nu})$ for the observed Phase I and Phase II data (red). The two-sided 90% coverage limit is given by the probability distribution of the test statistic t as defined in Equation 7.7. The corresponding p-value of the data is shown in the bottom panel. See text for details.

data set	sensitivity [10^{25} yr]	exposure [kg · yr]
Phase I	2.6	23.6
Phase II	2.4	10.8
Phase I + II	4.0	34.4

Table 7.3: Median sensitivity on $T_{1/2}^{0\nu}$ for Phase I (golden/silver/BEGe/extra), Phase II (BEGe/Coax) and combined Phase I and Phase II data sets.

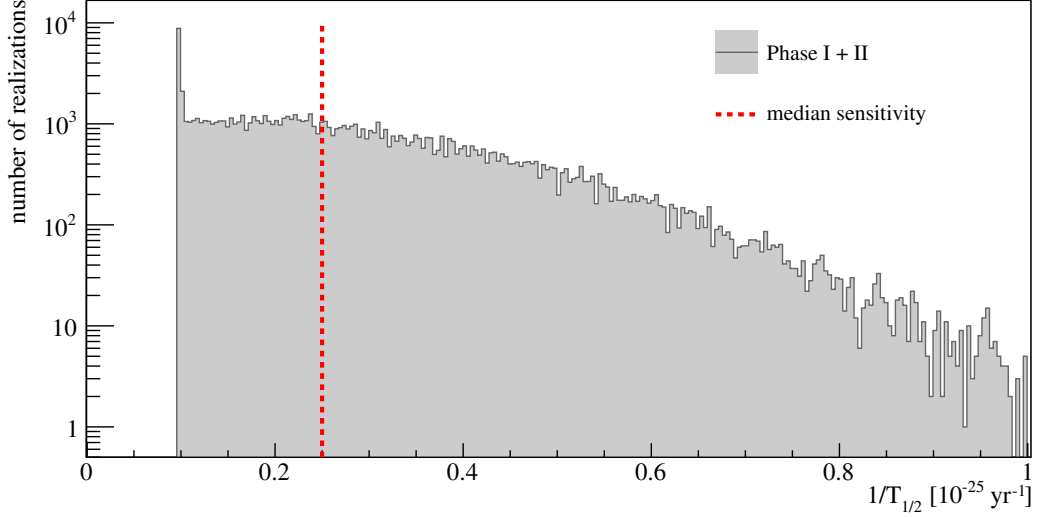


Figure 7.3: Median sensitivity on $1/T_{1/2}^{0\nu}$ for the combined Phase I and Phase II data sets. See text for details.

Median Sensitivity

To determine the experimental sensitivity 10^5 MC simulations are generated according to the BI in Table 7.1 and zero signal counts. The sensitivity is given by the median of the obtained 90% C.L. limits on $1/T_{1/2}^{0\nu}$ in the MC (see Figure 7.3): The median sensitivity of the combined GERDA Phase I and Phase II data on the lower limit of the half-life of $0\nu\beta\beta$ decay of ^{76}Ge assuming no signal is

$$4.0 \cdot 10^{25} \text{ yr at 90\% C.L.} \quad (7.11)$$

The median sensitivity of the first Phase II data is $2.4 \cdot 10^{25}$ yr, similar to the Phase I sensitivity, $2.6 \cdot 10^{25}$ yr. However, the first Phase II data have an exposure of 10.8 kg · yr only, which is about a factor of 2 less than in Phase I (compare Table 7.3). This demonstrates the large impact of the BI on the sensitivity and proves the GERDA Phase II concept.

Summary and Discussion

The GERDA experiment searches for the neutrinoless double beta ($0\nu\beta\beta$) decay of ^{76}Ge using bare, isotopically enriched high purity germanium (HPGe) detectors operated in liquid argon (LAr). The aim of the GERDA experiment is to explore half-lives of the $0\nu\beta\beta$ decay up to the range of 10^{26} yr.

The experimental signature of $0\nu\beta\beta$ decay is a mono-energetic peak at the Q-value of the decay. In the case of ^{76}Ge the Q-value is $Q_{\beta\beta} = 2039$ keV. The experimental sensitivity on the detection of $0\nu\beta\beta$ -decay crucially depends on the background index (BI), i.e. the number of background events normalized to the collected exposure and the energy region of the observation. Any process that can deposit part of its energy in the signal region and, thus, fake a $0\nu\beta\beta$ event is considered as background, e.g. radioactive decays with Q-values larger than ^{76}Ge or muons.

The experimental setup is optimized to passively shield the HPGe detectors against external background. Furthermore, active background reduction techniques are applied. Such techniques are based on instrumentation of the experiment and data analysis. The muon veto is such an active background reduction technique: the water tank, housing the LAr cryostat with the detector array, is equipped with photomultiplier tubes (PMTs) to detect the Cherenkov light produced by muons passing through the detector [73]. Further discrimination of signal ($0\nu\beta\beta$ -) from background events, e.g. γ -rays, is based on the different interaction of electrons and γ -rays with the detector material and the resulting spatial distribution of the energy deposition: signal-like events deposit their energy very locally within a single detector, so-called single-site events (SSE), while background events may do so in several locations, resulting in multi-site events (MSE). SSE are discriminated against MSE by means of pulse shape analysis (PSA), i.e. the analysis of the time structure of the germanium detector signals. Moreover, the technique identifies α - and β -decays on the detector surface.

The GERDA experiment uses two different types of HPGe detector designs: semi-coaxial detectors previously used in the Heidelberg-Moscow [1] and IGEX [2] experiments and new Broad Energy Germanium (BEGe) detectors. The latter type features an improved energy resolution and enhanced pulse shape discrimination (PSD) compared to the semi-coaxial design. The work presented in this thesis focuses on BEGe detectors and their performance in GERDA Phase I and Phase II, with special focus on PSA. For BEGe detectors, a PSA based on a single parameter, the ratio of the maximum amplitude of the current pulse over the energy (A/E), has been developed in [3] for prototype BEGe detectors operated in vacuum cryostat.

Events in the double escape peak (DEP) of the 2.6 MeV γ -line of ^{208}Tl have single-site energy deposition and thus can be used as a proxy for $0\nu\beta\beta$ events.

The GERDA experiment proceeds in two phases: in Phase I of the experiment five new enriched BEGe detectors with a total mass of 3.6 kg and eight semi-coaxial detectors with 17.7 kg were installed. This was the first time that the BEGe technology was used in the search for $0\nu\beta\beta$ decay, and that BEGe detectors were operated over a long period in liquid argon (LAr): the new BEGe detectors proved to be a reliable technology with improved energy resolution and enhanced discrimination of signal- from background-like events compared to semi-coaxial detectors.

In this thesis the A/E analysis as applied to the Phase I BEGe data set is presented. The A/E cut is calibrated using (bi-)weekly ^{228}Th calibration data. Unexpected time instabilities of the A/E parameter in-between and during the calibration runs are observed and corrected for. A blind analysis is performed, i.e. events in a symmetric 40 keV energy window around $Q_{\beta\beta}$ are not available for the analysis until all analysis cuts are fixed. A time and energy independent A/E cut is applied to the Phase I BEGe data. 83 % of the background events in a 232 keV region around $Q_{\beta\beta}$ are rejected with a high signal efficiency, $\epsilon_{PSD} = (92.1 \pm 1.9) \%$. The achieved $\text{BI} = (0.5_{-0.3}^{+0.4}) \cdot 10^{-2} \frac{\text{counts}}{\text{keV} \cdot \text{kg} \cdot \text{yr}}$ provides an improvement of a factor 10 with respect to previous germanium based $0\nu\beta\beta$ experiments [62]. One event at 2036.6 keV is found in the region of interest (ROI), i.e. $Q_{\beta\beta} \pm 4 \text{ keV}$. The A/E analysis, however, clearly characterizes the event as background.

The sensitivity of GERDA Phase I is dominated by the data collected with the semi-coaxial detectors. Due to the reduced PSD of signal- from background-like events, the BI of the semi-coaxial data set is higher than for the BEGe data set. Given the BI and collected exposure of the semi-coaxial data set, at the end of Phase I two background events were expected in the ROI, limiting the experimental sensitivity because of statistical fluctuations in the background.

To test $0\nu\beta\beta$ decay up to half-lives of the order of 10^{26} yr, GERDA needs to re-enter the background free regime in which the experimental sensitivity scales as $T_{1/2}^{0\nu} \propto M \cdot t$, where $M \cdot t$ is the exposure. Therefore, the BI needs to be as low as $10^{-3} \frac{\text{counts}}{\text{keV} \cdot \text{kg} \cdot \text{yr}}$ in order to expect less than one background count in the signal region up to an exposure of 100 kg · yr.

To achieve such an unprecedented BI, a hardware upgrade of the GERDA experiment is necessary. Additional 25 enriched BEGe detectors are installed. The total detector mass is increased to 35.6 kg, of which 20.0 kg are of BEGe type. Consequently, the Phase II exposure is expected to be dominated by the new detector technology with increased energy resolution and enhanced PSD. The HPGe detectors are arranged in a densely packed array of seven strings to optimize the multi-detector coincidence. Furthermore, the LAr cryostat is instrumented to detect scintillation light produced by energy deposition in the LAr [80, 81, 82]. The enlarged array and the LAr instrumentation require a new lock to the LAr cryostat.

Since the average detector mass of BEGe detectors (~ 670 g) is much smaller than the mass of semi-coaxial detectors (2-3 kg), the radioactivity induced by the detector support needs to be reduced dramatically. Low mass holders have been constructed using a new contacting scheme [75]. Furthermore, to make use of the improved energy resolution of BEGe detectors, new read-out electronics were designed [82] in which the front-end (FE) electronics is split into two stages: the very front-end (VFE) with the feed-back circuit and the JFET is brought as close as possible to the detector. This reduces the input capacitance, thus the noise. The signal-to-noise ratio is improved, while the second stage, the CC3 pre-amplifier, is

experiment	isotope	mass [kg]	FWHM [keV]	$0\nu\beta\beta$ efficiency	BI [$\frac{\text{counts}}{\text{FWHM}\cdot\text{t}\cdot\text{yr}}$]
GERDA Phase II*	^{76}Ge	36	3	0.60	5
MAJORANA D*	^{76}Ge	30	3	0.54	6
EXO-200*	^{136}Xe	150	72	0.85	179
KamLAND-Zen*	^{136}Xe	383	270	1	50
Cuore	^{130}Te	988	5	0.22	227
NEXT	^{136}Xe	100	19	28	30
nEXO	^{136}Xe	5000	60	0.77	5
SNO+	^{130}Te	468	270	0.001	158
AMORE	^{100}Mo	5	5	0.47	11

Table 8.1: Comparison of BI in current and future experiments for the search of $0\nu\beta\beta$ decay. The list is by no means complete. The definition of mass is not uniform. The $0\nu\beta\beta$ efficiency includes signal efficiency and fraction of the $\beta\beta$ isotope. The BI is normalized to the FWHM and the signal efficiency. As of November 2016, experiments marked with * are taking data. Details on the numbers can be found in Appendix H.

placed further away from the detectors, which reduces the background in close vicinity of the detectors.

This thesis sketches the integration of the new Phase II detector array. Encountered problems have been solved by small changes in the original design. For instance, the detector support has been changed to minimize the risk of detector leakage current. Moreover, a major modification of the FE electronics has been carried out: due to a high mortality of the JFETs, the VFE is connected directly to the CC3. No degradation of the energy resolution and pulse shape discrimination is observed, however, the detector assembly is greatly simplified.

Prior to the start of GERDA Phase II, the performance of the newly integrated detectors and LAr instrumentation was tested. The combined PSD and LAr veto suppress main background components in the signal region, such as ^{208}Tl in the detector support, by up to two orders of magnitude.

The work presented in this thesis focuses on the analysis of the first GERDA Phase II data release. The data collected with the BEGe detectors have an exposure of $5.8 \text{ kg}\cdot\text{yr}$, and are blinded in a 50 keV window centered around $Q_{\beta\beta}$ for the analysis. Similar to Phase I, a pulse shape analysis based on the A/E parameter is performed. However, the majority of the BEGe detectors show a significantly higher noise level and a broader A/E resolution compared to Phase I. Therefore, a detector-based A/E cut is applied, accounting for the individual A/E resolution and the energy-dependent broadening.

The applied Phase II A/E cut is stronger than in Phase I, as at $Q_{\beta\beta}$ the background contribution of γ -background, such as ^{208}Tl and ^{214}Bi , is much higher. The signal efficiency of the A/E cut is $\epsilon_{PDS} = (87.3 \pm 0.2(\text{stat}) \pm 2.4(\text{sys}))\%$. A sample with a high fraction ($\sim 97\%$) of $2\nu\beta\beta$ events is selected by the LAr veto [110]. The efficiency of the $2\nu\beta\beta$ events is $\epsilon_{PSD} = (85.4 \pm 0.8(\text{stat}) + 1.7(\text{sys}))\%$ and in good agreement with the derived signal efficiency. 76% of the background events around $Q_{\beta\beta}$ are rejected by the A/E cut.

The LAr veto further identifies background events. After PSD and LAr veto, the BI of the

BEGe data set is reduced to

$$\text{BI} = (0.7_{-0.5}^{+1.3}) \cdot 10^{-3} \frac{\text{counts}}{\text{keV} \cdot \text{kg} \cdot \text{yr}}.$$

This is the best BI achieved in experiments for $0\nu\beta\beta$ search so far (compare Table 8.1). No event is left in the signal region at $Q_{\beta\beta} = (2039 \pm 5)$ keV.

For the GERDA experiment, the presented PSA proved to be a simple but efficient active background technique with high background rejection on the expense of a small signal efficiency loss. Furthermore, PSA and the new LAr veto are complementary techniques: while the LAr veto rejects, e.g., single Compton scattered events, the PSD identifies background events on the detector surface for which the LAr veto is less sensitive.

As in Phase I, the uncertainty on the signal efficiency is dominated by the difference in the topologies of $0\nu\beta\beta$ and DEP events. In this work Monte Carlo (MC) and pulse shape simulations (PSS) were used to estimate the induced systematic uncertainty. However, the PSS need to be revised and validated further. This can be done including calibration measurements with ^{56}Co sources which feature prominent DEPs at different energies including in the vicinity of $Q_{\beta\beta}$.

In addition to background rejection, the A/E analysis provides input for the background decomposition. However, A/E cannot distinguish MSE from n^+ -surface events. Therefore, an analysis to identify n^+ -surface events would complement the understanding of the background components, but is not mandatory for the suppression. With a better understanding of the background composition in the $2\nu\beta\beta$ region, one may use the $2\nu\beta\beta$ events to derive the systematic uncertainty on the difference between DEP and $0\nu\beta\beta$. Furthermore, if the background is well described by a model, the A/E cut may be optimized for a high signal efficiency at maximum background rejection.

Within this work, a frequentist statistical analysis is performed on the combined data collected in GERDA Phase I and the first Phase II release (semi-coaxial and BEGe detectors): a new lower limit on the half-life of $0\nu\beta\beta$ decay of ^{76}Ge is set to

$$T_{1/2}^{0\nu} > 5.3 \cdot 10^{25} \text{ yr at } 90\% \text{ C.L.}$$

The median sensitivity is $T_{1/2}^{0\nu} > 4.0 \cdot 10^{25} \text{ yr at } 90\% \text{ C.L.}$

In Phase II of the $0\nu\beta\beta$ experiment KamLAND-Zen, a ^{136}Xe exposure of 504 kg·yr has been collected with a median sensitivity on the limit of the half-life of the $0\nu\beta\beta$ decay of ^{136}Xe of $5.6 \cdot 10^{25} \text{ yr}$ [59]. This has to be compared to the median sensitivity of the combined GERDA Phase I and Phase II data with an exposure of 29 kg·yr of ^{76}Ge : the GERDA experiment with its extremely low BI and excellent energy resolution reaches a comparable sensitivity, even with a 10-fold smaller detector mass.

Assuming the exchange of light Majorana neutrinos to be the mechanism of $0\nu\beta\beta$ decay, the derived half-life limit for the $0\nu\beta\beta$ decay of ^{76}Ge corresponds to an effective Majorana neutrino mass of $m_{0\nu} < 320 \text{ meV}$ using the smallest nuclear matrix element in the recent literature [117]. As of November 2016, the KamLAND-Zen experiment puts the most stringent limit on the effective Majorana neutrino mass: $m_{0\nu} < 165 \text{ meV}$ [44]. However, the liquid-scintillator-based experiment has a BI per FWHM which is an order of magnitude larger than in GERDA Phase II. For the final analysis, the background in the ROI of KamLAND-Zen needs to be

modeled and systematic uncertainties on the background model have to be considered. On the contrary, in the GERDA experiment, the background at $Q_{\beta\beta}$ can be modeled with a flat shape, greatly simplifying the final statistical analysis on the limit of the half-life $T_{1/2}^{0\nu}$. Furthermore, the high energy resolution of HPGe detectors is beneficial for the identification of individual background components, i.e. γ -lines.

GERDA Phase II alone reaches a median sensitivity on the lower limit of the half-life of $0\nu\beta\beta$ decay of ^{76}Ge of 2.4 yr at 90 % C.L. This is compatible to the achieved sensitivity of GERDA Phase I, although the exposure of the Phase II data set is a factor of 2 smaller. This demonstrates the impact of the BI on the experimental sensitivity and proves the concept of the improved active background reduction techniques used by GERDA. GERDA Phase II proves to be a high resolution background-free experiment. Until its design exposure of 100 kg · yr, the number of expected background events in the ROI is < 1 to explore half-lives of $0\nu\beta\beta$ decay of ^{76}Ge of the order of 10^{26} yr.

To explore longer and longer half-lives of $0\nu\beta\beta$ decay, experiments need an extremely low and flat shaped background. Eventually, the $2\nu\beta\beta$ decay will become an unavoidable background for the observation of $0\nu\beta\beta$ decay in experiments with poor energy resolution. Finally, in case of a discovery, excellent energy resolution and efficient discrimination of signal- from background-like events will be needed to unambiguously confirm if the observed peak is the $0\nu\beta\beta$ peak or an unexpected γ -line from an unknown nuclear transition. The GERDA concept to operate bare HPGe detectors in LAr brings all the key prerequisites together: an excellent energy resolution and an efficient PSA. Furthermore, as shown in Table 8.1, the germanium based $0\nu\beta\beta$ experiments are amongst the experimental approaches with the best BI per ROI. GERDA Phase II already proved to be able to reach a BI of $5 \frac{\text{counts}}{\text{FWHM} \cdot \text{t} \cdot \text{yr}}$.

As of November 2016, a possible upgrade of the GERDA experiment is being discussed in the frame of a new world-wide collaboration for a future 1-ton germanium-based experiment [119]: with small modifications of the current setup, the GERDA cryostat can accommodate up to 200 kg of enriched HPGe detectors. Similar background reduction techniques as in GERDA Phase II, i.e. a LAr veto and PSD, will be key features. The goal is to lower the background index by a factor of 3-5 compared to GERDA Phase II. Eventually, the new experiment aims to explore half-lives of the $0\nu\beta\beta$ decay of ^{76}Ge of the order of 10^{28} yr and effective Majorana neutrino masses below (10-20) meV [4].

Calculation of Survival Efficiency in the Compton Region

In the Compton region the survival efficiency is given by

$$\epsilon_{CC} = \frac{n^+}{n} \quad (\text{A.1})$$

where $n = n^+ + n^-$ is the total number of events in a given energy region and n^\pm being the number of accepted (+) and non-accepted (-) events by the cut.

Assuming n^+ and n^- are independent and Poissonian distributed, their uncertainty is given by

$$\Delta n^\pm = \sqrt{n^\pm} \quad (\text{A.2})$$

The uncertainty on the survival efficiency may then be calculated with the usual error propagation

$$\begin{aligned} \Delta \epsilon_{CC} &= \sqrt{\left(\frac{\partial \epsilon}{\partial n^+}\right)^2 \cdot (\Delta n^+)^2 + \left(\frac{\partial \epsilon}{\partial n^-}\right)^2 \cdot (\Delta n^-)^2} \\ &= \sqrt{\frac{(n^-)^2}{(n^+ + n^-)^4} \cdot n^+ + \frac{(n^+)^2}{(n^+ + n^-)^4} \cdot n^-} \\ &= \sqrt{\frac{(n^- \cdot n^+) \cdot (n^+ + n^-)}{(n^+ + n^-)^4}} = \sqrt{\frac{n^- \cdot n^+}{n^3}} \\ &= \sqrt{\frac{n^+}{n} \cdot \frac{1}{n} \cdot \frac{n^-}{n}} = \sqrt{\frac{\epsilon}{n} \cdot \left(\frac{n - n^+}{n}\right)} \\ \Delta \epsilon_{CC} &= \sqrt{\frac{\epsilon}{n} \cdot (1 - \epsilon)} \end{aligned} \quad (\text{A.3})$$

Calculation of Survival Efficiency in the FEP/SEP

The survival efficiency in the FEP and SEP is calculated as

$$\epsilon_{FEP} = \frac{n_{FEP}^+ - n_{bck}^+}{n_{FEP} - n_{bck}} \quad (\text{A.4})$$

where $n_{FEP} = n_{FEP}^+ + n_{FEP}^-$ is the total number of events in the FEP, $n_{bck} = n_{bck}^+ + n_{bck}^-$ in the background. n^\pm is the number of accepted/rejected events after the cut. The number of background events is estimated from two energy regions around the peak, see Figure A.1. In the standard PSA the range of the energy windows is:

- Region peak: $[\text{FEP} - 4.5 \cdot \sigma_{FEP}, \text{FEP} + 4.5 \cdot \sigma_{FEP}]$
- Region bck: $[\text{FEP} - 2 \cdot 4.5 \cdot \sigma_{FEP}, \text{FEP} - 4.5 \cdot \sigma_{FEP}]$
- Region bck: $[\text{FEP} + 4.5 \cdot \sigma_{FEP}, \text{FEP} + 2 \cdot 4.5 \cdot \sigma_{FEP}]$

where FEP is the peak position and σ_{FEP} the energy resolution in the FEP in sigma. $n_{FEP,bck}^\pm$ are independent and Poissonian distributed, thus $\Delta n_{FEP,bck}^\pm = \sqrt{n_{FEP,bck}^\pm}$. The uncertainty on the survival efficiency is calculated as

$$\begin{aligned} \Delta \epsilon_{FEP} = & \sqrt{\left(\frac{\partial \epsilon}{\partial n_{FEP}^+} \right)^2 \cdot (\Delta n_{FEP}^+)^2 + \left(\frac{\partial \epsilon}{\partial n_{FEP}^-} \right)^2 \cdot (\Delta n_{FEP}^-)^2} \\ & + \sqrt{\left(\frac{\partial \epsilon}{\partial n_{bck}^+} \right)^2 \cdot (\Delta n_{bck}^+)^2 + \left(\frac{\partial \epsilon}{\partial n_{bck}^-} \right)^2 \cdot (\Delta n_{bck}^-)^2} \end{aligned} \quad (\text{A.5})$$

$$\begin{aligned} \Delta \epsilon_{FEP} = & \sqrt{\frac{1}{(n_{FEP}^+ + n_{FEP}^- - n_{bck}^+ - n_{bck}^-)^4} \cdot \{ \\ & \frac{[(n_{FEP}^+ + n_{FEP}^- - n_{bck}^+ - n_{bck}^-) - (n_{FEP}^+ - n_{bck}^+)]^2 \cdot n_{FEP}^+}{+ [(n_{FEP}^+ + n_{FEP}^- - n_{bck}^+ - n_{bck}^-) - (n_{FEP}^+ - n_{bck}^+)]^2 \cdot n_{bck}^+} \\ & \frac{+ [-(n_{FEP}^+ - n_{bck}^+)]^2 \cdot n_{FEP}^-}{+ [-(n_{FEP}^+ - n_{bck}^+)]^2 \cdot n_{bck}^-} \}} \end{aligned} \quad (\text{A.6})$$

$$\begin{aligned} = & \frac{1}{(n_{FEP} - n_{bck})^2} \cdot \{ \\ & \frac{\sqrt{[n_{FEP}^- - n_{bck}^-]^2 \cdot n_{FEP}^+ + [n_{FEP}^- - n_{bck}^-]^2 \cdot n_{FEP}^-}}{+ [n_{FEP}^+ - n_{bck}^+]^2 \cdot n_{FEP}^- + [n_{FEP}^+ - n_{bck}^+]^2 \cdot n_{bck}^-} \} \end{aligned} \quad (\text{A.7})$$

$$\Delta \epsilon_{FEP} = \frac{\sqrt{[n_{FEP}^- - n_{bck}^-]^2 \cdot [n_{FEP}^+ + n_{bck}^+] + [n_{FEP}^+ - n_{bck}^+]^2 \cdot [n_{FEP}^- + n_{bck}^-]}}{(n_{FEP} - n_{bck})^2} \quad (\text{A.8})$$

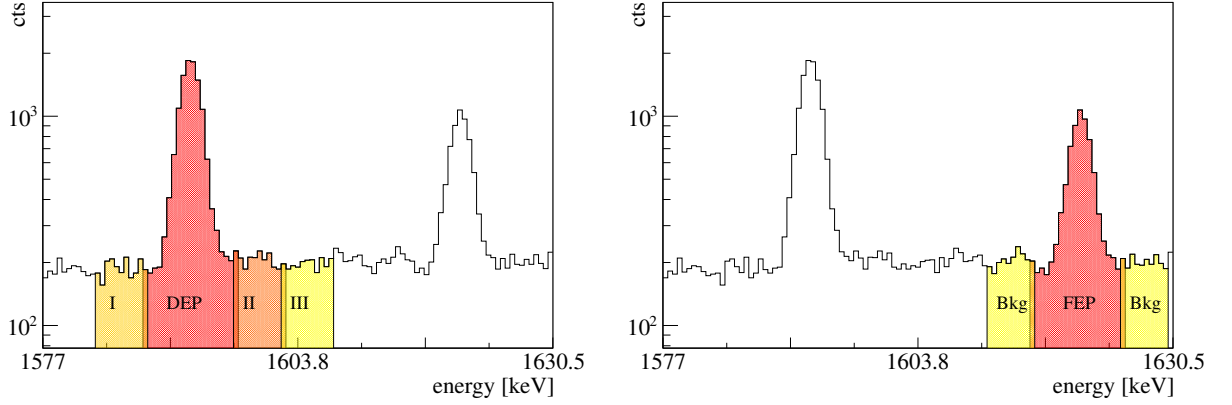


Figure A.1: ^{228}Th Spectrum around DEP and FEP. The energy window of the peak region is indicated in red, in yellow/ orange the window for the background subtraction.

Calculation of Survival Efficiency in the DEP

The survival efficiency in the DEP is given by

$$\epsilon_{DEP} = \frac{n_{DEP}^+ - n_{bck}^+}{n_{DEP} - n_{bck}} \quad (\text{A.9})$$

where $n_{DEP} = n_{DEP}^+ + n_{DEP}^-$ is the total number of events in the peak region, n_{DEP}^\pm being the number of accepted (+) and non-accepted (-) events by the cut. In the standard analysis the peak region is defined as $DEP - 4.5 \cdot \sigma_{DEP}$ to $DEP + 4.5 \cdot \sigma_{DEP}$, where DEP is the peak position and σ_{DEP} the energy resolution in the DEP given in sigma.

The number of background events is estimated from three different energy regions, as indicated in Figure A.1. The range of the different regions is defined as [3]

- Region I: $[DEP - 2 \cdot 4.5 \cdot \sigma_{DEP}, DEP - 4.5 \cdot \sigma_{DEP}]$
- Region II: $[DEP + 4.5 \cdot \sigma_{DEP}, DEP + 2 \cdot 4.5 \cdot \sigma_{DEP}]$
- Region III: $[DEP + 2 \cdot 4.5 \cdot \sigma_{DEP}, DEP + 3 \cdot 4.5 \cdot \sigma_{DEP}]$

To take into account the step in the underlying background the number of background events is calculated as $n_{bkg} = n_{regI} + 2 \cdot n_{regII} - n_{regIII}$ where $n_{I,II,III} = n_{I,II,III}^+ + n_{I,II,III}^-$ being the number of accepted (+) and rejected (-) events in the corresponding energy regions.

Thus, the survival efficiency expressed in independent variables is given by

$$\epsilon_{DEP} = \frac{n_{DEP}^+ - (n_I^+ + 2 \cdot n_{II}^+ - n_{III}^+)}{n_{DEP}^+ + n_{DEP}^- - (n_I^+ + 2 \cdot n_{II}^+ - n_{III}^+) - (n_I^- + 2 \cdot n_{II}^- - n_{III}^-)} \quad (\text{A.10})$$

$n_{DEP,I,II,III}^\pm$ are independent and Poissonian distributed, thus $\Delta n_{DEP,I,II,III}^\pm = \sqrt{n_{DEP,I,II,III}^\pm}$.

The uncertainty on the survival efficiency is calculated as follows:

$$\begin{aligned}
 \Delta\epsilon_{DEP} = & \sqrt{\left(\frac{\partial\epsilon}{\partial n_{DEP}^+}\right)^2 \cdot (\Delta n_{DEP}^+)^2 + \left(\frac{\partial\epsilon}{\partial n_{DEP}^-}\right)^2 \cdot (\Delta n_{DEP}^-)^2} \\
 & + \frac{\left(\frac{\partial\epsilon}{\partial n_I^+}\right)^2 \cdot (\Delta n_I^+)^2 + \left(\frac{\partial\epsilon}{\partial n_{II}^+}\right)^2 \cdot (\Delta n_{II}^+)^2 + \left(\frac{\partial\epsilon}{\partial n_{III}^+}\right)^2 \cdot (\Delta n_{III}^+)^2}{\sqrt{\left(\frac{\partial\epsilon}{\partial n_I^-}\right)^2 \cdot (\Delta n_I^-)^2 + \left(\frac{\partial\epsilon}{\partial n_{II}^-}\right)^2 \cdot (\Delta n_{II}^-)^2 + \left(\frac{\partial\epsilon}{\partial n_{III}^-}\right)^2 \cdot (\Delta n_{III}^-)^2}} \quad (A.11)
 \end{aligned}$$

$$\begin{aligned}
 \Delta\epsilon_{DEP} = & \frac{1}{(n_{DEP} - n_{bck})^2} \cdot \sqrt{(n_{DEP}^- - n_I^- - 2 \cdot n_{II}^- + n_{III}^-)^2 \cdot n_{DEP}^+} \\
 & + \frac{[-(n_{DEP}^+ - n_I^+ - 2 \cdot n_{II}^+ + n_{III}^+)]^2 \cdot n_{DEP}^-}{\sqrt{(n_{DEP}^- - n_I^- - 2 \cdot n_{II}^- + n_{III}^-)^2 \cdot n_I^+}} \\
 & + \frac{4 \cdot (n_{DEP}^- - n_I^- - 2 \cdot n_{II}^- + n_{III}^-)^2 \cdot n_{II}^+}{\sqrt{[-(n_{DEP}^+ - n_I^+ - 2 \cdot n_{II}^+ + n_{III}^+)]^2 \cdot n_I^-}} \\
 & + \frac{4 \cdot [-(n_{DEP}^+ - n_I^+ - 2 \cdot n_{II}^+ + n_{III}^+)]^2 \cdot n_{II}^-}{\sqrt{[-(n_{DEP}^+ - n_I^+ - 2 \cdot n_{II}^+ + n_{III}^+)]^2 \cdot n_{III}^-}} \\
 & + \frac{[-(n_{DEP}^+ - n_I^+ - 2 \cdot n_{II}^+ + n_{III}^+)]^2 \cdot n_I^-}{\sqrt{[-(n_{DEP}^+ - n_I^+ - 2 \cdot n_{II}^+ + n_{III}^+)]^2 \cdot n_{III}^-}} \quad (A.12)
 \end{aligned}$$

$$\begin{aligned}
 \Delta\epsilon_{DEP} = & \frac{1}{(n_{DEP} - n_{bck})^2} \cdot \sqrt{(n_{DEP}^- - n_{bck}^-)^2 \cdot (n_{DEP}^+ + n_I^+ + 4 \cdot n_{II}^+ + n_{III}^+)} \\
 & + \frac{(n_{DEP}^+ - n_{bck}^+)^2 \cdot (n_{DEP}^- + n_I^- + 4 \cdot n_{II}^- + n_{III}^-)}{\sqrt{(n_{DEP}^- - n_{bck}^-)^2 \cdot (n_{DEP}^+ + n_I^+ + 4 \cdot n_{II}^+ + n_{III}^+)}} \quad (A.13)
 \end{aligned}$$

B

Decay Schemes of Gerda Background

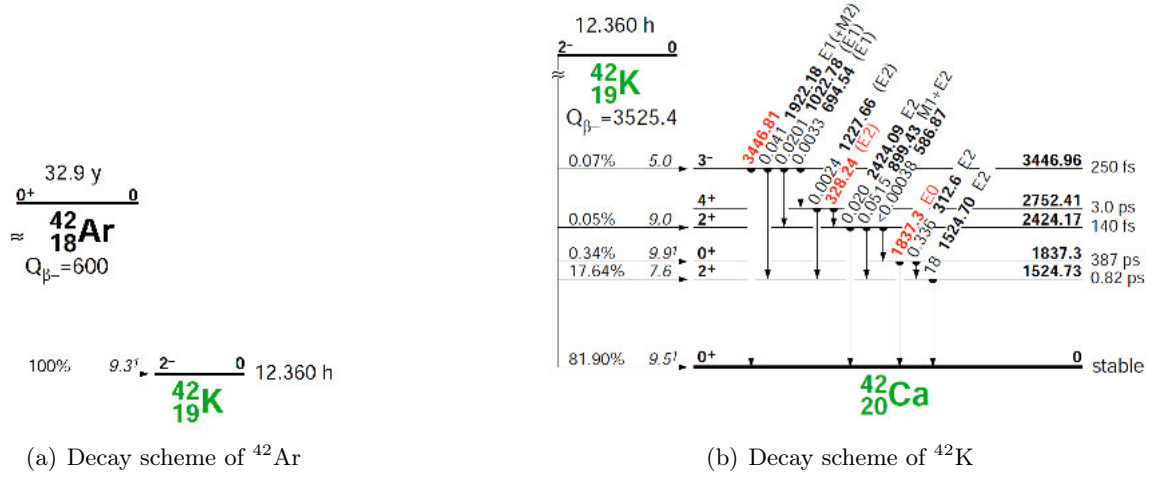


Figure B.1: Decay schemes of ^{42}Ar and its daughter nuclide ^{42}K . Figure taken from [93].

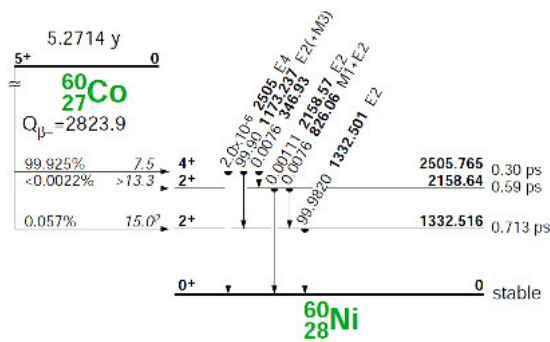
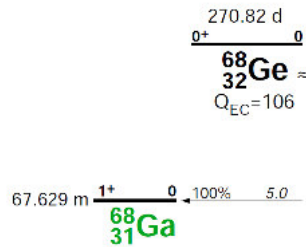
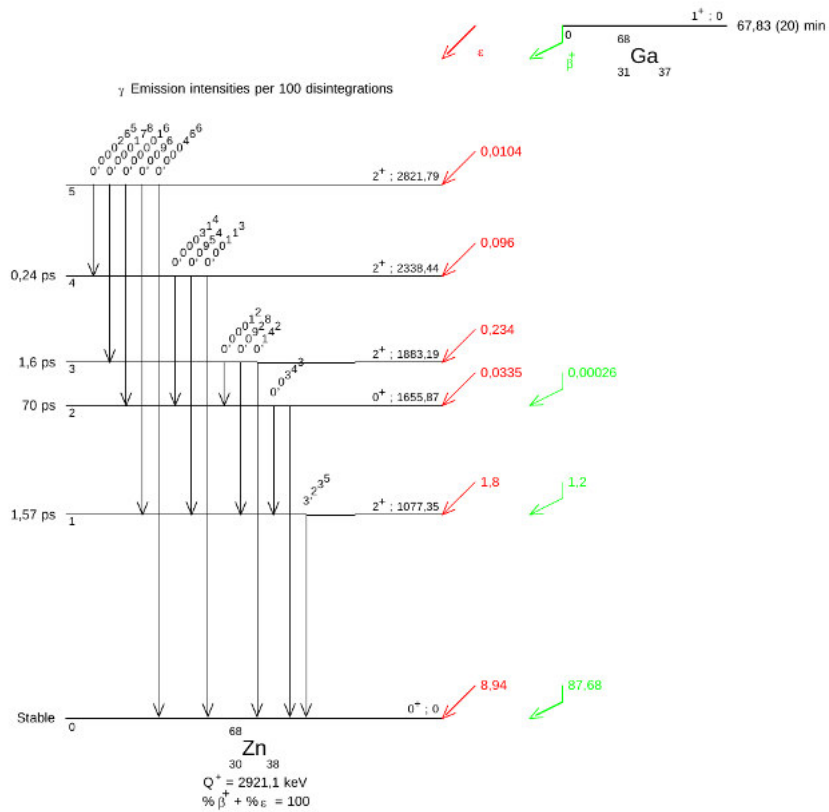


Figure B.2: Decay scheme of ^{60}Co . Taken from [93].



(a) Decay Scheme of ${}^{68}\text{Ge}$. Figure taken from [93].



(b) Decay Scheme of ${}^{68}\text{Ga}$. Figure taken from [97].

Figure B.3: Decay Scheme of ${}^{68}\text{Ge}$



Phase II HPGe Detectors

Detector	Mass [g]	string position	DAQ channel	HV _{op}
GD00A	496	s6.1	30	2500
GD00B	697	s1.4	3	3500
GD00C	815	s3.8	18	3500
GD00D	813	s4.4	22	3500
GD02A	545	s3.1	11	2500
GD02B	625	s1.3	2	3000
GD02C	788	s6.2	31	3500
GD02D	662	s1.7	6	4000
GD32A	458	s3.3	13	3000
GD32B	716	s3.2	12	4000
GD32C	743	s3.4	14	4000
GD32D	720	s6.5	34	4000
GD35A	768	s4.6	24	4000
GD35B	810	s1.2	1	4000
GD35C	634	s4.1	19	3500
GD61A	731	s1.5	4	4500
GD61B	751	s4.8	26	4000
GD61C	634	s3.6	16	4000
GD76B	384	s3.7	17	3500
GD76C	824	s4.2	20	3500
GD79B	736	s6.3	32	3500
GD79C	812	s4.5	23	3500
GD89A	524	s6.6	35	4000
GD89B	620	s1.6	5	3500
GD89C	595	s3.5	15	4000
GD89D	526	s4.3	21	4000
GD91A	627	s1.1	0	3500
GD91B	650	s4.7	25	3500
GD91C	627	s1.8	7	4000
GD91D	693	s6.4	33	4500
ANG1	969	s6.7	36	4000
ANG2	2878	s5.1	27	3500
ANG3	2447	s2.3	10	3500
ANG4	2375	s5.3	29	3500
ANG5	2782	s2.1	8	2500
RG1	2152	s2.2	9	4500
RG2	2194	s5.2	28	4000
GTF32	2321	s7.2	38	3000
GTF45	2334	s7.3	37	3000
GTF112	2967	s7.1	37	3000

Table C.1: Table summarizing mass [112], string position, DAQ channel and operational bias voltages of GERDA Phase II detectors. The string position is given as $sx.y$, where x denotes the string number and y the position in the string starting with the top detector.



Data Processing: Extraction of A/E Parameter

For off-line processing all GERDA germanium data are digitized using commercial analog-to-digital converters (FADC) SIS3301 from Struck with 14 bits and a 100 MHz sampling rate. Traces with a length of $160 \mu\text{s}$ are stored. The data are compressed by summing four 10 ns samples. This artificially reduces the sampling rate from 100 MHz to 25 MHz. For PSA a $5 \mu\text{s}$ ($10 \mu\text{s}$) window around the trigger with a 10 ns sampling is kept during Phase I (Phase II) data taking.

The acquired data are processed off-line with the software framework GELATIO [92, 120]. Since the pulses have negative polarity, the traces are inverted. In a first step the baseline of the compressed trace is analyzed: the average baseline as well as the root-mean-square deviation (RMS) in a $70 \mu\text{s}$ window before the trigger is calculated. Subsequently, the average baseline is subtracted, see Figure D.1(a).

A Gaussian filter is approximated by a differentiation using a $10 \mu\text{s}$ deconvolution of the trace followed by a $13 \times 10 \mu\text{s}$ moving window averaging (MWA) for integration. The information on the event energy is given by the maximum amplitude of the shaped trace, see Figure D.1(d).

To extract the maximum of the current pulse, the short trace with 10 ns sampling is used. First, a $3 \times 50 \text{ ns}$ MWA is applied for smoothing. The pulse is differentiated and the samples are interpolated to a 1 ns sampling. The A parameter is given by the maximum amplitude of the current pulse, see Figure D.1(g).

Furthermore, parameters to identify non-physical pulses are determined [120]:

- **position of leading edge:** the position of the leading edge should be around the center of the trace. In case of random coincidence the trigger position may be much later. Events are reconstructed incorrectly as applied filters e.g. for energy reconstruction may fail.
- **number of leading edges:** pile-up events, i.e. multiple physical pulses within a trace, typically feature multiple leading edges.
- **position of maximum amplitude:** if the leading edge is in the center of the trace, the maximum amplitude in Figure D.1(d) should be reconstructed in a defined range of the trace.
- **baseline slope:** the baseline before the trigger is approximated by $a + b \cdot \exp(-\frac{t}{\tau})$. The slope is non-zero if the baseline is not yet restored due to a previous recorded event.

Such events are called pre-trigger pile-up events.

- **signal rise time:** the time in which the signal rises from 10 % to 90 % of the total signal height is used to identify fast and slow non-physical pulses.
- **signal polarity:** discharge or cross-talk events feature a reverse polarity.

Typically, the measure of the amplitude of pile-up events fails, i.e. the energy reconstruction is incorrect. Furthermore, pile-up events may be misidentified as multi-site events (MSE). Since pulse shape cuts and efficiencies are determined using calibration data pile-up events need to be removed from the data set. The pile-up rate is proportional to the event rate and negligible in physics data.

Events passing the quality selection are considered as physical. The detector-detector anti-coincidence cut (AC) is defined by the number of channels containing physical pulses in a recorded event. For a detailed description of the data processing see [92] and [120].

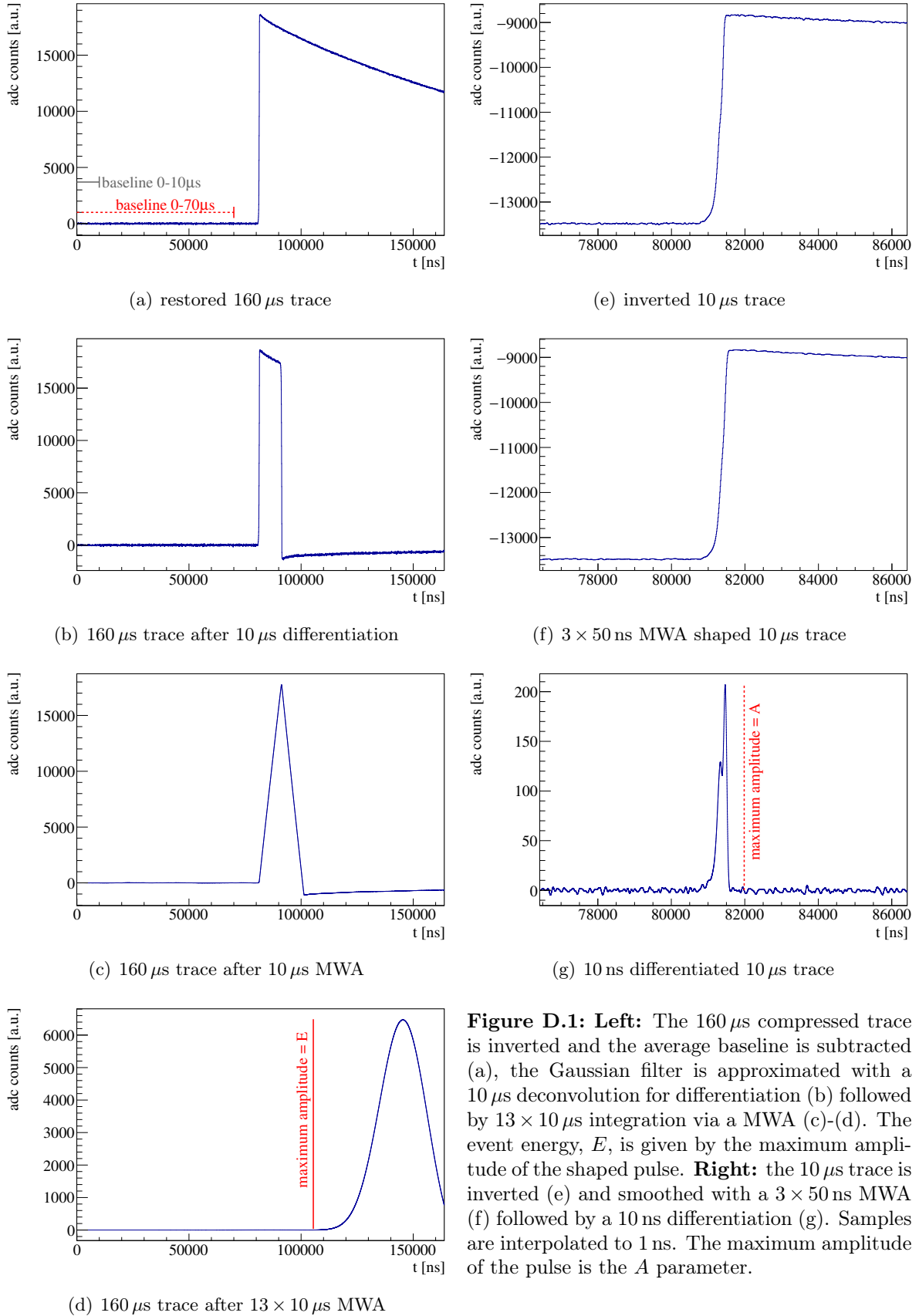


Figure D.1: **Left:** The $160 \mu\text{s}$ compressed trace is inverted and the average baseline is subtracted (a), the Gaussian filter is approximated with a $10 \mu\text{s}$ deconvolution for differentiation (b) followed by $13 \times 10 \mu\text{s}$ integration via a MWA (c)-(d). The event energy, E , is given by the maximum amplitude of the shaped pulse. **Right:** the $10 \mu\text{s}$ trace is inverted (e) and smoothed with a $3 \times 50 \text{ ns}$ MWA (f) followed by a 10 ns differentiation (g). Samples are interpolated to 1 ns . The maximum amplitude of the pulse is the A parameter.

Pulse Shape Analysis of BEGe Detectors in Gerda Phase I

Chapter 2 of the following GERDA publication discusses the A/E -based pulse shape analysis applied to the GERDA Phase I BEGe data set. The analysis is published in the GERDA publication “Pulse shape discrimination for GERDA Phase I data” in [5]. The calibration of the A/E parameter is described using ^{228}Th calibration data. Time instabilities of the A/E parameter in-between and during the calibration are observed and corrected for. Furthermore, the energy dependence of A/E is corrected. The background suppression as well as the signal efficiency of the applied PSD is presented.

The work on the A/E analysis in Phase I was performed by a group of people under the supervision of D. Budjáš. The author of this work significantly contributed to the calibration of the A/E cut, as well as the determination of the signal efficiency and background suppression.

The author of this work is responsible for the A/E analysis for the first data release of Phase II. The calibration is based on the experience gained during GERDA Phase I and is added to the appendix for the sake of completeness but without repetition.

Pulse shape discrimination for GERDA Phase I data

M. Agostini¹⁴, M. Allardt³, E. Andreotti^{5,17}, A.M. Bakalyarov¹², M. Balata¹, I. Barabanov¹⁰, M. Barnabé Heider^{6,14,b}, N. Barros³, L. Baudis¹⁸, C. Bauer⁶, N. Becerici-Schmidt¹³, E. Bellotti^{7,8}, S. Belogurov^{11,10}, S.T. Belyaev¹², G. Benato¹⁸, A. Bettini^{15,16}, L. Bezrukov¹⁰, T. Bode¹⁴, V. Brudanin⁴, R. Brugnera^{15,16}, D. Budjáš¹⁴, A. Caldwell¹³, C. Cattadori⁸, A. Chernogorov¹¹, F. Cossavella¹³, E.V. Demidova¹¹, A. Domula³, V. Egorov⁴, R. Falkenstein¹⁷, A. Ferella^{18,c}, K. Freund¹⁷, N. Frodyma², A. Gangapshev^{10,6}, A. Garfagnini^{15,16}, C. Gotti^{8,d}, P. Grabmayr^{17,a}, V. Gurentsov¹⁰, K. Gusev^{12,4,14}, K.K. Guthikonda¹⁸, W. Hampel⁶, A. Hegai¹⁷, M. Heisel⁶, S. Hemmer^{15,16}, G. Heusser⁶, W. Hofmann⁶, M. Hult⁵, L.V. Inzhechik^{10,e}, L. Ioannucci¹, J. Janicskó Csáthy¹⁴, J. Jochum¹⁷, M. Junker¹, T. Kihm⁶, I.V. Kirpichnikov¹¹, A. Kirsch⁶, A. Klimenko^{6,4,f}, K.T. Knöpfle⁶, O. Kochetov⁴, V.N. Kornoukhov^{11,10}, V.V. Kuzminov¹⁰, M. Laubenstein¹, A. Lazzaro¹⁴, V.I. Lebedev¹², B. Lehnert³, H.Y. Liao¹³, M. Lindner⁶, I. Lippi¹⁶, X. Liu^{13,g}, A. Lubashevskiy⁶, B. Lubsandorzhev¹⁰, G. Lutter⁵, C. Macolino¹, A.A. Machado⁶, B. Majorovits¹³, W. Maneschg⁶, M. Misiaszek², I. Nemchenok⁴, S. Nisi¹, C. O'Shaughnessy^{13,h}, L. Pandola¹, K. Pelczar², G. Pessina^{7,8}, A. Pullia⁹, S. Riboldi⁹, N. Romyantseva⁴, C. Sada^{15,16}, M. Salathe⁶, C. Schmitt¹⁷, J. Schreiner⁶, O. Schulz¹³, B. Schwingenheuer⁶, S. Schönert¹⁴, E. Shevchik⁴, M. Shirchenko^{12,4}, H. Simgen⁶, A. Smolnikov⁶, L. Stanco¹⁶, H. Strecker⁶, M. Tarka¹⁸, C.A. Ur¹⁶, A.A. Vasenko¹¹, O. Volynets¹³, K. von Sturm^{17,15,16}, V. Wagner⁶, M. Walter¹⁸, A. Wegmann⁶, T. Wester³, M. Wojcik², E. Yanovich¹⁰, P. Zavarise^{1,i}, I. Zhitnikov⁴, S.V. Zhukov¹², D. Zinatulina⁴, K. Zuber³, G. Zuzel²

¹INFN Laboratori Nazionali del Gran Sasso, LNGS, Assergi, Italy²Institute of Physics, Jagiellonian University, Cracow, Poland³Institut für Kern- und Teilchenphysik, Technische Universität Dresden, Dresden, Germany⁴Joint Institute for Nuclear Research, Dubna, Russia⁵Institute for Reference Materials and Measurements, Geel, Belgium⁶Max-Planck-Institut für Kernphysik, Heidelberg, Germany⁷Dipartimento di Fisica, Università Milano Bicocca, Milano, Italy⁸INFN Milano Bicocca, Milano, Italy⁹Dipartimento di Fisica, Università degli Studi di Milano e INFN Milano, Milano, Italy¹⁰Institute for Nuclear Research of the Russian Academy of Sciences, Moscow, Russia¹¹Institute for Theoretical and Experimental Physics, Moscow, Russia¹²National Research Centre "Kurchatov Institute", Moscow, Russia¹³Max-Planck-Institut für Physik, München, Germany¹⁴Physik Department and Excellence Cluster Universe, Technische Universität München, München, Germany¹⁵Dipartimento di Fisica e Astronomia, Università di Padova, Padova, Italy¹⁶INFN Padova, Padova, Italy¹⁷Physikalisches Institut, Eberhard Karls Universität Tübingen, Tübingen, Germany¹⁸Physik Institut der Universität Zürich, Zürich, Switzerland

Received: 9 July 2013

© The Author(s) 2013. This article is published with open access at Springerlink.com

^a e-mail: gerda-eb@mpi-hd.mpg.de^b Present address: CEGEP St-Hyacinthe, Québec, Canada.^c Present address: INFN LNGS, Assergi, Italy.^d Also at: Università di Firenze, Italy.^e Also at: Moscow Inst. of Physics and Technology, Russia.^f Also at: Int. Univ. for Nature, Society and Man "Dubna", Russia.^g Present address: Shanghai Jiaotong University, Shanghai, China.^h Present address: University North Carolina, Chapel Hill, USA.ⁱ Present address: University of L'Aquila, Dipartimento di Fisica, L'Aquila, Italy.

Abstract The GERDA experiment located at the Laboratori Nazionali del Gran Sasso of INFN searches for neutrinoless double beta ($0\nu\beta\beta$) decay of ^{76}Ge using germanium diodes as source and detector. In Phase I of the experiment eight semi-coaxial and five BEGe type detectors have been deployed. The latter type is used in this field of research for the first time. All detectors are made from material with enriched ^{76}Ge fraction. The experimental sensitivity can be improved by analyzing the pulse shape of the detector signals with the aim to reject background events. This

Published online: 09 October 2013

Springer

paper documents the algorithms developed before the data of Phase I were unblinded. The double escape peak (DEP) and Compton edge events of 2.615 MeV γ rays from ^{208}Tl decays as well as two-neutrino double beta ($2\nu\beta\beta$) decays of ^{76}Ge are used as proxies for $0\nu\beta\beta$ decay.

For BEGe detectors the chosen selection is based on a single pulse shape parameter. It accepts 0.92 ± 0.02 of signal-like events while about 80 % of the background events at $Q_{\beta\beta} = 2039$ keV are rejected.

For semi-coaxial detectors three analyses are developed. The one based on an artificial neural network is used for the search of $0\nu\beta\beta$ decay. It retains 90 % of DEP events and rejects about half of the events around $Q_{\beta\beta}$. The $2\nu\beta\beta$ events have an efficiency of 0.85 ± 0.02 and the one for $0\nu\beta\beta$ decays is estimated to be $0.90^{+0.05}_{-0.09}$. A second analysis uses a likelihood approach trained on Compton edge events. The third approach uses two pulse shape parameters. The latter two methods confirm the classification of the neural network since about 90 % of the data events rejected by the neural network are also removed by both of them. In general, the selection efficiency extracted from DEP events agrees well with those determined from Compton edge events or from $2\nu\beta\beta$ decays.

1 Introduction

The GERDA (GERmanium Detector Array) experiment searches for neutrinoless double beta decay ($0\nu\beta\beta$ decay) of ^{76}Ge . Diodes made from germanium with an enriched ^{76}Ge isotope fraction serve as source and detector of the decay. The sensitivity to detect a signal, i.e. a peak at the decay's Q value of 2039 keV, depends on the background level. Large efforts went therefore into the selection of radio pure materials surrounding the detectors. The latter are mounted in low mass holders made from screened copper and PTFE and are operated in liquid argon which serves as cooling medium and as a shield against external backgrounds. The argon cryostat is immersed in ultra pure water which provides additional shielding and vetoing of muons by the detection of Čerenkov radiation with photomultipliers. The background level achieved with this setup is discussed in Ref. [1]. Details of the apparatus which is located at the Laboratori Nazionali del Gran Sasso of INFN can be found in Ref. [2].

It is known from past experiments that the time dependence of the detector current pulse can be used to identify background events [3–8]. Signal events from $0\nu\beta\beta$ decays deposit energy within a small volume if the electrons lose little energy by bremsstrahlung (single site event, SSE). On the contrary, in background events from, e.g., photons interacting via multiple Compton scattering, energy is often deposited at several locations well separated by a few cm in the detector (multi site events, MSE). The pulse shapes will

in general be different for the two event classes and can thus be used to improve the sensitivity of the experiment. Energy depositions from α or β decays near or at the detector surface lead to peculiar pulse shapes as well that allows their identification.

GERDA proceeds in two phases. In Phase I, five semi-coaxial diodes from the former Heidelberg-Moscow (HDM) experiment (named ANG 1–ANG 5) [9] and three from the IGEX experiment (named RG 1–RG 3) [10] are deployed. For Phase II, 30 new detectors of BEGe type [11] have been produced of which five have already been deployed for part of Phase I (GD32B, GD32C, GD32D, GD35B and GD35C). The characteristics of all detectors are given in Refs. [1, 2].

Each detector is connected to a charge sensitive amplifier and the output is digitized with Flash ADCs with 100 MHz sampling frequency. The deposited energy and the parameters needed for pulse shape analysis are reconstructed offline [12, 13] from the recorded pulse.

The effect of the PSD selection on the physics data is typically always compared in the energy interval 1930–2190 keV which is used for the $0\nu\beta\beta$ analysis [1]. The blinded energy window 2034–2044 keV and two intervals 2099–2109 keV (SEP of ^{208}Tl line) and 2114–2124 keV (^{214}Bi line) are removed. The remaining energy range is referred to as the “230 keV window” in the following.

Events with an energy deposition in the window $Q_{\beta\beta} \pm 5$ keV ($Q_{\beta\beta} \pm 4$ keV) were hidden for the semi-coaxial (BEGe) detectors and were analyzed after all selections and calibrations had been finalized. This article presents the pulse shape analysis for GERDA Phase I developed in advance of the data unblinding.

2 Pulse shape discrimination

Semi-coaxial and BEGe detectors have different geometries and hence different electric field distributions. Figure 1 shows a cross section of a semi-coaxial and a BEGe detector with the corresponding weighting potential profiles. The latter determine the induced signal on the readout electrode for drifting charges at a given position in the diode [14]. For both detectors, the bulk is p type, the high voltage is applied to the $n+$ electrode and the readout is connected to the $p+$ electrode. The electrodes are separated by an insulating groove.

2.1 BEGe detectors

The induced current pulse is largest when charges drift through the volume of a large weighting potential gradient. For BEGe detectors this is the case when holes reach the readout electrode. Electrons do not contribute much since they drift through a volume of low field strength. The electric field profile in BEGes causes holes to approach the $p+$

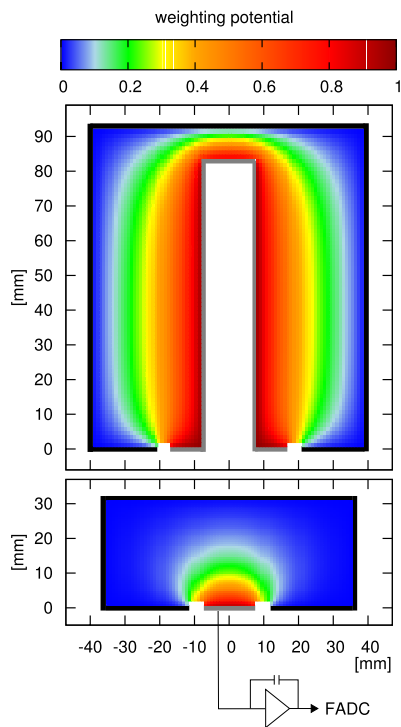


Fig. 1 Cross section of a semi-coaxial detector (*top*) and a BEGe detector (*bottom*). The $p+$ electrode is drawn in grey and the $n+$ electrode in black (thickness not to scale). The electrodes are separated by an insulating groove. Color profiles of the weighting potential [14] are overlaid on the detector drawings. Also sketched for the BEGe is the readout with a charge sensitive amplifier

electrode along very similar trajectories, irrespective where the energy deposition occurred [15]. For a localized deposition consequently, the maximum of the current pulse is nearly always directly proportional to the energy. Only depositions in a small volume of 3–6 % close to the $p+$ electrode exhibit larger current pulse maxima since electrons also contribute in this case [15, 16]. This behavior motivates the use of the ratio A/E for pulse shape discrimination (PSD) with A being the maximum of the current pulse and E being the energy. The current pulses are extracted from the recorded charge pulses by differentiation.

For double beta decay events ($0\nu\beta\beta$ or two-neutrino double beta decay, $2\nu\beta\beta$), the energy is mostly deposited at one location in the detector (SSE). Figure 2 (top left) shows an example of a possible SSE charge and current trace from the data. For SSE in the bulk detector volume one expects a nearly Gaussian distribution of A/E with a width dominated by the noise in the readout electronics.

For MSE, e.g. from multiple Compton scattered γ rays, the current pulses of the charges from the different locations will have—in general—different drift times and hence two

or more time-separated current pulses are visible. For the same total energy E , the maximum current amplitude A will be smaller in this case. Such a case is shown in the top right plot of Fig. 2.

For surface events near the $p+$ electrode the current amplitude, and consequently A/E , is larger and peaks earlier in time than for a standard SSE. This feature allows these signals to be recognized efficiently [17]. A typical event is shown in the bottom left trace of Fig. 2.

The $n+$ electrode is formed by infusion of lithium, which diffuses inwards resulting in a fast falling concentration profile starting from saturation at the surface. The $p-n$ junction is below the $n+$ electrode surface. Going from the junction towards the outer surface, the electric field decreases. The point when it reaches zero corresponds to the edge of the conventional $n+$ electrode dead layer, that is 0.8–1 mm thick (1.5–2.3 mm) for the BEGe (semi-coaxial) detectors. However, charges (holes) from particle interactions can still be transferred from the dead layer into the active volume via diffusion (see e.g. Ref. [18]) up to the point near the outer surface where the Li concentration becomes high enough to result in a significant recombination probability. Due to the slow nature of the diffusion compared to the charge carrier drift in the active volume, the rise time of signals from interactions in this region is increased. This causes a ballistic deficit loss in the energy reconstruction. The latter might be further reduced by recombination of free charges near the outer surface. The pulse integration time for A is ~ 100 times shorter than the one for energy causing an even stronger ballistic deficit and leading to a reduced A/E ratio. This is utilized to identify β particles penetrating through the $n+$ layer [19]. The bottom right trace of Fig. 2 shows a candidate event.

A pulse shape discrimination based on A/E has been developed in preparation for Phase II. It is applied here and has been tested extensively before through experimental measurements both with detectors operated in vacuum cryostats [16] and in liquid argon [20–22] as well as through pulse-shape simulations [15].

For double beta decay events, bremsstrahlung of electrons can reduce A and results in a low side tail of the A/E distribution while events close to the $p+$ electrode cause a tail on the high side. Thus the PSD survival probability of double beta decay is < 1 .

2.2 Semi-coaxial detectors

For semi-coaxial detectors, the weighting field also peaks at the $p+$ contact but the gradient is lower and hence a larger part of the volume is relevant for the current signal. Figure 3 shows examples of current pulses from localized energy depositions. These simulations have been performed using the software described in Refs. [15, 23]. For energy depositions

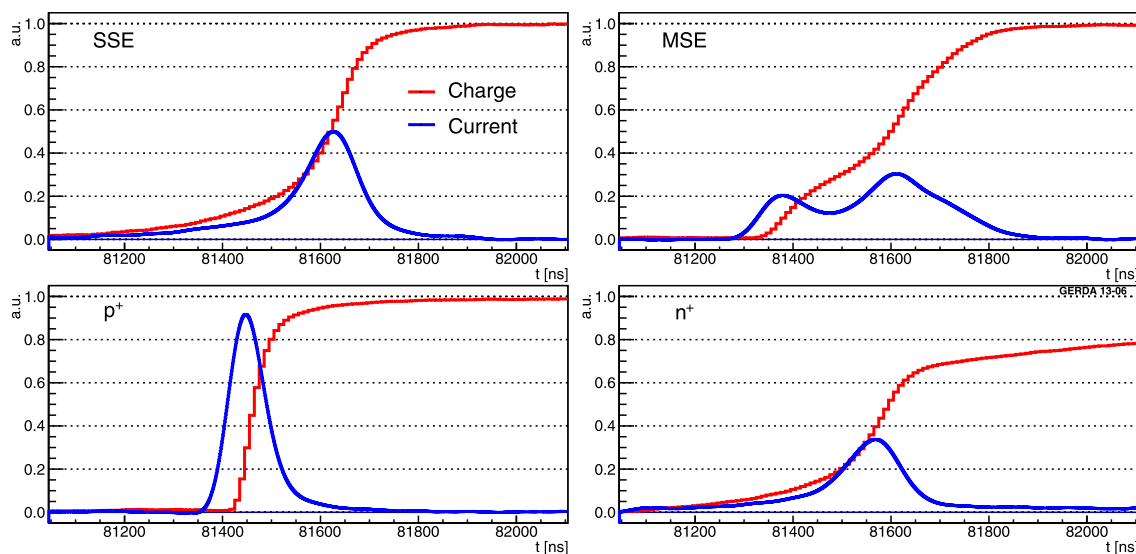


Fig. 2 Candidate pulse traces taken from BEGe data for a SSE (*top left*), MSE (*top right*), $p+$ electrode event (*bottom left*) and $n+$ surface event (*bottom right*). The maximal charge pulse amplitudes are

set equal to one for normalization and current pulses have equal integrals. The current pulses are interpolated

close to the $n+$ surface (at radius 38 mm in Fig. 3) only holes contribute to the signal and the current peaks at the end. In contrast, for surface $p+$ events close to the bore hole (at radius 6 mm) the current peaks earlier in time. This behavior is common to BEGe detectors. Pulses in the bulk volume show a variety of different shapes since electrons and holes contribute. Consequently, A/E by itself is not a useful variable for coaxial detectors. Instead three significantly different methods have been investigated. The main one uses an artificial neural network to identify single site events; the second one relies on a likelihood method to discriminate between SSE like events and background events; the third is based on the correlation between A/E and the pulse asymmetry visible in Fig. 3.

2.3 Pulse shape calibration

Common to all methods and for both detector types is the use of calibration data, taken once per week, to test the performance and—in case of pattern recognition programs—to train the algorithm. The ^{228}Th calibration spectrum contains a peak at 2614.5 keV from the ^{208}Tl decay. The double escape peak (DEP, at 1592.5 keV) of this line is used as proxy for SSE while full energy peaks (FEP, e.g. at 1620.7 keV) or the single escape peak (SEP, at 2103.5 keV) are dominantly MSE. The disadvantage of the DEP is that the distribution of the events is not homogeneous inside the detector as it is for $0\nu\beta\beta$ decays. Since two 511 keV photons escape, DEP events are dominantly located at the corners. Events due to

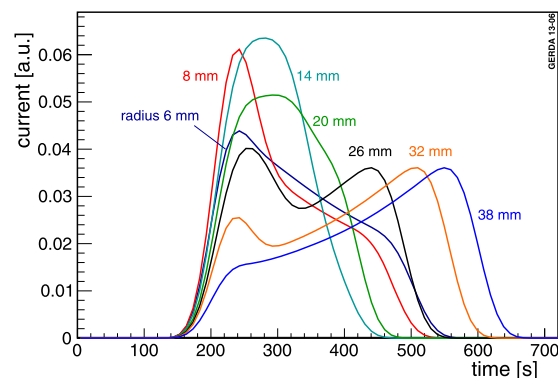


Fig. 3 Simulated pulse shapes for SSE in a semi-coaxial detector. The locations vary from the outer $n+$ surface (radius 38 mm) towards the bore hole (radius 6 mm) along a radial line at the midplane in the longitudinal direction. The integrals of all pulses are the same. The pulses are shaped to mimic the limited bandwidth of the readout electronics

Compton scattering of γ rays span a wide energy range and also contain a large fraction of SSE. Therefore they are also used for characterizing the PSD methods, especially their energy dependencies.

The $2\nu\beta\beta$ decay is homogeneously distributed and thus allows a cross check of the signal detection efficiency of the PSD methods.

3 Pulse shape discrimination for BEGe detectors

BEGe detectors from Canberra [11] feature not only a small detector capacitance and hence very good energy resolution but also allow a superior pulse shape discrimination of background events compared to semi-coaxial detectors. The PSD method and its performance is discussed in this section. The full period of BEGe data taking during Phase I (July 2012–May 2013) with an exposure of 2.4 kg yr is used in this analysis. One of the five detectors (GD35C) was unstable and is not included in the data set.

3.1 PSD calibration

Compton continuum and DEP events from ²²⁸Th calibration and the events in the 2νββ energy range in physics data feature A/E distributions with a Gaussian part from SSE and a low side tail from MSE as shown in Fig. 4. It can be fitted by the function:

$$f(x = A/E) = \frac{n}{\sigma_{A/E} \cdot \sqrt{2\pi}} \cdot e^{-\frac{(x-\mu_{A/E})^2}{2\sigma_{A/E}^2}} + m \cdot \frac{e^{f \cdot (x-l)} + d}{e^{(x-l)/t} + l} \tag{1}$$

where the Gaussian term is defined by its mean $\mu_{A/E}$, standard deviation $\sigma_{A/E}$ and integral n . The MSE term is parameterized empirically by the parameters m, d, f, l and t . $\sigma_{A/E}$ is dominated by the resolution σ_A of A which is independent of the energy, i.e. for low energies $\sigma_{A/E} \propto \sigma_A/E \propto 1/E$.

There are a few effects which are corrected in the order they are discussed below. To judge their relevance, already here it is stated that events in the interval $0.965 < A/E < 1.07$ are accepted as signal (see Sect. 3.2).

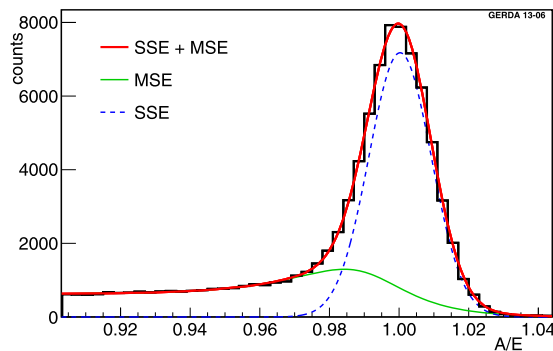


Fig. 4 A/E distribution for Compton continuum data fitted with function (1). The dashed blue curve is the Gaussian component and the green curve is the component approximating the MSE contribution (Color figure online)

1. After the deployment in July 2012, $\mu_{A/E}$ drifted with a time scale of about one month for all detectors (see Fig. 5). The total change was 1 to 5 % depending on the detector. The behavior is fitted with an exponential function which is then used to correct A/E of calibration and physics data as a function of time. Additionally, jumps occurred e.g. after a power failure. These are also corrected.
2. $\mu_{A/E}$ increases by up to 1 % during calibration runs which last typically one hour (Fig. 6). During physics data taking, $\mu_{A/E}$ returns to the value from before the calibration on a time scale of less than 24 hours, which is short compared to the one week interval between calibrations. This causes $\mu_{A/E}$ in calibrations to be shifted to slightly higher values compared to physics data taking. This effect is largely removed by applying a linear correction in time (fit shown in Fig. 6) to calibra-

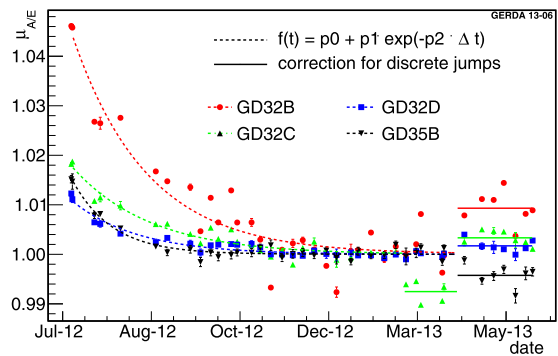


Fig. 5 Gaussian mean $\mu_{A/E}$ for DEP events for individual ²²⁸Th calibrations. The data points in the period before the occurrence of jumps are fitted with an exponential function as specified. Each A/E distribution is normalized such that the constant of the fit (p_0) is one. Separate constant corrections are determined as averages over the periods corresponding to the discrete jumps

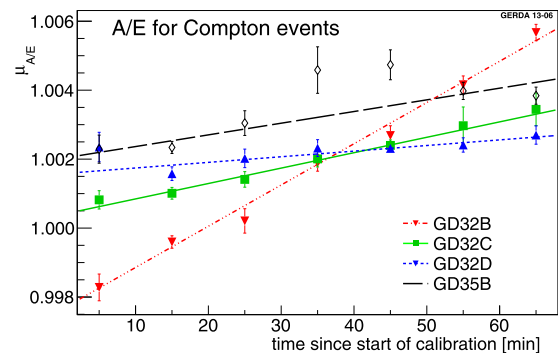


Fig. 6 Gaussian mean $\mu_{A/E}$ of the A/E distribution for Compton events as a function of the time since the start of a calibration run. The data from all calibrations are combined after the correction according to Fig. 5 has been applied

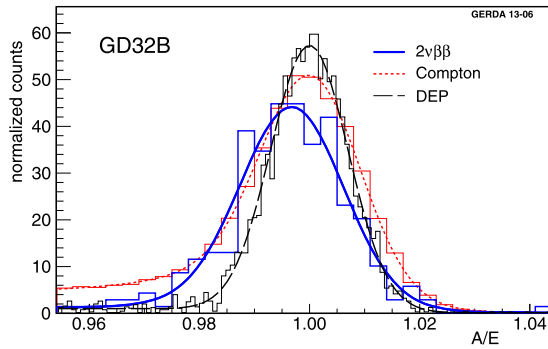


Fig. 7 A/E distribution of GD32B from physics data events between 1.0 and 1.3 MeV (blue, dominantly $2\nu\beta\beta$ decays), Compton continuum in the same energy range (red) and DEP events (black). The latter two are taken from the sum of all calibrations. All corrections are applied. The tail on the left side of the Gaussian is larger in the Compton events due to a higher fraction of MSE compared to the physics data in this energy range (Color figure online)

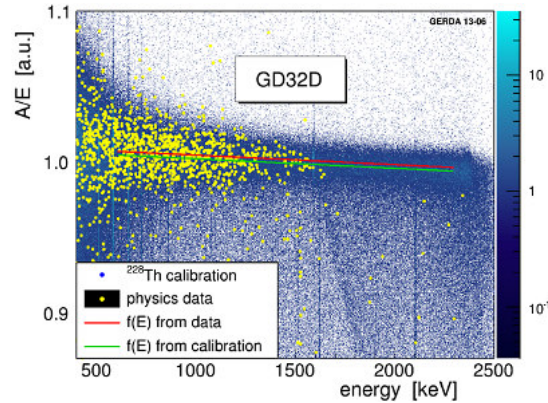


Fig. 8 A/E energy dependence shown with ^{228}Th calibration data (blue density plot) and events from physics data taking (predominantly $2\nu\beta\beta$, yellow points). The distributions of $\mu_{A/E}$ for the different energy bins are fitted with a linear function (green line). The $2\nu\beta\beta$ continuum is fitted with the same function, leaving only the constant of the fit free (red line). The data from GD32D are shown (Color figure online)

tion data. Afterwards, $\mu_{A/E}$ of physics data in the interval 1.0–1.3 MeV agrees approximately with Compton events from calibration data in the same energy region (see Fig. 7).

- A/E shows a small energy dependence (Fig. 8). It is measured by determining the Gaussian mean $\mu_{A/E}$ at different energies in the ^{208}Tl Compton continuum between 600 and 2300 keV. The size is about 0.5 to 1 % per MeV. This approach is documented and validated in Refs. [16, 24]. The correction is applied to both calibration and physics data.

The corrections discussed above are empirical and result in energy and time independent A/E distributions. The ori-

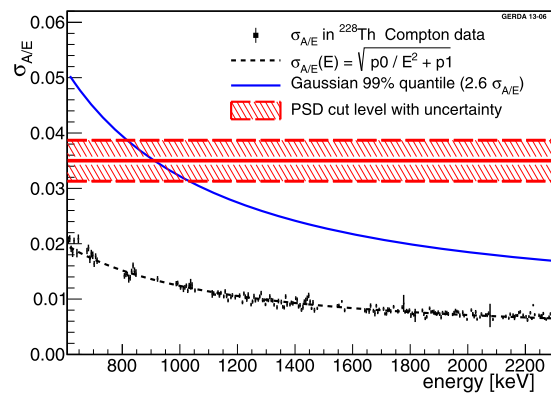


Fig. 9 Width $\sigma_{A/E}$ of the A/E Gaussian versus energy (points with error bars) for GD35B with a fit (black dashed line). The blue full line shows the 99 % quantile of the Gaussian ($2.6 \sigma_{A/E}$). The red horizontal line corresponds to the low side PSD cut distance from the nominal $\mu_{A/E} = 1$. The uncertainty band is given by the maximal deviation of the A/E scale as determined in Table 1 (Color figure online)

gin of the time drifts might be due to electric charges collected from LAr on the surface of the insulating groove. This is a known phenomenon [25] and pulse shape simulations show that A/E changes of the observed size are conceivable. The small observed energy dependence of A/E (item 3) is thought to be an artefact of data acquisition and/or signal processing.

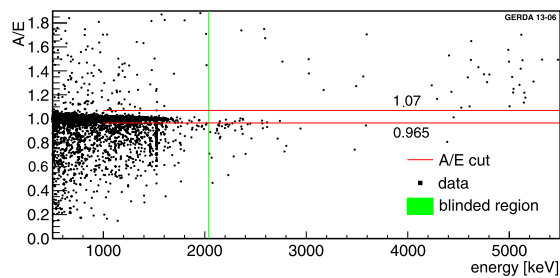
Since A/E has arbitrary units, it is convenient to rescale the distribution at the end such that the mean of the Gaussian is unity after all corrections. This eases the combination of all detectors.

The compatibility of calibration data with physics data after the application of all corrections is verified in Fig. 7. The A/E Gaussian parameters are quantitatively compared in Table 1. The agreement of $\mu_{A/E}$ for DEP and $2\nu\beta\beta$ events validates also the energy dependence correction (item 3). Small differences remain due to imperfections of the applied corrections. They will be taken into account as a systematic uncertainty in the determination of the $0\nu\beta\beta$ efficiency in Sect. 3.3.

In contrast to the SSE Gaussian, the MSE part of the A/E distribution and the part from $p+$ electrode events is only negligibly affected by the A/E resolution and its change with energy. This motivates the use of an A/E cut that is constant at all energies: If the cut position is many $\sigma_{A/E}$ of the Gaussian resolution away from one, the survival fraction is practically independent of the energy. Only at low energies this is no longer the case. At about 1 MeV, the cut position $A/E > 0.965$ corresponds to a separation from one by $2.6 \sigma_{A/E}$ corresponding to the 99 % quantile of a Gaussian (see Fig. 9). For lower energies the efficiency loss of the Gaussian peak becomes relevant. Therefore the efficiency determination is restricted to energies above 1 MeV.

Table 1 Comparison of A/E Gaussian mean $\mu_{A/E}$ and width $\sigma_{A/E}$ from physics data (events between 1.0 and 1.3 MeV, dominantly $2\nu\beta\beta$ decays) and calibration data (Compton continuum in the region 1.0–1.3 MeV and DEP at 1592.5 keV) after applying all corrections

Detector	$\mu_{A/E}(2\nu\beta\beta)-\mu_{A/E}(\text{DEP})$	$\mu_{A/E}(2\nu\beta\beta)-\mu_{A/E}(\text{Compton})$	$\sigma_{A/E}(2\nu\beta\beta)$	$\sigma_{A/E}(\text{Compton})$
GD32B	-0.0032 ± 0.0007	-0.0037 ± 0.0007	0.0094 ± 0.0006	0.0089 ± 0.0001
GD32C	-0.0001 ± 0.0011	0.0003 ± 0.0011	0.0096 ± 0.0005	0.0094 ± 0.0001
GD32D	-0.0002 ± 0.0009	0.0004 ± 0.0009	0.0118 ± 0.0006	0.0095 ± 0.0001
GD35B	0.0014 ± 0.0007	0.0018 ± 0.0008	0.0097 ± 0.0006	0.0109 ± 0.0001

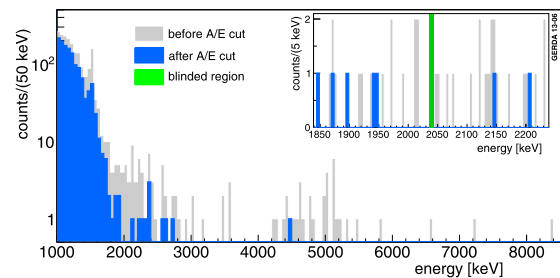

Fig. 10 A/E versus energy in a wide energy range for the combined BEGe data set. The acceptance region boundaries are marked by the red lines. The blinded region is indicated by the green band (Color figure online)

The energy dependence of $\mu_{A/E}$ is determined between 600 keV and 2300 keV. Since the dependence is weak, even beyond these limits the cut determination is accurate to within a few percent. This is acceptable for example to determine the fraction of α events at the $p+$ electrode passing the SSE selection cut.

3.2 Application of PSD to data

Figure 10 shows A/E plotted versus energy for physics data in a wide energy range together with the acceptance range. The data of all detectors have been added after all applicable corrections and the normalization of the Gaussian mean to one. The cut rejects events with $A/E < 0.965$ (“low A/E cut”) or $A/E > 1.07$ (“high A/E cut”). The high side cut interval was chosen twice wider due to the much lower occurrence and better separation of $p+$ electrode events. The cut levels result in a high probability to observe no background event in the final $Q_{\beta\beta}$ analysis window for the Phase I BEGe data set, while maintaining a large efficiency with small uncertainties. As can be seen from Fig. 9, at $Q_{\beta\beta}$ the cut is $\geq 4.5 \sigma_{A/E}$ apart from one.

Figure 11 shows the combined energy spectrum of the BEGe detectors before and after the PSD cut. In the physics data set with 2.4 kg yr exposure, seven out of 40 events in the 400 keV wide region around $Q_{\beta\beta}$ (excluding an 8 keV blinding window) are kept and hence the background for BEGe detectors is reduced from (0.042 ± 0.007) to $(0.007^{+0.004}_{-0.002})$ cts/(keV kg yr). In the smaller 230 keV region


Fig. 11 Energy spectrum of the combined BEGe data set: grey (blue) before (after) the PSD cut. The inset shows a zoom at the region $Q_{\beta\beta} \pm 200$ keV with the 8 keV blinded region in green (Color figure online)

three out of 23 events remain. Table 2 shows the surviving fractions for several interesting energy regions in the physics data and ^{228}Th calibration data. The suppression of the ^{42}K γ line at 1525 keV in physics data is consistent with the one of the ^{212}Bi line at 1621 keV. The rejection of α events at the $p+$ electrode is consistent with measurements with an α source in a dedicated setup [17].

The energy spectrum of the physics data can be used to identify the background components at $Q_{\beta\beta}$ as described in Ref. [1]. About half of the events are from ^{42}K decays on the $n+$ electrode surface which are rejected by the low side A/E cut with large efficiency [19]. About one third of the background at $Q_{\beta\beta}$ is due to ^{214}Bi and ^{208}Tl . Their survival probability can be determined from the calibration data (52 % for ^{208}Tl) or extrapolated from previous studies [21, 22] (36 % for ^{214}Bi). The remaining backgrounds e.g. from ^{68}Ga inside the detectors and from the $p+$ surface are suppressed efficiently [15, 17]. The rejection of 80 % of the physics events at $Q_{\beta\beta}$ is hence consistent with expectation.

In Fig. 12, the A/E distribution of physics data in the $Q_{\beta\beta} \pm 200$ keV region is compared with the distributions from different background sources. The peak at 0.94 can be attributed to $n+$ surface events. The A/E distribution of the other events is compatible within statistical uncertainty with the ones expected from the different background sources.

3.3 Evaluation of $0\nu\beta\beta$ cut survival fraction for BEGes

The PSD survival fraction of DEP events can vary from the one for $0\nu\beta\beta$ events because of the difference of the event

Table 2 Removed fractions by the low A/E cut and high A/E cut and total surviving fractions applying both cuts in several energy regions in physics data and ^{228}Th calibration data (combined data sets of all detectors). In the physics data set, the 1839–2239 keV region excludes the blinded 8 keV window around $Q_{\beta\beta}$. Peak regions have the underlying Compton continuum subtracted. Uncertainties are statistical only

Region	low A/E cut $A/E < 0.965$	high A/E cut $A/E > 1.07$	surviving fraction $0.965 < A/E < 1.07$
^{228}Th calibration			
DEP 1592.5 keV	0.054 ± 0.003	0.015 ± 0.001	0.931 ± 0.003
FEP 1620.7 keV	0.771 ± 0.008	0.009 ± 0.002	0.220 ± 0.008
SEP 2103.5 keV	0.825 ± 0.005	0.011 ± 0.001	0.165 ± 0.005
physics data			
FEP 1524.7 keV	0.69 ± 0.05	0.027 ± 0.015	0.29 ± 0.05
1000–1450 keV	0.230 ± 0.011	0.022 ± 0.004	0.748 ± 0.011
1839–2239 keV	30/40	3/40	7/40
>4 MeV (α at $p+$)	1/35	33/35	1/35

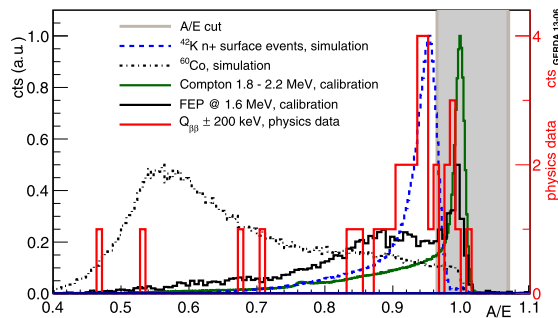


Fig. 12 A/E histogram of the physics data within 200 keV of $Q_{\beta\beta}$ (red) compared to Compton continuum events (green dot-dot-dashed) and 1621 keV FEP events (black) from calibration data. Also shown are simulations of ^{42}K decays at the $n+$ electrode surface (blue dashed) and ^{60}Co (black dot-dashed) [15]. The scalings of the histograms are arbitrary. Three physics data events have large A/E values ($p+$ electrode events) and are out of scale. The accepted interval is shown in grey (Color figure online)

locations in a detector (see Sect. 2.3) and due to the different energy release and the resulting bremsstrahlung emission.

The influence of these effects was studied by simulations. The first effect was irrelevant in past publications since only a low A/E cut was studied and $p+$ electrode events have higher A/E . In the present analysis, we required also $A/E < 1.07$. Therefore we use a pulse shape simulation of $0\nu\beta\beta$ events [15] to determine the rejected fraction of signal events by the high A/E cut.

The second effect can influence the low A/E cut survival. To estimate its size, we compare the pulse shape simulation result [15] with a Monte Carlo simulation [16] which selects events according to the bremsstrahlung energy. The latter is approximately equivalent to a cut on the spatial extent of the interaction since higher energy bremsstrahlung γ rays interact farther from the main interaction site (electron-positron pair creation vertex for DEP or $0\nu\beta\beta$ decay vertex). The fraction of DEP events with a Compton scattering before the pair creation was taken into account. The determined frac-

tion of MSE in DEP and $0\nu\beta\beta$ events was the same within uncertainties. In contrast, the pulse shape simulation removes 1.8 % events more for $A/E < 0.965$. This difference could be caused by a larger fraction of bremsstrahlung in $0\nu\beta\beta$ compared to DEP or due to simulation artefacts [15]. Here we follow the result of the Monte Carlo simulation, i.e. use the DEP survival fraction for the low A/E cut, and take the difference to the pulse shape simulation as systematic error.

Thus, the survival fraction $\epsilon_{0\nu\beta\beta}$ of the $0\nu\beta\beta$ signal is estimated as follows:

- the rejected fraction for the low side cut of 0.054 is determined from DEP events (Table 2). This value varies from 0.042 ± 0.006 to 0.062 ± 0.010 for the different detectors and is hence within uncertainties the same for all of them.
- the rejected fraction by the high A/E cut of 0.025 is determined from the $0\nu\beta\beta$ pulse-shape simulation [15].

Finally, the efficiency is $\epsilon_{0\nu\beta\beta} = 0.92 \pm 0.02$. The uncertainty is the quadratic sum of the following components:

- statistical uncertainty of the DEP survival fraction: 0.003
- uncertainty from the A/E energy dependence (item 3 in Sect. 3.1): 7.5×10^{-5}
- uncertainty due to the residual differences between calibration and physics data (change of the cut by the largest difference between $\mu_{A/E}$ for $2\nu\beta\beta$ and Compton events in Table 1): 0.004
- systematic uncertainty due to the difference between the survival fraction of $0\nu\beta\beta$ from the pulse shape simulation [15] and the one measured with DEP events: 0.018.

The $0\nu\beta\beta$ survival fraction can be cross checked with the one determined for $2\nu\beta\beta$ decays. The energy region is chosen between 1 and 1.45 MeV to exclude the γ lines at 1461 keV from ^{40}K and 1525 keV from ^{42}K . The spectral decomposition of the BEGe data [1] yields a fraction of $f_{2\nu\beta\beta} = 0.66 \pm 0.03$ of $2\nu\beta\beta$ decays. The parts f_i of the remaining components are listed in Table 3 together with the PSD survival fractions ϵ_i . The background origins mostly

Table 3 Decomposition of events in the region between 1 MeV and 1.45 MeV. Listed are the estimated fraction f_i [1] and the total efficiency ϵ_i for each component i

Component	f_i	ϵ_i
^{40}K	0.032 ± 0.009	0.56 ± 0.03
^{42}K in LAr	0.187 ± 0.022	0.49 ± 0.05
^{42}K at $n+$ surface	0.030 ± 0.017	0.30 ± 0.04
^{60}Co	0.013 ± 0.013	0.29 ± 0.02
^{60}Co intrinsic	0.002 ± 0.001	0.21 ± 0.02
^{68}Ga intrinsic	0.007 ± 0.007	0.33 ± 0.02
^{214}Bi	0.036 ± 0.014	0.41 ± 0.02
^{228}Th	0.003 ± 0.002	0.54 ± 0.03
$p+$ events	0.003 ± 0.002	0.02 ± 0.02
other	0.024 ± 0.024	0.45 ± 0.45

from Compton scattered γ quanta. The fractions ϵ_i were extrapolated from several studies involving experimental measurements as well as simulations. For ^{228}Th , ϵ_i is determined from present calibration data.

The PSD survival fraction for $2\nu\beta\beta$ decays $\epsilon_{2\nu\beta\beta}$ is then related to the overall PSD survival fraction for events in the interval $\epsilon_{\text{data}} = 0.748 \pm 0.011$ (Table 2) by:

$$\epsilon_{\text{data}} = f_{2\nu\beta\beta} \cdot \epsilon_{2\nu\beta\beta} + \sum_i f_i \cdot \epsilon_i \quad (2)$$

The resulting survival fraction of $2\nu\beta\beta$ events is $\epsilon_{2\nu\beta\beta} = 0.90 \pm 0.05$. This number needs a small correction due to decays in the $n+$ transition layer. The long pulse rise time for these events (see Sect. 2.1) leads to a ballistic deficit in the reconstructed energy, i.e. $0\nu\beta\beta$ events do not reconstruct at the peak position. This loss is already accounted for in the definition of the dead layer thickness. For $2\nu\beta\beta$ events the energy spectrum is continuous, i.e. the effective dead volume is smaller. But A/E is reduced as well and a fraction of about 0.015 ± 0.005 is rejected according to simulations. For the comparison with the $0\nu\beta\beta$ PSD survival fraction, this correction should be added such that finally a fraction of 0.91 ± 0.05 is obtained. It agrees well with $\epsilon_{0\nu\beta\beta} = 0.92 \pm 0.02$.

3.4 PSD summary for BEGe detectors

Due to their small area $p+$ contact BEGe detectors offer a powerful pulse shape discrimination between ^{76}Ge $0\nu\beta\beta$ signal events of localized energy deposition and background events from multiple interactions in the detector or energy deposition on the surface.

The parameter A/E constitutes a simple discrimination variable with a clear physical interpretation allowing a robust PSD analysis. The characteristics of this quantity have been studied for several years and are applied for the first

time in a $0\nu\beta\beta$ analysis. ^{228}Th data taken once per week are used to calibrate the performance of A/E and to correct for the observed time drifts and small energy dependencies. The whole procedure of the PSD analysis was verified using $2\nu\beta\beta$ events from ^{76}Ge recorded during physics data taking.

The chosen cut accepts a fraction of 0.92 ± 0.02 of $0\nu\beta\beta$ events and rejects 33 out of 40 events in a 400 keV wide region around $Q_{\beta\beta}$ (excluding the central 8 keV blinded window). The latter is compatible with the expectation given our background composition and PSD rejection. The background index is reduced to $(0.007^{+0.004}_{-0.002})$ cts/(keV kg yr).

Applying the PSD cut to $2\nu\beta\beta$ events results in an estimated $0\nu\beta\beta$ signal survival fraction of 0.91 ± 0.05 that agrees very well with the value extracted from DEP and simulations.

4 Pulse shape discrimination for semi-coaxial detectors

In the current Phase I analysis, three independent pulse shape selections have been performed for the semi-coaxial detectors. They use very different techniques but it turns out that they identify a very similar set of events as background. The neural network analysis will be used for the $0\nu\beta\beta$ analysis while the other two (likelihood classification and PSD selection based on the pulse asymmetry) serve as cross checks.

All methods optimize the event selection for every detector individually. They divide the data into different periods according to the noise performance. Two detectors (ANG 1 and RG 3) had high leakage current soon after the deployment. The analyses discussed here consider therefore only the other six coaxial detectors.

4.1 Pulse shape selection with a neural network

The entire current pulse or—to be more precise—the rising part of the charge pulse is used in the neural network analysis. The following steps are performed to calculate the input parameters:

- baseline subtraction using the recorded pulse information in the 80 μs before the trigger. If there is a slope in the baseline due to pile up, the event is rejected. This selection effects practically only calibration data,
- smoothing of the pulse with a moving window averaging of 80 ns integration time,
- normalization of the maximum pulse height to one to remove the energy dependence,
- determination of the times when the pulse reaches 1, 3, 5, ..., 99 % of the full height. The time when the pulse height reaches $A_1 = 50\%$ serves as reference. Due to the 100 MHz sampling frequency, a (linear) interpolation is required between two time bins to determine the corresponding time points (see Fig. 13).

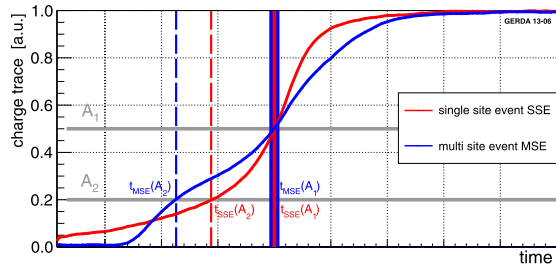


Fig. 13 Example physics data pulses for SSE and MSE candidate events. The determination of the input parameters for the TMVA algorithms is shown for pulse heights A_1 and A_2

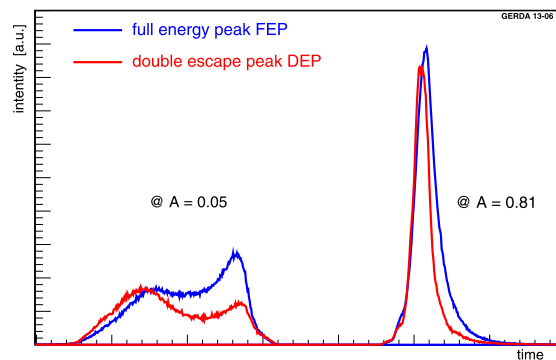


Fig. 14 Time distribution for crossing the 5% (left) and 81% (right) pulse height for ^{228}Th calibration events with energy close to the DEP (red) and close to the 1621 keV FEP (blue) (Color figure online)

The resulting 50 timing informations of each charge pulse are used as input to an artificial neural network analyses. The TMVA toolkit implemented in ROOT [26] offers an interface for easy processing and evaluation. The selected algorithm TMlpANN [27] is based on multilayer perceptrons. Two hidden layers with 51 and 50 neurons are used. The method is based on the so called “supervised learning” algorithm.

Calibration data are used for training. DEP events in the interval $1593 \text{ keV} \pm 1\text{-FWHM}$ serve as proxy for SSE while events of the full energy line of ^{212}Bi in the equivalent interval around 1621 keV are dominantly MSE and are taken as background sample. Figure 14 shows as an example of the separation power the distribution of the time of 5% and 81% pulse height for the two event classes. Note that both event classes are not pure samples but a mixture of SSE and MSE because of the Compton events under the peaks.

The calibrations are grouped in three intervals. The first period spans from the start of data taking to July 2012 when the detector configuration and some electronics was changed (p1). The second period (p2) lasts the first four weeks afterwards and the third period (p3) the rest of Phase I. For RG 2,

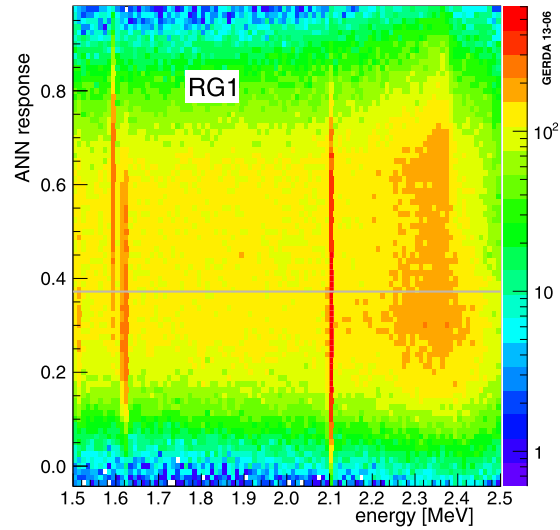


Fig. 15 TMlpANN response versus energy for ^{228}Th calibration events. Shown is the distribution for RG 1. The line at ~ 0.38 marks the position for 90% DEP survival fraction

the second period spans until November 2012 when its operating voltage was reduced. For each period at least 5000 events are available per detector and event class for training.

The output of the neural network is a qualifier, i.e. a number between ≈ 0 (background like event) and ≈ 1 (signal like event). Figure 15 shows a scatter plot of this variable versus the energy. The distribution peaks for DEP events at higher qualifier values while for FEP events at 1621 keV and SEP events at 2104 keV the intensity is shifted to lower values. The qualifier distribution from Compton events at different energies can be compared to estimate a possible energy dependence of the selection (see Fig. 16). For most detectors no drift is visible. Only RG 2 shows a larger variation. An energy dependent empirical correction of the qualifier is deduced from such distributions.

The qualifier threshold which keeps 90% of the DEP events is determined for each detector and each period individually. The cut values vary between 0.31 and 0.42. Figure 17 shows a ^{228}Th calibration spectrum with and without PSD selection. For the analysis, the survival fraction of MSE is studied. The survival is defined as the fraction of the peak content remaining after the cut, i.e. the Compton events under the peak are subtracted by scaling linearly the event counts from energies below and above the peak. The fractions are listed in Table 4 for the different periods. The last column lists the number of events in the 230 keV window around $Q_{\beta\beta}$ before and after the cut. About 45% of the events are classified as background.

Figure 18 shows the ANN response for DEP and SEP events. Shown are also the qualifier distributions for differ-

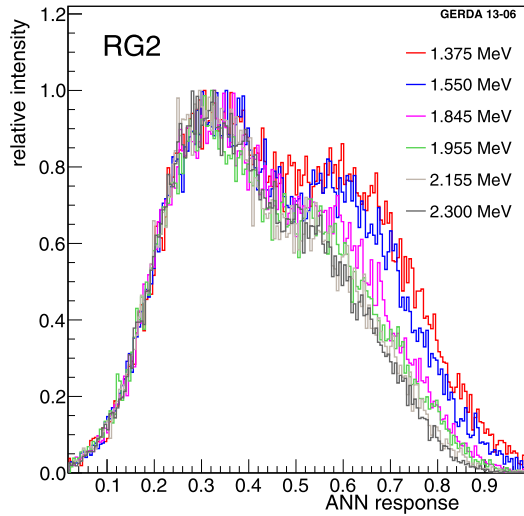


Fig. 16 TMIpANN response for Compton events for RG 2 at different energies. The energy dependence for RG 2 is about twice bigger than for any other detector

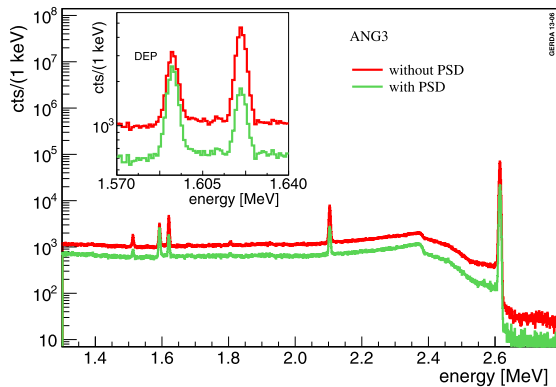


Fig. 17 ²²⁸Th calibration spectrum without and with TMIpANN pulse shape discrimination for ANG 3. The PSD cut is fixed to retain 90 % of DEP events (see inset)

ent samples from physics data taking: from the interval 1.0–1.4 MeV (dominantly $2\nu\beta\beta$ events, MSE part subtracted), from the 1525 keV ⁴²K γ line (dominantly MSE) and the qualifier for events in the 230 keV window. The events from the 1525 keV gamma peak are predominantly MSE and the shape agrees with the SEP distribution. The events in the 1.0–1.4 MeV region are dominantly SSE and their distribution agrees quite well with the one for DEP events. The red curve shows the DEP survival fraction versus the cut position (right scale).

The training was performed for the periods individually by combining all calibration data. The rules can then be applied to every single calibration to look for drifts in time.

Table 4 Survival fractions of the neural network PSD for different event classes and different detectors. Numbers are given for calibration (cal.) or physics data from the periods p1, p2 and p3. The statistics of physics data for p2 are small and hence not always listed. “ $2\nu\beta\beta$ ” stands for the 1.0–1.4 MeV interval which consists dominantly of $2\nu\beta\beta$ decays. ⁴²K signifies the 1525 keV full energy peak. ROI is here the 230 keV window around $Q_{\beta\beta}$. The errors are typically 0.01 for SEP and ROI for calibration, 0.02 for the $2\nu\beta\beta$ data interval and 0.06 for the ⁴²K γ peak. The last column list the event count after/before the PSD cut

det.	period	cal.		data		
		SEP	ROI	$2\nu\beta\beta$	⁴² K	ROI
ANG 2	p1	0.33	0.58	0.74	0.30	2/4
ANG 2	p2	0.50	0.65	0.65		0/1
ANG 2	p3	0.47	0.63	0.73	0.40	6/8
ANG 3	p1	0.32	0.56	0.79	0.43	6/9
ANG 3	p2	0.34	0.56	0.75		2/3
ANG 3	p3	0.40	0.63	0.82	0.44	4/6
ANG 4	p1	0.29	0.54	0.78	0.45	1/1
ANG 4	p2	0.28	0.53	0.63		0/1
ANG 4	p3	0.33	0.58	0.83	0.44	2/4
ANG 5	p1	0.26	0.55	0.79	0.41	2/11
ANG 5	p2	0.21	0.45	0.57		0/2
ANG 5	p3	0.33	0.59	0.80	0.30	6/16
RG 1	p1	0.45	0.63	0.80	0.52	2/6
RG 1	p2	0.43	0.60	0.77		2/3
RG 1	p3	0.41	0.62	0.81	0.48	3/4
RG 2	p1	0.30	0.53	0.82	0.49	10/12
RG 2	p2	0.37	0.60	0.81	0.48	3/3
RG 2	p3	0.45	0.61	0.76	0.56	2/2

Figure 19 shows the DEP survival fraction (blue triangles) for the entire Phase I from November 2011 to May 2013 for all detectors. The plots show a stable performance. Also shown are the equivalent entries (red circles) for events with energy around the SEP position. For several detectors the rejection of MSE is not stable. Especially visible is the deterioration starting in July 2012. This is related to different conditions of high frequency noise.

The distribution of the qualifier for all events in the 230 keV window around $Q_{\beta\beta}$ is shown in Fig. 20. Events rejected by the neural network are marked in red. Circles mark events rejected by the likelihood method and diamonds those rejected by the method based on the current pulse asymmetry. Both methods are discussed below. In the shown energy interval, all events removed by the neural network are also removed by at least one other method and for about 90 % of the cases, all three methods discard the events. In a larger energy range about 3 % of the rejected events are only identified by the neural network.

Figure 21 shows the energy spectrum of all semi-coaxial detectors added up before and after the PSD selection.

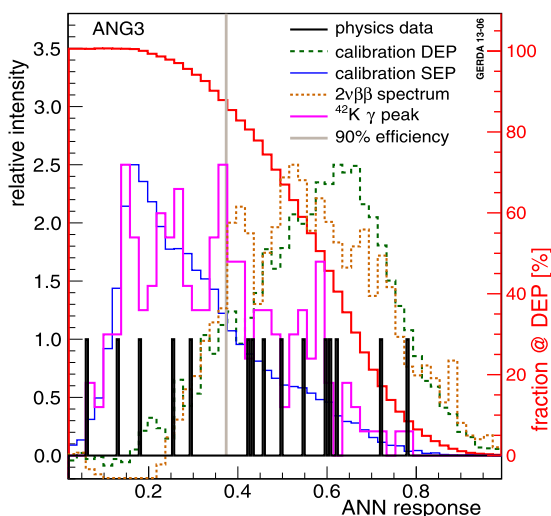


Fig. 18 ANN response for ^{228}Th calibration events for DEP (green, long dashes) and SEP (dark blue) for ANG 3 in the first period. The distributions from Compton events at these energies are subtracted statistically using events in energy side bands. Also shown in black are the qualifier values of events from physics data taking from a 230 keV window around $Q_{\beta\beta}$. The grey vertical line marks the cut position. Physics data events from the 1525 keV FEP of ^{42}K are shown in magenta and the ones from the interval 1.0–1.4 MeV by brown dashes (dominantly $2\nu\beta\beta$, MSE part subtracted) (Color figure online)

4.2 Systematic uncertainty of the neural network signal efficiency

In this analysis we use the survival fraction of DEP events as efficiency for $0\nu\beta\beta$ events.

The distribution of DEP events in a detector is not homogeneous since the probability for the two 511 keV photons to escape is larger in the corners. It is therefore conceivable that the ANN—instead of selecting SSE—is mainly finding events at the outer surface. The DEP survival fraction would in this case not represent the efficiency for $0\nu\beta\beta$ decay which are distributed homogeneously in the detector.

$2\nu\beta\beta$ events are also SSE and homogeneously distributed inside the detector. Hence a comparison of its pulse shape identification efficiency with the preset 0.90 value for DEP events is a powerful test.

Another SSE rich sample are events at the Compton edge of the 2614.5 keV γ line. The energy range considered is 2.3–2.4 MeV, i.e. higher than $Q_{\beta\beta}$. The comparison to the DEP survival fraction allows also to check for an energy dependence. The distribution of Compton edge events in detector volume is similar to DEP.

4.2.1 Efficiency of $2\nu\beta\beta$ for neural network PSD

The energy range between 1.0 and 1.3 MeV (position of the Compton edge of the 1525 keV line) is suited for the com-

parison of the SSE efficiency. At lower energies the electronic noise will deteriorate the discrimination between SSE and MSE. In this interval, the data set consists to a fraction $f_{2\nu\beta\beta} = 0.76 \pm 0.01$ of $2\nu\beta\beta$ decays according to the GERDA background model [1]. The remaining 24 % are Compton events predominantly of the 1525 keV line from ^{42}K decays, of the 1460 keV line from ^{40}K decays and from ^{214}Bi decays. Hence it is a good approximation to use the pulse shape survival fraction $\epsilon_{\text{Compton}}$ from the calibration data to estimate the suppression of the events not coming from $2\nu\beta\beta$ decays. Typical values for $\epsilon_{\text{Compton}}$ are between 0.6 and 0.7 for the different detectors, i.e. higher than the values quoted in Table 4 due to a small energy dependence (see Fig. 17).

Figure 22 shows the physics data (red) overlaid with the background model (blue, taken from Ref. [1]) and the same distributions after the PSD cut (in magenta for the data and in light blue for the model). For the model, the $2\nu\beta\beta$ fraction is scaled by the DEP survival rate while the remaining fraction is scaled according to $\epsilon_{\text{Compton}}$ taken from the ^{228}Th calibration data for each detector. Both pairs of histograms agree roughly in the range 1.0–1.3 MeV. This is qualitatively confirmed if the $2\nu\beta\beta$ PSD efficiency is calculated using (2). Its distribution is also shown as the green filled histogram in Fig. 22. The average efficiency for the range 1.0–1.3 MeV is $\epsilon_{2\nu\beta\beta} = 0.85 \pm 0.02$ where the error is dominated by the systematic uncertainty of $\epsilon_{\text{Compton}}$. The latter is estimated by a variation of the central value by 10 % which is the typical variation of $\epsilon_{\text{Compton}}$ between 1 MeV and 2 MeV.

The obtained efficiency $\epsilon_{2\nu\beta\beta}$ is close to the DEP survival fraction of $\epsilon_{\text{DEP}} = 0.9$ and indicates that there are no sizable systematic effects related to the differences in the distribution of DEP and $2\nu\beta\beta$ events in the detectors.

4.2.2 Neural network PSD survival fraction of Compton edge events

Calibration events at the Compton edge of the 2615 keV γ line, i.e. in the region close to 2.38 MeV, are enhanced in SSE and distributed similar to DEP events in the detector. The qualifier distribution for these events can be approximated as a linear combination of the DEP distribution and the one from multiple Compton scattered γ ray events (MCS). Events with energy larger than the Compton edge (e.g. in the interval 2420–2460 keV) consists almost exclusively of MCS. The total counts in the qualifier interval 0 to 0.2 for Compton edge events and MCS are used for normalization and the MCS distribution is then subtracted.

The “MCS subtracted” Compton edge distribution (red curve in Fig. 23) shows an acceptable agreement with the DEP distribution (green dotted curve). The survival fraction is defined as the part above the selection cut. Its value varies for the 3 periods and the 6 detectors between 0.85 and 0.94.

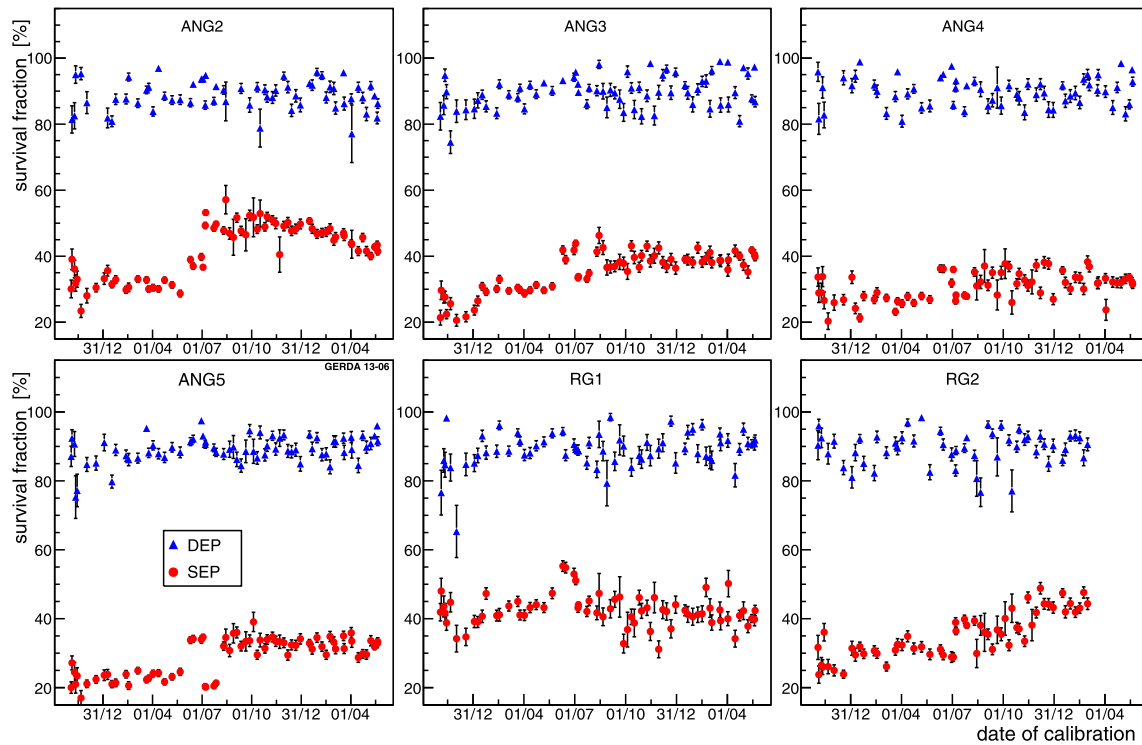


Fig. 19 DEP (blue) and SEP (red) survival fraction for individual calibrations for the entire Phase I (Color figure online)

No systematic shift relative to the DEP value e.g. due to an energy dependence of the efficiency is visible. If SEP events are used to model the multi site event contribution, consistent values are obtained.

4.2.3 Summary of systematic uncertainties

The cross checks of the PSD efficiency address a possible energy dependence and a volume effect due to the different distributions of DEP and $0\nu\beta\beta$ events. All studies performed are based on calibration or physics data and are hence independent of simulations.

The possible deviations from 0.90 seen are combined quadratically and scaled up to allow for additional sources of systematic uncertainties. The $0\nu\beta\beta$ efficiency is $\epsilon_{ANN} = 0.90^{+0.05}_{-0.09}$.

4.3 Alternative PSD methods

Two more PSD methods have been developed. They are used here to cross check the event selection of the neural network method (see Fig. 20). No systematic errors for the signal efficiency has been evaluated for them.

4.3.1 Likelihood analysis

In a second PSD analysis, 8 input variables calculated from the charge pulse trace are used as input to the projective likelihood method implemented in TMVA. Each input variable is the sum of four consecutive pulse heights of 10 ns spacing after baseline subtraction and normalization by the energy. The considered trace is centered around the time position where the derivative of the original trace is maximal, i.e. around the maximum of the current.

The training is performed for two periods: before (pI) and after (pII) June 2012. Instead of DEP events, the Compton edge in the interval 2350–2370 keV is used as signal region and the interval 2450–2570 keV as background sample. The latter contains only multiple Compton scattered photons and is hence almost pure MSE. The Compton edge events are a mixture of SSE and MSE. From the two samples a likelihood function for signal L_{sig} and background L_{bkg} like events is calculated and the qualifier q_{PL} is the ratio $q_{\text{PL}} = L_{\text{sig}} / (L_{\text{sig}} + L_{\text{bkg}})$.

Figure 24 shows for the calibration data the scatter plot of the qualifier versus energy. The separation of DEP (1593 keV) and FEP at 1621 keV is visible by the different population densities at low and high qualifier values. The

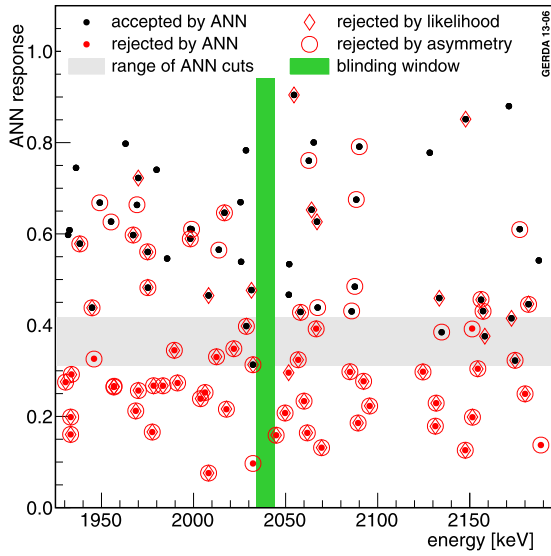


Fig. 20 Neural network qualifier for events with energy close to $Q_{\beta\beta}$. Events marked by a red dot are rejected. Circles and diamonds mark events which are rejected by the likelihood analysis and the method based on the pulse asymmetry, respectively (Color figure online)

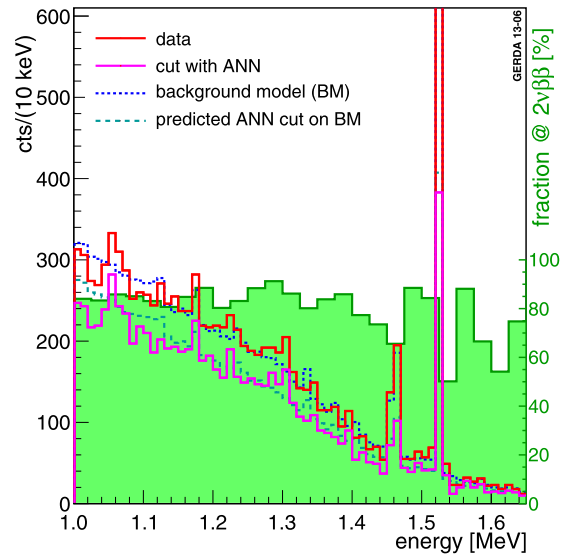


Fig. 22 Effect of the PSD selection on the data (in red and magenta) and the expected effect on the background model (dark blue dotted and light blue dashed). Overlaid is also the extracted PSD efficiency (green filled histogram) for $2\nu\beta\beta$ events (right side scale) (Color figure online)

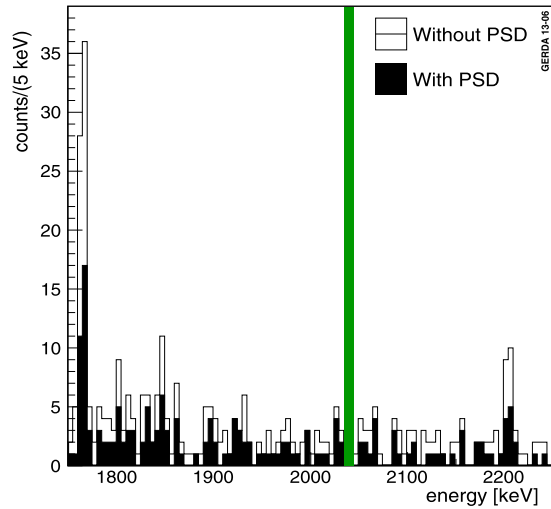


Fig. 21 Energy spectrum of semi-coaxial detectors with and without neural network PSD selection

cut position is independent of energy and fixed to about 0.80 survival fraction for DEP events. The SEP survival fractions and for comparison also the ones for several other subsets are listed in Table 5. About 65 % of the events in the 230 keV window around $Q_{\beta\beta}$ are rejected.

Figure 25 shows the distribution of the qualifier for different event classes. The distribution for physics data events

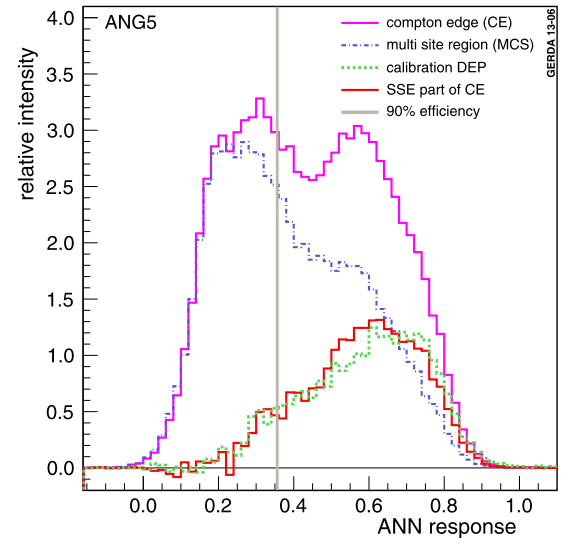


Fig. 23 Qualifier distribution for events at the Compton edge (magenta) as a linear combination of MCS (blue) and DEP (green dotted) distributions. The Compton edge distribution after the subtraction of the SEP part is shown in red (Color figure online)

from the ^{42}K line are well described by the FEP distribution in calibration data and the events in the 1.0–1.4 MeV interval are clearly enhanced in SSE as expected for $2\nu\beta\beta$ events.

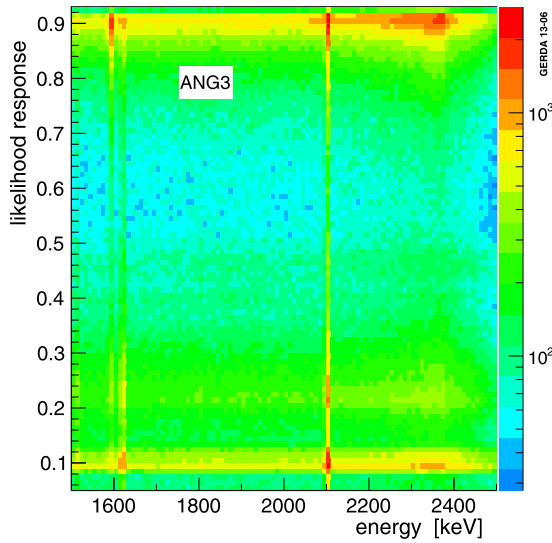


Fig. 24 Likelihood response versus energy distribution for ^{228}Th calibration events. Data are shown for ANG 3

Table 5 Survival fractions of the projective likelihood PSD for different event classes and the different detectors. The cut for each subset is set to yield a DEP survival fraction of 0.8. Numbers are given for calibration data (cal.) or physics data. pI and pII indicate the two periods. The meaning of the columns are identical to Table 4 and the same applies to the size of statistical errors for the different samples

det.	period	cal.		data		
		SEP	ROI	$2\nu\beta\beta$	^{42}K	ROI
ANG 2	pI	0.47	0.57	0.61	0.35	1/3
ANG 2	pII	0.50	0.56	0.57	0.37	4/10
ANG 3	pI	0.49	0.58	0.60	0.36	2/7
ANG 3	pII	0.52	0.61	0.64	0.40	3/11
ANG 4	pI	0.52	0.60	0.65	0.54	1/1
ANG 4	pII	0.50	0.62	0.71	0.51	2/5
ANG 5	pI	0.45	0.57	0.62	0.42	0/8
ANG 5	pII	0.40	0.51	0.61	0.31	3/21
RG 1	pI	0.50	0.63	0.63	0.59	2/6
RG 1	pII	0.51	0.62	0.65	0.46	2/7
RG 2	pI	0.49	0.60	0.70	0.46	6/8
RG 2	pII	0.51	0.61	0.63	0.50	7/9

4.3.2 PSD based on pulse asymmetry

In a third approach, only two variables are used to select single site events for the semi-coaxial detectors. As discussed above, the A/E variable alone is not a good parameter for semi-coaxial detectors. However, if A/E is combined with the pulse asymmetry, the PSD selection is much more effec-

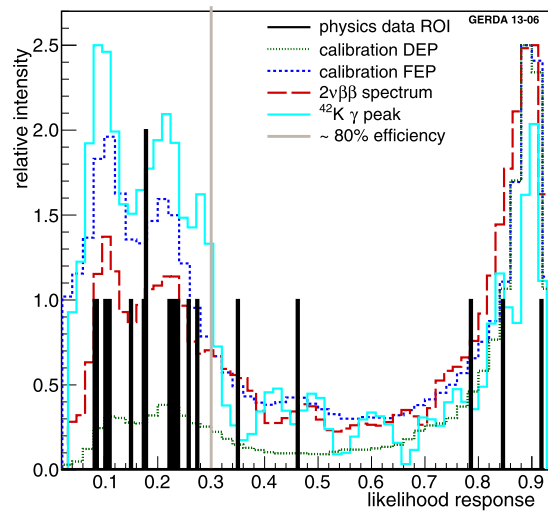


Fig. 25 Likelihood response for ^{228}Th calibration DEP (green dotted) and FEP (dark blue dashed) events for ANG 3. The distributions from Compton events at these energies are subtracted statistically using events in energy side bands. Also shown in black are the qualifier values of events from physics data taking from a 230 keV window around $Q_{\beta\beta}$. The grey vertical line marks the cut position. Shown are also distributions of physics data events from the ^{42}K γ line (light blue) and from the interval 1.0–1.4 MeV (red, dominantly $2\nu\beta\beta$) (Color figure online)

tive. The asymmetry A_s is defined as

$$A_s = \frac{\sum_{i=0}^{i=n_m} I(i) - \sum_{i=n_m}^{i=200} I(i)}{\sum_{i=0}^{i=200} I(i)} \quad (3)$$

Here $I(i)$ is the current pulse height, i.e. the differentiated charge pulse at time i , and n_m the time position of the maximum. A window of 200 samples (i.e. a 2 μs time interval) around the time of the trigger is analyzed.

To reduce noise, different moving window averaging with integration times of 0 (no filter), 20, 40, 80, 160 and 320 ns for the charge pulse are applied. For each shaping time, A/E and A_s are determined. Empirically, the combination

$$q_{AS} = A/E \cdot (c + A_s) \quad (4)$$

exhibits good PSD performance. For SSE, the current pulse might contain more than one maximum (Fig. 3). To reduce ambiguities, A_s is shaped with larger integration times.

An optimization is performed by comparing the DEP survival fraction ϵ_{DEP} from calibration data to the fraction of background events f_{bkg} between 1700 and 2200 keV (without a 40 keV blinded interval around $Q_{\beta\beta}$) that remains after the PSD selection. The lower cut value of the qualifier q_{AS} is determined by maximizing the quantity $S = \epsilon_{\text{DEP}} / \sqrt{f_{\text{bkg}} + 3/N_{\text{bkg}}}$; the upper cut is fixed at $\approx +4\sigma$ of

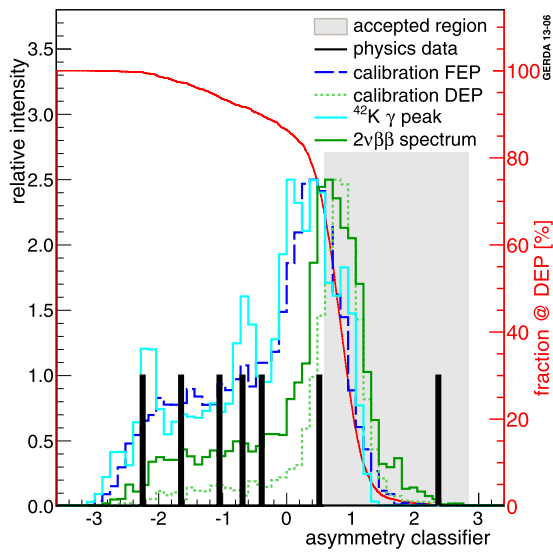


Fig. 26 Distribution of qualifier for DEP (dotted green) and FEP (dashed dark blue) calibration events for ANG 3 after a statistical subtraction of the Compton events below the peaks. The grey band marks the acceptance range. Overlaid are also the PSD qualifier for physics data in the 230 keV window around $Q_{\beta\beta}$ (black), data events from the 1525 keV ^{42}K peak (light blue) and from the interval 1.0–1.4 MeV (dark green dotted). The DEP survival fraction is displayed in red (right scale) (Color figure online)

the Gaussian width of the DEP qualifier distribution (see Fig. 26). All combinations of shaping times for A/E and A_s are scanned as well as different values for c in the range of 1–4. The one with the highest S is selected.

The term $3/N_{\text{bkg}}$ with N_{bkg} being the total number of background events is added to avoid an optimization for zero background. For $N_{\text{bkg}} \approx 40$ the optimization yields a DEP survival fraction of 0.7–0.9 (see Table 6) and about 75 % of the events in the interval 1.7–2.2 MeV are rejected.

Figure 27 shows a scatter plot of the PSD qualifier versus the energy. A separation between the DEP and multi site events at the energy of the FEP or SEP is visible. Figure 26 shows qualifier distributions for DEP and FEP calibration events after Compton events below the peaks are statistically subtracted. Overlaid is also the PSD qualifier for physics data in the 230 keV window around $Q_{\beta\beta}$ (black histogram), from the 1525 keV γ line (light blue) and the interval 1.0–1.4 MeV (yellow). The right scale shows the DEP survival fraction (red) as a function of the cut position. The grey area indicates the accepted range. The qualifier distribution of physics data around $Q_{\beta\beta}$ has a larger spread than the one of FEP events. This is the reason why events at $Q_{\beta\beta}$ are rejected stronger than MSE (see Table 6). A possible explanation is that the physics data contain a large fraction of events which are not MSE. These can be for example surface $p+$

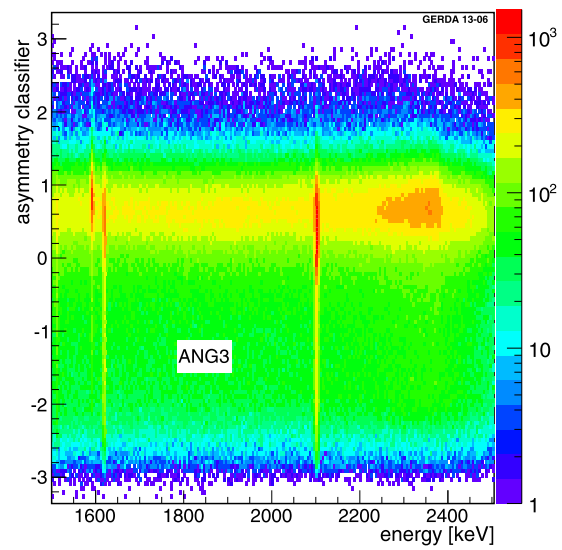


Fig. 27 Distribution of the ANG 3 qualifier versus energy for ^{228}Th calibration data for the PSD based on the pulse asymmetry

Table 6 Survival fractions of the PSD based on the current pulse asymmetry for different event classes and the different detectors. Numbers are given for calibration data (cal.) or physics data. pI and pII stand for the two periods. The DEP survival fractions are listed in the third column. Note that the selection of data files is slightly different for this analysis such that the total observed event counts (last column) are different compared to the other PSD methods. The meaning of the different columns is explained in Table 4 and the same applies to the size of statistical errors for the different samples

det.	time	cal.		data		ROI
		DEP	SEP	$2\nu\beta\beta$	^{42}K	
ANG 2	pI	0.69	0.32	0.52	0.28	1/5
ANG 2	pII	0.70	0.40	0.50	0.33	4/6
ANG 3	pI	0.90	0.51	0.74	0.55	3/13
ANG 3	pII	0.69	0.22	0.49	0.23	1/7
ANG 4	pI	0.78	0.28	0.63	0.41	1/9
ANG 4	pII	0.78	0.45	0.66	0.41	2/8
ANG 5	pI	0.81	0.33	0.65	0.39	2/13
ANG 5	pII	0.67	0.16	0.65	0.39	2/8
RG 1	pI	0.92	0.64	0.78	0.65	2/9
RG 1	pII	0.69	0.23	0.55	0.38	3/6
RG 2	pI	0.86	0.38	0.71	0.44	2/11
RG 2	pII	0.86	0.38	0.65	0.56	1/6

events. The “maximal” background model of GERDA [1] is compatible with a significant fraction of $p+$ events. A pulse shape simulation also shows that the selection corresponds to a volume cut: events close to the $p+$ contact and in the center of the detectors are removed.

4.4 Summary of PSD analysis for coaxial detectors

For the semi-coaxial detectors three different PSD methods are presented following quite different concepts. The one based on an artificial neural network will be used for the $0\nu\beta\beta$ analysis. It has been tuned to yield 90 % survival fraction for DEP events of the 2.6 MeV γ line of ^{208}Tl decays. Most of these events are SSE like $0\nu\beta\beta$ decays. For the study of a possible volume effect and energy dependence of the efficiency, $2\nu\beta\beta$ decays ($\epsilon_{2\nu\beta\beta} = 0.85 \pm 0.02$) and events with energy close the Compton edge (efficiency between 0.85 and 0.95) have been used. We conclude that the $0\nu\beta\beta$ efficiency is $\epsilon_{\text{ANN}} = 0.90^{+0.05}_{-0.09}$.

The event selection of the neural network is cross checked by two other methods. One is based on a likelihood ratio. Training is performed with events at the Compton edge (SSE rich) and at slightly higher energies (almost pure MSE). For a cut with a DEP survival fraction of about 0.8 only 45 % of the events around $Q_{\beta\beta}$ remain.

Another method is only based on the A/E parameter and the current pulse asymmetry A_S . Different signal shapings are tried and an optimization of a signal over background ratio is performed. The DEP survival fraction varies between 0.7 and 0.9 for the different detectors and periods. The background is reduced by a factor of four.

Of the events rejected by the neural network analysis in the 230 keV window around $Q_{\beta\beta}$, about 90 % are also identified as background by both other methods. This gives confidence that the classification is meaningful.

5 Summary

The neural network analysis rejects about 45 % of the events around $Q_{\beta\beta}$ for the semi-coaxial detectors and the A/E selection reduces the corresponding number for BEGe detectors by about 80 %. With a small loss in efficiency the GERDA background index is hence reduced from (0.021 ± 0.002) cts/(keV kg yr) to (0.010 ± 0.001) cts/(keV kg yr). These values are the averages over all data except for the period p2, the “silver” data set, that covers the time period around the BEGe deployment and which corresponds to 6 % of the Phase I exposure [1].

The estimated $0\nu\beta\beta$ decay signal efficiencies for semi-coaxial detectors are $0.90^{+0.05}_{-0.09}$ and for BEGe detectors 0.92 ± 0.02 . Despite this loss of efficiency, the GERDA sensitivity defined as the expected median half life limit of the $0\nu\beta\beta$ decay improves by about 10 % with the application of the pulse shape discrimination.

Acknowledgements The GERDA experiment is supported financially by the German Federal Ministry for Education and Research (BMBF), the German Research Foundation (DFG) via the Excellence Cluster Universe, the Italian Istituto Nazionale di Fisica Nucleare (INFN), the Max Planck Society (MPG), the Polish National Science Centre (NCN), the Foundation for Polish Science (MPD programme), the Russian Foundation for Basic Research (RFBR), and the Swiss National Science Foundation (SNF). The institutions acknowledge also internal financial support.

The GERDA Collaboration thanks the directors and the staff of the LNGS for their continuous strong support of the GERDA experiment.

We acknowledge guidance concerning the $n+$ surface layer modeling from D. Radford.

Open Access This article is distributed under the terms of the Creative Commons Attribution License which permits any use, distribution, and reproduction in any medium, provided the original author(s) and the source are credited.

References

1. M. Agostini et al. (GERDA Collaboration), [arXiv:1306.5084](https://arxiv.org/abs/1306.5084). Eur. Phys. J. C (submitted)
2. K.H. Ackermann et al., Eur. Phys. J. C **73**, 2330 (2013)
3. F.S. Goulding et al., IEEE Trans. Nucl. Sci. **NS-31**, 285 (1984)
4. J. Roth et al., IEEE Trans. Nucl. Sci. **NS-31**, 367 (1984)
5. D. Gonzalez et al., Nucl. Instrum. Methods Phys. Res., Sect. A **515**, 634 (2003)
6. F. Petry et al., Nucl. Instrum. Methods Phys. Res., Sect. A **332**, 107 (1993)
7. B. Majorovits, H.V. Klapdor-Kleingrothaus, Eur. Phys. J. A **6**, 463 (1999)
8. J. Hellmig, H.V. Klapdor-Kleingrothaus, Nucl. Instrum. Methods Phys. Res., Sect. A **455**, 638 (2000)
9. H.V. Klapdor-Kleingrothaus et al., (HDM Collaboration), Eur. Phys. J. A **12**, 147 (2001)
10. C.E. Aalseth et al., (IGEX Collaboration) Phys. Rev. D **65**, 092007 (2002)
11. Canberra Semiconductor NV, Lammerdries 25, B-2439 Olen, Belgium
12. M. Agostini et al., J. Instrum. **6**, P08013 (2011)
13. M. Agostini et al., J. Phys. Conf. Ser. **368**, 012047 (2012)
14. Z. He, Nucl. Instrum. Methods Phys. Res., Sect. A **463**, 250 (2001)
15. M. Agostini et al., J. Instrum. **6**, P03005 (2011). [arXiv:1012.4300](https://arxiv.org/abs/1012.4300)
16. D. Budjáš et al., J. Instrum. **4**, P10007 (2009). [arXiv:0909.4044](https://arxiv.org/abs/0909.4044)
17. M. Agostini, Dissertation, Technical University Munich, 2013
18. E. Aguayo et al., Nucl. Instrum. Methods Phys. Res., Sect. A **701**, 176 (2013). [arXiv:1207.6716](https://arxiv.org/abs/1207.6716)
19. A. Lazzaro, Master's thesis, University Milan Bicocca, 2012
20. M. Barnabé Heider et al., J. Instrum. **5**, P10007 (2010)
21. M. Agostini et al., J. Phys. Conf. Ser. **375**, 042009 (2012)
22. M. Heisel, Dissertation, University of Heidelberg, 2011
23. P. Medina, C. Santos, D. Villaume, in *Procs. of the 21st IEEE (IMTC 04)*, vol. 3 (2004), p. 1828
24. D. Budjáš, Dissertation, University of Heidelberg, 2009
25. M. Barnabé Heider et al., [arXiv:0812.1907](https://arxiv.org/abs/0812.1907)
26. <http://tmva.sourceforge.net>
27. <http://root.cern.ch/root/html/TMultiLayerPerceptron.html>

F

Phase II Run Summary

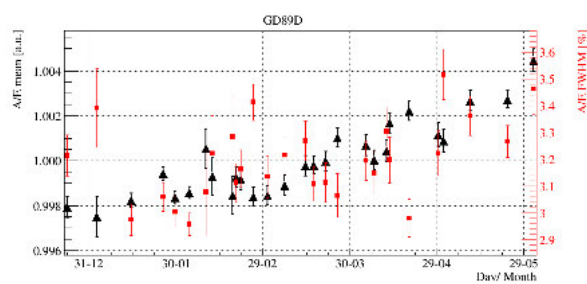
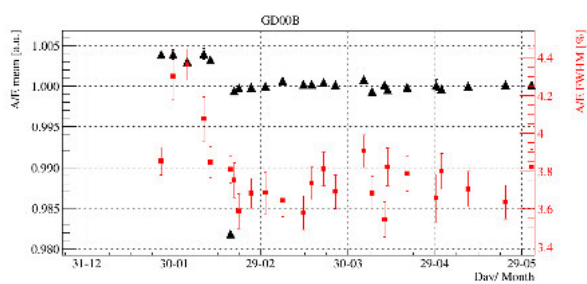
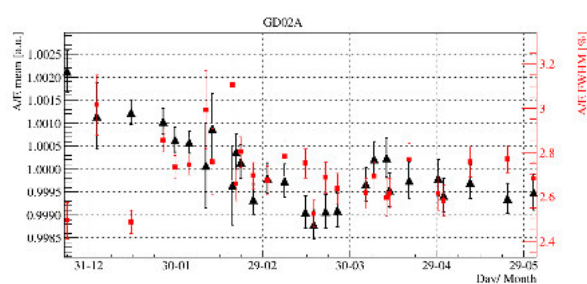
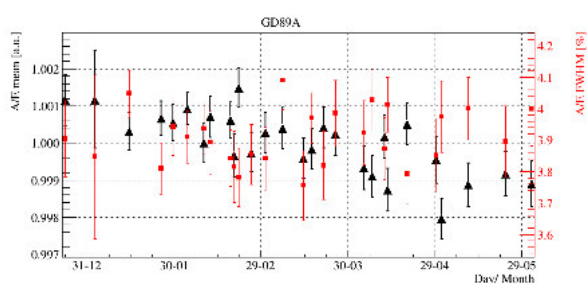
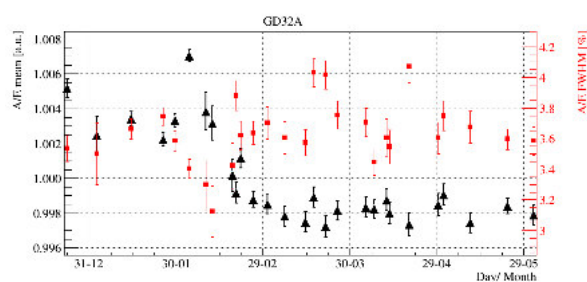
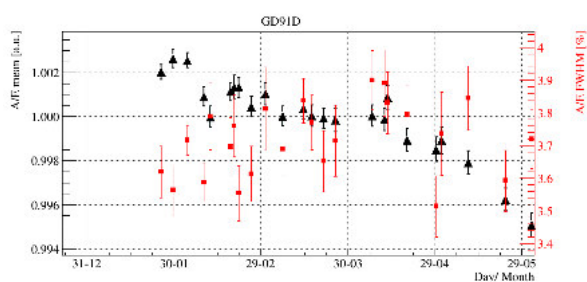
Appendix F. Phase II Run Summary

physics run	start	stop	lifetime [days]	calibration run	detector in AC only
53	20.12.15	25.01.16	18.702	23.12.15 02.01.16 14.01.16 19.01.16	GD00B, GD32B, GD02C, GD91C: HV changes GD00C: tripping during calibrations GD61B, GD61C, GD79C, GD32D: TP drifts GD79C, GD91B: instable
54	25.01.16	29.01.16	3.478	25.01.16	GD61A, GD89B, GD02D, GD91C missing TP
55	29.01.16	03.02.16	4.947	29.01.16	GD79C: TP instable
56	03.02.16	18.02.16	14.543	03.02.16 09.02.16 11.02.16 18.02.16	GD79C: TP instable
57	19.02.16	24.02.16	4.572	19.02.16 21.02.16	GD79C: TP instable
58	25.02.16	09.03.16	11.936	25.02.16 01.03.16 07.03.16	GD79C: TP instable
59	12.03.16	17.03.16	4.669	14.03.16	GD79C, GD79B: TP instable
60	17.03.16	06.04.16	18.504	17.03.16 21.03.16 25.03.16 04.04.16	GD79C, GD79BC: TP instable
61	06.04.16	12.04.16	2.974	07.04.16 11.04.16	GD79C: TP instable
62	12.04.16	29.04.16	15.909	12.04.16 19.04.16 29.04.16	
63	29.04.16	23.05.16	22.357	01.05.16 10.05.16 23.05.16	GD79B, GD32D: TP instable
64	23.05.16	01.06.16	8.522	01.06.16	GD79B, GD32D: TP instable

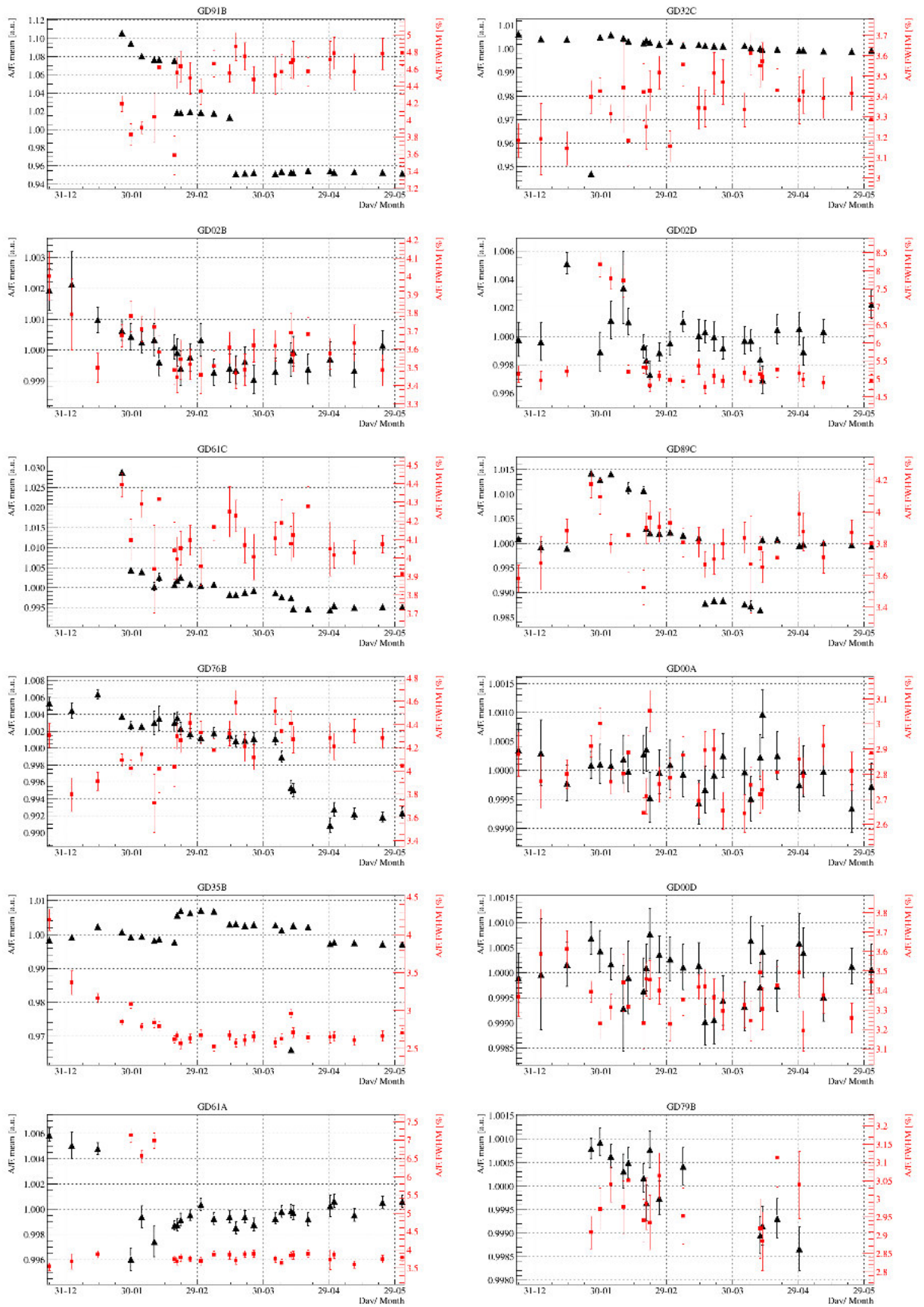
Table F.1: Summary of GERDA Phase II BEGe data set for the first data release in June 2016. Physics data taking is divided into runs. The date of start and stop of each physics run is given, as well as the total lifetime. Regular calibration runs are taken and specified by the date. BEGe channels used for anti-coincidence (AC) only are listed. The test pulse is abbreviated TP. Coaxial detectors are neglected.

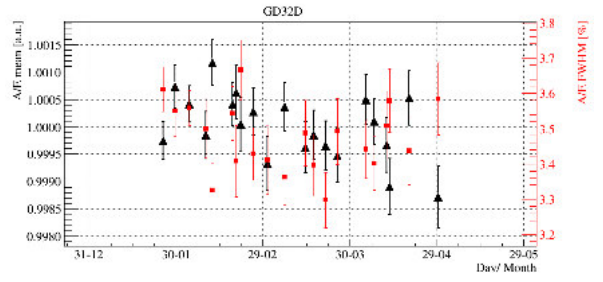
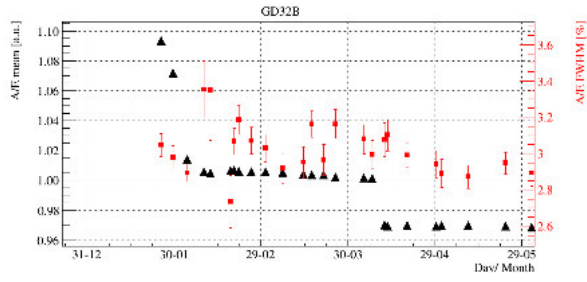
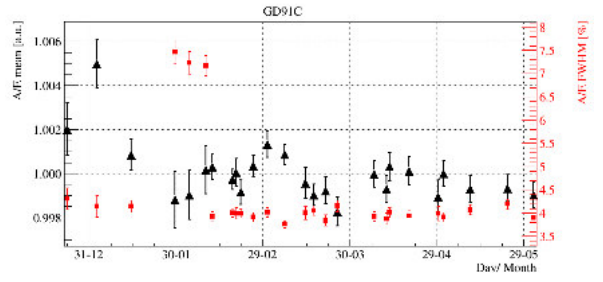
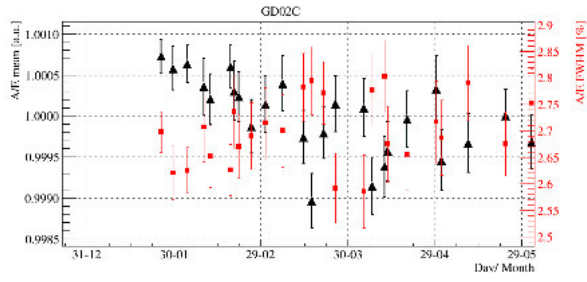
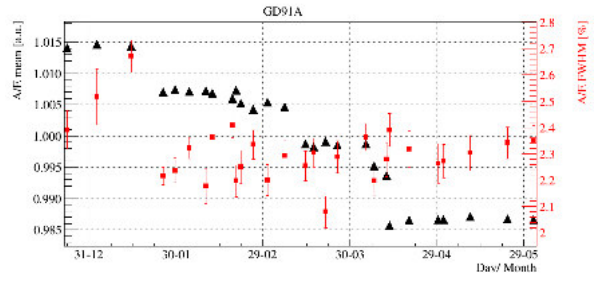
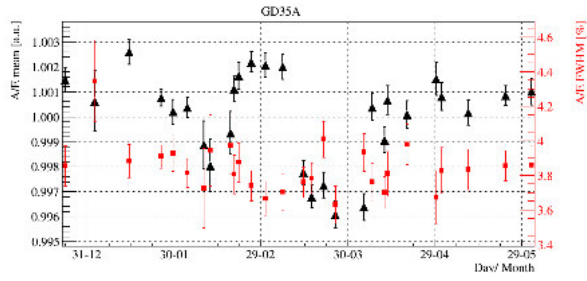
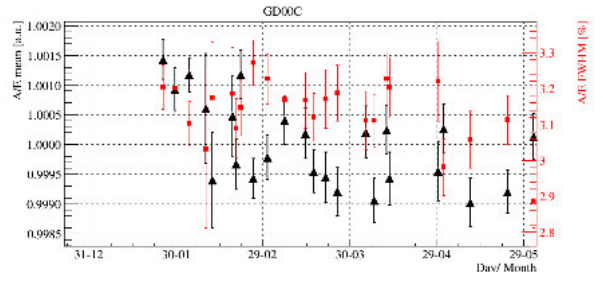
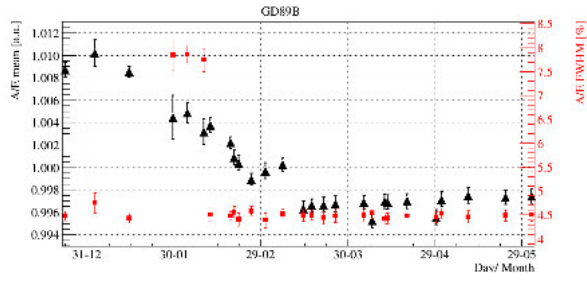
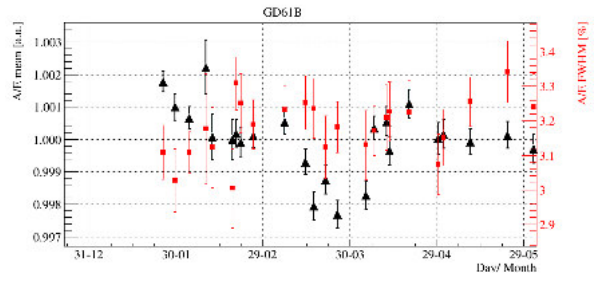
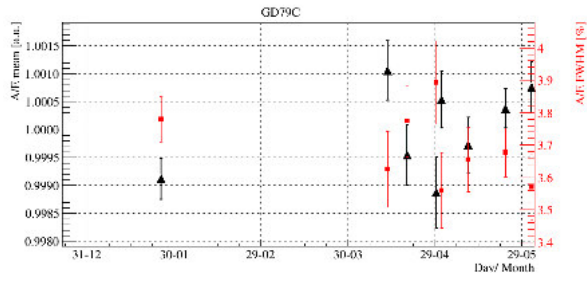
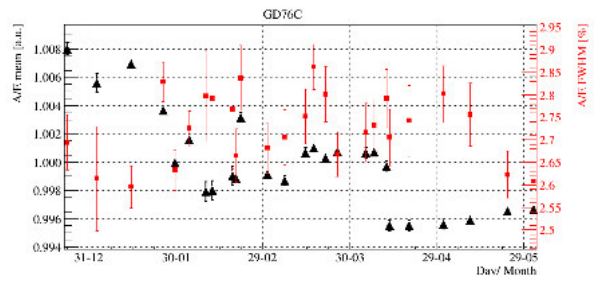
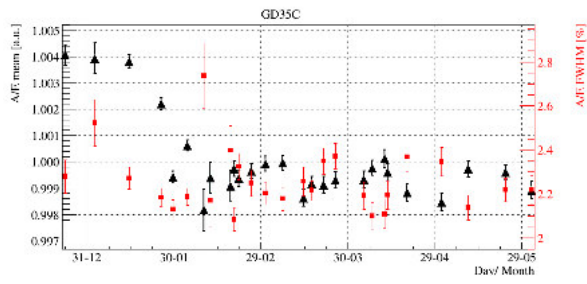


A/E Stability in Phase II



Appendix G. A/E Stability in Phase II





Appendix G. A/E Stability in Phase II

Detector (exposure [kg yr])	period Run (calib)	Detector (exposure [kg yr])	period Run (calib)	Detector (exposure [kg yr])	period Run (calib)	Detector (exposure [kg yr])	period Run (calib)
GD91A (0.224)	53 54-58 59-60 61 62-64	GD35B (0.263)	53 54-56 57-58 59-60 62-62 (04-19) 62 (04-19) - 64	GD02B (0.224)	53-64	GD00B (0.201)	54-56 (02-11) 57-64
GD61A (0.230)	53 56 (11-02) - 64	GD89B (0.195)	53 56 (11-02) - 58 59-64	GD02D		GD91C (0.197)	53 56 (11-02) - 64
GD02A (0.195)	53-64	GD32B (0.187)	56 (09-02) - 60 62-64	GD32A (0.164)	53-57 58-64	GD32C (0.259)	53 55-58 59-64
GD89C (0.213)	53 54-56 57-59 60-61 62-64	GD61C (0.188)	55-58 59-61 62 63-64	GD76B (0.137)	53-58 59-61 62-64	GD00C (0.250)	54-64
GD35C (0.221)	53 55-64	GD76C (0.295)	53 54-61 62-64	GD89D (0.188)	53 54-59 60-64	GD00D (0.291)	53-64
GD79C* (0.104)	62-64	GD35A (0.275)	53 54-56 57-58 59-60 61-64	GD91B		GD61B (0.230)	54-58 59-60 61-64
GD00A (0.177)	53-64	GD02C (0.242)	53-64	GD79B (0.117)	54-58 61-62	GD91D (0.212)	54-64
GD32D (0.160)	54-62	GD89A (0.187)	53-64				

Table G.1: Summary of the periods in which A/E is considered stable. Periods are defined according to physics runs as listed in Table F.1. Calibration runs are indicated in brackets. Detectors are listed according to CC3 channel. GD79C* shares a CC3 with coax detectors. GD02D and GD91B are excluded from the analysis.

Comparison of Background Indices of $0\nu\beta\beta$ Experiments

In Section 2.2 different experimental approaches for the search of $0\nu\beta\beta$ decay are introduced. In this chapter, the background indices (BI) of different current and future experiments are compared. The list is by no means complete.

Some experiments, e.g. GERDA, give the BI for the total mass, while the enrichment fraction is included in the signal efficiency. On the other side, experiments, e.g. KamLAND-Zen, may give the exposure in $\text{kg}\cdot\text{yr}$ of the $\beta\beta$ isotope. Furthermore, the size of the signal region is very different for different detector technologies. Therefore, in a meaningful comparison the achieved or envisioned background indices (BI) need be normalized to the individual energy resolution (FWHM), the signal efficiency and the fraction of the $\beta\beta$ isotope. Table H.1 summarizes the normalized BI for a selection of current and future experiments. In the following the parameters entering the comparison are discussed.

GERDA In GERDA Phase II 36 kg of enriched HPGe detectors are deployed. For the comparison, the energy resolution and the $0\nu\beta\beta$ efficiency of BEGe detectors in Phase II as quoted in Table 7.1 are used as a reference. The efficiency includes enrichment fraction (87%), active volume fraction (89%), $0\nu\beta\beta$ FEP efficiency (92%) as well as PSD and LAr efficiency. A BI of $10^{-3} \frac{\text{counts}}{\text{keV}\cdot\text{kg}\cdot\text{yr}}$ is assumed.

MAJORANA Demonstrator The MAJORANA Demonstrator uses 30 kg of enriched HPGe detectors. For the energy resolution a FWHM of 3 keV at $Q_{\beta\beta}$ is assumed. The Majorana collaboration [102] aims to reach a BI of $1 \cdot 10^{-3} \frac{\text{counts}}{\text{keV}\cdot\text{kg}\cdot\text{yr}}$. The $0\nu\beta\beta$ efficiency includes a signal efficiency of 61% and the enrichment fraction of 88% [102], giving a total $0\nu\beta\beta$ efficiency of 0.52%.

EXO-200 The experiment uses a time projection chamber filled with 150 kg of liquid xenon (LXe) [57] which is isotopically enriched in ^{136}Xe up to 80%. The fiducial volume is 76.5 kg ^{136}Xe mass. A FWHM of 72 keV at $Q_{\beta\beta}$ is assumed. The signal efficiency is 84.6%. EXO-200 achieved a BI of $1.7 \frac{\text{counts}}{\text{keV}\cdot\text{kg}\cdot\text{yr}}$ for a ^{136}Xe exposure of $123.7 \text{kg}\cdot\text{yr}$, corresponding to $2.1 \frac{\text{counts}}{\text{keV}\cdot\text{kg}\cdot\text{yr}}$ of corrected to the ^{136}Xe exposure.

experiment	isotope	mass [kg]	FWHM [keV]	$0\nu\beta\beta$ efficiency	BI [$\frac{\text{counts}}{\text{FWHM}\cdot\text{t}\cdot\text{yr}}$]
GERDA Phase II*	^{76}Ge	36	3	0.60	5
MAJORANA D*	^{76}Ge	30	3	0.54	6
EXO-200*	^{136}Xe	150	72	0.85	179
KamLAND-Zen*	^{136}Xe	383	270	1	50
Cuore	^{130}Te	988	5	0.22	227
NEXT	^{136}Xe	100	19	28	30
nEXO	^{136}Xe	5000	60	0.77	5
SNO+	^{130}Te	468	270	0.001	158
AMORE	^{100}Mo	5	5	0.47	11

Table H.1: Comparison of BI in current and future experiments for the search of $0\nu\beta\beta$ decay. The list is by no means complete. The definition of mass is not uniform. The $0\nu\beta\beta$ efficiency includes signal efficiency and (mass-) fraction of the $\beta\beta$ isotope. The BI is normalized to the FWHM and the signal efficiency. As of November 2016, experiments marked with * are taking data. See text for details.

KamLAND-Zen In Phase II of the experiment 383 kg of xenon doped liquid scintillator are used. The xenon is enriched in ^{136}Xe to 90%. A ^{136}Xe exposure of 504 kg·yr was collected, corresponding to the volume with 1.5 m radius [59]. An energy resolution of 270 keV FWHM at $Q_{\beta\beta}$ is assumed. The enrichment fraction is contained in the exposure, a signal efficiency of 1 is assumed. 11 events in a 400 keV window around $Q_{\beta\beta}$ in a volume of 1 m radius were observed, corresponding to 149 kg·yr ^{136}Xe exposure.

CUORE The experiment operates 988 kg of $^{\text{nat}}\text{TeO}_2$. The signal efficiency after analysis cuts of 81% and the energy resolution at $Q_{\beta\beta}$, 5 keV, are taken from CUORE-0 [121]. The natural abundance of ^{130}Te is 35%, the mass fraction 79% in the $^{\text{nat}}\text{TeO}_2$: the total $0\nu\beta\beta$ efficiency is 22%. CUORE aims to reach a $\text{BI} = 10^{-2} \frac{\text{counts}}{\text{keV}\cdot\text{kg}\cdot\text{yr}}$.

NEXT The NEXT experiment [60] is a high pressure gas xenon time projection chamber (TPC). The experiment plans to use 100-150 kg of enriched xenon (90%). The aim is to reach an energy resolution of <1% FWHM at $Q_{\beta\beta}$. An energy resolution of 19 keV (corresponding to 0.75% FWHM at $Q_{\beta\beta}$), a BI of $4\cdot 10^{-4} \frac{\text{counts}}{\text{keV}\cdot\text{kg}\cdot\text{yr}}$ and a $0\nu\beta\beta$ signal efficiency of 28% are assumed [122].

nEXO The nEXO detector [58] will be a LXe TPC filled with 5 t of enriched xenon. The collaboration aims at an enrichment fraction of 90% or higher and an energy resolution of 60 keV (FWHM) at $Q_{\beta\beta}$. The same signal efficiency as for EXO-200 is assumed, giving a $0\nu\beta\beta$ efficiency of 77% with the enrichment fraction. The BI goal is to reach $4 \frac{\text{counts}}{\text{ROI}\cdot\text{t}\cdot\text{yr}}$ [123].

SNO+ The SNO+ experiment [55] plans to use 780 t liquid scintillator. An energy resolution of 270 keV at $Q_{\beta\beta}$ is assumed. The fiducial volume (FV) corresponds to 20% of the total mass, i.e. 156 t. With a scintillator loading of 0.3% Tl, this corresponds to 468 kg natural tellurium. All together the $0\nu\beta\beta$ efficiency is 0.1%. The collaboration expects 107 background events within 230 keV in the FV in five years.

AMORE In Phase I of the AMORE experiment [51] 5 kg of $^{40}\text{Ca}^{100}\text{MoO}_4$ crystals. A FWHM of 5 keV at $Q_{\beta\beta}$ is assumed. The mass fraction of ^{100}Mo is 49 %, the material will be isotopically enriched to 95 %: the total $0\nu\beta\beta$ is 47 % without efficiency loss due to analysis cuts. The collaboration aims to achieve a BI of $10^{-3} \frac{\text{counts}}{\text{keV} \cdot \text{kg} \cdot \text{yr}}$.

Bibliography

- [1] H. V. Klapdor-Kleingrothaus et al. Latest results from the Heidelberg-Moscow double beta decay experiment. *Eur. Phys. J.*, A12:147–154, 2001.
- [2] C. E. Aalseth et al. The IGEX Ge-76 neutrinoless double beta decay experiment: Prospects for next generation experiments. *Phys. Rev.*, D65:092007, 2002.
- [3] D. Budjáš. *Germanium detector studies in the framework of the GERDA experiment*. PhD thesis, Heidelberg U., 2009.
- [4] M. Agostini et al. Background free search for neutrinoless double beta decay with GERDA Phase II. *submitted to nature*.
- [5] M. Agostini et al. Pulse shape discrimination for GERDA Phase I data. *Eur. Phys. J.*, C73(10):2583, 2013.
- [6] M. Agostini et al. Results on Neutrinoless Double- β Decay of ^{76}Ge from Phase I of the GERDA Experiment. *Phys. Rev. Lett.*, 111(12):122503, 2013.
- [7] Lindner, M. and Rodejohann, W. Introduction to the Standard Model of Particle Physics II . University Lecture, Heidelberg U., 2010.
- [8] Lindner, M. and Marrodán Undagoitia, T. Neutrino physics: Theory and experiment. University Lecture, Heidelberg U., 2013.
- [9] K. A. Olive et al. Review of Particle Physics. *Chin. Phys.*, C38:090001, 2014.
- [10] C. Giunti and C. W. Kim. *Fundamentals of Neutrino Physics and Astrophysics*. Oxford, UK: Univ. Pr. (2007) 710 p, 2007. ISBN-9780198508717.
- [11] K. Zuber. *Neutrino physics*. Boca Raton: USA: CRC Pr. (2012) 448p, 2004. ISBN-9780750307505.
- [12] N. Schmitz. *Neutrino Physik*. Stuttgart: Teubner, 1997. ISBN-3519032368.
- [13] C. S. Wu, E. Ambler, R. W. Hayward, D. D. Hoppes, and R. P. Hudson. Experimental Test of Parity Conservation in Beta Decay. *Phys. Rev.*, 105:1413–1414, 1957.

- [14] M. Goldhaber, L. Grodzins, and A. W. Sunyar. Helicity of Neutrinos. *Phys. Rev.*, 109:1015–1017, 1958.
- [15] R. Davis. Solar neutrinos. II: Experimental. *Phys. Rev. Lett.*, 12:303–305, 1964.
- [16] R. Davis. A review of the Homestake solar neutrino experiment. *Prog. Part. Nucl. Phys.*, 32:13–32, 1994.
- [17] J. N. Bahcall and R. K. Ulrich. Solar models, neutrino experiments, and helioseismology. *Rev. Mod. Phys.*, 60:297–372, Apr 1988.
- [18] P. Anselmann et al. Solar neutrinos observed by GALLEX at Gran Sasso. *Physics Letters B*, 285(4):376 – 389, 1992.
- [19] M. Altmann et al. Complete results for five years of GNO solar neutrino observations. *Physics Letters B*, 616(3–4):174 – 190, 2005.
- [20] J.N Abdurashitov et al. Measurement of the solar neutrino capture rate in SAGE. *Nuclear Physics B - Proceedings Supplements*, 118:39 – 46, 2003.
- [21] S. M. Bilenky. Bruno Pontecorvo and the neutrino. *Physics-Uspokhi*, 57(5):489, 2014.
- [22] S. Fukuda et al. The Super-Kamiokande detector . *Nuclear Instruments and Methods in Physics Research Section A: Accelerators, Spectrometers, Detectors and Associated Equipment*, 501(2–3):418 – 462, 2003.
- [23] Y. Fukuda et al. Measurement of the flux and zenith angle distribution of upward through going muons by Super-Kamiokande. *Phys. Rev. Lett.*, 82:2644–2648, 1999.
- [24] T. Kajita, E. Kearns, and M. Shiozawa. Establishing atmospheric neutrino oscillations with Super-Kamiokande. *Nuclear Physics*, B908:14 – 29, 2016. Neutrino Oscillations: Celebrating the Nobel Prize in Physics 2015.
- [25] Y. Fukuda et al. Evidence for oscillation of atmospheric neutrinos. *Phys. Rev. Lett.*, 81:1562–1567, Aug 1998.
- [26] E. Kearns. Super-K at Boston U., ATMOSPHERIC NEUTRINOS. <http://hep.bu.edu/~superk/atmnu/>. Accessed: 2016.
- [27] N. Jelley, A. B. McDonald, and R. G. H. Robertson. The Sudbury Neutrino Observatory. *Ann. Rev. Nucl. Part. Sci.*, 59:431–465, 2009.
- [28] Q. R. Ahmad et al. Direct evidence for neutrino flavor transformation from neutral current interactions in the Sudbury Neutrino Observatory. *Phys. Rev. Lett.*, 89:011301, 2002.
- [29] The nobel prize in physics 2015. http://www.nobelprize.org/nobel_prizes/physics/laureates/2015/. Accessed January 4, 2016.
- [30] G. Bellini, L. Ludhova, G. Ranucci, and F. L. Villante. Neutrino oscillations. *Adv. High Energy Phys.*, 2014:191960, 2014.

-
- [31] S. P. Mikheyev and A. Yu. Smirnov. Resonant amplification of ν oscillations in matter and solar-neutrino spectroscopy. *Il Nuovo Cimento C*, 9(1):17–26, 1986.
- [32] Ch. Kraus et al. Final results from phase II of the Mainz neutrino mass search in tritium beta decay. *Eur. Phys. J.*, C40:447–468, 2005.
- [33] P. A. R. Ade et al. Planck 2013 results. XVI. Cosmological parameters. *Astron. Astrophys.*, 571:A16, 2014.
- [34] B. Povh, K. Rith, C. Scholz, and F. Zetsche. *Teilchen und Kerne. Eine Einführung in die physikalischen Konzepte*. Springer-Verlag GmbH, sixth edition, 2004. ISBN-3540210652.
- [35] M. Goepfert-Mayer. Double beta-disintegration. *Phys. Rev.*, 48:512–516, Sep 1935.
- [36] Y. Ren and Z. Ren. Systematic law for half-lives of double- β decay with two neutrinos. *Phys. Rev. C*, 89:064603, Jun 2014.
- [37] Z. Sujkowski and S. Wycech. Neutrinoless double electron capture: A tool to search for majorana neutrinos. *Phys. Rev. C*, 70:052501, Nov 2004.
- [38] W. H. Furry. On transition probabilities in double beta-disintegration. *Phys. Rev.*, 56:1184–1193, Dec 1939.
- [39] W. Rodejohann. Neutrino-less Double Beta Decay and Particle Physics. *Int. J. Mod. Phys.*, E20:1833–1930, 2011.
- [40] J. Schechter and J. W. F. Valle. Neutrinoless double- β decay in $SU(2)\times U(1)$ theories. *Phys. Rev. D*, 25:2951–2954, Jun 1982.
- [41] Michael Duerr, Manfred Lindner, and Alexander Merle. On the Quantitative Impact of the Schechter-Valle Theorem. *JHEP*, 1106:091, 2011.
- [42] M. Dürr. *Phenomenological Aspects of Theories for Baryon and Lepton Number Violation*. PhD thesis, Heidelberg U., 2013.
- [43] W. Maneschg. Review of neutrinoless double beta decay experiments: Present status and near future. *Nucl. Part. Phys. Proc.*, 260:188–193, 2015.
- [44] Y. Shirai. Results and Future Plans for the KamLAND-ZEN. Talk at XXVII International Conference on Neutrino Physics and Astrophysics (Neutrino 2016), London, July 2016.
- [45] F. Deppisch and H. Päs. Pinning down the mechanism of neutrinoless double β decay with measurements in different nuclei. *Phys. Rev. Lett.*, 98:232501, Jun 2007.
- [46] R. G. H. Robertson. Empirical Survey of Neutrinoless Double Beta Decay Matrix Elements. *Mod. Phys. Lett.*, A28:1350021, 2013.
- [47] T. Iida et al. Status and future prospect of ^{48}Ca double beta decay search in CANDLES. *Journal of Physics: Conference Series*, 718(6):062026, 2016.
- [48] K. H. Ackermann et al. The GERDA experiment for the search of $0\nu\beta\beta$ decay in ^{76}Ge . *Eur. Phys. J.*, C73(3):2330, 2013.

- [49] N. Abgrall et al. The Majorana Demonstrator Neutrinoless Double-Beta Decay Experiment. *Adv. High Energy Phys.*, 2014:365432, 2014.
- [50] D. Waters. Latest Results from NEMO-3 and Status of the SuperNEMO Experiment. Talk at XXVII International Conference on Neutrino Physics and Astrophysics (Neutrino 2016), London, July 2016.
- [51] V. Alenkov et al. Technical Design Report for the AMoRE $0\nu\beta\beta$ Decay Search Experiment. 2015. arXiv:1512.05957.
- [52] R. Arnold et al. Results of the search for neutrinoless double- β decay in ^{100}Mo with the NEMO-3 experiment. *Phys. Rev.*, D92:072011, Oct 2015.
- [53] J. Ebert et al. The COBRA demonstrator at the LNGS underground laboratory. *Nuclear Instruments and Methods in Physics Research Section A: Accelerators, Spectrometers, Detectors and Associated Equipment*, 807:114 – 120, 2016.
- [54] K. Zuber. COBRA - A new approach to double beta decay. *Nuclear Physics B - Proceedings Supplements*, 138:236 – 238, 2005.
- [55] S. Andringa et al. Current Status and Future Prospects of the SNO+ Experiment. *Adv. High Energy Phys.*, 2016:6194250, 2016.
- [56] D. R. Artusa et al. Searching for neutrinoless double-beta decay of ^{130}Te with CUORE. *Adv. High Energy Phys.*, 2015:879871, 2015.
- [57] J. B. Albert et al. Search for Majorana neutrinos with the first two years of EXO-200 data. *Nature*, 510:229–234, 2014.
- [58] L. Yang. Status and Prospects for the EXO-200 and nEXO Experiments. Talk at XXVII International Conference on Neutrino Physics and Astrophysics (Neutrino 2016), London, July 2016.
- [59] A. Gando et al. Search for Majorana Neutrinos near the Inverted Mass Hierarchy Region with KamLAND-Zen. *Phys. Rev. Lett.*, 117(8):082503, 2016. [Addendum: *Phys. Rev. Lett.*117,no.10,109903(2016)].
- [60] F. Monrabal and the Next Collaboration. Discovering neutrinoless double beta decay with next100 detector. *Journal of Physics: Conference Series*, 375(4):042019, 2012.
- [61] A. Barabash. Review of double beta decay experiments. In *Proceedings, 16th Lomonosov Conference on Elementary Particle Physics: Particle Physics at the Year of Centenary of Bruno Pontecorvo: Moscow, Russia, August 22-28, 2013*, pages 295–299, 2015. arXiv:1403.2870.
- [62] H. V. Klapdor-Kleingrothaus, I. V. Krivosheina, A. Dietz, and O. Chkvorets. Search for neutrinoless double beta decay with enriched Ge-76 in Gran Sasso 1990-2003. *Phys. Lett.*, B586:198–212, 2004.
- [63] L. Canonica. Status and prospects for CUORE. Talk at XXVII International Conference on Neutrino Physics and Astrophysics (Neutrino 2016), London, July 2016.

-
- [64] G. Drexlin. Direct neutrino mass searches. *Nuclear Physics B - Proceedings Supplements*, 138:282 – 288, 2005.
- [65] G. Knoll. *Radiation Detection and Measurement (4th ed.)*. John Wiley and Sons, New York, 1989. ISBN-0-471-81504-7.
- [66] H. Kolanoski and N. Wermes. *Teilchendetektoren*. Springer, 2016. ISBN 978-3-662-45350-6.
- [67] Ortec, AMETEK, Inc. Review of the Physics of Semiconductor Detectors. <http://www.ortec-online.com>. Accessed: 2016.
- [68] B. Lehnert. *Search for $2\nu\beta\beta$ Excited State Transitions and HPGe Characterization for Surface Events in GERDA Phase II*. PhD thesis, Technische Universität Dresden, 2016.
- [69] M. Agostini et al. The background in the $0\nu\beta\beta$ experiment GERDA. *Eur. Phys. J.*, C74(4):2764, 2014.
- [70] M. Barnabe-Heider, D. Budjáš, K. Gusev, and S. Schönert. Operation and performance of a bare broad-energy germanium detector in liquid argon. *JINST*, 5:P10007, 2010.
- [71] M. Agostini et al. Limits on uranium and thorium bulk content in GERDA Phase I detectors. 2016. arXiv:1611.06884.
- [72] Canberra Industries, Inc. Broad Energy Germanium Detectors (BEGe). <http://www.canberra.com/products/detectors/germanium-detectors.asp>. Accessed: 2016.
- [73] K. Freund et al. The Performance of the Muon Veto of the GERDA Experiment. *Eur. Phys. J.*, C76:298, 2016.
- [74] K. von Sturm. *Confined event samples using Compton coincidence measurements for signal and background studies in the GERDA experiment*. PhD thesis, Università degli Studi di Padova, 2016.
- [75] T. Bode. *The neutrinoless double beta decay experiment GERDA Phase II: a novel ultra-low background contacting technique for germanium detectors and first background data*. PhD thesis, TU München, 2016.
- [76] S. Riboldi. private communication.
- [77] K. T. Knöpfle. Upgrade of the GERDA experiment. *PoS*, TIPP2014:109, 2014.
- [78] A.-K. Schütz and K. von Sturm. Background model. Talk at GERDA Collaboration Meeting, June 2016.
- [79] M. Agostini et al. LArGe: active background suppression using argon scintillation for the Gerda $0\nu\beta\beta$ -experiment. *Eur. Phys. J.*, C75(10):506, 2015.
- [80] A. Wegmann. *Characterization of the liquid argon veto of the GERDA experiment and its application for the measurement of the ^{76}Ge half-life*. PhD thesis, Heidelberg U., 2017, to be published.

- [81] C. Wiesinger. Active background suppression with the liquid argon scintillation veto of GERDA Phase II. Proceeding XXVII International Conference on Neutrino Physics and Astrophysics (Neutrino 2016), London, July 2016, to be published.
- [82] M. Agostini et al. Upgrade for Phase II of the GERDA experiment. *manuscript in preparation*.
- [83] A. Kirsch. *Search for the neutrinoless double β -decay in GERDA Phase I using a Pulse Shape Discrimination technique*. PhD thesis, Heidelberg U., 2014.
- [84] NIST. Stopping Power and Range Tables for Electrons, Protons and Helium. <http://www.nist.gov/pml/data/star>. Accessed: 2016.
- [85] M. Boswell et al. MaGe-a Geant4-based Monte Carlo Application Framework for Low-background Germanium Experiments. *IEEE Trans. Nucl. Sci.*, 58:1212–1220, 2011.
- [86] M. Agostini, C. A. Ur, D. Budjáš, E. Bellotti, R. Brugnera, C. M. Cattadori, A. di Vacri, A. Garfagnini, L. Pandola, and S. Schönert. Signal modeling of high-purity Ge detectors with a small read-out electrode and application to neutrinoless double beta decay search in Ge-76. *JINST*, 6:P03005, 2011.
- [87] H. Zhong. Review of the Shockley-Ramo Theorem and its application in semiconductor gamma-ray detectors. *Instruments and Methods in Physics Research A*, 463(1-2):250–267, 2001.
- [88] B. Bruyneel, B. Birkenbach, and P. Reiter. Pulse shape analysis and position determination in segmented HPGe detectors: The AGATA detector library. *Eur. Phys. J.*, A52(3):70, 2016.
- [89] M. Salathe. *Study on modified point contact germanium detectors for low background applications*. PhD thesis, Heidelberg U., 2015.
- [90] B. Schwingenheuer. private communication.
- [91] D. Budjáš. private communication.
- [92] M. Agostini, L. Pandola, P. Zavarise, and O. Volynets. GELATIO: A General framework for modular digital analysis of high-purity Ge detector signals. *JINST*, 6:P08013, 2011.
- [93] R. B. Firestone. *Table of Isotopes*. Wiley-Interscience, 1996.
- [94] P. Cennini et al. On atmospheric ^{39}Ar and ^{42}Ar abundance. *Nucl. Instrum. Meth.*, A356(2-3):526–529, 1995.
- [95] A. J. Peurrung, T. W. Bowyer, R. A. Craig, and P. L. Reeder. Expected atmospheric concentration of ^{42}Ar . *Nucl. Instrum. Meth.*, A396:425–426, 1997.
- [96] E. Aguayo et al. Cosmic Ray Interactions in Shielding Materials. *Prepared for the U.S. Department of Energy under Contract DE-AC05-76RL01830*, (PNNL-20693), July 2011.
- [97] Laboratoire National Henri Becquerel. Recommended Data. http://www.nucleide.org/DDEP_WG/DDEPdata.htm. Accessed: 2016.

-
- [98] C. E. Aalseth et al. The IGEX experiment revisited: A Response to the critique of Klapdor-Kleingrothaus, Dietz and Krivosheina. *Phys. Rev.*, D70:078302, 2004.
- [99] I. Abt, A. Caldwell, D. Gutknecht, K. Kroninger, M. Lampert, X. Liu, B. Majorovits, D. Quirion, F. Stelzer, and P. Wendling. Characterization of the first true coaxial 18-fold segmented n-type prototype detector for the GERDA project. *Nucl. Instrum. Meth.*, A577:574–584, 2007.
- [100] I. Abt, A. Caldwell, K. Kroninger, J. Liu, X. Liu, and B. Majorovits. Identification of photons in double beta-decay experiments using segmented germanium detectors: Studies with a GERDA Phase II prototype detector. *Nucl. Instrum. Meth.*, A583:332–340, 2007.
- [101] R.J. Cooper, D.C. Radford, K. Lagergren, James F. Colaresi, Larry Darken, R. Henning, M.G. Marino, and K. Michael Yocum. A pulse shape analysis technique for the majorana experiment. *Nuclear Instruments and Methods in Physics Research Section A: Accelerators, Spectrometers, Detectors and Associated Equipment*, 629(1):303 – 310, 2011.
- [102] S. Elliott. Initial Results from the MAJORANA DEMONSTRATOR. Talk at XXVII International Conference on Neutrino Physics and Astrophysics (Neutrino 2016), London, July 2016.
- [103] M. Agostini et al. Production, characterization and operation of ^{76}Ge enriched BEGe detectors in GERDA. *Eur. Phys. J.*, C75(2):39, 2015.
- [104] V. Wagner. Investigation of Pulse Shape Performance of the First GERDA Phase II Detectors. Diploma thesis, Heidelberg U., 2012.
- [105] M. Wojcik and G. Zuzel. Behavior of the ^{222}Rn daughters on copper surfaces during cleaning. *AIP Conference Proceedings*, 897(1):53–58, 2007.
- [106] M. Walter. *Background Reduction Techniques for the GERDA Experiment*. PhD thesis, Zurich U., 2015.
- [107] K. Gusev. GERDA status and background levels. Talk at NG-Ge76 meeting 28-30 October 2016, Atlanta.
- [108] M. Agostini et al. Full BEGe Characterization. manuscript in preparation.
- [109] A. Lazzaro. *tba*. PhD thesis, TU München, 2017, to be published.
- [110] C. Wiesinger. private communication.
- [111] C. Wiesinger. *tba*. PhD thesis, TU München, 2017, to be published.
- [112] M. Maneschg et al. Full Charge Collection Depth and Active Volume of GERDA Phase II BEGe detectors. internal note (GSTR-16-002).
- [113] G. Benato. *Data Reconstruction and Analysis for the GERDA Experiment*. PhD thesis, Zurich U., 2015.

- [114] L. Pandola. Parameters and facts for the analysis dataset of the $0\nu\beta\beta$ decay of GERDA Phase II. internal note (GSTR-16-007).
- [115] M. Agostini et al. Limit on Neutrinoless Double Beta Decay of ^{76}Ge by GERDA. *Phys. Procedia*, 61:828–837, 2015.
- [116] G. Cowan, K. Cranmer, E. Gross, and O. Vitells. Asymptotic formulae for likelihood-based tests of new physics. *Eur. Phys. J.*, C71:1554, 2011. [Erratum: *Eur. Phys. J.*C73,2501(2013)].
- [117] J. Engel and J. Menéndez. Status and Future of Nuclear Matrix Elements for Neutrinoless Double-Beta Decay: A Review. 2016. arXiv:1610.06548.
- [118] S. Stoica and M. Mirea. New calculations for phase space factors involved in double- β decay. *Phys. Rev. C*, 88:037303, Sep 2013.
- [119] B. Schwingenheuer. Possible upgrade of gerda. <https://agenda.infn.it/getFile.py/access?contribId=3&sessionId=1&resId=0&materialId=slides&confId=9608>. Accessed November, 2016.
- [120] M. Agostini, L. Pandola, and P. Zavarise. Off-line data processing and analysis for the GERDA experiment. *Journal of Physics: Conference Series*, 368(1):012047, 2012.
- [121] K. Alfonso et al. Search for Neutrinoless Double-Beta Decay of ^{130}Te with CUORE-0. *Phys. Rev. Lett.*, 115:102502, Sep 2015.
- [122] J. Martín-Albo et al. Sensitivity of NEXT-100 to neutrinoless double beta decay. *JHEP*, 05:159, 2016.
- [123] A. Pocar. Neutrinoless Double Beta-Decay Experiment II - Xenon TPCs. Talk at workshop Neutrino Mass: From the Terrestrial Laboratory to the Cosmos, UMass Amherst 2015.

Acknowledgements

I consider myself very lucky to have met so many supporting people who I had the pleasure to work with during my PhD thesis. Many fruitful discussions have deepened my understanding of the search for the $0\nu\beta\beta$ decay and for germanium detectors. They all have contributed one way or the other to the work presented in this thesis. In particular, I would like to thank

- Prof. Manfred Lindner for providing the opportunity to write this thesis. For all the support and the many, many trips to LNGS, meetings and an unforgettable summer school at SNOlab.
- Dr. Loredana Gastaldo who agreed to be the second referee. I greatly enjoyed her lecture on low temperature detectors.
- Dr. Bernhard Schwingenheuer for introducing me to the integration team. For all his support during the last four years. With his great knowledge he always had answers to hardware and analysis related questions. Finally, a great thanks for providing the starting code for the statistical analysis on the $T_{1/2}$ limit. Not to forget the proofreading.
- Dr. Werner Maneschg for his excellent support throughout the last four years. He always had an open door to listen to my concerns and questions. Also, many thanks for the thorough proofreading.
- the full integration team. I learned a lot during this intense but fulfilling time at LNGS. A special thanks to Dr. Konstantin Gusev. I am particularly proud that he trusted me mounting even enriched semi-coaxial detectors. I also would like to thank Dr. Tobias Bode who introduced me to the skills of wire bonding.
- Dr. Dušan Budjáš who introduced me to the A/E “world” and put me on board for the Phase I analysis. I am very grateful for the many fruitful discussions on the analysis.
- Dr. Luciano Pandola for the support, many helpful discussions and especially his patience, even if I overwrote freshly unblinded data (I suppose I still owe him at least a coffee).
- Dr. Matteo Agostini for his great support and all the fruitful discussions, be it on A/E , statistics or anything else.

- Janina Hakenmüller for providing the MC of the GERDA Phase II calibration runs which I used as a black box to motivate pulse shape discrimination. And Dr. Andrea Kirsch for helping me with the pulse shape simulations I performed in the same context. I would like to thank Andrea Lazzaro for the processing of the template pulses.
- my “Theoretiker des Vertrauens”, among them Dr. Pascal Humbert, Johannes Welter and Dr. Partick Ludl.
- Dr. Stefan Schoppmann and Ludwig Rauch for the many helpful discussions on statistics, even on short notice.
- Anne Wegmann, my “fellow sufferer”: “Geteiltes Leid, ist halbes Leid” (Zitat B. Schwingenheuer).
- the GERDA collaboration for many unforgettable meetings, as well as the whole GERDA group and the Lindner division at the MPIK that made my PhD an unforgettable experience.

Der letzte Dank gilt meiner Familie, für ihre unendliche und bedingungslose Unterstützung. Insbesondere möchte ich auch Thorsten Heußler für seine Unterstützung und Geduld während der letzten Jahre danken. Vor allem in der Endphase der Arbeit hat er sich als meine wichtigste Stütze erwiesen, Zweifel ausgeräumt und mich wieder zum lachen gebracht.

Vielen Dank!